



Electronic Structure Engineering via Functionalization of Two-Dimensional Quantum Materials

INAUGURAL-DISSERTATION

zur

Erlangung des Doktorgrades
der Mathematisch-Naturwissenschaftlichen Fakultät
der Universität zu Köln

vorgelegt von

M.SC. NIELS EHLEN

aus

BAD HONNEF

Köln, 2021

Berichterstatter (Gutachter):

Prof. Dr. Alexander GRÜNEIS

Prof. Dr. Markus GRÜNINGER

Prof. Dr. Andrea DAMASCELLI

Vorsitzender:

Prof. Dr. Achim ROSCH

Beisitzer:

Dr. Wouter JOLIE

Tag der mündlichen Prüfung: 16.06.2021

Contents

List of Figures	iii
1 Introduction	3
2 Van der Waals Materials	9
2.1 Band Structure Engineering of Two-Dimensional Matter	11
2.2 From Bulk Dispersion to Two-Dimensions	14
2.3 Black Phosphorus	18
2.4 Molybdenum Disulfide	22
2.5 Monolayer and Bilayer Graphene	27
2.5.1 Monolayer Graphene	27
2.5.2 Bilayer Graphene	30
3 Theory	35
3.1 Process of Photoemission	35
3.1.1 Photoemission Theory	36
3.2 Tight-Binding Approximation	39
3.2.1 Tight-Binding in Second Quantization	42
3.3 Many Body Effects in Angle-Resolved Photoemission Spectra	44
3.4 Spin-Orbit Coupling	52
4 Methods	57
4.1 Tight Binding Formalism	57
4.2 Angle-Resolved Photoemission Spectroscopy	58
4.2.1 Fermi Surface Mapping	59
4.3 Photoluminescence Spectroscopy	64
4.4 Sample Preparation	67
4.4.1 Black Phosphorus	67
4.4.2 Molybdenum Disulfide/Graphene/Iridium(111)	67

4.4.3	Bilayer Graphene/Iridium(111)	69
5	Results	71
5.1	Band Structure Engineering in Black Phosphorus	71
5.1.1	Insight into the Band Dispersion of Few-Layer Phosphorene from Measurements of the Three-Dimensional Bulk Crystal	73
5.1.2	Inducing Surface Band Inversion and a Surface Resonance State in Black Phosphorus via Caesium Functionalization	88
5.2	Optical Properties in Heterostructures of Epitaxial Monolayer MoS2 on Graphene/Ir(111) Substrates.	101
5.3	Strained Alkali Metal Quantum Wells Synthesized on Bilayer Graphene	115
6	Conclusions	129
	Bibliography	135
A	Appendix	159
A.1	Momentum Space Wave Function of the Infinite Quantum Well	159
A.2	Works by the Author	161
A.2.1	Summaries of other works related to the topic of this thesis	161
A.2.2	List of Publications	165
A.2.3	List of Major Presentations	167
A.3	Dedication and Thanks	168
A.4	Data Availability	170
A.5	Used Tools	171
A.6	Declaration of Authorship	172

List of Figures

2.1	Development of Out-of-Plane Dispersion From $N = 1$ Layer to $N = 4$ Layers	16
2.2	Structural and Electronic Properties of Black Phosphorus	19
2.3	Structures of Monolayer MoS ₂	23
2.4	Band Structure of MoS ₂	24
2.5	Band Structure of Monolayer Graphene	28
2.6	Band Structure of AA-Stacked Bilayer Graphene	31
2.7	Band Structure of AB-Stacked Bilayer Graphene	33
3.1	Schematic for Photoemission Spectroscopy	36
3.2	Many Body Effects in Angle-Resolved Photoemission Spectroscopy	49
3.3	Rashba and Dresselhaus Spin Orbit Coupling	54
4.1	Transform Between Laboratory and Sample Frame of Reference in Angle-Resolved Photoemission Spectroscopy	60
4.2	Schematic of the Photoluminescence Process	66
4.3	Low-Energy Electron Diffraction Image of a Cleaved Black Phosphorus Surface.	67
4.4	Low-Energy Electron Diffraction Images of MoS ₂	68
4.5	Low-Energy Electron Diffraction Images of Mono- and Bilayer Graphene	69

Abstract

The goal of this thesis is to investigate and establish methods of electronic structure engineering in (quasi-)two-dimensional quantum materials. Since the inception of the field of two-dimensional matter, many production methods have been established for a broad range of materials. While these crystals by themselves show many interesting properties from a fundamental physics perspective, one of their main advantages is their “all-surface” nature. This property allows for manipulation of the inherent electronic behaviour of a given material from the outside, often leading to fundamental changes in the electronic structure. As part of the maturation of the field, it is important to establish methods for band structure engineering and investigate their effects on the known materials. This thesis thus focuses on ways to manipulate the electronic properties in three distinct material families.

In black phosphorus, the electronic structure of the pristine bulk crystal is established using angle-resolved photoemission spectroscopy (ARPES) and investigated *via* a tight-binding (TB) model fitted to the experimental dispersion. From this bulk fit, the layer-dependent band gap is determined with a zone-folding approach. Comparing the zone-folded band structure with a direct calculation of the few-layer bands shows good agreement between both methods. The agreement confirms that interlayer hybridization and surface effects barely affect the dispersion of few-layer samples and allows to infer many properties of few-layer phosphorene from the bulk crystal. The tight-binding model is used to predict the doping dependent Fermi surface of bulk and few-layer black phosphorus.

Modifying the band structure of bulk black phosphorus by caesium doping is shown leading to a band inversion at the Γ -point. Angle-dependent X-ray photoemission spectroscopy confirms the caesium is adsorbed on top of black phosphorus rather than intercalated. A bilayer version of the TB model developed for the pristine crystal is used to explain the experimental observation of the band inversion. A strong reduction of the interlayer interaction is inferred. This reduction is explained with density functional theory calculations. The best fit to the experimental observation is reproduced by assuming a stacking fault of the topmost black phosphorus layer, thereby reducing the interlayer interaction. These calculations confirm the surface nature of the down-shifted conduction band and thus establish the experimental observation of a surface resonance state.

The optoelectronic properties of a $\text{MoS}_2/\text{Gr}/\text{Ir}(111)$ heterostructure are investigated

using ARPES, photoluminescence and Raman spectroscopy. A sharp photoluminescence peak is observed. The lack of quenching is explained with a low interaction between MoS₂ and graphene. The growth of the MoS₂/graphene heterostructure consequently allows for photoluminescent properties where they would usually be quenched on a metallic substrate due to non-radiative recombination channels. Combining photoluminescence spectroscopy of the pristine sample with the electronic band gap of lithium doped MoS₂ determined from ARPES in conjunction with theoretical calculations for the doping-dependent band gap renormalization, the exciton binding energy in the heterostructure is predicted.

Investigating the high-doping regime of bilayer graphene by deposition of large amounts of caesium leads to the observation of a strained alkali metal quantum well structure grown on the bilayer graphene substrate. The resulting band structure is investigated using ARPES. A 2×2 superstructure is observed. Combining the experimental results with theoretical calculations elucidates the microscopic structure of the resulting sample. The two most likely structures are determined from theoretically evaluated total energy considerations and good agreement with the experimental band structure. The broadening of the bands arising from the Cs quantum well structure is found to be close to the resolution limit of the instrument suggesting only very small many-body renormalization in the Cs derived states.

Chapter 1

Introduction

For the longest time, solid state physics concerned itself mostly with properties of three-dimensional (3D) materials. This changed with the experimental discovery of graphene in 2004 [1]. The experimental proof of the existence of stable two-dimensional (2D) crystals finally showed, that the Mermin-Wagner theorem [2] on the stability of lower-dimensional crystals is not applicable in real-world conditions. The discovery netted Andre Geim and Konstantin Novoselov the Nobel prize in physics in 2010 [3] and lead to huge interest in research on low-dimensional systems. Today, there are many more low-dimensional materials with many established ways of producing them, including top-down methods producing two-dimensional crystals from three-dimensional base material and bottom-up fabrication producing these crystals from atomic/molecular constituents *via* self-assembly.

The first method of producing two-dimensional materials was exfoliation of individual layers by sticky tape from bulk Van der Waals crystals. This way, graphene was obtained from bulk graphite crystals [1]. Similarly, monolayers of hexagonal-boron nitride (h-BN), transition-metal dichalcogenides (TMDs) and other 2D materials can be produced by this method. The exfoliation technique results in flakes of very high quality but the sample size is limited to micrometer-sized flakes. This limits exfoliation as a production technique. It is not suitable for experimental setups that require large sample sizes. Exfoliation also is an inherently non-scalable procedure, preventing the introduction of two-dimensional materials outside of laboratories.

To overcome problems of exfoliated samples, bottom up fabrication techniques were developed for many 2D materials. These bottom-up procedures allow for large sample sizes but often come with compromises in sample quality. For example, TMDs can be synthesized on several metallic substrates by molecular beam epitaxy (MBE) [4, 5].

This is done by evaporation of a transition-metal in an ultra-high vacuum (UHV) setup while supplying a source for the chalcogenide needed for the formation of MX_2 (with M a transition-metal and X either sulfur, selenium or tellurium). Small MX_2 islands will form on the surface of the metal and slowly grow outward at their edges, acting as nucleation sites. Growing TMDs this way, large areas can be covered with these monolayers. As a downside however, bilayers will generally start growing before the full surface is covered with monolayer TMDs since the growth method is not self-limiting. The covered surface area thus has to be weighed *versus* the growth of pure single-layered structures.

Two-dimensional crystals have many interesting properties for research purposes. In three-dimensional crystals, the bulk of the crystal is well insulated from the environment. Changing the properties of the crystals from the outside after growth is limited and complicated. 2D crystals on the other hand are “all surface”, their properties are thus open to controlled engineering by many different methods.

The properties of two-dimensional crystals can be strongly influenced by interaction with their substrate, making the choice of the substrate an important part of sample and device fabrication. For example, hybridization with a gold substrate leads to an enhancement of spin-orbit coupling in graphene [6]. The optical response of molybdenum disulfide (MoS_2) can be strongly enhanced by sandwiching the MoS_2 between two layers of hexagonal boron-nitride [7]. On the other hand, the optical response can also be completely quenched by depositing MoS_2 monolayers on metallic substrates [8].

The layered characteristics of two-dimensional matter also allow stacking of different materials with different properties. This way, very thin devices can be fabricated by combining different layered materials with beneficial properties into a heterostructure [9–11].

Another advantage of the large surface to body ratio of two-dimensional materials is the possibility of inducing large shifts of the Fermi level *via* doping with alkali metals. This enables the induction and engineering of quantum phase-transitions through the influence on the electronic density of states at the Fermi level. If graphene is doped towards 5/8-filling, theoretical models predict interesting phenomena such as chiral superconductivity [12]. Even without reaching such high doping concentrations the electron-phonon coupling strength shows a strong increase with Cs-doping [13, 14] and conventional superconductivity can be induced in graphene *via* lithium deposition [15]. As another example, in black phosphorus (BP), the band gap strongly depends on the doping and can thus be adjusted by controlled deposition of alkali metals [16, 17].

All these different pathways to engineer the material properties of 2D matter establish these materials as ideal candidates in modern condensed matter physics research. The plasticity of the properties enables the study of quantum phases such as charge density waves (CDW) or surface resonance states. In this thesis, the complex interactions of several (quasi-)two dimensional Van der Waals materials with their substrates and adlayers are discussed. As angle-resolved photoemission spectroscopy (ARPES) enables the direct observation of band structures, it is the main experimental technique used in this thesis. The technique is used for the observation of many different effects from Fermi level shifts due to doping over hybridization effects from interlayer interactions to the determination of many-body renormalization effects. The experimental determination is combined with theoretical band structure calculations from tight-binding (TB) and density function theory (DFT). Manipulation of substrate and adlayer interaction in combination with the inherent properties of the many individual materials leads to a broad range of phenomena which needs to be characterized and understood from an experimental and theoretical perspective. The resulting understanding can be used in targeted growth of samples with distinct properties for a broad range of applications. The structure of this thesis is as follows:

Chapter 2 gives an introduction to Van der Waals materials. Known methods of band structure engineering are discussed in subsection 2.1. Afterwards, the distinction between bulk, multilayer and monolayer Van der Waals crystals is specified from a band structure perspective in section 2.2. In sections 2.3, 2.4, and 2.5 black phosphorus, molybdenum disulfide, as well as mono- and bilayer graphene are introduced respectively with a focus on their electronic properties.

Chapter 3 discusses the theoretical background of this thesis. Section 3.1 explains the process of photoemission underpinning the main experimental method used. Afterwards, the principle of band formation is discussed in the context of tight-binding theory in section 3.2. The limitations of the one-electron tight-binding models are then explored in section 3.3. The Green's function approach for consideration of many-body effects in the band structures is introduced. Next, spin-orbit coupling (SOC) and spin-splitting of electronic states are explained with toy-models for Rashba- and Dresselhaus spin-orbit interaction in crystals. Additionally, the inclusion of SOC effects in tight-binding theory *via* LS -coupling is detailed.

Chapter 4 introduces the main experimental methods and growth procedures. Section 4.1 shortly explains the use of the tight-binding theory introduced in section 3.2 in conjunction with experimentally determined band structures. Section 4.2 then goes into details on the experimental determination of these band structures from the pho-

toemission theory established in 3.1. The transformation of electron \vec{k} -vectors from laboratory frame to sample frame is discussed. Afterwards, section 4.3 shortly introduces photoluminescence spectroscopy. Finally, 4.4 explains the sample preparation details for black phosphorus, MoS₂ and (bilayer) graphene.

The publications this cumulative thesis is based on, are included as individual sections of this thesis in chapter 5.

In section 5.1.1, the band structure of a bulk black phosphorus crystal is investigated with the help of ARPES and TB. From the bulk electronic dispersion, the dispersion of two-dimensional few-layer phosphorene is inferred by application of zone-folding. The resulting band structures are compared with exact calculations of few-layer samples using the hopping parameters of bulk BP. The predicted development of the band gap from bulk to 2D via zone-folding is compared with the development determined from other calculations and experiments. Comparisons confirm the zone-folding method as a good approximation for the dispersion of two-dimensional BP samples. Many of the properties of low-dimensional phosphorene can thus be inferred from the dispersion of the bulk phase at carefully determined out-of-plane wavevectors.

In section 5.1.2, a band inversion is induced in black phosphorus by the adsorption of Cs atoms. The results from section 5.1.1 are used to model the band gap inversion and compare theory with experiment. A two-dimensional tight-binding model is used to model the band inversion due to the Stark effect. A strong reduction of interlayer interaction for the topmost layer upon Cs adsorption is found. X-ray photoemission spectroscopy confirms the adsorption of Cs on top of the BP crystal. Density functional theory calculations reproduce the experimental results when assuming a stacking fault of the topmost black phosphorus layer upon Cs adsorption and confirm a surface resonance state for the shifted conduction band.

For MoS₂ grown epitaxially on a graphene/iridium(111) substrate, the electronic and optical properties are investigated in section 5.2. A sharp photoluminescence peak is found at low temperatures. Comparing the peak position of the photoluminescence peak with the band gap of lithium doped MoS₂ in conjunction with a theoretical prediction of the doping-dependent band gap renormalization, the exciton binding energy is estimated. The lack of quenching for the photoluminescence peak is explained by a low interaction between MoS₂ and graphene. The small interaction is confirmed *via* temperature dependent Raman measurements, ARPES measurements and x-ray photoemission spectroscopy (XPS).

Finally, the properties of bilayer graphene after exposure to a high caesium flux are discussed in section 5.3. The growth of a Cs quantum well in a 2×2 superstructure

is observed. The interplay between Cs and bilayer graphene is investigated using a combination of ARPES with theoretical DFT calculations. Two candidates for the total structure are determined from total energy considerations and overall agreement with the experimental band structure. From these two candidates it is clear that Cs forms a 11% strained fcc-lattice atop bilayer graphene and additionally intercalates between the two graphene layers as well as between the bottom graphene layer and the substrate.

The final conclusions are then summed up in chapter 6.

In appendix A.1, the momentum space wave function of the infinite quantum well is derived from the position space solutions.

Appendix A.2 first gives summaries of several other papers the author of this thesis contributed to which are thematically related to the topic of this thesis. These papers are not to be understood as a part of the current work but merely as extended references since their results are cited several times throughout the thesis. After the summaries, a full list of works contributed to up to this point in time by the author of this thesis is given followed by a list of major presentations at conferences.

Appendix A.3 is reserved for dedications and thanks.

The data availability is detailed in appendix A.4.

Appendix A.6 contains the declaration of authorship in German.

Chapter 2

Van der Waals Materials

Van der Waals crystals are materials made up of individual stacked layers. Atoms within the individual layers are bound *via* covalent bonds. The layers can be thought of as themselves being self-contained complete crystals without dangling bonds [18–21]. The termination of the individual layers strongly reduces the interlayer interaction and bonding. In fact, the only relevant bonding force between the layers is Van der Waals interaction [18–21] giving the class of materials its name. As a consequence, bulk Van der Waals crystals easily cleave at the interface of their individual layers. A property that has long been exploited for applications such as pencils or lubricants [19, 21].

The few-layer counterparts of bulk Van der Waals crystals have garnered a lot of attention. A large class of materials can be grown in this fashion with an accordingly wide variety of physical properties [20, 21]. For modern research, the termination of the single layers leaving no dangling bonds is advantageous. Surfaces of bulk Van der Waals materials as well as few-layer crystals are chemically relatively inert. The passivation leads to very clean, well defined surfaces with low defect densities [18, 19]. The reduced interlayer interaction lessens problems concerning surface reconstructions and furthermore significantly decreases the importance of matching lattice parameters in epitaxial growth [18–21]. With lattice mismatch being much less of a problem for growth of Van der Waals heterostructures, many combinations of different layers are possible. The combinations allow for tuning of a wide range of properties over a large amount of sample structures. Using different types of Van der Waals materials as building blocks for combined heterostructures thus enables a wide range of physical effects and a large malleability concerning the crystal properties [18–21]. The resulting materials show interesting emergent behaviour not present in the individual layers. For example, formation of interlayer excitons was observed in $\text{WSe}_2\text{-MoSe}_2$ heterostructures [22] where the electron part of the exciton is bound to the hole on a different layer

made up of different atoms. Due to the relative band alignment of these two layers, a gate voltage inducing a staggered potential in the heterostructure can be used to shift the bands against each other and thus directly control the energy of the interlayer excitons [23].

As the two-dimensional few-layer counterparts of Van der Waals crystals can not be grown floating in a vacuum, the interaction with their substrate is another topic of high importance. While the lack of dangling bonds reduces the interaction of the layers with adsorbates or the substrate and prevents the formation of strong chemical bonds, the essentially infinite surface to body ratio of monolayers still lends a big importance to the interaction with the environment. Substrates have been shown to have a large impact on the properties of the few-layer systems both grown epitaxially directly onto the surface or later deposited there by exfoliation techniques.

The following section gives an overview over the current state of affairs in research on some of the most promising Van der Waals materials and their two-dimensional single- to few-layer counterparts. First, the current possibilities of band structure engineering are discussed with a focus on Alkali metal doping and substrate interaction. Afterwards, the quantization of the out-of-plane electronic dispersion relation when going from bulk Van der Waals crystals to few-layer samples is discussed. Finally, black phosphorus, MoS₂, and mono- and bilayer graphene are introduced with a focus on their electronic band structure.

2.1 Band Structure Engineering of Two-Dimensional Matter

One of the major advantages of two-dimensional materials is their big surface area. The whole crystal is surface and thus easily accessible for modifications from the outside. This accessibility can be exploited in many ways to influence the electronic structure of a two-dimensional crystal. Combinations of the effects discussed below can be used to strongly influence the electronic band structures of two-dimensional materials which consequently heavily affects many of their properties. A comprehensive review of different techniques used to modify electronic and magnetic properties in graphene is given in [24]. This plasticity is very helpful in fundamental research when trying to investigate the onset of competing quantum phase transitions and their dependence on the fundamental properties of the crystal. The large potential of engineering of the sample properties is also promising for targeted production of devices with very specific requirements and thus highly interesting for applications outside of the laboratory.

A straightforward method for modification of the electronic structure is evaporation of dopants onto the surface of the crystals. In the most simple case, these dopants distribute randomly on the surface and locally change the chemical environment. Depending on the relative electronegativity between crystal and dopant, the electron wave function of the dopants either spreads into the crystal or the electron wave function of the crystal is attracted towards the dopant. Consequently, the dopant either donates negative electric charge to the sample or withdraws charge from the crystal [13, 25–29]. In a simple approximation, this raises or lowers the Fermi level across the material and rigidly shifts the electronic bands accordingly [29–34]. In a tight-binding picture, the doping modifies the on-site parameters shifting the bands versus the Fermi energy [35, 36]. The rigid band shift regime only holds for low doping levels [30]. Donating electrons into the crystal populates anti-bonding states [37]. So, for higher doping levels this weakens the bonding and increases the bond length. The larger interatomic distance decreases orbital overlap and reduces the band widths of the electronic bands [37, 38]. In a semiconductor, the reduction of the wave function overlap on neighbouring sites additionally decreases the band gap of the material [38–43]. Doping *via* evaporation of adatoms onto the surface is particularly useful in two-dimensional crystals as the dopant density can reach similar values as the atomic density of the monolayer crystal being doped. Large changes in the electron density over several orders of magnitude thus become possible and allow for large induced shifts of the Fermi level (compare also appendix A.2.1.3 and A.2.1.4). Doping can hence be used to shift

the Fermi level to Van Hove singularities of the electronic density of states and induce electronic phase transitions. The large density of states of the Van Hove singularities favours transitions into new ground states such as superconductivity [12,44], ferromagnetism [45,46] or charge density waves [47]. Furthermore, intercalation and adsorption of magnetic dopants can be used to induce magnetic behaviour in non-magnetic materials [24,29,48]. Two-dimensional materials are consequently perfect platforms for the study of these ground state phase transitions and their respective interplay and modification.

The doping effects which are direct consequences of the donation or removal of electrons in the crystal can also be achieved by electrostatic doping in field effect transistors [49–51]. Due to limitations of the gate dielectrics used for these setups, the achieved doping levels are much smaller than for electron donation or withdrawal by adatoms. On the other hand, doping *via* randomly distributed adatoms on the surface introduces scattering centers for Bloch electrons [52]. The increased scattering decreases the lifetime of the Bloch states and leads to a broadening in the experimental band structure (compare also section 3.3). In photoemission experiments, the dopant density thus has to be weighed *versus* the introduction of scattering and the loss of exact information of the unperturbed system due to the increased lifetime-broadening. Increasing the dopant density to a point, where the dopants are forced into formation of a periodic superstructure can mitigate the adverse effects arising from scattering. In this superstructure phase is often not really helpful anymore, to think of the system as a standalone monolayer sample with additional dopants on top. The periodic superstructure of the dopants can be accommodated for by the Bloch electrons of the whole crystal. The Bloch states of the monolayer-adatom structure can hence propagate through the combined crystal without scattering. Due to the crystallinity of the superstructure, the dopants form their own energy bands and may additionally affect the bands of the original crystal in several ways. If the additional crystal potential imprinted by the superstructure is strong enough, the spectral contribution of the states in the original crystal is shifted from the dispersion in the original Brillouin zone to the zone-folded band structure in the smaller Brillouin zone of the superstructure (see also A.2.1.4). The zone-folding leads to opening of gaps in the dispersion at the Brillouin zone boundaries of the 2×2 superstructure [53]. Furthermore, the bands of the original crystal can hybridize with the dopant based bands. The band mixing leads to the opening of additional gaps in the dispersion due to quantum mechanical level repulsion (compare A.2.1.4).

In multi-layered samples, the effects of the adatoms decrease with distance from the

dopant layer. The dopants thus induce a layer dependent potential which locally shifts the chemical environment. The modulation of the chemical environment is reflected in a relative shift of electronic bands against each other depending on the layer localization of their constituent basis states. This is known as the Stark effect [54–56]. Additionally, dopants intercalating between the individual Van der Waals layers increase the Van der Waals gap and decrease the interlayer interaction accordingly [57, 58]. This can be used purposefully if hybridization between electronic states localized on different layers is unwanted. The layers are decoupled from each other, leading to electronic behaviour much closer to the behaviour of the monolayer crystals.

On the other hand, the interlayer interaction between layers can also be used explicitly in band structure engineering and device fabrication by abusing the localization of states on the different layers [23, 59, 60]. The emerging field of moiré physics heavily relies on the interlayer interaction between Van der Waals layers to induce the formation of flat bands living in the moiré-supercell [61–63].

Related to the interlayer interaction between different Van der Waals materials is the interaction between the Van der Waals layer and the substrate it is grown on. Substrate choice can significantly affect the band structure of a two-dimensional crystal. The substrate interaction breaks the out-of-plane mirror symmetry of many freestanding structures thus inducing Rashba-like spin orbit coupling effects (compare section 3.4) in the band structure [6]. The strength of the effect depends on the choice of substrate. Additionally, charge transfer between substrate and two-dimensional crystal can lead to doping of the Van der Waals layer [53, 58, 64]. If the Van der Waals layer is semiconducting, but the substrate is metallic hybridization of the bands opens up non-radiative recombination channels, thus quenching any optical response of the Van der Waals layer [8, 65–67]. As with the interlayer interaction for multi-layered samples, the hybridization with the substrate band structure can induce gaps at the points of band mixing due to avoided level crossing. The moiré emerging from a lattice mismatch between substrate and adlayer may induce further minigaps in the dispersion at the Brillouin zone boundaries of the moiré cell [53]. If the effects of the substrate are unwanted, they can be minimized by adsorption and intercalation of dopants which decreases the interlayer interaction between substrate and Van der Waals layer [68].

2.2 From Bulk Dispersion to Two-Dimensions

One of the main differences in the electronic structure of two-dimensional matter and three-dimensional bulk crystals is the lack of an out-of-plane electronic dispersion for the former [69].

For single-layer materials, the strong localization of the wave function within the plane of the crystal leads to a broad distribution in k -space for the out-of-plane momentum. The perpendicular momentum \vec{k}_\perp is hence not a good quantum number for monolayer samples [69]. Excitation-energy-dependent angle-resolved photoemission experiments are able to probe the out-of-plane dispersion (compare section 4.2). And indeed, the band structures of monolayer samples show essentially no dependence on the excitation energy over a broad range of energies [16, 69]. To understand how the out-of-plane dispersion emerges when going from monolayer to bulk samples, it is instructive to look at the excitation-energy-dependent photoemission intensity for few-layer samples. Adding a second layer to the monolayer crystal doubles the electronic bands and interlayer interaction lifts their degeneracy. In ARPES measurements of bilayer samples one would thus expect to observe two related bands in the bilayer sample for each band in the monolayer crystal. While this is generally the case (compare also the band structures in section 2.5), the relative photoemission intensity of the pair of related bilayer bands oscillates with excitation energy [69]. The energy-split bands can be understood as bonding and anti-bonding states for the interlayer coupling [37]. Using the linear combination of atomic orbitals (LCAO) method, the out-of-plane orbitals can be written in the form

$$\psi = c_A \varphi_A + c_B \varphi_B \quad (2.1)$$

with φ_i the atomic wavefunctions in layers A and B. Symmetry requirements impose $c_A = \pm c_B$ [70]. This gives a symmetric orbital ψ^s and an antisymmetric orbital ψ^a with

$$\psi^s \propto \varphi_A + \varphi_B \quad (2.2)$$

$$\psi^a \propto \varphi_A - \varphi_B. \quad (2.3)$$

Understanding these orbitals as a linear combination of the two basis orbitals with a relative phaseshift, they can be written

$$\psi^{s/a} \propto \varphi_A + e^{ik_\perp d} \varphi_B \quad (2.4)$$

with d the interlayer distance. The symmetric bonding state is thus reached for an out-of-plane $k_{\perp} = z\frac{2\pi}{d}$ with $z \in \mathbb{Z}$. The anti-symmetric anti-bonding state is given with $k_{\perp} = (2z + 1)\frac{\pi}{d}$ which is exactly the out-of-plane Brillouin-zone boundary wavevector of the bulk dispersion. However, the states are still relatively well localized along the perpendicular direction in real space. This again leads to a broadening of the states in k -space around the determined values for k_{\perp} and explains the broad intensity modulation with excitation energy/ out-of-plane wavevector in ARPES.

Adding more layers to the crystal introduces more bands which can again be understood as a linear combination of atomic wave functions φ_n located on different layers. The total wave function is then given by

$$\psi \propto \sum_{n=1}^N e^{ik_{\perp}nd} \varphi_n. \quad (2.5)$$

This is essentially a Bloch function as used in section 3.2. Increasing the layer number from 2 to N leads to more allowed values for k_{\perp} and a better localization in momentum space, slowly converging towards the bulk limit with a well-defined out-of-plane dispersion relation. In the limit of infinite layers, the bulk dispersion is reproduced [37, 69]. Figure 2.1 shows a schematic of the ARPES intensity oscillations with excitation energy for $N \in \{1, 2, 3, 4\}$ layers. The states get more localized in k -space with increasing layer number and the dispersion relation converges towards the out-of-plane band structure of the bulk crystal. For an experimental observation of these oscillations in multi-layered graphene samples and the convergence towards the out-of-plane bulk band dispersion see reference [69, Figure 2].

A slightly different approach to the quantization of the out-of-plane dispersion can be undertaken in a simple potential well picture. The surfaces of the crystal act as potential barriers. If the thickness of the sample is small this potential well imposes a quantization condition on the allowed wavelengths of the electron wave functions within the well. By extension, the out-of-plane wavevector is quantized. The solutions of the centered infinite potential well with width L are given by [71]

$$\psi_n(x) = \begin{cases} \sqrt{\frac{2}{L}} \sin(k_n x), & \text{for } n \text{ even} \\ \sqrt{\frac{2}{L}} \cos(k_n x), & \text{for } n \text{ odd.} \end{cases} \quad (2.6)$$

With k_n corresponding to the k_{\perp} from the LCAO picture above. The k_n are derived from the boundary conditions on the wave function $k_n = \frac{n\pi}{L}$. The momentum space wave function can be derived *via* a Fourier transform of the real space wave function

2.2. FROM BULK DISPERSION TO TWO-DIMENSIONS

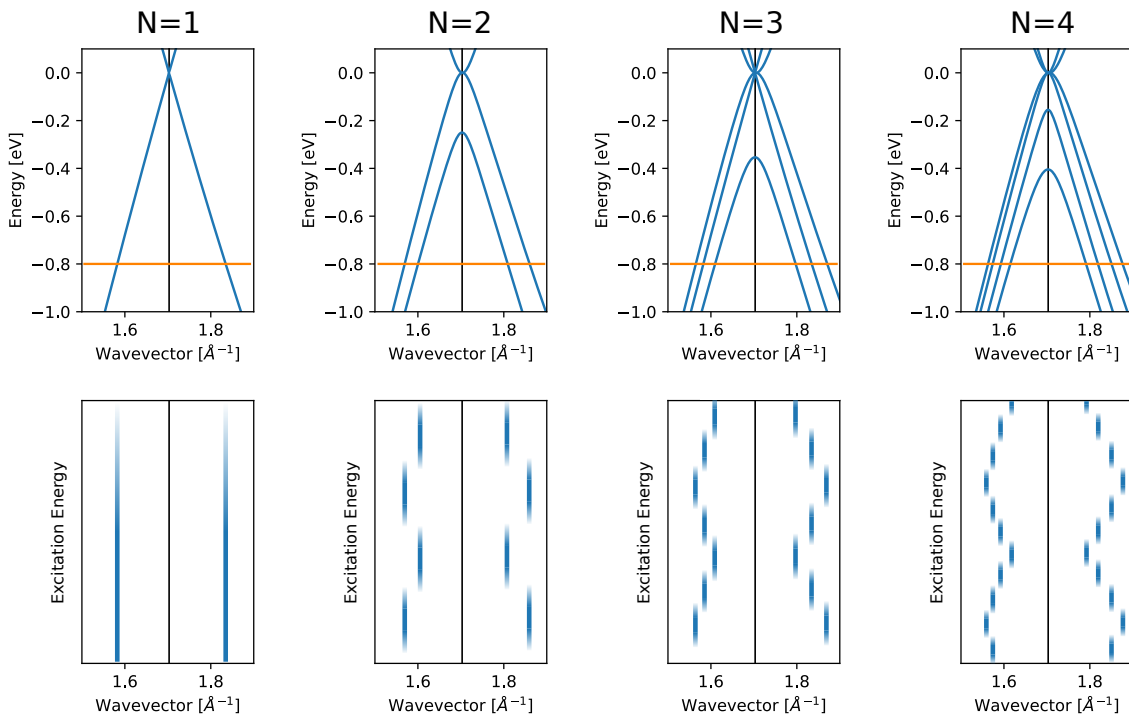


Figure 2.1: Development of out-of-plane dispersion from $N = 1$ layer to $N = 4$ layers. The in-plane band structure is shown in the top row, the bottom row shows a schematic for the ARPES intensities with changing excitation energy at a constant energy cut of -0.8 eV binding energy as indicated by the orange bars in the top row.

(see appendix A.1)

$$\Phi_n(k) = \frac{1}{\sqrt{2\pi\hbar}} \int_{-L/2}^{L/2} \psi_n(x, t) \exp(-ikx) dx \quad (2.7)$$

$$\propto \sqrt{\frac{L}{\pi\hbar}} \left(\frac{n\pi}{n\pi + kL} \right) \text{sinc} \left(\frac{1}{2}(n\pi - kL) \right). \quad (2.8)$$

An important distinction has to be made between the continuous k used in the Fourier transform – and consequently also in the final formula of the Fourier transformed wave function – and the quantized k_n of the real space wave functions. The k used in equations (2.7) and (2.8) is defined by the relation $k = p/\hbar$. The momentum space wave functions are broadened around the values of k_n . The relation $p \approx \hbar k_n$ is only approximately enforced by the sinc-function in (2.8). This leads to the k -space broadening of the states around the quantized values of k_n . The larger the width L of the quantum well, the sharper the localization in k around the quantized k_n values. This behaviour is reflected in ARPES experiments as an oscillation of the photoemission intensity of the bands corresponding to different out-of-plane wave function states with excitation energy.

Interestingly, this relation can be inverted. With a given bulk dispersion at hand, the low-dimensional dispersion can often be approximated by cutting the bulk dispersion relation at the perpendicular momentum planes derived from the boundary conditions on the wavelength (or alternatively from the symmetry requirements on equation 2.5). This allows for the determination of features of a potential two-dimensional system by careful evaluation of the dispersion relation of its three-dimensional counterpart at appropriately chosen out-of-plane wave vectors (compare also section 5.1.1).

2.3 Black Phosphorus

Black phosphorus is one of several allotropes of phosphorus [72]. Similar to graphite, it is a Van der Waals material with individual covalently bonded layers [72, 73]. The crystal structure of a single layer is shown in Figures 2.2(a) and (b). The bulk crystal grows in a base centered orthorhombic crystal lattice containing four atoms in the unit cell [72–77]. Due to sp_3 -hybridization, three phosphorus atoms always connect in a pyramidal structure with a lone electron pair on top [78, 79]. This leads to a buckled structure of the individual layers. The puckered nature imprints strongly anisotropic electronic properties between armchair- and zigzag directions [80]. Interestingly, the electrons show a gapped Dirac-like dispersion along armchair direction, whereas the dispersion along zigzag direction is parabolic [73, 80, 81]. The layered structure is AB-stacked, the second layer is shifted half a unit cell along zigzag-direction against the first layer [76, 77].

Black phosphorus is a direct band gap semiconductor with the band gap changing from approximately 0.3 eV in the bulk crystal to 2.0 eV in monolayers [81, 82]. Like with MoS_2 (see section 2.4), the direct band gap is highly desirable for the fabrication of opto-electronic devices based on two-dimensional materials. The higher carrier mobility in comparison with MoS_2 [80, 81, 83, 84] allows for faster switching characteristics and more reliable performance if used in field-effect transistor (FET) devices. As such, BP has emerged as one of the most researched two-dimensional crystals with a strong focus on potential applications in devices. In particular, the layer-dependent band gap is interesting for use in the opto-electronic devices, providing high tunability for interactions with light from infra-red to the visible part of the spectrum [85–87]. The material has already been used in lab settings to produce many different devices, such as field-effect transistors [82, 85, 88], phototransistors [89], photodetectors [90], or chemical sensors [91].

The basic features of the band structure of BP around the Γ -point can be caught by a simple low-energy Hamiltonian [92, 93]

$$\hat{H}_{BP} = \begin{pmatrix} E_c + \alpha_x k_x^2 + \alpha_y k_y^2 + \alpha_z k_z^2 & \delta k_y \\ \delta k_y & E_v - \beta_x k_x^2 - \beta_y k_y^2 - \beta_z k_z^2 \end{pmatrix} \quad (2.9)$$

where δ describes the interband coupling and α_i, β_i depend on the effective band masses of conduction (α_i) and valence (β_i) band in the respective directions with $\alpha_i = \frac{\hbar^2}{2m_{c,i}}$ and $\beta_i = \frac{\hbar^2}{2m_{v,i}}$. E_c (E_v) determines the lowest (highest) point of the dispersion of the conduction (valence) band. For a low-energy model of monolayer phosphorene, the

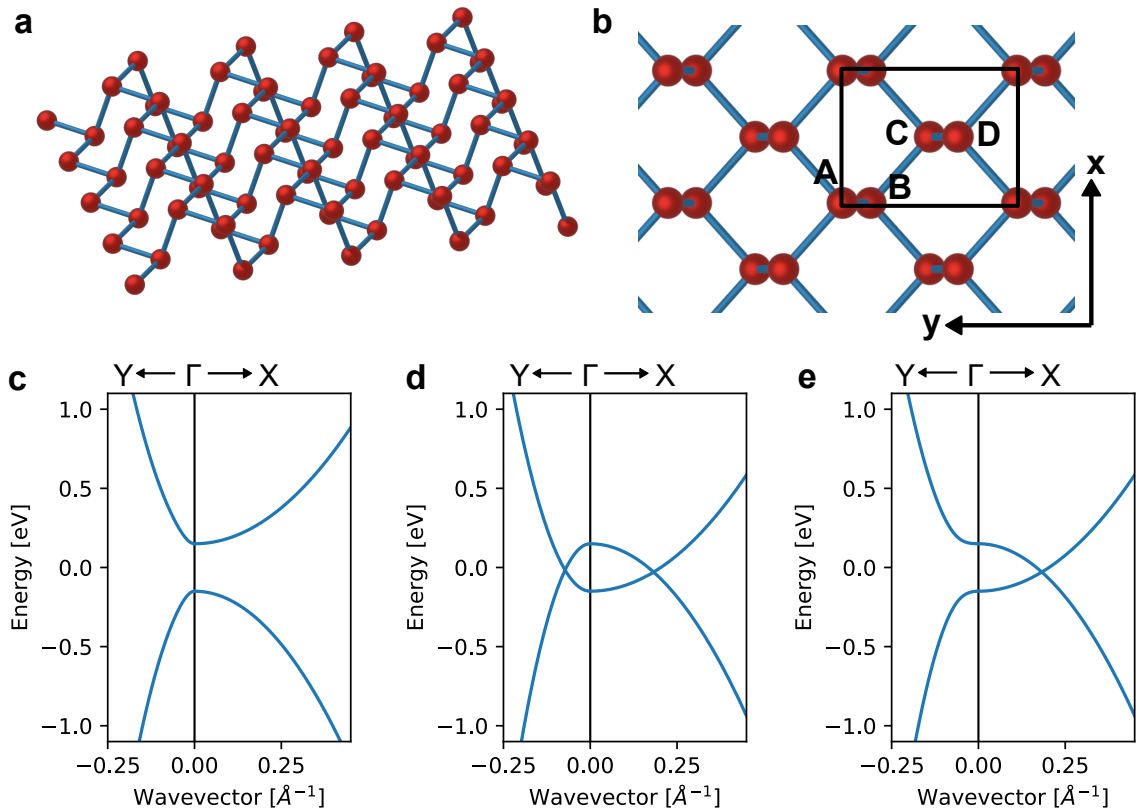


Figure 2.2: (a) A single Van der Waals layer of black phosphorus. (b) Top view of a single black phosphorus layer. The base-centered orthorhombic unit cell with atoms A, B, C, and D in the basis is indicated by the black box. The x -direction (y -direction) is pointed along zigzag-direction (armchair-direction) of black phosphorus. (c) The low-energy band structure with the bulk gap. (d) The band inverted band structure without pseudo-spin orbit coupling. (e) The band inverted band structure with pseudo-spin orbit coupling.

k_z -dispersion of the Hamiltonian has to be removed $\alpha_z = \beta_z = 0$. Note that in some publications, the x -, y -, and z -directions are switched around *versus* the directions chosen here. The resulting band structure is shown in figure 2.2(c). The off-diagonal term is responsible for the resulting massive Dirac dispersion along the armchair direction. The off-diagonal interband Hamiltonian can be expressed using Pauli matrices

$$\hat{H}_{\text{inter}} = \begin{pmatrix} 0 & \delta k_y \\ \delta k_y & 0 \end{pmatrix} = \frac{\delta}{2} k_y \hat{\sigma}_1 + \frac{\delta}{2} k_y \hat{\sigma}_1 + \frac{\delta}{2} k_x \hat{\sigma}_2 - \frac{\delta}{2} k_x \hat{\sigma}_2 \quad (2.10)$$

$$= \frac{\delta}{2} (k_y \hat{\sigma}_1 + k_x \hat{\sigma}_2) - \frac{\delta}{2} (k_x \hat{\sigma}_2 - k_y \hat{\sigma}_1). \quad (2.11)$$

These two terms possess the symmetries of the Hamiltonians for Dresselhaus and Rashba spin-orbit coupling respectively (compare section 3.4) [93]. Due to this symmetry, the material shows effects upon band inversion usually associated with spin-orbit coupling. This peculiar behaviour of BP is known as pseudo spin-orbit coupling and arises from the structural asymmetry in the material [93]. It should be distinguished from actual spin-orbit coupling effects. As phosphorus is a light element, intrinsic spin-orbit coupling is small and spin-splitting is prohibited by the inversion symmetry of the crystal (compare section 3.4). As the pseudo spin-orbit coupling is determined and topologically protected by the crystal structure, the resulting effects are a feature of the bulk crystal and do not require time-reversal symmetry. Any effect arising from the pseudo SOC is thus protected against perturbations as long as the structure of the crystal is unchanged. In particular, unlike actual SOC, the pseudo SOC effects are protected against magnetic perturbations or surface defects [93].

The most interesting effect of the pseudo SOC arises upon band inversion of the conduction and valence band. Inverting the order of both bands can be achieved in the low-energy Hamiltonian by setting $E_c < E_v$. The resulting band structure without pseudo spin-orbit coupling is shown in Figure 2.2(d), the bands with pseudo spin-orbit coupling are shown in 2.2(e). When inverting valence and conduction band, the interband interaction of the pseudo SOC mixes the states and imposes an anti-crossing of the bands. This reopens the band gap for the in-plane dispersion at every hypothetical crossing point except right along zigzag-direction. Along this direction, the band crossing is topologically protected by the glide mirror symmetry of the material [17, 94, 95]. As a result, Dirac cones form in the dispersion at the symmetry-protected crossing points of the band structure.

In an actual BP crystal, the inversion of the two bands can be achieved in different ways. Calculations suggest the application of uniaxial pressure to close the band gap and in-

roduce band inversion [93]. The giant Stark effect can also be used to induce band inversion *via* application of out-of-plane electric fields, putting the different layers of multi-layered BP on different potentials [54, 95, 96]. This can be achieved with electrostatic doping in a field-effect setup [96] or by doping of the surface with adatoms [17, 55].

Alkali metal and alkaline earth metal intercalation is furthermore known to induce superconductivity in black phosphorus [97]. The transition temperature of $T_c = 3.8$ K is intercalant independent which suggests an intrinsic mechanism of electron-doped black phosphorus for superconductivity [97]. For hole-doped black phosphorus, superconductivity is predicted by theory [98]. High pressure also leads to observations of superconductivity in bulk black phosphorus [99]. Theoretical calculations suggest a tunability of the symmetry of the superconducting state in monolayer phosphorene from *s*- and *p*-wave symmetry to *d*- and *f*-wave symmetries by application of planar strain [100].

2.4 Molybdenum Disulfide

The class of materials belonging to the transition metal dichalcogenide family has garnered significant interest in two-dimensional materials research. As these materials are all related, growth techniques developed for one member are often broadly applicable to other members of the family with minor adjustments [4, 101]. While the growth procedures are similar, the many combinations allow wildly different fundamental physics in individual members of the family. Combining one of the many transition-metals with either sulfur, selenium or tellurium leads to a broad range of materials with many different physical properties. The members can range from semiconductors like 2H-MoS₂ and 2H-WSe₂ to metals like 2H-TaS₂ or 1T-VSe₂ [101]. They can exhibit exotic ground states such as superconductivity or charge density waves [102–107] (compare also appendix A.2.1.1 and A.2.1.2). This broad range of physical properties combined with similar growth characteristics and matching lattice parameters introduces TMDs as ideal building blocks for Van der Waals heterostructures [20, 21, 108–110]. Furthermore, the appearance of superconductivity and charge density waves in closely related material systems establishes them as perfect candidates for research into mechanisms driving these competing quantum phase transitions.

Molybdenum Disulfide is part of the family of transition-metal dichalcogenides. As with all TMDs, the bulk crystals grow in a layered fashion with strongly bonded individual trilayer structures. These trilayers then form Van der Waals bonds with each other holding the bulk crystal together [108, 111]. An individual trilayer is made up from one hexagonal molybdenum layer sandwiched between two sulfur layers [111–113]. Monolayer MoS₂ can grow in trigonal-prismatic 1H-MoS₂ and trigonal anti-prismatic 1T-MoS₂ structures. Several distorted phases of the 1T-structure also exist, the most prominent being the 1T' structure [111]. Figure 2.3 depicts the 1H-, 1T- and 1T'-structures of monolayer MoS₂. For MoS₂, the 1H structure is highly stable, the 1T and 1T' structures are metastable phases [4, 111, 115]. The 1H-structure is thus favoured during growth and the following discussion is focused on this trigonal-prismatic phase. 1H-MoS₂ grows in a hexagonal lattice with lattice constant $a \approx 3.15 \text{ \AA}$ [112, 113, 115]. The unit cell contains one molybdenum atom and two sulfur atoms (one in each sulfur layer). The crystal is semiconducting. For bulk to bilayer MoS₂, the band gap is indirect. For the monolayer, a direct band gap is located at the K -point of the Brillouin zone with approximately 2.5 eV gap size [115, 116].

One important feature of monolayer MoS₂ is the missing inversion symmetry in conjunction with strong spin orbit coupling arising from the large mass of the molybdenum

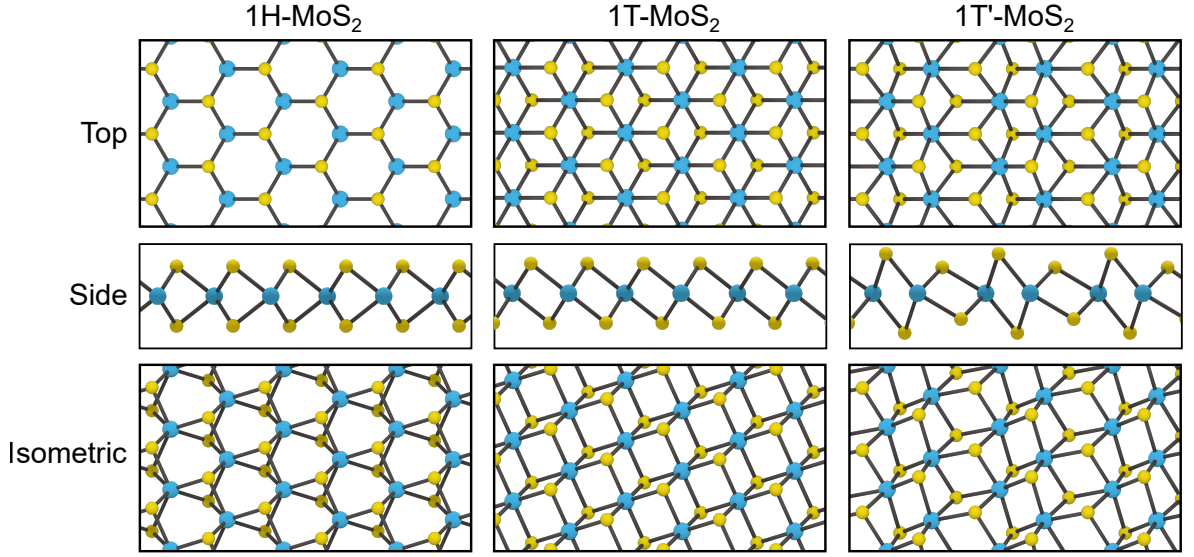


Figure 2.3: 1H-, 1T- and 1T'-structures of monolayer MoS_2 from top, side and isometric views. Adapted from [114].

atoms leading to a spin-split dispersion relation [111–113, 115–119]. The band structure along high-symmetry directions is depicted in figure 2.4(a). The spin-split band structure around the K - and K' -points is clearly discernible. The σ_h mirror symmetry as part of the D_{3h}^1 symmetry of monolayer MoS_2 ensures an out-of-plane alignment of the spins [120–124]. For monolayer MoS_2 , the spin-splitting at the K -point is approximately 150 meV [125, 126]. As the K and K' high symmetry points are linked by time-reversal symmetry, the spin direction for the bands of same energy at the different valleys must be opposite [123].

To model the band structure of MoS_2 in tight-binding, an orbital basis set of the d_{xy} , d_{yz} , d_{zx} , $d_{x^2-y^2}$, and d_{z^2} orbitals located at the molybdenum sites needs to be combined with the p_x , p_y , and p_z orbitals located at each of the two sulfur sites. This basis-set containing eleven orbitals can be used with nearest neighbour in-plane and nearest-neighbour out-of-plane hopping to quantitatively describe the band structure of 2H- MoS_2 without spin-orbit coupling [113, 127]. To include spin-orbit interaction, the basis states need to be split into spin-up and spin-down states effectively doubling the size of the basis. This can be done using the tensor product with the spin-1/2 space. If \hat{H}_{MoS_2} is the 11-band Hamiltonian without spin-orbit interaction, then

$$\hat{H}_{\text{double}} = \hat{H}_{\text{MoS}_2} \otimes \mathbb{1}_{2 \times 2} = \begin{pmatrix} \hat{H}_{\text{MoS}_2} & 0 \\ 0 & \hat{H}_{\text{MoS}_2} \end{pmatrix} \quad (2.12)$$

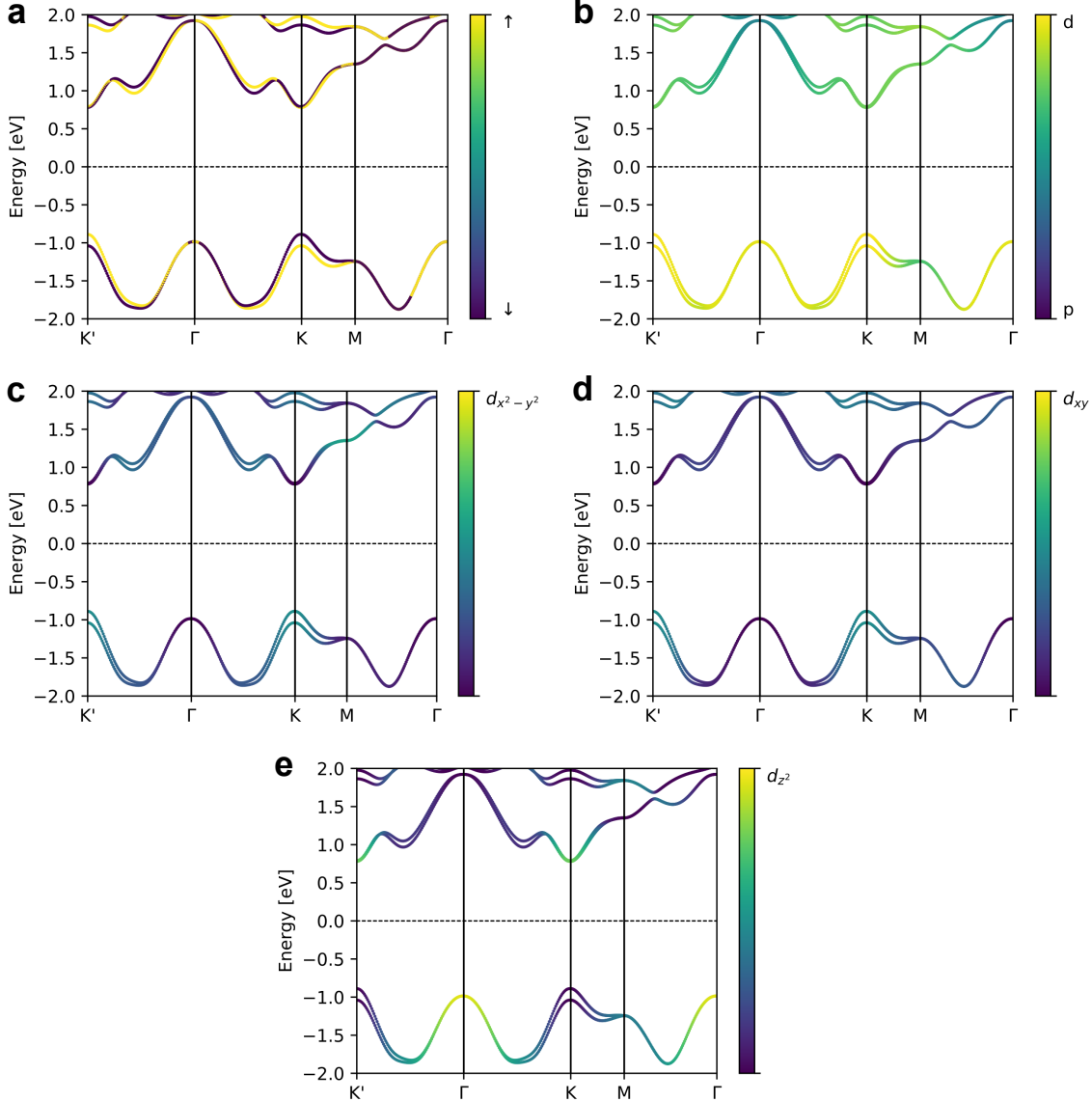


Figure 2.4: Band structure of MoS₂ along high-symmetry directions. The colors of the bands represent different projections of the wave function. (a) Out-of-plane spin projection, purple for spin down, yellow for spin up. (b) Orbital-projection showing d -type or p -type character of the bands. (c) Orbital projection showing $d_{x^2-y^2}$ character of the bands. Purple means no $d_{x^2-y^2}$ character, yellow means fully $d_{x^2-y^2}$ character. (d) Orbital projection showing d_{xy} character of the bands. Purple means no d_{xy} character, yellow means fully d_{xy} character. (e) Orbital projection showing d_{z^2} character of the bands. Purple means no d_{z^2} character, yellow means fully d_{z^2} character.

gives a 22-band Hamiltonian with orbitals distinguished by spin. However, without coupling terms introducing an interaction between spin-up and spin-down states on the off block-diagonals, the calculated bands are still spin-degenerate. These coupling terms can be introduced by taking the intrinsic intra-atomic LS -coupling into account as discussed in the final part of section 3.4.

The full tight-binding description of MoS₂ including spin-splitting is then given by [112, 113]

$$\hat{H}_{\text{SOC}} = \hat{H}_{\text{double}} + \hat{H}_{\text{LS}}^{\text{real}}. \quad (2.13)$$

The total Hamiltonian now has cross-terms on the off block-diagonals. These cross terms mix the spin-up and spin-down states and are responsible for the spin-splitting around the K -point.

The resulting band structure with different orbital projections is shown in figure 2.4. Figure 2.4(b) shows the projection of the d -orbitals localized at the molybdenum sites *versus* the p -orbitals localized at the sulfur sites. The valence band is nearly fully d -type, the conduction band is a mixture of p - and d -states. Subfigures 2.4(c) through (e) show projections of individual d -orbitals. The states making up the bands of the direct band gap at the K -/ K' -points are of particular interest. The valence band at the band gap is a mixture of $d_{x^2-y^2}$ and d_{xy} orbitals, the conduction band is a mixture of the d_{z^2} orbital of molybdenum and the p -orbitals of sulfur. In summary, the orbital character of the valence band changes from fully spin-degenerate d_z^2 at Γ to spin-split $\frac{1}{\sqrt{2}}(d_{x^2-y^2} + id_{xy})$ at K and $\frac{1}{\sqrt{2}}(d_{x^2-y^2} - id_{xy})$ at K' respectively [123]. The main contribution to the orbital character of the conduction band at the K / K' points is d_{z^2} with a partial mixed in p -character, the spin-splitting of the conduction band is negligibly small.

A low energy Hamiltonian describing the dynamics at the K / K' -points is given by [123]

$$\hat{H} = \left[a\gamma_0(\tau q_x \hat{\sigma}_1 + q_y \hat{\sigma}_2) + \frac{\Delta}{2} \hat{\sigma}_3 \right] \otimes \hat{s}_0 - \lambda\tau \frac{\hat{\sigma}_3 - \mathbb{1}}{2} \otimes \hat{s}_3. \quad (2.14)$$

$\tau = \pm 1$ is called the valley-index with $\tau = +1$ at K and $\tau = -1$ at K' . The Pauli matrices $\hat{\sigma}_i$ in the Hamiltonian given in (2.14) are expressed in the basis of the two orbital basis functions. \hat{s}_0 and \hat{s}_3 are the Pauli matrices for the spin subspace, $\hat{s}_0 = \mathbb{1}_{2 \times 2}$ is used to “double” the spin-degenerate part of the Hamiltonian, \hat{s}_3 implements the spin-orbit splitting of the valence band at K and K' . As discussed above, the mirror symmetry of freestanding monolayer MoS₂ leads to fully out-of-plane spin-projection.

The \hat{s}_3 Pauli matrix thus captures the full spin dynamics at the valleys. The spin-degenerate part of the Hamiltonian is equivalent to the low-energy Hamiltonian of graphene (see section 2.5.1) with an additional staggered potential breaking sublattice symmetry. The additional term is introduced because of the different on-site energies of the molybdenum and sulfur atoms in the two sublattices [123].

Diagonalizing the Hamiltonian and using the resulting eigenfunctions $|1\rangle$ and $|2\rangle$, the coupling strength of circularly polarized optical fields can be calculated by [123]

$$\mathcal{P}_\pm(\vec{q}) = \mathcal{P}_x(\vec{q}) \pm i\mathcal{P}_y(\vec{q}) \quad (2.15)$$

$$\mathcal{P}_i(\vec{q}) = m_0 \langle 1 | \frac{1}{\hbar} \frac{\partial \hat{H}}{\partial q_i} | 2 \rangle. \quad (2.16)$$

The resulting coupling strength is found to be

$$|\mathcal{P}_\pm(\vec{k})|^2 = \frac{m_0^2 a^2 \gamma_0^2}{\hbar^2} \left(1 \pm \tau \frac{\Delta'}{\sqrt{\Delta'^2 + 4a^2 \gamma_0^2 q^2}} \right)^2 \quad (2.17)$$

with $\Delta' = \Delta - \tau s_z \lambda$ the size of the direct band gap. $s_z = \pm 1$ is chosen depending on spin-up or spin-down orientation of the upper valence band states [123].

Right at the K -point ($\tau = +1$), where the momentum \vec{q} relative to the high symmetry point is $q = 0$ the polarization dependent coupling strength is thus [123]

$$|\mathcal{P}_+(\vec{0})|^2 = \frac{m_0^2 a^2 \gamma_0^2}{\hbar^2} 4 \quad (2.18)$$

$$|\mathcal{P}_-(\vec{0})|^2 = 0. \quad (2.19)$$

At the K -point σ^+ polarized light couples to the electronic states and induces an interband transition from valence to conduction band, whereas σ^- polarized light does not. For small finite momenta $q^2 \ll \frac{\Delta'}{4a^2 \gamma_0^2}$ this is still approximately true. On the K' -point, the coupling is switched around due to time-reversal symmetry.

This allows for controlled excitation in K or K' valleys *via* circular polarized light and gives direct experimental access to the valley degree of freedom. The spin-split nature of the valence band in conjunction with the polarization-dependent coupling to photons in the two inequivalent valleys around K and K' allows for the controlled excitation of particles in one particular valley with a pure spin polarization [123, 128]. The linking of valley and spin degree of freedom is known as spin-valley coupling [129, 130]. These spin- and valley degrees of freedom and the coupling of both enable the potential use of monolayer MoS₂ in spintronic and valleytronic devices [123, 131–136].

2.5 Monolayer and Bilayer Graphene

2.5.1 Monolayer Graphene

One individual layer of a graphite bulk crystal is called graphene. The lattice structure of monolayer graphene is shown in Figure 2.5(a). The real-space unit cell is indicated with a yellow diamond in the background of the lattice. Monolayer graphene grows in a honeycomb lattice consisting of two sublattices A and B with one atom centered at each of the sublattices. The Brillouin zone of the reciprocal lattice is hexagonal with high symmetry points Γ , M , K and K' . K and K' are inequivalent but linked via time reversal symmetry [137–139]. Good overviews on the electronic structure of monolayer and bilayer graphene are given in [138] and [139].

The lattice vectors of graphene are given by [137–139]

$$\vec{a}_1 = \frac{a}{2}(3, \sqrt{3})^T \quad (2.20)$$

$$\vec{a}_2 = \frac{a}{2}(3, -\sqrt{3})^T \quad (2.21)$$

with $a \approx 1.42 \text{ \AA}$ the distance between two carbon atoms. The reciprocal lattice vectors are then [137, 138]

$$\vec{b}_1 = \frac{2\pi}{3a}(1, \sqrt{3})^T \quad (2.22)$$

$$\vec{b}_2 = \frac{2\pi}{3a}(1, -\sqrt{3})^T. \quad (2.23)$$

The honeycomb lattice of graphene forms due to sp_2 -hybridization [137, 139, 140]. The σ -bands resulting from the hybridization are responsible for the covalent bonds in the lattice. The remaining p_z orbitals form delocalized, metallic π -bands. The well known Dirac-like dispersion of graphene arises from these π -bands [139–141].

The Dirac-like nature of the π -bands can be captured with a simple tight-binding model using only nearest neighbour coupling with one p_z orbital located at each of the two sublattice sites. The nearest neighbour hopping directions are given by [137, 139, 140]

$$\delta_1 = \frac{a}{2}(1, \sqrt{3})^T \quad (2.24)$$

$$\delta_2 = \frac{a}{2}(1, -\sqrt{3})^T \quad (2.25)$$

$$\delta_3 = a(-1, 0)^T. \quad (2.26)$$

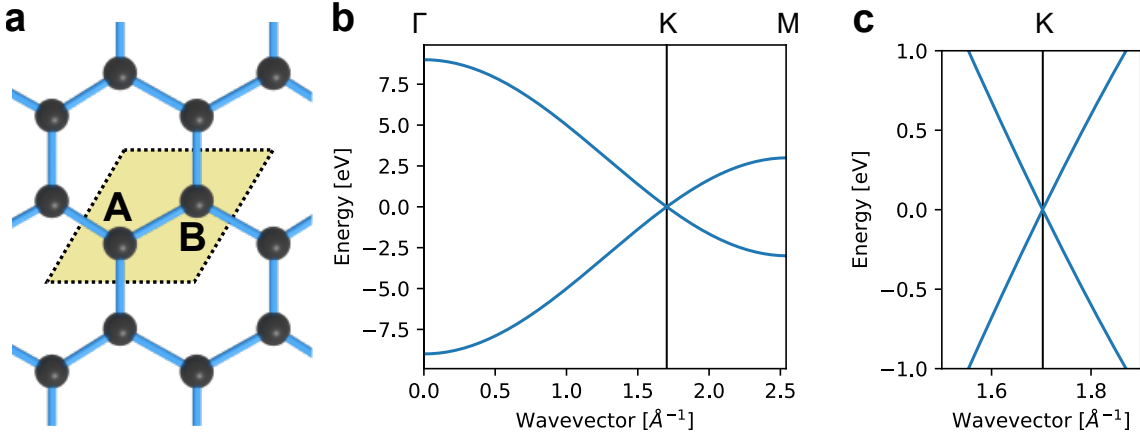


Figure 2.5: (a) Top view of the honeycomb lattice structure of graphene. The unit cell is indicated by the yellow diamond. A and B signify the two sublattice sites within the unit cell. (b) Nearest neighbour tight-binding band structure of monolayer graphene along the high-symmetry Γ -K-M direction. (c) Close-up view of the Dirac cone around the K-point.

The resulting Hamiltonian for the π -bands is of the form

$$\hat{H}(\vec{k}) = \begin{pmatrix} \varepsilon_A & -\gamma_0 f(\vec{k}) \\ -\gamma_0 f^*(\vec{k}) & \varepsilon_B \end{pmatrix} \quad (2.27)$$

$$f(\vec{k}) = \sum_j \exp(i\vec{k} \cdot \vec{\delta}_j) = \exp(-ik_x a) + 2 \exp(-ik_x a/2) \cos(k_y a \sqrt{3}/2). \quad (2.28)$$

With the on-diagonal terms ε_A , ε_B set to zero, the Dirac point of the dispersion is located at the Fermi level. The resulting band structure is shown in figure 2.5(b) along high-symmetry direction Γ -K-M with a zoomed in view of the Dirac cone feature around the K-point shown in figure 2.5(c). The bands meet in a single point at the Fermi energy. Setting the on-site terms to a value other than zero leads to a rigid band shift relative to the Fermi level. In freestanding graphene, the atoms of sublattice A and sublattice B are both carbon atoms and thus symmetry requires $\varepsilon_A = \varepsilon_B$. Breaking this sublattice symmetry leads to the formation of a band gap [123, 142–144]. The broken sublattice symmetry is naturally the case for hexagonal-boron nitride or MoS₂ (compare section 2.4), where different elements occupy sublattice A and B of the honeycomb lattice [144, 145]. A similar situation can also happen with graphene adsorbed on a surface if the interaction with the substrate gives a different chemical environment for atoms of sublattice A *versus* atoms of sublattice B [142, 146, 147]. For the rest of the discussion on monolayer graphene, the on-site energies ε_A and ε_B are set to zero to model pristine graphene. For low energies, the Hamiltonian can be expanded

around K in the form [137, 139]

$$\hat{H}_{\vec{K}}(\vec{q}) = \hbar v_F \begin{pmatrix} 0 & q_x - iq_y \\ q_x + iq_y & 0 \end{pmatrix} \quad (2.29)$$

$$v_F = \frac{3\gamma_0 a}{2\hbar} \quad (2.30)$$

with $v_F \approx 10^6 \text{ m s}^{-1}$ the Fermi velocity [137, 139, 148]. The electronic dispersion determined from this Hamiltonian is given by

$$E_{\pm} = \pm \hbar v_F |\vec{q}| \quad (2.31)$$

and the linear dispersion relation is recovered. This means the Fermi surface for undoped graphene is point-like and there are no states right at the Fermi energy.

Rewriting the Hamiltonian (2.29) in terms of the Pauli matrices, it becomes

$$\hat{H}_{\vec{K}}(\vec{q}) = \hbar v_F (q_x \hat{\sigma}_1 + q_y \hat{\sigma}_2) = \hbar v_F \vec{\sigma} \cdot \vec{q} \quad (2.32)$$

$$\vec{\sigma} = (\hat{\sigma}_1, \hat{\sigma}_2)^T. \quad (2.33)$$

The low-energy Hamiltonian is analogous to the Hamiltonian of massless spin 1/2 particles in high-energy particle physics. This equivalence enables the exploration of Dirac physics at much lower energy scales in laboratory environments [137, 139, 149, 150]. The eigenfunctions around K of the Hamiltonian can be determined as [137, 139]

$$\psi_{\vec{K}}^{\pm}(\vec{q}) = \frac{1}{\sqrt{2}} \begin{pmatrix} \exp(i\vartheta_{\vec{q}}/2) \\ \pm \exp(-i\vartheta_{\vec{q}}/2) \end{pmatrix} \quad (2.34)$$

$$\vartheta_{\vec{q}} = \arctan q_x/q_y \quad (2.35)$$

with the \pm index indicating whether the eigenfunction describes the states belonging to the positive or negative energy branch. This is a spinor-like structure with the phase of $\psi_{\vec{K}}^{\pm}(\vec{q})$ changing by π for a full rotation around K in \vec{q} mimicking the behaviour of fundamental spin-1/2 particles. With these peculiar similarities, it is important to keep in mind that the spinor-like wave function in this case is not actually describing the spin of the electrons in graphene. In fact, the spin degeneracy is not lifted at any point of this discussion. Instead, the Hamiltonian describes a pseudo-spin structure encoded in the orbital wave functions localized on one of the two sublattice sites A and B.

This property is only approximately valid for low-energy excitations around the K point (an equivalent calculation can be done for the K' point) so it is not immediately clear

how many of these properties remain intact in real graphene with substrate hybridization and other effects not taken into account by such a simple tight-binding model. However, the predicted behaviour actually manifests in experiments and can, for example, be probed by analyzing the k-space dependent photoemission matrix elements *via* ARPES [151] or by the peculiar Landau level splitting observed in transport [152]. The spin was ignored in the discussion above, as the intrinsic spin-orbit interaction in graphene is small due to the low mass of carbon atoms. Interaction with the substrate can be used to increase the spin-orbit interaction however. Hybridization with gold states for graphene grown on Au(111) surfaces leads to a giant Rashba splitting observed in the Dirac cone dispersion of graphene [6]. Intercalation of europium is known to induce paramagnetic or ferromagnetic behaviour depending on the structural phase of the intercalated atoms [29]. For adsorbates, it is known that alkali-metal adsorption increases electron-phonon coupling in monolayer graphene [14, 153]. There is experimental evidence of superconductivity in lithium-doped single-layer graphene [15] as well as in calcium-doped graphene laminates [154].

Several competing ground states are predicted when doping the material past the saddle-point instability in the band structure. Amongst them are chiral superconductivity [12, 155], spin-density waves [156], and other exotic phases of matter [157–159]. Experimentally, such high doping levels have been achieved several times – compare amongst others A.2.1.3 and A.2.1.4 in the appendix as well as citations [160, 161] – but experimental evidence for these exotic ground states is still scarce.

2.5.2 Bilayer Graphene

Bilayer graphene – as the name suggests – consists of two stacked layers of graphene. There are two possible stacking configurations. In AA stacked bilayer graphene, the atoms of one layer lie directly above the atoms of the other layer. With Bernal (AB) stacking on the other hand, the top layer is shifted *versus* the bottom layer. In normal conditions, AB stacked bilayer graphene is the more stable configuration [138, 139].

From the simple tight-binding Hamiltonian of monolayer graphene, simple Hamiltonians for AA- and AB-stacked bilayer graphene can be constructed. The Hamiltonians are then of the form

$$\hat{H}_{\text{BLG}} = \begin{pmatrix} \hat{H}_{\text{MLG}} & \hat{H}_{\text{int}} \\ \hat{H}_{\text{int}}^\dagger & \hat{H}_{\text{MLG}} \end{pmatrix} \quad (2.36)$$

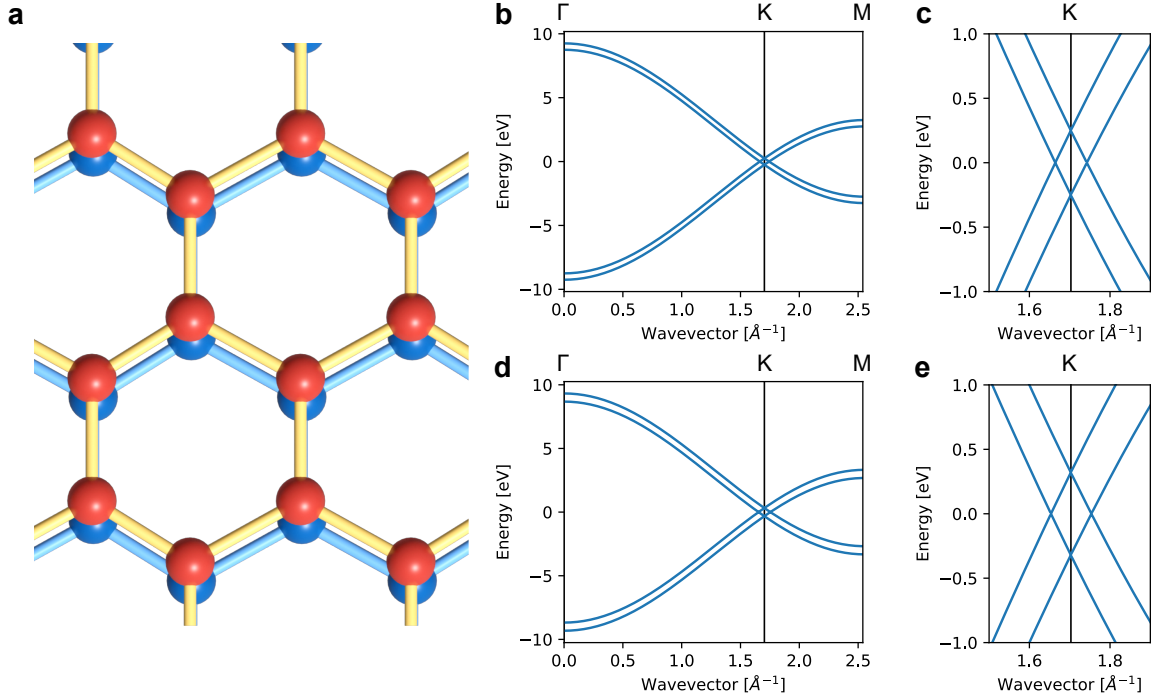


Figure 2.6: (a) AA-stacked bilayer graphene shown from above. A slight tilt of the camera is used to show both layers lying atop each other. The bottom layer is tinted blue, the top layer tinted red. (b) Tight-binding band structure of AA-stacked bilayer graphene along the high symmetry cut Γ - K - M . (c) Close-up view of the double Dirac cone structure around the K -point. (d) and (e) same as (b) and (c) but with an on-site potential difference of $U = 0.4$ eV split equally between top and bottom layer.

where each entry is itself a 2×2 matrix. The entries of \hat{H}_{MLG} are given by equation (2.27). \hat{H}_{int} describes the interlayer interaction and thus differs between the AA- and AB-stacked structures [138, 139]. The atomic structure of AA stacked graphene is shown in figure 2.6(a). The individual layers grow in the same honeycomb lattice as monolayer graphene. As mentioned in the beginning of this section, the two layers of AA-stacked bilayer graphene lie directly above each other. A simple description of the interlayer hopping thus only includes hopping terms γ_1 between atoms sitting on top of each-other. In this case, the interlayer hopping is described *via*

$$H_{\text{int}}^{AA} = \begin{pmatrix} \gamma_1 & 0 \\ 0 & \gamma_1 \end{pmatrix} \quad (2.37)$$

and the full Hamiltonian becomes [138, 139]

$$H_{\text{BLG}}^{\text{AA}} = \begin{pmatrix} \varepsilon_{A1} & -\gamma_0 f(\vec{k}) & \gamma_1 & 0 \\ -\gamma_0 f^*(\vec{k}) & \varepsilon_{B1} & 0 & \gamma_1 \\ \gamma_1 & 0 & \varepsilon_{A2} & -\gamma_0 f(\vec{k}) \\ 0 & \gamma_1 & -\gamma_0 f^*(\vec{k}) & \varepsilon_{B2} \end{pmatrix}. \quad (2.38)$$

Note that for freestanding bilayer graphene, the on-site energies are all equal due to symmetry. For an undoped crystal, setting the on-site energies to zero fixes the touching points of the bands to the Fermi level. The resulting band structure is shown in figure 2.6(b) in a high symmetry cut along Γ - K - M direction. An approximately constant energy splitting between electron- and hole-like bands is visible. The splitting is proportional to the out-of-plane hopping term γ_1 . The dispersion around the K -point is shown in detail in figure 2.6(c). The low-energy band structure is that of two intersecting Dirac cones, the linear dispersion around the Fermi level is maintained.

Applying an out-of-plane electrical field to the freestanding bilayer system puts the bottom layer on a different potential from the top layer. An equivalent effect can happen for bilayer graphene on a substrate, where the substrate induces a gradient in the chemical environment and puts the bottom layer on a different chemical potential *versus* the top layer. The difference in potential between both layers can be modeled by setting the on-site energies of the lower layer to a different value from the upper layer. To keep the overall doping level the same, the relative shift in on-site energies can be split symmetrically between both layers $\varepsilon_{A1} = \varepsilon_{B1} = U$ and $\varepsilon_{A2} = \varepsilon_{B2} = -U$. Figure 2.6(d) shows the resulting band structure including the effect of a potential difference between both layers. The dispersion is qualitatively unchanged by the application of a field. The energy separation between each of the two pairs of parallel running bands is increased. The topology of the electronic structure of AA-stacked bilayer graphene is thus stable against perturbations by a staggered out-of-plane crystal potential. Including higher-order hopping terms in Hamiltonian (2.38), the electron-hole symmetry is broken and trigonal warping is introduced [139]. Theoretical calculations consistently predict a superconducting ground state for alkali and alkaline earth metal intercalated AA-stacked bilayer graphene [162–165]. Furthermore, AA-stacked bilayer graphene in an electric field is predicted to show chiral $d + id$ superconductivity [166].

The atomic structure of Bernal stacked bilayer graphene is shown in figure 2.7(a). The two layers are shifted against each other. The corresponding tight-binding model for Bernal stacked bilayer graphene can be set up by using the interlayer interaction

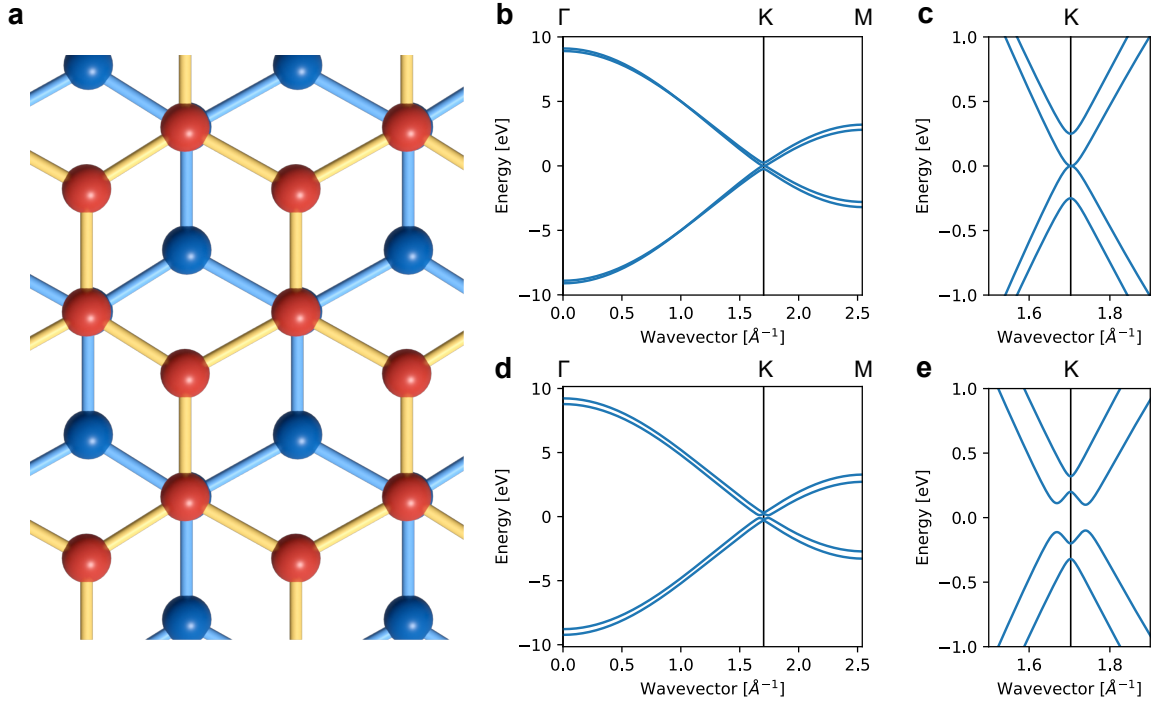


Figure 2.7: (a) AB-stacked bilayer graphene shown from above. The bottom layer is tinted blue, the top layer tinted red. (b) Tight-binding band structure of AB-stacked bilayer graphene along the high symmetry cut Γ -K-M. (c) Close-up view of the band structure around the K-point. (d) and (e) same as (b) and (c) but with an on-site potential difference of $U = 0.4$ eV split equally between top and bottom layer.

term [138, 139]

$$H_{\text{int}}^{AB} = \begin{pmatrix} \gamma_4 f(\vec{k}) & -\gamma_3 f^*(\vec{k}) \\ \gamma_1 & \gamma_4 f(\vec{k}) \end{pmatrix}. \quad (2.39)$$

This gives the Hamiltonian for AB-stacked bilayer graphene

$$H_{BLG}^{AB} = \begin{pmatrix} \varepsilon_{A1} & -\gamma_0 f(\vec{k}) & \gamma_4 f(\vec{k}) & -\gamma_3 f^*(\vec{k}) \\ -\gamma_0 f^*(\vec{k}) & \varepsilon_{B1} & \gamma_1 & \gamma_4 f(\vec{k}) \\ \gamma_4 f^*(\vec{k}) & \gamma_1 & \varepsilon_{A2} & -\gamma_0 f(\vec{k}) \\ -\gamma_3 f(\vec{k}) & \gamma_4 f^*(\vec{k}) & -\gamma_0 f^*(\vec{k}) & \varepsilon_{B2} \end{pmatrix} \quad (2.40)$$

with the in-plane hopping constant γ_0 and three out-of-plane hopping terms γ_1 , γ_3 , and γ_4 [138, 139]. Due to the distance between hopping sites, the in-plane term γ_0 is much bigger than any of the out-of-plane hopping terms and γ_1 (the out-of-plane hopping term describing the overlap between two orbitals sitting on atomic sites directly above each-other) dominates the properties of the out-of-plane dispersion. Again, the on-site

terms are equal in freestanding AB-stacked graphene due to symmetry and are set to zero for the pristine case. The dispersion of the Bernal-stacked structure for the pristine case is shown in figure 2.7(b). The band structure again is in many ways similar to that of monolayer graphene but the out-of-plane interactions modify key points of the dispersion. Throughout the whole Brillouin zone, a small splitting of bands induced by the interlayer interaction is seen for pairs of bands arising from the original monolayer states. The dispersion around the K -point is shown in detail in figure 2.7(c). The out-of-plane hopping modifies the linear dispersion of the original monolayer Dirac cone leading to parabolic bands touching each other in one point right at the Fermi level. A second set of bands runs parallel to the parabolically dispersing bands. The separation in energy between the pair of bands on the same side of the Fermi energy is dominated by hopping term γ_1 [138, 139].

The dispersion for AB-stacked graphene with an applied potential difference between both layers is shown in figure 2.7(d). A band gap opening is observed with a direct band gap slightly shifted away from the K -point. As the potential difference between the two layers is naturally induced when bilayer graphene is adsorbed on a substrate, the band structure is prone to a band gap opening in experimental observations. The gap is proportional to the applied potential difference and can be engineered with the application of electric fields or dopants [167, 168].

The fundamentally different dispersion of the two different stacking orders makes it trivial to distinguish these two phases in angle-resolved photoemission spectra. In twisted bilayer graphene samples, the moiré-pattern between both layers leads to the existence of both stacking orders in the same sample [169].

Chapter 3

Theory

3.1 Process of Photoemission

The photoelectric effect was first observed in the 19th century [170], the theoretical explanation of the effect by Albert Einstein was one of the first results of the emerging quantum theory [171]. Light shining on the surface of a metal is able to induce the emission of electrons. Crucially, the appearance of a photocurrent is dependent on the wavelength of the light and not its intensity.

The kinetic energy E_k of the emitted electrons is given by the equation

$$E_k = h\nu - \Phi - |E_B| \quad (3.1)$$

with $h\nu$ the energy of the light, Φ the material dependent work function (given by the energy difference between the vacuum level and the Fermi energy) and E_B the binding energy of the electrons within the solid. For a given material, the kinetic energy of the emitted electrons is thus directly related to their binding energy within the solid. By measuring the amount of emitted electrons for a given kinetic energy, it is then possible with photoemission spectroscopy (PES) to directly observe the density of electronic states within the sample (compare Figure 3.1). Of particular interest are the electronic states of the valence bands close to the Fermi edge as these states dominate the electronic transport as well as optical properties in the visible and low ultra-violet range of any material.

A good review of the theory of angle-resolved photoemission spectroscopy was written by Andrea Damascelli [172,173], a short summary of the main points based on his work is given in the following. This summary is in parts based on the one given in [114].

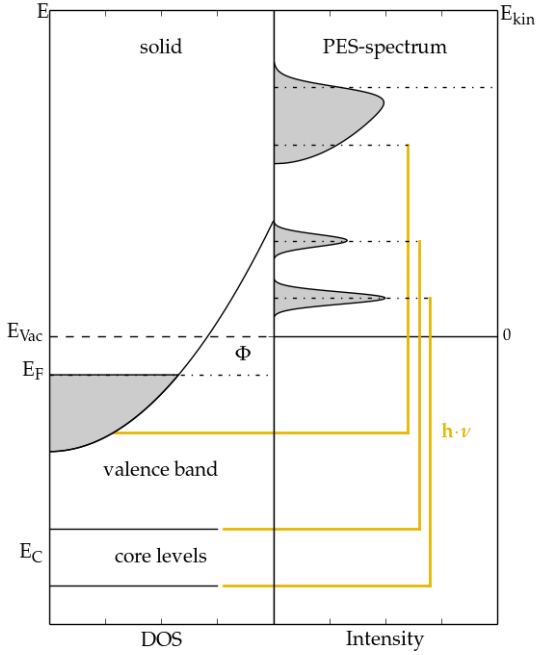


Figure 3.1: Schematic for the relationship between detected photoemission spectra and the density of states within the sample. Reproduced from [114], based on [172, Fig. 2].

3.1.1 Photoemission Theory

The process of photoemission is given by describing the excitation of an N -electron system *via* a photon into an excited state. The energy of the ground state is given by

$$E_i^N = E_i^{N-1} - E_B^{\vec{k}} \quad (3.2)$$

with $E_B^{\vec{k}}$ the binding energy of one of the N electrons with wavevector \vec{k} and E_i^{N-1} the energy of the other ($N-1$) electrons. In this case, all electrons are still within the solid. The energy of the excited state after absorbing the photon is given by

$$E_f^N = E_f^{N-1} + E_k \quad (3.3)$$

with E_k the kinetic energy of the electron emitted from the surface and E_f^{N-1} the energy of the ($N-1$) electrons left behind within the crystal.

The transition probability from the initial ground state to the final excited state is given by Fermi's golden rule

$$w_{fi} = \frac{2\pi}{\hbar} |\langle \psi_f^N | H_{int} | \psi_i^N \rangle|^2 \delta(E_f^N - E_i^N - h\nu). \quad (3.4)$$

The interaction Hamiltonian H_{int} is given by the dipole approximation within the minimal coupling framework

$$H_{int} = -\frac{e}{mc}\vec{A}\cdot\vec{p}. \quad (3.5)$$

The whole process of photoemission is usually approximated within a three step model, splitting the process up into steps of

- (i) excitation of the electron system within the bulk
- (ii) travel of the excited electron to the surface of the crystal
- (iii) escape of the excited electron into the vacuum.

The second step can then be accounted for with an effective mean free path for the excited electron and the third step by a transmission probability from the surface into the vacuum. To model the first step, it is assumed, that the excitation happens instantaneously and there is no interaction between the excited electron and the photohole left behind. This approximation is known as the *sudden approximation* and is only applicable to situations where the excited electron has a high kinetic energy. With this approximation, it is possible to factorize the wave function of the final excited state

$$\psi_f^N = \mathcal{A}\phi_f^{\vec{k}}\psi_f^{N-1}. \quad (3.6)$$

In this case \mathcal{A} is the antisymmetric operator, ensuring satisfaction of the Pauli principle, $\phi_f^{\vec{k}}$ is the wave function of the excited single photoelectron with wavevector \vec{k} and ψ_f^{N-1} is the final state of the (N-1) electron system left behind in an excited state. ψ_f^{N-1} can be assumed to be in an eigenstate ψ_m^{N-1} of the (N-1) system with energy E_m^{N-1} . The total transition probability can then be calculated by a sum over all those final eigenstates m (see below).

Assuming the initial state can also be factorized in the same way given in equation (3.6), it can be written

$$\langle\psi_f^N|H_{int}|\psi_i^N\rangle = \langle\phi_f^{\vec{k}}|H_{int}|\phi_i^{\vec{k}}\rangle\langle\psi_m^{N-1}|\psi_i^{N-1}\rangle. \quad (3.7)$$

In this formula, $\langle\phi_f^{\vec{k}}|H_{int}|\phi_i^{\vec{k}}\rangle = M_{i,f}^{\vec{k}}$ is the one-electron dipole matrix element and $\langle\psi_m^{N-1}|\psi_i^{N-1}\rangle = c_{m,i}$ gives the overlap between initial and final state. Plugging (3.7)

3.1. PROCESS OF PHOTOEMISSION

into (3.4), the total photoemission intensity $I(\vec{k}, E_k) = \sum_{f,i} w_{fi}$ is given by

$$I(\vec{k}, E_k) \propto \sum_{f,i} |M_{f,i}^{\vec{k}}|^2 \sum_m |c_{m,i}|^2 \delta(E_k + E_m^{N-1} - E_i^N - h\nu). \quad (3.8)$$

In this case $|c_{m,i}|^2$ gives the probability for the system to be left in final state m when removing one electron from initial state i . If the initial state ψ_i^{N-1} is also an eigenstate m_0 of the (N-1) system, then $|c_{m,m_0}|^2 = \delta_{m,m_0}$ and the photoemission intensity is given by a single delta-peak located at the binding energy of the orbital making up the initial state

$$\delta(E_k + E_{m_0}^{N-1} - E_{m_0}^N - h\nu) = 1 \Leftrightarrow E_k + E_{m_0}^{N-1} - E_{m_0}^N - h\nu = 0 \quad (3.9)$$

$$E_k + E_{m_0}^{N-1} - E_{m_0}^N + E_B^{\vec{k}} - h\nu = 0 \quad (3.10)$$

$$E_B^{\vec{k}} = h\nu - E_k. \quad (3.11)$$

In strongly correlated systems however, the initial state ψ_i^{N-1} is not an eigenstate of the excited system and several satellite peaks are part of the observed spectrum.

3.2 Tight-Binding Approximation

A good introduction on the tight-binding formalism is given in “Solid State Physics” by Ashcroft and Mermin [38]. The following quick summary of the TB method is focused on the general method and will not talk about ways to calculate the parameters of the model from first principles. Some small parts of the following description are based on the section on tight-binding theory in the author’s master thesis [114].

The idea of the tight-binding formalism, as the name suggests, is to start from the sum of all atomic Hamiltonians H_{at} for the singular atoms and model the influence of the other atoms in a crystal on the atomic potential by a small perturbation ΔU

$$\hat{H} = \sum_i \hat{H}_{at}^i + \Delta U. \quad (3.12)$$

Because the perturbation in this formalism is assumed to be small, atomic wave functions $|\varphi_{i,n}\rangle$ that solve

$$\hat{H}_{at}^i |\varphi_{i,n}\rangle = E_n |\varphi_{i,n}\rangle \quad (3.13)$$

are used to construct the wave functions at site i

$$|\phi_i\rangle = \sum_n b_n |\varphi_{i,n}\rangle. \quad (3.14)$$

This assumption lies at the heart of the tight-binding theory. A full solution of the Schrödinger equation $\hat{H} |\psi\rangle = \varepsilon |\psi\rangle$ is then given by a linear combination of wave functions $|\phi_i\rangle$

$$|\psi\rangle = \frac{1}{\sqrt{N}} \sum_i \exp(i\vec{k} \cdot \vec{R}_i) |\phi_i\rangle. \quad (3.15)$$

The prefactors are chosen in such a way, that the wave function $|\psi\rangle$ describes a Bloch state. Using the constructed orbitals, it is possible to solve the Schrödinger equation

$$\hat{H} |\psi_v\rangle = \left(\sum_i \hat{H}_{at}^i + \Delta U \right) |\psi_v\rangle = \varepsilon(\vec{k}) |\psi_v\rangle \quad (3.16)$$

by multiplying from the left with $\langle\psi_u|$

$$\langle\psi_u|\hat{H}|\psi_v\rangle = \varepsilon(\vec{k}) \langle\psi_u|\psi_v\rangle \quad (3.17)$$

3.2. TIGHT-BINDING APPROXIMATION

and solving the matrix equation. For orthogonal tight-binding methods with

$$S_{u,v} = \langle \psi_u | \psi_v \rangle = \delta_{u,v} \quad (3.18)$$

$$S = \mathbb{1} \quad (3.19)$$

equation (3.17) is a normal eigenvalue equation

$$(H_{u,v} - \varepsilon S_{u,v})c_u = 0. \quad (3.20)$$

The orbitals in this case form an orthogonal basis set. For non-orthogonal tight-binding with the overlap matrix $S \neq \mathbb{1}$, equation (3.17) can be transformed into a simple eigenvalue equation *via* the Löwdin transform [174]

$$0 = (S^{-1/2}HS^{1/2} - \varepsilon\mathbb{1})(S^{1/2}\vec{c}S^{-1/2}) = (\tilde{H} - \varepsilon\mathbb{1})\vec{z}. \quad (3.21)$$

This new eigenvalue problem for \vec{z} can be solved and the original \vec{c} be recovered from \vec{z} .

The biggest advantage of the TB formalism however lies in the easy physical interpretation of the entries in the Hamiltonian. Using linearity, $\langle \psi_u | \hat{H} | \psi_v \rangle$ can be split

$$\langle \psi_u | \hat{H} | \psi_v \rangle = \sum_p \langle \psi_u | \hat{H}_{\text{at}}^p | \psi_v \rangle + \langle \psi_u | \Delta U | \psi_v \rangle. \quad (3.22)$$

Inserting the definition of the wave functions the first summand is

$$\sum_p \langle \psi_u | \hat{H}_{\text{at}}^p | \psi_v \rangle = \frac{1}{N} \sum_{i,j,m,n,p} b_m^* b_n \exp(i\vec{k} \cdot (\vec{R}_j - \vec{R}_i)) \langle \varphi_{i,m} | \hat{H}_{\text{at}}^p | \varphi_{j,n} \rangle \quad (3.23)$$

$$\approx \sum_m |b_m|^2 E_m + \frac{1}{N} \sum_{i \neq j, j, m, n} b_m^* b_n \exp(i\vec{k} \cdot (\vec{R}_j - \vec{R}_i)) E_m \langle \varphi_{i,m} | \varphi_{j,n} \rangle \quad (3.24)$$

$$= \sum_m |b_m|^2 E_m + \frac{1}{N} \sum_{i \neq j, j, m, n} b_m^* b_n e^{i\vec{k} \cdot (\vec{R}_j - \vec{R}_i)} E_m \alpha_{m,n}(\vec{R}_j - \vec{R}_i) \quad (3.25)$$

with E_m the energy of orbital $|\varphi_{i,m}\rangle$. In step two, the two-center approximation was used, meaning parts of the sum with \hat{H}_{at}^p , $\langle \varphi_{i,m} |$ and $|\varphi_{j,n}\rangle$ located at three different sites were ignored. The overlap between orbitals on different atomic sites

$$\alpha_{m,n}(\vec{R}) = \int \varphi_m(\vec{r})^* \varphi_n(\vec{r} - \vec{R}) d\vec{r} \quad (3.26)$$

is usually small and thus the contribution is negligible compared to the energies E_m . Doing a similar calculation for the second summand in (3.22) one finds

$$\langle \psi_u | \Delta U | \psi_v \rangle = \frac{1}{N} \sum_{i,j,m,n} b_m^* b_n \exp(i\vec{k} \cdot (\vec{R}_j - \vec{R}_i)) \langle \varphi_{i,m} | \Delta U | \varphi_{j,n} \rangle \quad (3.27)$$

$$= \sum_{i,n,m} b_n b_m^* \langle \varphi_{i,m} | \Delta U | \varphi_{i,n} \rangle + \frac{1}{N} \sum_{i \neq j, j, m, n} b_m^* b_n \exp(i\vec{k} \cdot (\vec{R}_j - \vec{R}_i)) \langle \varphi_{i,m} | \Delta U | \varphi_{j,n} \rangle \quad (3.28)$$

$$\approx \sum_{n,m} b_n b_m \beta_{m,n} + \frac{1}{N} \sum_{i \neq j, j, m, n} b_m^* b_n \exp(i\vec{k} \cdot (\vec{R}_j - \vec{R}_i)) \gamma_{m,n}(\vec{R}_j - \vec{R}_i). \quad (3.29)$$

In the last step, the two-center approximation was used again, leading to the hopping terms $\gamma_{m,n}(\vec{R})$ and the lattice contribution $\beta_{m,n}$ given by

$$\beta_{m,n} = \int \varphi_m(\vec{r})^* \Delta U(\vec{r}) \varphi_n(\vec{r}) d\vec{r} \quad (3.30)$$

$$\gamma_{m,n}(\vec{R}) = \int \varphi_m(\vec{r})^* \Delta U(\vec{r}) \varphi_n(\vec{r} - \vec{R}) d\vec{r}. \quad (3.31)$$

The lattice contribution $\beta_{m,n}$ can usually be ignored as it is a minor on-site contribution that modifies the on-site eigenenergies of the atomic Hamiltonian. Additionally, the hopping parameters $\gamma_{m,n}$ fall off rapidly with increasing distance between the different sites. This means that the sum in line (3.29) can safely be terminated for some nearest neighbour order. Often it is not necessary to include more than one order of neighbours in a tight-binding model to qualitatively reproduce an experimental band structure. A few additional assumptions can help with making the result a little bit more clear. Assuming the solutions are only made up from atomic s-orbitals $|\phi_i\rangle = |\varphi_{i,s}\rangle$ (so $b_n = \delta_{n,s}$) and further assuming $\alpha_{m,n}(\vec{R} \neq 0) = 0$, equation (3.25) becomes

$$\sum_p \langle \psi_u | \hat{H}_{\text{at}}^p | \psi_v \rangle = E_s. \quad (3.32)$$

On the other hand, equation (3.29) becomes

$$\langle \psi_u | \Delta U | \psi_v \rangle = \beta_{s,s} + \frac{1}{N} \sum_{i \neq j, j} \exp(i\vec{k} \cdot (\vec{R}_j - \vec{R}_i)) \gamma_{s,s}(|\vec{R}_j - \vec{R}_i|). \quad (3.33)$$

Since the hopping parameters $\gamma_{s,s}$ fall off rapidly with increasing distance, the sum can be truncated after the nearest neighbour contribution. In this case, the full solution of

3.2. TIGHT-BINDING APPROXIMATION

equation (3.22) is given by

$$\langle \psi_s | \hat{H} | \psi_s \rangle = E_s + \beta_{s,s} + \gamma_{s,s}^{NN} \sum_{\langle i,j \rangle} \exp \left(i \vec{k} \cdot (\vec{R}_j - \vec{R}_i) \right). \quad (3.34)$$

Since $\Delta U < 0$, the lattice contribution $\beta_{s,s}$ lowers the energy of the state *versus* the energy E_s of the isolated atomic s-orbital. On the other hand, the hopping integral $\gamma_{s,s}^{NN}$ can be positive or negative. The \vec{k} -dependence of the sum introduces the k -space dispersion of the electronic bands. The bigger the hopping integral $\gamma_{s,s}^{NN}$, the bigger the band width. For a one-dimensional chain with one atom in the unit cell and lattice spacing a , the solution becomes

$$\langle \psi_s | \hat{H} | \psi_s \rangle = E_s + \beta_{s,s} + \gamma_{s,s}^{NN} [\exp(ika) + \exp(-ika)] \quad (3.35)$$

$$= E_s + \beta_{s,s} + 2\gamma_{s,s}^{NN} \cos(ka). \quad (3.36)$$

3.2.1 Tight-Binding in Second Quantization

The tight-binding method can also be formulated in second quantization. Introductions to the formalism are given for example in [175] and [176]. The real-space tight-binding Hamiltonian in second quantization is given by

$$\hat{H}_{TB} = - \sum_{i,j,n,m} \left(t_{i,j,n,m} c_{i,n}^\dagger c_{j,m} + t_{i,j,n,m}^* c_{j,m}^\dagger c_{i,n} \right) \quad (3.37)$$

The sum describes an electron hopping from orbital n on site i to orbital m on site j (or vice versa for the hermitian conjugate part). Assuming a real hopping amplitude t for nearest neighbour hopping and no hopping otherwise and additionally assuming orthogonal tight-binding so that an electron in orbital n only jumps to orbitals of the same type n on other sites, the Hamiltonian can be simplified. The Hamiltonian for band n made up from orbitals of type n is then

$$\hat{H}_{TB}^n = -t \sum_{\langle i,j \rangle} \left(c_{i,n}^\dagger c_{j,n} + h.c. \right). \quad (3.38)$$

Where the sum only runs over nearest neighbours. The k -space Hamiltonian can be derived by substituting in the Fourier-transformed creation and annihilation operators

$$c_j^\dagger = \frac{1}{\sqrt{N}} \sum_{\vec{k}} \exp(-i\vec{k} \cdot \vec{r}_j) c_{\vec{k}}^\dagger \quad (3.39)$$

$$c_j = \frac{1}{\sqrt{N}} \sum_{\vec{k}} \exp(i\vec{k} \cdot \vec{r}_j) c_{\vec{k}}. \quad (3.40)$$

Example: One Dimensional Chain For the one-dimensional chain the sum over nearest neighbours can be rewritten

$$\hat{H}_{TB} = -t \sum_{\langle i,j \rangle} \left(c_i^\dagger c_j + h.c. \right) \quad (3.41)$$

$$= -t \sum_j c_j^\dagger c_{j+1} + c_{j+1}^\dagger c_j. \quad (3.42)$$

Inserting the Fourier transforms of the creation/annihilation operators and writing the position of site j as $r_j = j \times a$ leads to

$$\hat{H}_{TB} = -t \sum_j c_j^\dagger c_{j+1} + c_{j+1}^\dagger c_j \quad (3.43)$$

$$= -t \sum_j \frac{1}{N} \sum_{k,k'} e^{-ikja} e^{ik'(j+1)a} c_k^\dagger c_{k'} + e^{-ik'(j+1)a} e^{ikja} c_k^\dagger c_{k'} \quad (3.44)$$

$$= -t \sum_j \frac{1}{N} \sum_{k,k'} e^{i(k'-k)ja} e^{ik'a} c_k^\dagger c_{k'} + e^{i(k-k')a} e^{-ik'a} c_k^\dagger c_{k'} \quad (3.45)$$

$$= -t \sum_k e^{ika} c_k^\dagger c_k + e^{-ika} c_k^\dagger c_k = -t \sum_k (e^{ika} + e^{-ika}) c_k^\dagger c_k \quad (3.46)$$

$$= \sum_k (-2t \cos(ka)) c_k^\dagger c_k. \quad (3.47)$$

In the jump to line (3.46) the identity $\sum_j \exp(i(k-k')ja) = N\delta_{k,k'}$ was used.

The resulting tight-binding Hamiltonian is diagonal in k and the cosine-dispersion of a simple one dimensional single band model is reproduced from a second quantization perspective.

3.3 Many Body Effects in Angle-Resolved Photoemission Spectra

While the tight-binding method presented in section 3.2 is a powerful tool in the analysis of band structures, it employs a one-electron approximation with a static lattice used for the calculation. These approximations mean, that the band structures calculated *via* tight-binding do not take electron-phonon coupling, electron-electron interactions or any other many-body effects into account.

It is not immediately clear, how the one-electron states calculated *via* the tight-binding model correspond to excitations in a system with many-body interactions. In this context, Landau developed his Fermi liquid theory [177, 178]. He realized, that in cases where the coupling is small, it is helpful to view the system not from a perspective of free fermions plus interactions but rather as a collection of quasi-particles which behave like free particles with renormalized energies, masses *et cetera*. When turning on interactions, the parameters of the free model adiabatically develop into the parameters of the interacting model, giving a one to one correspondence of non-interacting to interacting states in the case of small interaction strength [177–179]. An introduction to Fermi liquid theory and the concept of adiabatic continuity is given in [179]. Real band structures measured with photoemission spectroscopy measure the dispersion of these quasi-particles and can deviate from the band structures predicted by the one-electron model [173, 180–182]. In materials with strongly correlated electrons, calculations employing a one-electron approximation thus fail to accurately reproduce experimental findings and more involved techniques need to be used to include these effects in calculations [173, 180–182].

In many cases however, the deviations from the one-electron model are small. To include the many-body effects with the one-electron non-interacting bare particle dispersion as a basis, a Green’s function approach can be used. Introductions to this method in the context of angle-resolved photoemission spectroscopy are given in [173], [180], and [182]. In the case of interacting particles, the δ -peaks in equation (3.8) are replaced with the spectral response function [180–182]

$$A(\vec{k}, \omega) = -\frac{1}{\pi} \text{Im}(G^R(\vec{k}, \omega)) \quad (3.48)$$

where $G^R(\vec{k}, \omega)$ is the retarded Green’s function for the one-electron removal/addition process [173, 180–182]. To understand this approach, it is useful to first apply it in the context of a non-interacting system. For a non-interacting system, the retarded free

propagator $G_0^R(\vec{k}, \omega)$ has the form [173, 182]

$$G_0^R(\vec{k}, \omega) = \frac{1}{\omega - \varepsilon_{\vec{k}} + i0^+} \quad (3.49)$$

with $\varepsilon_{\vec{k}}$ the dispersion relation of the one-electron model. The free propagator has poles at the energies of the one-electron dispersion $\omega = \varepsilon_{\vec{k}}$. With the help of the Dirac identity [182] $\lim_{\eta \rightarrow 0^+} \frac{1}{x \pm i\eta} = \mathcal{P}(\frac{1}{x}) + i\pi\delta(x)$ the spectral function for non-interacting particles reproduces the δ -peaks at energy $\omega = \varepsilon_{\vec{k}}$.

Modeling the many-body interactions as a perturbation series to the free particle Hamiltonian, the retarded Green's function for the interacting system can be found self-consistently *via* the Dyson equation [176]

$$G^R(\vec{k}, \omega) = G_0^R(\vec{k}, \omega) + G_0^R(\vec{k}, \omega)\Sigma(\vec{k}, \omega)G^R(\vec{k}, \omega) \quad (3.50)$$

$$\Leftrightarrow G^R(\vec{k}, \omega) = \frac{1}{\omega - \varepsilon_{\vec{k}} - \Sigma(\vec{k}, \omega)}. \quad (3.51)$$

The complex self-energy $\Sigma(\vec{k}, \omega)$ includes the many-body effects of the interacting system. It is the sum of all irreducible one-particle Feynman diagrams [176, 182]. The explicit theoretical calculation of the self-energy is arbitrarily complex. Rewriting the self-energy as $\Sigma(\vec{k}, \omega) = \Sigma'(\vec{k}, \omega) + i\Sigma''(\vec{k}, \omega)$, the retarded dressed Green's function can be split into real and imaginary parts

$$G^R(\vec{k}, \omega) = \frac{1}{\omega - \varepsilon_{\vec{k}} - \Sigma'(\vec{k}, \omega) - i\Sigma''(\vec{k}, \omega)} \quad (3.52)$$

$$\begin{aligned} &= \frac{\omega - \varepsilon_{\vec{k}} - \Sigma'(\vec{k}, \omega)}{\left(\omega - \varepsilon_{\vec{k}} - \Sigma'(\vec{k}, \omega)\right)^2 + \left(\Sigma''(\vec{k}, \omega)\right)^2} \\ &\quad + i \frac{\Sigma''(\vec{k}, \omega)}{\left(\omega - \varepsilon_{\vec{k}} - \Sigma'(\vec{k}, \omega)\right)^2 + \left(\Sigma''(\vec{k}, \omega)\right)^2}. \end{aligned} \quad (3.53)$$

The spectral function is then given by

$$A(\vec{k}, \omega) = -\frac{1}{\pi} \text{Im}(G^R(\vec{k}, \omega)) = -\frac{1}{\pi} \frac{\Sigma''(\vec{k}, \omega)}{\left(\omega - \varepsilon_{\vec{k}} - \Sigma'(\vec{k}, \omega)\right)^2 + \left(\Sigma''(\vec{k}, \omega)\right)^2}. \quad (3.54)$$

The real part Σ' of the self-energy shifts the pole of the dressed propagator away from the dispersion of the non-interacting system leading to a renormalization of effective mass, Fermi velocity, and other parameters. The imaginary part of the self-energy

is related to the real part *via* the Kramers-Kronig relations [176,182]. It leads to a damping of the response and manifests as a broadening of the spectral function. This broadening is inversely related to the lifetime τ of the quasi-particles in the interacting system, $\Sigma'' \propto \frac{1}{\tau}$ [173,180–182].

In real systems, many contributions to the self-energy are present. These different contributions add up to give the final resulting spectral response. In the following, two major contributions to the self-energy are discussed.

Fermi liquid Landau’s idea of a Fermi liquid posits that the states of the non-interacting system develop smoothly when turning on electron-electron interactions. For small interactions there is a one-to-one correspondence between non-interacting and interacting states [180]. This preserves the analyticity of the self-energy and allows the expansion of $\Sigma(\vec{k}, \omega)$ around the bare dispersion $\varepsilon_{\vec{k}}$ [180]

$$\Sigma(\omega) \approx \Sigma(\varepsilon_{\vec{k}}) + \left. \frac{\partial \Sigma(\omega)}{\partial \omega} \right|_{\omega=\varepsilon_{\vec{k}}} (\omega - \varepsilon_{\vec{k}}) \quad (3.55)$$

$$= \left[\Sigma'(\varepsilon_{\vec{k}}) + \left. \frac{\partial \Sigma'(\omega)}{\partial \omega} \right|_{\omega=\varepsilon_{\vec{k}}} (\omega - \varepsilon_{\vec{k}}) \right] + i \left[\Sigma''(\varepsilon_{\vec{k}}) + \left. \frac{\partial \Sigma''(\omega)}{\partial \omega} \right|_{\omega=\varepsilon_{\vec{k}}} (\omega - \varepsilon_{\vec{k}}) \right]. \quad (3.56)$$

Note that the explicit \vec{k} -dependence of the self-energy is dropped because the screened electron-electron interaction is highly local and thus Σ varies slowly in \vec{k} -space [182]. Causality imposes odd-symmetry in ω around the Fermi energy for the real part of the self-energy and even symmetry for the imaginary part [182]. This means that in proximity to the Fermi energy, the partial derivative of the imaginary part $\frac{\partial \Sigma''(\omega)}{\partial \omega}$ is negligibly small. The real part on the other hand changes linearly around the Fermi energy. The electron-electron coupling constant $\lambda_{ee} = -\left. \frac{\partial \Sigma'(\omega)}{\partial \omega} \right|_{\omega=\varepsilon_{\vec{k}}}$ and the renormalization constant $Z = 1 + \lambda_{ee}$ are introduced. Inserting the approximation for the self-energy in the Green’s function of the interacting system (3.52) and using Z and λ_{ee} , the spectral function becomes [180]

$$A(\vec{k}, \omega) = -\frac{1}{\pi} Z^{-1} \frac{Z^{-1} \Sigma''(\varepsilon_{\vec{k}})}{(\omega - \varepsilon_{\vec{k}} - Z^{-1} \Sigma'(\varepsilon_{\vec{k}}))^2 + (Z^{-1} \Sigma''(\varepsilon_{\vec{k}}))^2}. \quad (3.57)$$

The spectral weight of the spectral function is reduced by a factor of $Z^{-1} \leq 1$. This is a consequence of the quasi-particle description. The new spectral function describes the coherent quasi-particles and their dispersion. The missing spectral weight is shifted to

an incoherent background [180, 182]. As interactions are getting stronger with increasing coupling constant λ_{ee} more and more spectral weight is shifted from the coherent to the incoherent part of the spectrum.

The coherent spectral function describes quasi-particles with renormalized dispersion relation $\omega(\vec{k}) = \varepsilon_{\vec{k}} + Z^{-1}\Sigma'(\varepsilon_{\vec{k}})$. As the self-energy does not depend strongly on \vec{k} the change of the real part with $\varepsilon_{\vec{k}}$ only depends on its change with ω and thus $\Sigma'(\varepsilon_{\vec{k}}) = -\lambda_{ee}\varepsilon_{\vec{k}}$. The bare dispersion is renormalized to

$$\omega(\vec{k}) = \varepsilon_{\vec{k}} - \frac{\lambda_{ee}}{1 + \lambda_{ee}}\varepsilon_{\vec{k}} = \frac{\varepsilon_{\vec{k}}}{1 + \lambda_{ee}} \quad (3.58)$$

leading to an enhancement of the effective mass $m^* = (1 + \lambda_{ee})m$ [180].

For a three-dimensional Fermi liquid, the imaginary part $\Sigma''(\varepsilon_{\vec{k}})$ is proportional to the square of the binding energy of the particles measured from the Fermi energy [183]. This leads to a total self-energy contribution for electron-electron interactions [180–182]

$$\Sigma_{3D-FL} = -\lambda_{ee}\varepsilon_{\vec{k}} - i\beta\varepsilon_{\vec{k}}^2. \quad (3.59)$$

In two dimensions, the imaginary part has contributions proportional to $\varepsilon_{\vec{k}}^2$ as well as $\varepsilon_{\vec{k}}^2 \ln(|\varepsilon_{\vec{k}}|)$ [182, 184–186]. At low energies, this still leads to a small imaginary part of the self-energy – and thus a small scattering rate and weak coupling – meaning the Fermi liquid picture is still valid for low-energy excitations around the Fermi surface.

Bosonic excitations On top of the electron-electron interactions leading to Fermi liquid behaviour, the electrons can also couple to bosonic excitations of the crystal such as phonons or magnons [15, 180, 182]. This contribution to the self-energy can simply be added on top of the Fermi liquid contribution. The qualitative energy dependence of the imaginary self-energy for a coupling to a bosonic mode at energy Ω_0 is easy to determine due to its inverse relationship with the lifetime of a given state. A photohole with energy ω less than Ω_0 can not be scattered *via* an interaction with this bosonic mode due to Pauli-blocking [180, 182]. The lifetime of this photohole is infinite (ignoring other scattering mechanisms) and thus the imaginary part of the self-energy is zero. For energies ω larger than Ω_0 , the scattering rate is approximately constant, leading to a step function for $\Sigma''(\varepsilon_{\vec{k}})$ [180]. With the imaginary part known, the real part can

be determined from Kramers-Kronig relations and the full self-energy is given by [180]

$$\Sigma'(\varepsilon_{\vec{k}}) = \frac{\lambda_{ep}\Omega_0}{2} \ln \left| \frac{\varepsilon_{\vec{k}} + \Omega_0}{\varepsilon_{\vec{k}} - \Omega_0} \right| \quad (3.60)$$

$$\Sigma''(\varepsilon_{\vec{k}}) = \Theta(|\varepsilon_{\vec{k}}| - \Omega_0) \frac{(-\lambda_{ep})\pi\Omega_0}{2} \quad (3.61)$$

with $\Theta(\omega)$ the Heaviside function. Coupling to these bosonic modes leads to a local renormalization of the band around the energy of the bosonic mode. This manifests as “kinks” in the dispersion.

Total Resulting Spectral Function In many materials, the Fermi liquid corrections and the bosonic kinks are the most important corrections to the spectral function. Scattering at localized defects merely adds an inherent energy-independent broadening to the coherent peaks [181]. The influence of more exotic effects such as a superconducting or a charge density wave transition can also be taken into account with the Green’s function approach [15, 180, 182].

Figure 3.2 shows the effects of Fermi liquid renormalization and coupling to bosonic modes on the bare particle dispersion. Figure 3.2(a) shows the spectral function of the bare dispersion with an inherent broadening of $\Sigma'' = 0.03$ eV added for visibility. The bare band dispersion used for the calculation of the spectral function is the free electron dispersion $\omega = \hbar^2 k^2 / 2m^*$, the effective mass chosen for the depicted case is equal to the free electron mass $m^* = m_e$. Figure 3.2(b) shows the effects of the self-energy for the Fermi liquid approximation. The bottom of the band is shifted to lower binding energies and the effective mass is enhanced *versus* the bare dispersion. As the band approaches the Fermi level, the lifetime of the quasi-particles increases and the broadening approaches the inherent broadening. Without inherent broadening, the lifetime of the quasi-particles is infinite at the Fermi energy. In figure 3.2(c), a coupling to a bosonic mode at $\Omega_0 = 100$ meV is added on top of the inherent broadening and the Fermi liquid effects. The kinks in the dispersion are obvious around points $(\pm 0.5 \text{ \AA}^{-1}, \pm 0.1 \text{ eV})$. The states with $|\omega - E_f| < \Omega_0$ are much sharper, as Pauli-blocking prevents scattering between these quasiparticle states and the bosonic excitations [180, 182].

To show the effect of coupling to bosonic modes more clearly, figure 3.2(d) displays the effect in greater detail for a bare linear band crossing the Fermi energy at 1.11 \AA^{-1} with a bosonic excitation at energy $\Omega_0 = 180$ meV. The corresponding real and imaginary parts of the self-energy are shown in figure 3.2(e). The quadratic background of the imaginary self-energy shown in orange arises from the electron-electron inter-

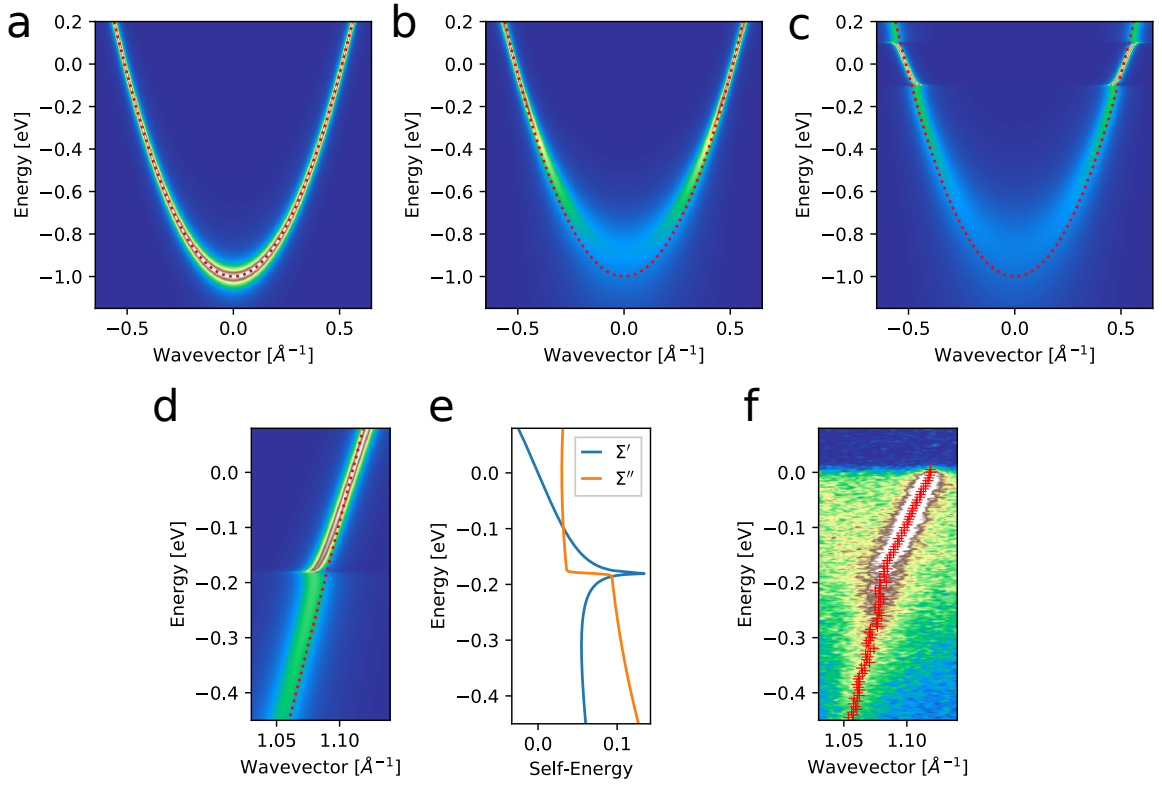


Figure 3.2: Effects of the self-energy on the electronic dispersion. (a) Free electronic dispersion, the bare band is plotted in red. (b) Fermi liquid renormalization effects. (c) Fermi liquid plus coupling to bosonic mode at $\Omega_0 = 100$ meV. (d) Detailed view of kink appearing in linear dispersing band due to coupling to bosonic mode at $\Omega_0 = 180$ meV. (e) Real (blue) and imaginary (orange) part of total energy for the dispersion shown in (d). (f) Example of a kink in the dispersion for real graphene, the peak positions of the dispersion are marked with red crosses.

actions, the step at 0.18 eV is caused by the coupling to the bosonic mode. The real part is displayed in blue and describes the shift in energy of the states *versus* the bare band. Figure 3.2(f) shows a similar situation as figure 3.2(d) for a real angle-resolved photoemission experiment. While the theoretical spectral function describes both electron removal as well as electron addition, ARPES only captures the electron removal/photohole part of the spectrum. The dispersion above the Fermi level is thus not accessible with conventional ARPES. The kink in the dispersion around 180 meV is clearly distinguishable but less sharp in comparison with the theoretical spectrum in 3.2(d). Experimental resolution as well as broadening of the bosonic modes somewhat smoothes out the kink.

Determination of the imaginary and real self-energies in general and the electron-phonon coupling constant in particular is nevertheless possible [14, 153, 180, 187, 188]. The imaginary self-energy can be determined from the broadening of the states in constant-energy cuts along the k -axis. It is directly related to the half width at half maximum of the peak times the Fermi velocity of the band [14, 153, 187, 188]. To independently determine the real self-energy, knowledge of the bare band dispersion is necessary. If the bare band is known, the real self-energy is given by the energy shift of the quasiparticle dispersion *versus* the bare band. In most cases however, the bare band is unfortunately not known. In these circumstances, several possibilities exist to determine a good approximation of the bare band. The most simple procedure is done *via* extrapolation of the bare band from parts of the band structure where renormalization is small [187, 188]. Another procedure is to determine the bare band from measurements at elevated temperatures, where renormalization effects are reduced [187, 188]. A more sophisticated bare band determination can be done self-consistently by using the Kramers-Kronig relations between real and imaginary self-energy [14, 15, 153, 187] (compare also appendix A.2.1.3 and A.2.1.4). Assuming a random bare band dispersion, determining the real and imaginary parts of the self-energy and checking if they are Kramers-Kronig related allows a fitting procedure to converge towards the correct bare band dispersion. As the Kramers-Kronig relations are integrated over the whole energy range, it is important to use a large enough energy window when trying to determine the bare band. Since the kink-structure is well localized in energy, the error from not integrating over the whole energy range is minimal if the termination point of the integration lies far enough away from the observed features. If such termination points are not reachable, a model has to be used to extend the measured real and imaginary parts of the self-energy towards infinity [182]. Accuracy of the Kramers-Kronig transform can be further improved by assuming electron-hole symmetry for the

self-energy around the Fermi energy [173, 182, 189].

With the bare band and the self-energies established, the electron-phonon coupling constant λ_{ep} can be determined in several ways. Going from formula (3.60), the real part of the self-energy is approximately linear in $\varepsilon_{\vec{k}}$ for low binding energies with a slope proportional to λ_{ep} . Alternatively, the step height of the imaginary part in formula (3.61) is also proportional to λ_{ep} . These equations can hence be used to get an approximation of the electron-phonon coupling. However, these equations are valid for ideal situations with coupling to only one bosonic mode. The actual experimentally determined real and imaginary self energy are usually more complicated. While the effects of impurity scattering and Fermi liquid corrections from electron-electron correlations can be accounted for relatively easily, the existence of more than one bosonic mode coupling to the electrons often complicates determination of the coupling constant *via* such simple models. An alternative determination of λ_{ep} comes from a fit of the Eliashberg function to the determined real and imaginary parts of the self energy [14, 15, 153, 187, 190, 191]. The additional fitting procedure with the Eliashberg function allows for the inclusion of several bosonic modes. In the most general case, the fitting can be done with an arbitrary Eliashberg function [15, 153, 190, 191]. The total coupling constant can then be determined by integrating out the energy dependence of the Eliashberg function [14, 15, 190, 191]. The general approach makes it hard to assign a coupling constant to individual bosonic excitations though. If additional information about the coupling strength of particular modes is already available and individual modes are known to dominate the coupling, the form of the Eliashberg function can be artificially limited to these modes to extract the corresponding coupling constant [14, 187].

3.4 Spin-Orbit Coupling

A toy-model description of spin-orbit effects in materials is straight forward to derive semi-classically. An electron moving with momentum \vec{k} in an electric field \vec{E} experiences a magnetic field \vec{B} in its rest frame with [192, Chapter 12]

$$\vec{B} \propto -(\vec{E} \times \vec{k}). \quad (3.62)$$

The energy of the electronic spin in a magnetic field is given by [193]

$$\hat{H} = -\vec{\mu} \cdot \vec{B} \quad (3.63)$$

$$\vec{\mu} = \frac{g_s \mu_B}{2} \vec{\sigma} \quad (3.64)$$

with $\vec{\sigma}$ the vector of Pauli matrices $\vec{\sigma} = (\hat{\sigma}_1, \hat{\sigma}_2, \hat{\sigma}_3)^T$. Inserting (3.62) and writing the electric field as the gradient of a potential $\vec{E} \propto \vec{\nabla}V$, the Hamiltonian becomes

$$\hat{H} \propto \vec{\sigma} \cdot (\vec{\nabla}V \times \vec{k}). \quad (3.65)$$

In the vicinity of a single atom, the potential V is radially symmetric, so $\vec{\nabla}V = \frac{\partial V}{\partial r} \frac{\vec{r}}{r}$ and the Hamiltonian is given by

$$\hat{H} \propto \frac{1}{r} \frac{\partial V}{\partial r} \vec{\sigma} \cdot (\vec{r} \times \vec{k}). \quad (3.66)$$

$(\vec{r} \times \vec{k})$ is proportional to the angular momentum \vec{L} , so the final Hamiltonian for a single atom is found to be

$$\hat{H} \propto \frac{1}{r} \frac{\partial V}{\partial r} \vec{\sigma} \cdot \vec{L}. \quad (3.67)$$

From the form of this Hamiltonian, the name “spin-orbit coupling” becomes clear. The $\vec{\sigma}$ -vector describes the spin degrees of freedom of the electron and \vec{L} its angular momentum – which is related to the state of orbital wave function [193].

Hamiltonian (3.67) lifts the degeneracy of orbitals with the same angular quantum number l within a single atom [193] and consequently also influences the structure of bands derived from these atomic basis states in a solid. However, when talking about spin-orbit coupling in crystals, the crystal potential is not radially symmetric in the space between the individual atoms and additional situations with different symmetries arise. In particular, time reversal symmetry imposes Kramers degeneracy and gives

the relation

$$E(\vec{k}, \uparrow) = E(-\vec{k}, \downarrow) \quad (3.68)$$

for the electronic dispersion [70, 194]. On the other hand, spacial inversion symmetry imposes [70]

$$E(\vec{k}, \uparrow) = E(-\vec{k}, \uparrow), \quad E(\vec{k}, \downarrow) = E(-\vec{k}, \downarrow). \quad (3.69)$$

Combining (3.68) and (3.69) gives

$$E(\vec{k}, \uparrow) = E(\vec{k}, \downarrow) \quad (3.70)$$

which enforces degeneracy of the spins. Spin-orbit interaction still lifts the degeneracy of orbitals with the same orbital quantum number l , but the spin states stay degenerate. This implies several ways to get spin split bands in a crystal. For example, time reversal symmetry can be broken explicitly by application of magnetic fields [195]. In the presence of time reversal symmetry, spin splitting can still be achieved *via* inversion symmetry breaking. The inversion symmetry can either be broken by the bulk crystal structure itself, or by a structural asymmetry like a surface or an interface [70]. Phenomenological models for these two distinct effects exist. The effects of a structural inversion asymmetry can be modeled *via* the Bychkov-Rashba Hamiltonian. A bulk crystal inversion asymmetry can be described with the Dresselhaus Hamiltonian. Both Hamiltonians are discussed below.

For a more accurate description of spin-orbit coupling in solids, more complicated methods involving the explicit crystal structures and structural asymmetries in the calculation can be used [196–199].

Bychkov-Rashba Spin Orbit Coupling At surfaces or interfaces, the potential V in Hamiltonian (3.65) changes rapidly perpendicular to the plane. Setting the interface/surface into the x - y -plane, the potential is thus given by $\vec{\nabla}V = -V_0(0, 0, 1)^T$. This leads to the Hamiltonian [70, 197, 199, 200]

$$\hat{H}_R \propto V_0 \vec{\sigma} \cdot \left((0, 0, 1)^T \times \vec{k} \right) \quad (3.71)$$

$$\hat{H}_R = \alpha(k_x \hat{\sigma}_2 - k_y \hat{\sigma}_1) = \alpha \begin{pmatrix} 0 & -ik_x - k_y \\ ik_x - k_y & 0 \end{pmatrix}. \quad (3.72)$$

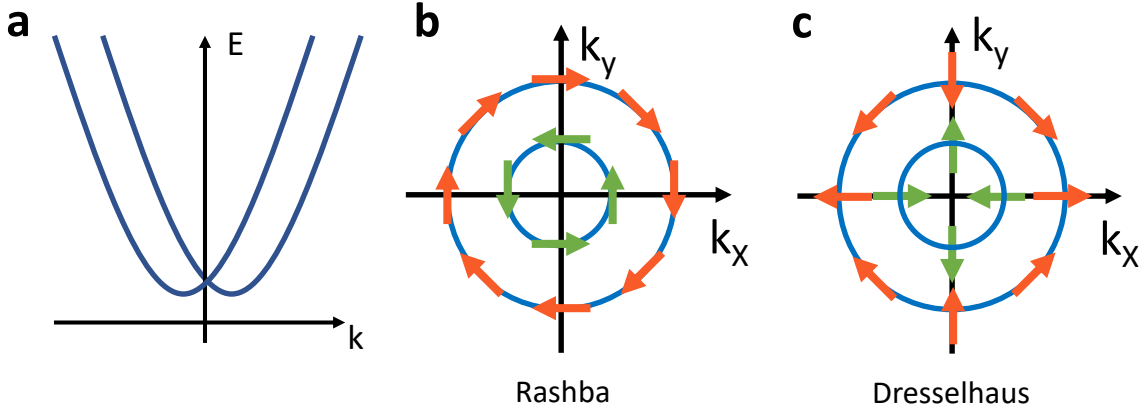


Figure 3.3: (a) Sketch of dispersion relation for Rashba and Dresselhaus SOC. (b) Spin structure of k -space for Rashba SOC. (c) Spin structure of k -space for Dresselhaus SOC.

Adding this Rashba Hamiltonian to the Hamiltonian of a spin-degenerate free particle Hamiltonian $\hat{H}_{free} = (k_x^2 + k_y^2)\hat{\sigma}_0$ it becomes clear that the Rashba Hamiltonian mixes spin-up and spin-down states and leads to an energy splitting of the spin states

$$\hat{H} = \hat{H}_{free} + \hat{H}_R = \begin{pmatrix} k_x^2 + k_y^2 & (-ik_x - k_y)\alpha \\ (ik_x - k_y)\alpha & k_x^2 + k_y^2 \end{pmatrix} \quad (3.73)$$

$$E_{\pm} = k_x^2 + k_y^2 \pm \alpha\sqrt{k_x^2 + k_y^2} = |\vec{k}|^2 \pm \alpha|\vec{k}|. \quad (3.74)$$

The spin splitting increases linear in $|\vec{k}|$, a sketch of the dispersion is shown in figure 3.3(a). The eigenvectors of the Hamiltonian are given by

$$|\psi\rangle_{\pm} = |\uparrow\rangle \pm e^{i\theta_k} |\downarrow\rangle \quad (3.75)$$

$$\theta_k = \arctan\left(\frac{k_x}{k_y}\right). \quad (3.76)$$

The eigenvectors imply a \vec{k} -dependent spin structure. For Bychkov-Rashba SOC, the spin points in-plane and perpendicular to momentum \vec{k} , the spin structure is shown in Figure 3.3(b).

Dresselhaus Spin Orbit Coupling The Dresselhaus spin orbit coupling Hamiltonian was derived by M. Dresselhaus [201] for the zincblende structure. It describes a spin-orbit coupling term arising from bulk inversion asymmetry in the crystal. The

three-dimensional Dresselhaus spin-orbit coupling Hamiltonian is given by [201]

$$\hat{H}_D^{3D} \propto k_x(k_y^2 - k_z^2)\hat{\sigma}_1 + k_y(k_z^2 - k_x^2)\hat{\sigma}_2 + k_z(k_x^2 - k_y^2)\hat{\sigma}_3. \quad (3.77)$$

Integrating out the k_z -direction, the two-dimensional Dresselhaus Hamiltonian is of the form

$$\hat{H}_D^{2D} \propto -k_x\langle z^2\rangle\hat{\sigma}_1 + k_y\langle z^2\rangle\hat{\sigma}_2 + k_xk_y^2\hat{\sigma}_1 - k_yk_x^2\hat{\sigma}_2. \quad (3.78)$$

The cubic part is usually dropped and the low-energy linear Dresselhaus Hamiltonian is given by

$$\hat{H}_D = \beta(k_y\hat{\sigma}_2 - k_x\hat{\sigma}_1). \quad (3.79)$$

Comparing the Hamiltonian with the one for Bychkov-Rashba SOC in (3.72), the indices of k_x and k_y are switched. This has no influence on the electronic dispersion giving the same linear dependence in $|\vec{k}|$ for spin splitting as for Rashba splitting. However, the relative phase θ_k in the eigenvector assignment rotates the other way, leading to the \vec{k} -dependent spin-structure shown in 3.3(c).

Intrinsic Spin Orbit Coupling Intrinsic spin-orbit coupling arises from the on-site atomic LS -coupling Hamiltonian in (3.67). This on-site interaction can be taken into account in a tight-binding picture by adding the LS -coupling Hamiltonian to the spin-degenerate TB-Hamiltonian. The LS -coupling Hamiltonian is given by [197, 198]

$$\hat{H}_{LS} = \sum_a \lambda_a \vec{L}_a \cdot \vec{S}_a = \sum_a \lambda_a \left(\frac{\hat{L}_a^+ \hat{S}_a^- + \hat{L}_a^- \hat{S}_a^+}{2} + \hat{L}_a^z \hat{S}_a^z \right) \quad (3.80)$$

with the sum going over the elements included in the material and λ_a the spin-orbit coupling strength for the corresponding element. \hat{L}_a^\pm and \hat{S}_a^\pm are the ladder operators for orbit and spin respectively, while \hat{L}_a^z and \hat{S}_a^z give the contribution along the z-axis. Tight-binding Hamiltonians are often formulated using a basis set of real atomic orbitals however [112, 113, 125, 127, 197, 199, 202]. These orbitals are linear combinations of the complex orbitals and thus do not have defined magnetic quantum number m_l . The angular momentum operators \hat{L}_a^+ , \hat{L}_a^- and \hat{L}_a^z thus cannot be applied directly to the basis orbitals of the Hamiltonian. Instead, the LS -coupling Hamiltonian must be calculated in the basis of complex orbitals. After determining the SOC Hamiltonian in complex orbital basis \hat{H}_{LS}^{comp} , a basis change can be carried out into the real orbital

3.4. SPIN-ORBIT COUPLING

basis using regular linear algebra. The LS -coupling Hamiltonian in the basis of real atomic orbitals is then given by

$$\hat{H}_{LS}^{real} = T_{comp}^{real} \hat{H}_{LS}^{comp} (T_{comp}^{real})^{-1}. \quad (3.81)$$

The coefficients of the basis change matrix T_{comp}^{real} can be found by expressing the complex orbitals in terms of the real orbitals [114].

The tight-binding approximation already includes the necessary symmetries to reproduce the bulk effects of the Dresselhaus approximation. However, if the effects of the structural asymmetry in the Rashba Hamiltonian are to be taken into account, it is sometimes necessary to manually introduce the asymmetry in the tight-binding Hamiltonian [197, 199]. When calculating the band structure of a monolayer sample without substrate, the symmetries of the Hamiltonian can prevent Rashba-like spin-orbit coupling effects. To include these effects without explicitly including the substrate interaction in the calculation, an artificial electric field perpendicular to the layer can be added. This artificial field modifies the hopping amplitudes and allows for Rashba-like SOC effects to be modeled using the LS -coupling Hamiltonian on a freestanding monolayer model [114]. It is important to include a full set of orbitals as basis states in this case, otherwise the artificial breaking of the symmetry might not be able to affect the hopping terms needed for interaction between opposite spin states to occur. A simple example is given by looking at the in-plane hopping of an electron from site i to site j . If only $p_{z,\uparrow}$ and $p_{z,\downarrow}$ are included in the calculation, the electron can hop from site i to site j , but the LS -coupling Hamiltonian does not mix the spin-up and spin-down states of the p_z orbital, so the spin states will always be degenerate within this model. If $p_{x,\sigma}$ and $p_{y,\sigma}$ ($\sigma \in \{\uparrow, \downarrow\}$) are included in the calculation however, the situation changes. For a freestanding, flat monolayer, the overlap of the p_z orbital on site i and the p_x , p_y orbitals on site j is zero due to symmetry. But when explicitly breaking the mirror symmetry with an artificial electric field, the overlap becomes non-zero and hopping can occur. In this case, the electron in $p_{z,\sigma}$ state on site i can hop to the $p_{x,\sigma}$ or $p_{y,\sigma}$ states of same spin on site j . The LS -Hamiltonian then locally couples the $p_{x,\sigma}$ and $p_{y,\sigma}$ states to the $p_{z,\bar{\sigma}}$ state of opposite spin. This effectively describes a hopping from $p_{z,\sigma}$ at site i to $p_{z,\bar{\sigma}}$ of opposite spin at site j and leads to Rashba-like SOC. Without explicitly including the p_x and p_y orbitals in the calculation, their effect would have to be projected onto the effective orbitals of a Hamiltonian with smaller basis to be able to reproduce the coupling [197, 199].

Chapter 4

Methods

4.1 Tight Binding Formalism

In order to understand experimental results and disentangle different effects that contribute to an overall observation, it is helpful to combine the experimental observations with a theoretical treatment. The tight-binding formalism introduced in section 3.2 is particularly useful in this case, as it allows for an easy physical interpretation of its constituents. With DFT calculations, most of the insight gained comes from the final outcome of the calculation. The final result is a mixture of many different effects included in the calculation and thus presents a similar problem as the interpretation of experimental results. In contrast, TB calculations allow for a direct interpretation of each element in the theoretical Hamiltonian. This enables the manual manipulation of individual parts of the modelled system and helps with understanding the influence of the different constituents on the overall result.

The tight-binding method can be used as an *ab-initio* method [203] but the more common approach is to fit the parameters of the model to experimental observations or theoretical results obtained *via* other methods such as DFT [113, 125, 127]. The hopping terms $\gamma_{m,n}(\vec{R})$ and on-site energies E_m introduced in section 3.2 are used as fit parameters in this case.

4.2 Angle-Resolved Photoemission Spectroscopy

Combining energy-dependent photoemission spectroscopy measurements with angle-resolved measurements, angle-resolved photoemission spectroscopy is able to directly measure the k-space dependent electronic band structure of a crystalline sample. The review by Damascelli mentioned in section 3.1 and partially followed in this section gives a good overview over the method [173]. In lab based ARPES experiments, the light beam is usually supplied by either gas-discharge lamps or ultraviolet lasers. Another option for light sources are electron synchrotrons, where the electrons are used to generate synchrotron radiation which is then sent through monochromators and focussed onto the sample. The latter is particularly useful due to the high brilliance and broad range of excitation energies supplied by synchrotron radiation sources.

Modern setups use hemispherical analyzers able to simultaneously measure angular and energy dependence of the photoemission intensity, resulting in two-dimensional spectra. The raw spectra are recorded with kinetic energy E_k and angular dependence α for a chosen azimuthal angle φ (see subsection on Fermi surface mapping below for a detailed description). To get the dispersion relation in binding energy *versus* wavevector, the angles have to be transformed into wavevector \vec{k} *via* [173]

$$\vec{k} = \vec{k}_{\parallel} + \vec{k}_{\perp} = \vec{p}/\hbar \quad (4.1)$$

$$|\vec{k}| = \sqrt{2mE_k}/\hbar \quad (4.2)$$

$$\vec{k}_{\parallel} = \frac{1}{\hbar} \sqrt{2mE_k} \sin(\alpha) (\cos(\varphi), \sin(\varphi))^T. \quad (4.3)$$

The kinetic energy can be transformed into binding energy by determining the Fermi level within the recorded spectra and shifting the energy scale accordingly.

Importantly, only the in-plane part \vec{k}_{\parallel} of the wavevector is conserved upon photoemission from the surface as the in-plane symmetry is preserved. The sample surface breaks the out-of-plane symmetry and \vec{k}_{\perp} is not a conserved quantity according to Noether's theorem. Without further assumptions, ARPES can thus only be used to gain insight into the in-plane electronic dispersion. For two-dimensional systems, this is not a limitation, as the containment of the wave function in a two-dimensional plane means that \vec{k}_{\perp} is not a meaningful quantum number anyway (compare section 2.2).

However, for three-dimensional crystals with an out-of-plane dispersion, additional assumptions about the final excited state have to be made if the out-of-plane dispersion is to be determined. A reasonable assumption often used is a free electron-like final state for the system, considering the final state is usually tens of electron-volts above

the Fermi level. In this case, the final state is given by

$$E_f(\vec{k}) = \frac{\hbar^2 \vec{k}^2}{2m} - |E_0| = \frac{\hbar^2 (\vec{k}_{\parallel} + \vec{k}_{\perp})^2}{2m} - |E_0| \quad (4.4)$$

with E_0 the lowest energy of the band the electron is excited from. Using $E_f = E_k + \Phi$ (in relation to the Fermi energy) and $\frac{\hbar^2 \vec{k}_{\parallel}^2}{2m} = E_k \sin^2(\alpha)$ (compare equation (4.3)) the perpendicular wavevector is determined with

$$k_{\perp} = \frac{1}{\hbar} \sqrt{2m(E_k \cos^2(\alpha) + V_0)} \quad (4.5)$$

where $V_0 = |E_0| + \Phi$ is called the “inner potential”.

4.2.1 Fermi Surface Mapping

A modern ARPES detector takes a single slice of a part of the Brillouin zone with one spectrum. To map out large parts of the Brillouin zone, the angles between the sample surface and the detector have to be varied and at each step, a spectrum has to be acquired. A change in the angles of the surface normal of the sample *versus* the analyzer affects the measured spectrum. This is understood by a coordinate transform between the reference frame of the analyzer and the reference frame of the sample. The following analysis of the geometry is based on a technical paper by Dmitry Usachov from Saint Petersburg State University available at the BaDElPh beamline in Elettra [204]. The reference frames are shown in figure 4.1(a). The coordinate system xyz is attached to the sample, z always points parallel to the surface normal of the sample. The coordinate system $x'y'z'$ is the laboratory reference frame and set in such a way, that z' is aligned along the center axis of the analyzer and y' is aligned along the direction of the manipulator (vertical in the figure). To transform between these two coordinate systems, three angles are necessary. These three angles are called polar angle ϑ , tilt angle τ , and azimuthal angle φ as displayed in figure 4.1(b) through (d). To transform from the laboratory frame $x'y'z'$ to an intermediate frame $x''y''z''$ (compare figure 4.1(b)), a polar rotation around axis y' is applied

$$\hat{P}(\vartheta) = \begin{pmatrix} \cos \vartheta & 0 & -\sin \vartheta \\ 0 & 1 & 0 \\ \sin \vartheta & 0 & \cos \vartheta \end{pmatrix}. \quad (4.6)$$

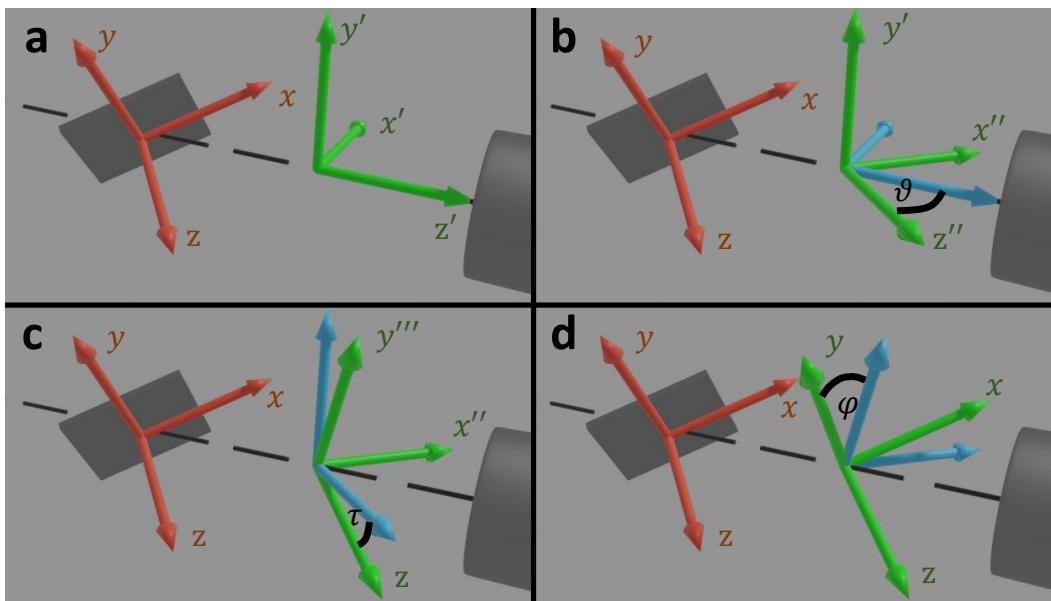


Figure 4.1: Transform from laboratory coordinate system into sample coordinate system. (a) Shows the exemplary sample coordinate system in red, analyzer laboratory coordinate system in green. (b) through (d) show the intermediate steps for the transform with (b) polar angle ϑ , (c) tilt angle τ , and (d) azimuthal angle φ . The orientation of the coordinate system before applying the corresponding transform is shown in blue, the orientation of the coordinate system after application of the transform is shown in green.

After this rotation, the x'' direction of the intermediate coordinate system $x''y'z''$ lies parallel to the rotational axis of the tilt on the manipulator. This means a rotation around the tilt axis leads to a second intermediate coordinate system $x''y'''z$ (compare figure 4.1(c))

$$\hat{T}(\tau) = \begin{pmatrix} 1 & 0 & 0 \\ 0 & \cos \tau & \sin \tau \\ 0 & -\sin \tau & \cos \tau \end{pmatrix}. \quad (4.7)$$

After this rotation, the z -axis of the second intermediate coordinate system lies parallel to the coordinate system of the sample. With this alignment, it is possible to use an azimuthal rotation around z , to align x'' with x and y''' with y (compare figure 4.1(d))

$$\hat{A}(\varphi) = \begin{pmatrix} \cos \varphi & \sin \varphi & 0 \\ -\sin \varphi & \cos \varphi & 0 \\ 0 & 0 & 1 \end{pmatrix}. \quad (4.8)$$

This means the direct transformation from laboratory frame $x'y'z'$ to the sample frame of reference xyz is given by

$$\hat{A}(\varphi)\hat{T}(\tau)\hat{P}(\vartheta) = \begin{pmatrix} \sin \vartheta \sin \varphi \sin \tau + \cos \vartheta \cos \varphi & \sin \varphi \cos \tau & \cos \vartheta \sin \varphi \sin \tau - \sin \vartheta \cos \varphi \\ \sin \vartheta \cos \varphi \sin \tau - \cos \vartheta \sin \varphi & \cos \varphi \cos \tau & \cos \vartheta \cos \varphi \sin \tau + \sin \vartheta \sin \varphi \\ \sin \vartheta \cos \tau & -\sin \tau & \cos \vartheta \cos \tau \end{pmatrix}. \quad (4.9)$$

For mapping of the dispersion, the photoemission intensity $I_{\vartheta,\tau,\varphi}(E_k, \alpha)$ is recorded for a given collection of angles ϑ, τ, φ as a function of kinetic energy E_k and entrance angle into the slit α . With the determined transform in (4.9) it is now possible to connect $(E_k, \alpha, \vartheta, \tau, \varphi)$ with (E_k, k_x, k_y) .

If \vec{k} is the wavevector with magnitude $k = \frac{\sqrt{2mE_k}}{\hbar}$ and $\vec{e} = \frac{1}{k}\vec{k}$ is the unit vector in the direction of the wavevector, then in the sample coordinate system

$$\vec{e} = \frac{1}{k} \begin{pmatrix} k_x \\ k_y \\ \sqrt{k^2 - k_x^2 - k_y^2} \end{pmatrix}. \quad (4.10)$$

In general, there are two different measurement geometries that will have to be taken into account for the following analysis. The construction of the sample holder in ARPES usually limits the reasonable mapping procedures with these two geometries.

Overall, there are three different mapping procedures that are typically employed in ARPES measurements. If the analyzer slit is parallel to the manipulator axis, the most effective mapping procedure is done by varying the polar angle ϑ while keeping the tilt τ and the azimuth φ at known, constant values. If the analyzer slit is perpendicular to the manipulator axis, it is possible to map out the tilt angle τ while keeping polar and azimuth constant. However, the range of the tilt angle is usually very limited due to engineering constraints. The more popular procedure for this geometry is thus a mapping of the azimuthal angle φ with known constant ϑ and τ .

Analyzer Entrance Slit Parallel to the Manipulator Axis If the entrance slit of the analyzer is parallel to the manipulator axis, α is measured in the $y'z'$ -plane of the laboratory frame. Thus, in the laboratory frame, it is $\vec{e}_{x'y'z'} = (0, \sin \alpha, \cos \alpha)^T$ and thus

$$\begin{pmatrix} e_x \\ e_y \\ e_z \end{pmatrix} = \hat{A}(\varphi)\hat{T}(\tau)\hat{P}(\vartheta) \begin{pmatrix} 0 \\ \sin \alpha \\ \cos \alpha \end{pmatrix}. \quad (4.11)$$

Plugging into (4.9) and rearranging gives the relations

$$\sin \alpha = e_x \sin \varphi \cos \tau + e_y \cos \varphi \cos \tau - e_z \sin \tau \quad (4.12)$$

$$\cos \vartheta = \frac{e_z + \sin \tau \sin \alpha}{\cos \tau \cos \alpha} \quad (4.13)$$

$$\sin \vartheta = \frac{\sin \alpha \sin \varphi \cos \tau - e_x + \cos \alpha \cos \vartheta \sin \varphi \sin \tau}{\cos \alpha \cos \varphi}. \quad (4.14)$$

These equations can be used to look up the intensity for a point (E, k_x, k_y) in the experimental dataset with known fixed φ, τ .

Analyzer Entrance Slit Perpendicular to the Manipulator Axis At $\alpha = 0$, the vector $\vec{e}_{x'y'z'}$ in the laboratory frame has coordinates $(0, 0, 1)^T$. In this geometry, the angle α is measured in the $x'z'$ -plane. This means α is measured along the polar angle direction. The direction of \vec{e}_{xyz} in the sample coordinate system is then

$$\begin{pmatrix} e_x \\ e_y \\ e_z \end{pmatrix} = \hat{A}(\varphi)\hat{T}(\tau)\hat{P}(\vartheta + \alpha) \begin{pmatrix} 0 \\ 0 \\ 1 \end{pmatrix}. \quad (4.15)$$

This relation can be rearranged into two sets of equations depending on what angles are kept constant in the corresponding mapping procedure.

For a **tilt scan**, the polar and azimuthal angles ϑ and φ are kept constant. Relation (4.15) can be rearranged into

$$\sin(\vartheta + \alpha) = e_y \sin \varphi - e_x \cos \varphi \quad (4.16)$$

$$\sin \tau = \frac{e_x \sin \varphi + e_y \cos \varphi}{\cos(\vartheta + \alpha)}. \quad (4.17)$$

From this set of equations, it is possible to determine where in the dataset to look for the intensity of a point (E, k_x, k_y) with fixed ϑ, φ .

For an **azimuthal scan** on the other hand, the polar and tilt angles ϑ and τ are fixed at known values. In this case, relation (4.15) can be rearranged to give

$$\sin \varphi = \frac{e_x e_z \tan \tau \pm e_y \sqrt{1 - e_x^2 / \cos^2 \tau}}{1 - e_z^2} \quad (4.18)$$

$$\cos \varphi = \frac{e_z \tan \tau - e_x \sin \varphi}{e_y} \quad (4.19)$$

$$\sin(\vartheta + \alpha) = e_y \sin \varphi - e_x \cos \varphi \quad (4.20)$$

$$\cos(\vartheta + \alpha) = \frac{e_z}{\cos \gamma}. \quad (4.21)$$

If $e_y = 0$, then (4.19) is not defined. In this case $\cos \varphi$ can be determined from $\sin \varphi$ in (4.18) by using

$$\cos \varphi = \pm \sqrt{1 - \sin^2 \varphi}. \quad (4.22)$$

Two pairs of angles α and φ can be determined for a point (E, k_x, k_y) with fixed ϑ and τ . Which of these two pairs should be used depends on the range of the scan in angles φ .

4.3 Photoluminescence Spectroscopy

Photoluminescence (PL) describes a process in semiconductors, where incoming photons get absorbed by excitation of an electron from the valence band to the conduction band and relaxing back into the ground state by emission of a new photon. This following short description of photoluminescence is based on chapter 5.3 in “Optical Properties of Solids” by Mark Fox [205, Chapter 5]. For a more in-depth treatment of the topic, the reader is referred to the whole chapter 5 in his book.

For the PL process to occur, the light emitted onto the semiconductor needs to be of an energy bigger than the (optical) band gap of the material. A schematic of the process is given in figure 4.2. The photon excites an electron from the valence band to the conduction band and creates an electron-hole pair. The recombination time of the electron-hole pair is much longer than the relaxation time of the electron and hole states within the corresponding bands. Thus, the electron in the conduction band migrates to the bottom of the band *via* emission of phonons. Similarly, the hole in the valence band migrates to the top of the band under phonon emission. As the recombination time is much slower than the relaxation time within the bands, the electrons at the bottom of the conduction band and the holes at the top of the valence band have enough time to thermalize. The distribution of the electrons (holes) in the conduction (valence) band can be calculated from Fermi-Dirac statistics. The total number density N_e of electrons in the conduction band must satisfy

$$N_e = \int_{E_g}^{\infty} g_e(E) f_e(E) dE \quad (4.23)$$

with $f_e(E)$ the Fermi-Dirac distribution for electrons

$$f_e(E) = \left[\exp\left(\frac{E - E_F^c}{k_B T}\right) + 1 \right]^{-1} \quad (4.24)$$

and $g_e(E)$ the density of states of the conduction band. E_F^c in this case is the Fermi energy of the electrons in the conduction band as measured from the top of the valence band. Because electrons and holes are not in equilibrium in this situation, the Fermi levels of the electrons in the conduction band and the holes in the valence band are not identical and also differ from the Fermi energy of the equilibrium state. The density

of states of the conduction band for a free-electron like band can be calculated as

$$g_e(E) = \frac{1}{2\pi^2} \left(\frac{2m_e^*}{\hbar^2} \right)^{3/2} (E - E_g)^{1/2} \quad (4.25)$$

when measured from the top of the valence band. The total number density the electrons in the conduction band have to satisfy is thus

$$N_e = \int_0^\infty \frac{1}{2\pi^2} \left(\frac{2m_e^*}{\hbar^2} \right)^{3/2} E^{1/2} \left[\exp\left(\frac{E - E_F^c}{k_B T}\right) + 1 \right]^{-1} dE \quad (4.26)$$

with the variables changed so that the integral starts at the bottom of the conduction band. Note that that also means, that the reference point for E_F^c has to be changed and the Fermi level of electrons is now measured from the bottom of the conduction band. Similarly, the total number density for holes in the valence band must satisfy

$$N_h = \int_0^\infty \frac{1}{2\pi^2} \left(\frac{2m_h^*}{\hbar^2} \right)^{3/2} E^{1/2} \left[\exp\left(\frac{E - E_F^v}{k_B T}\right) + 1 \right]^{-1} dE. \quad (4.27)$$

with $E = 0$ at the top of the valence band and the energy of the states is measured from the top downwards. When a light source shines upon a sample and excites a given number density of electrons (and thus also creates the same number density of holes), equations (4.26) and (4.27) can be used to determine the Fermi levels of both distributions.

After this process of migration and thermalization, the electron-hole pair finally recombines under emission of a photon at the energy of the (optical) band gap. The optical band gap can thus be experimentally determined in photoluminescence spectroscopy *via* the energy of the emitted photons. Importantly, the excited electron-hole pair is usually excited into a bound state called an exciton. This means the energy of the optical band gap is reduced *versus* the electronic band gap by the binding energy of the exciton.

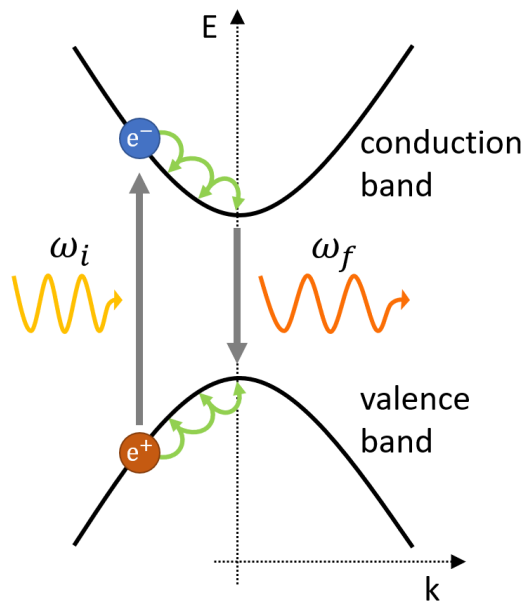


Figure 4.2: Schematic of the photoluminescence process in a direct-band gap semiconductor. Green arrows show the relaxation processes within the bands *via* phonon emission. Grey arrows show excitation and recombination of the electron-hole pair. The incoming photon is shown in yellow, the outgoing photon with lower energy and longer wavelength is shown in orange. Reproduced from [114], based on [205, Figure 5.5(a)].

4.4 Sample Preparation

4.4.1 Black Phosphorus

Black phosphorus bulk crystals were bought from industrial suppliers. The crystals are prepared on air by glueing small copper top-posts to their surface using two-component silver epoxy glue. After insertion into the ultra-high vacuum chambers, the copper top-post is removed by applying a shear force with a wobble-stick. As the top-post

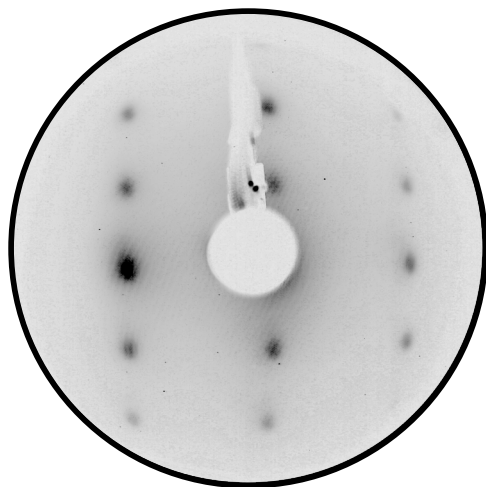


Figure 4.3: Low-energy electron diffraction image of a cleaved black phosphorus surface.

is attached to the crystal *via* glue, the crystal cleaves along the Van der Waals layers and a pristine surface is left behind ready for the experiment. The cleaved surface is checked with low-energy electron diffraction (LEED), an example is shown in figure 4.3. This procedure can be repeated several times if the cleaved surface is not good enough for sensitive measurements such as ARPES.

4.4.2 Molybdenum Disulfide/Graphene/Iridium(111)

The growth procedure for MoS₂ on a graphene/iridium(111) substrate was established by Joshua Hall *et al.* [4]. Graphene is grown *via* chemical vapour deposition on a clean Ir(111) crystal surface [64]. For the growth, a carbon source such as propene or propylene is injected into the ultra-high vacuum chamber. After introduction of the carbon-rich molecules, the iridium crystal is heated to approximately 1200 °C. At these temperatures small graphene islands form and align along the iridium substrate. After a minute, the temperature is decreased to approximately 900 °C. The crystal is held at this temperature for approximately 15 minutes. During this time, more carbon-containing gas is injected into the chamber. At the end, the crystal is slowly cooled to room temperature to avoid formation of wrinkles [64]. As the iridium surface

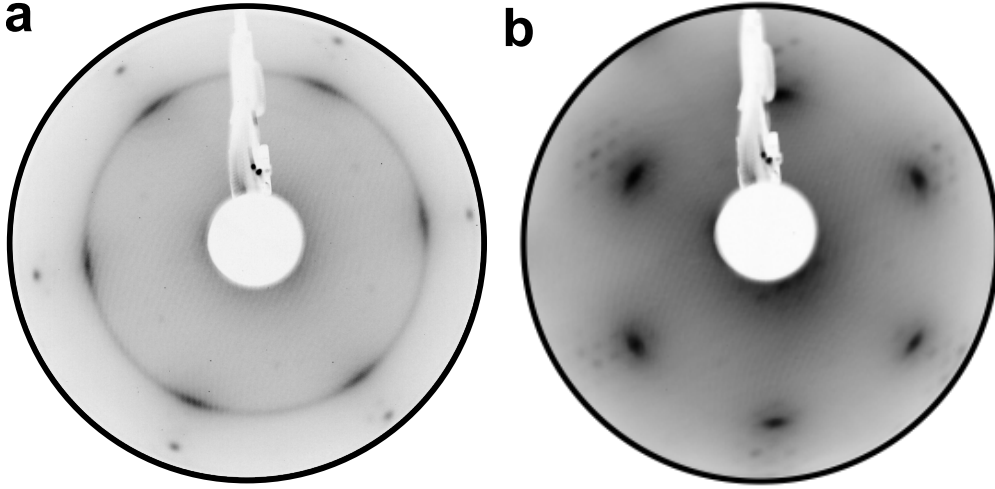


Figure 4.4: Low-energy electron diffraction image of MoS₂ with (a) bad angular alignment and (b) good angular alignment.

is needed as a catalyst for the formation of graphene, the growth is inherently self-limiting and large area high quality single-layer graphene growth is achieved. The quality is confirmed with low-energy electron diffraction.

On the graphene layer, MoS₂ is grown using molecular beam epitaxy. The growth uses two distinct steps. In the first step, molybdenum ions are evaporated onto a sample kept at room temperature from a molybdenum rod using electron-beam heating. At the same time, sulfur is co-evaporated from a Knudsen cell containing FeS₂. The rate of molybdenum evaporation can be checked with a quartz micro balance, the sulfur is supplied according to a measurement of the background pressure, keeping the pressure around 2×10^{-9} mbar. In the second step, the molybdenum evaporation is stopped and the crystal is heated in the sulfur atmosphere to around 1050 K for five to ten minutes. The second step heals any potential sulfur vacancies and ensure good crystal quality as well as good macroscopic alignment of the MoS₂ islands. The two steps constitute one cycle. For optimal sample quality, the first step should be kept short to allow for growth of small islands that can easily diffuse and align with each other in the second step. For bigger surface coverage, the cycle can be repeated several times. The quality and alignment of the final sample can again be checked using low-energy electron diffraction. Figure 4.4(a) shows the LEED pattern of a grown MoS₂ layer with bad macroscopical alignment. the pattern is circular with an increased intensity for R0-oriented MoS₂ flakes. Figure 4.4(b) shows the LEED pattern of a well aligned sample. The microscopic MoS₂ islands are all aligned macroscopically with the graphene/iridium(111) substrate. A slight angular broadening is still visible. In both

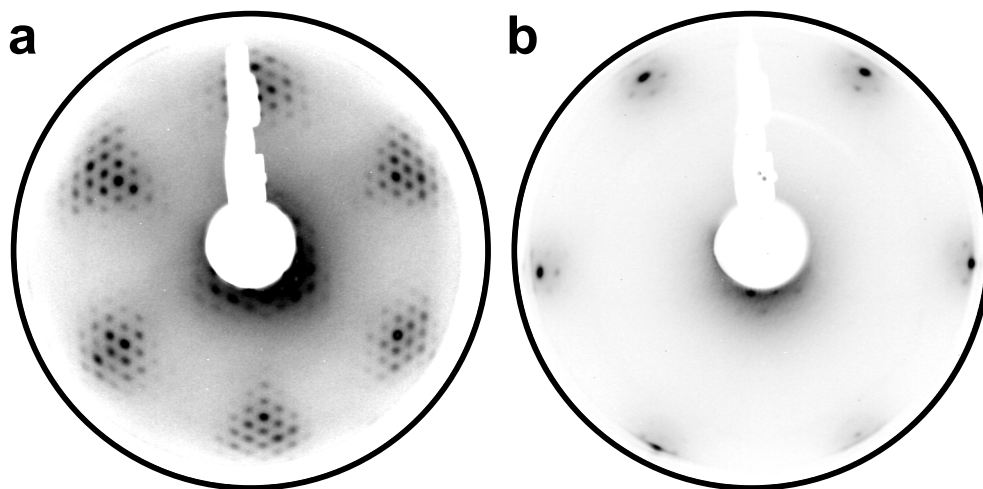


Figure 4.5: Low-energy electron diffraction image of (a) monolayer graphene and (b) bilayer graphene.

cases, the graphene/iridium(111) moiré pattern is also visible (see section 4.4.3 below). As the growth is not self-limiting, any amount of layers can be achieved this way. However, the next layers will generally start growing before the old layer is completely finished. Thus, a trade-off has to be made between coverage and layer numbers. With slight variations, this growth procedure works for many other transition-metal dichalcogenides as well.

4.4.3 Bilayer Graphene/Iridium(111)

For the growth of bilayer graphene on iridium(111), a monolayer has to be grown first. The monolayer growth *via* chemical vapour deposition is the same as described in section 4.4.2. The growth of bilayer graphene was developed by Charlotte Herbig *et al.* [206]. After successful growth of monolayer graphene, carbon is evaporated from a carbon sublimation source [206, 207] onto the monolayer sample kept at 1000 °C. Evaporation time dictates the formation of bilayer graphene and the growth can be monitored using Raman spectroscopy. The resulting structure is evaluated again using LEED. Figure 4.5(a) shows the LEED pattern of monolayer graphene grown on an iridium(111) surface. The moiré pattern arising from the lattice mismatch of graphene and iridium(111) is responsible for the many observed diffraction orders around the main peaks of iridium and graphene. For bilayer graphene, the increased corrugation on iridium(111) destroys the coherent scattering and the higher diffraction orders disappear as shown in figure 4.5(b).

Chapter 5

Results

5.1 Band Structure Engineering in Black Phosphorus

Black phosphorus is an interesting material to study because its inherent in-plane structural anisotropy imposes anisotropic electronic behavior along these directions [81] (compare also section 2.3). While the electronic dispersion of BP is quadratic along the ZT direction, it is linear along ZU direction. This anisotropy leads to direction dependent phenomena in the material [81, 208, 209]. Since BP is a direct band gap semiconductor, it is also a potential candidate for many different applications in optical devices. In particular, the size of the band gap strongly depends on the number of layers, changing from approximately 0.3 eV in bulk to 2.2 eV for monolayer phosphorene [202, 210–214]. Experimentally, an additional strong dependence of the electronic band gap upon chemical doping with potassium was found in bulk BP [17, 55]. This tunability of the band gap is interesting for usage in devices, allowing adjustment of optical absorption properties for optoelectronic applications [85]. With the theoretical prediction and experimental confirmation of phonon-mediated superconductivity in lithium doped BP [97, 215], alkali metal doped black phosphorus has garnered additional interest in the context of controlling and inducing superconductivity in two-dimensional materials. However, production of few-layer phosphorene is complicated and dangerous and thus mostly done *via* exfoliation from bulk crystals. Exfoliation techniques only allow sample sizes in the micrometer range, however [216]. Experimental methods that rely on large-area samples are hence limited to investigating bulk properties of the three-dimensional BP Van der Waals crystal.

In order to gain information on the two-dimensional phosphorene from its 3D coun-

terpart, in section 5.1.1 a tight-binding model for bulk BP was developed and fitted to experimental observations. A rigid band shift upon lithium doping was found. The rigid band shift allowed for the determination of the electronic band gap. This allowed the inclusion of the band gap in the tight-binding fit. The TB model was then reduced to its two-dimensional representation of few-layer phosphorene. It could be shown, that the dispersion for few-layer phosphorene can be explained with zone-folding of the three-dimensional band structure. The tight-binding models for bulk and few-layer BP were used to predict the Fermi surfaces of doped BP samples with a rigid band shift. The Fermi surfaces are important for the determination of potential couplings which can lead into superconducting or charge density wave ground states (compare also appendix A.2.1.1 and A.2.1.2).

In section 5.1.2, a non-rigid band shift upon caesium doping was observed. Doping was able to induce a band inversion of the original conduction and valence bands. The conduction band showed no out-of-plane dispersion in ARPES and was hence determined to be localized at the surface of the crystal. A two-dimensional TB model based on the one developed in section 5.1.1 was used to explain the observations. Density functional theory corroborated the results and established the conduction band as a surface resonance state.

5.1.1 Insight into the Band Dispersion of Few-Layer Phosphorene from Measurements of the Three-Dimensional Bulk Crystal

Niels Ehlen, Boris V. Senkovskiy, Alexander V. Fedorov, Andrea Perucchi, Paola Di Pietro, Antonio Sanna, Gianni Profeta, Luca Petaccia, and Alexander Grüneis

Evolution of electronic structure of few-layer phosphorene from angle-resolved photoemission spectroscopy of black phosphorus.

Physical Review B **94**, 245410 (2016) © [2016] American Physical Society

Doi: <https://doi.org/10.1103/PhysRevB.94.245410>

The bulk tight binding model used in this publication was developed as part of the author's BSc thesis [217].

In order to gain information on the behavior of two-dimensional phosphorene *via* angle-resolved photoemission spectroscopy large area samples are required. As fabrication of few-layer phosphorene was limited to exfoliation from bulk crystals, the typical sample sizes ruled out ARPES as an experimental technique. To circumvent this problem, ARPES data was collected on bulk crystals which were available in the required sizes. A full tight-binding model for bulk black phosphorus was developed and fitted to the ARPES data of the bulk dispersion. Zone-folding was applied to the bulk model to determine the evolution of the band gap from monolayer to the bulk crystal.

The tight-binding model used the base centered orthorhombic unit cell description of the bulk crystal with four atomic sites in the unit cell. A full basis set of $3s$, $3p_x$, $3p_y$ and $3p_z$ orbitals for each atomic site was used, resulting in a 16×16 matrix for the Hamiltonian. To reduce the parameter space of the Hamiltonian, the Slater-Koster scheme was employed [218]. The model was finally fitted using a steepest descent algorithm to the experimental band structure recorded in ARPES experiments. The Hamiltonian had to go up to the fifth shell of in-plane neighbours and the second shell of out-of-plane neighbours in order to be able to reproduce the experimental ARPES results. Crucially, the band gap of the material and the effective masses along different directions of the conduction band were included in the fit. This was possible as the conduction band could be shifted below the Fermi level in experiment using lithium doping. A rigid band shift upon doping was assumed in order to include the band gap in the fit. The justification for the rigid band shift was threefold. For one, As the doping was purposely left small, non-linear effects were minimized. Second, comparing

the dispersion of the valence band in the pristine and the doped case showed a perfect match after accounting for a rigid energy shift. And finally, in experiments with potassium the same rigid band shift behaviour was observed for low doping levels [55]. In contrast to potassium doping [17, 55], lithium deposition was thus determined to be a good way of rigidly shifting the Fermi level in the material. The inclusion of the conduction band information in the TB model allowed for a good description of bottom of the conduction band. This enabled the determination of the Fermi surfaces for different doping levels. These are important for understanding of phonon-mediated superconductivity in BP [97, 215] as Fermi surface nesting can influence the coupling mechanism.

The same crystal that was used for ARPES measurements was also investigated using optical absorption spectroscopy. In these experiments, the optical band gap was found to be 0.261 eV at 40 K. Comparison with the electronic band gap extracted from the ARPES experiments showed an exciton binding energy of 140 meV. Additionally, an anomalous temperature dependence of the optical band gap was found, as the band gap increased with temperature.


From the information on the bulk crystal, the two-dimensional electronic dispersion was determined using the zone-folding method. With this method, the quantization of the out-of-plane dispersion for thin layers was used to cut the three-dimensional bulk dispersion at the correct k_z values to reproduce the dispersion of few-layer phosphorene. The quantization condition for the wavelength of the electron states when modeling the out-of-plane direction as a quantum well is $n\lambda = (N + 1)d$. This leads to quantization condition of $k_z = \frac{n\pi}{(N+1)d}$. With this quantization condition, the dispersion of N -layer phosphorene could be deduced from the bulk dispersion. The determined dependence of the band gap on the number of layers showed good agreement with other experiments and theoretical calculations.

Importantly, as the zone-folding method does not include hybridization of electronic states between different layers or surface effects, they are established to play little role in the explanation of electronic features of few-layer BP. A comparison of the direct calculation of the few-layer band structure using a few-layer version of the bulk Hamiltonian with the band structure obtained from zone-folding showed only small differences across large parts of the Brillouin zone.

Contributions to this publication:

- Main authors of the publication are N. Ehlen and A. Grüneis with smaller contributions from the co-authors
 - Develop tight-binding Hamiltonian
 - Record and analyze angle-resolved photoemission spectroscopy data
 - Fit TB-Hamiltonian to ARPES data
 - Adapt zone-folding method to this material, analyze Fermi surfaces and layer-dependence of electronic gap
 - Adapt the bulk Hamiltonian into a two-dimensional few-layer Hamiltonian
 - Produce Figures 1-6, 8-15
-

Publication

PHYSICAL REVIEW B **94**, 245410 (2016)


Evolution of electronic structure of few-layer phosphorene from angle-resolved photoemission spectroscopy of black phosphorous
N. Ehlen,^{1,*} B. V. Senkovskiy,¹ A. V. Fedorov,^{1,2,3} A. Perucchi,⁴ P. Di Pietro,⁴ A. Sanna,⁵ G. Profeta,⁶ L. Petaccia,⁴ and A. Grüneis^{1,†}¹*II. Physikalisches Institut, Universität zu Köln, Zùlpicher Strasse 77, 50937 Köln, Germany*²*IFW Dresden, P.O. Box 270116, D-01171 Dresden, Germany*³*St. Petersburg State University, 198504 St. Petersburg, Russia*⁴*Elettra Sincrotrone Trieste, Strada Statale 14 km 163.5, 34149 Trieste, Italy*⁵*Max-Planck-Institut für Mikrostrukturphysik, Weinberg 2, D-06120 Halle, Germany*⁶*Department of Physical and Chemical Sciences and SPIN-CNR, University of L'Aquila, Via Vetoio 10, I-67100 Coppito, Italy*

(Received 16 August 2016; revised manuscript received 11 November 2016; published 7 December 2016)

A complete set of tight-binding parameters for the description of the quasiparticle dispersion relations of black phosphorous (BP) and N -layer phosphorene with $N = 1 \dots \infty$ is presented. The parameters, which describe valence and conduction bands, are fit to angle-resolved photoemission spectroscopy (ARPES) data of pristine and lithium doped BP. We show that zone-folding of the experimental three-dimensional electronic band structure of BP is a simple and intuitive method to obtain the layer-dependent two-dimensional electronic structure of few-layer phosphorene. Zone folding yields the band gap of N -layer phosphorene in excellent quantitative agreement to experiments and *ab initio* calculations. A combined analysis of optical absorption and ARPES spectra of pristine and doped BP is used to estimate a value for the exciton binding energy of BP.

DOI: 10.1103/PhysRevB.94.245410

I. INTRODUCTION

Black phosphorous (BP) is a layered crystal which was first discovered in 1914 by Bridgman [1]. The availability of large high-quality BP single crystals laid the foundation for the modern study of this material in the early 1980s [2–8]. Black phosphorous is a semiconductor with a moderate direct band gap 0.31–0.35 eV (Ref. [3,9,10]), as found in electrical transport measurements as a function of temperature. The optical gap of BP is reduced with respect to the transport gap to 0.276 eV for the lowest excitonic state and the light polarized along the armchair edge [7]. The quasiparticle (QP) band structure of BP single crystals was also directly measured using angle-resolved photoemission spectroscopy (ARPES) [5,11]. By using variable photon energies from a synchrotron radiation source the electron dispersion perpendicular to the layers was measured indicating a substantial interlayer bandwidth of about 2 eV [6,12].

Recently, the interest in the fundamental physics of BP and its potential application prospectives has been renewed [13–15] after the successful exfoliation of few-layer phosphorene (Refs. [16,17]). Phosphorene is the two-dimensional allotrope of BP which shows interesting properties sensibly different with respect to the bulk BP. The tunability of the fundamental direct electronic band gap of phosphorene together with its luminescent properties enables its use in devices. In fact, few-layer phosphorene was already successfully integrated as the active element in a field effect transistor [17], and its electron mobility reaches values up to $1000 \text{ cm}^2 \text{ V}^{-1} \text{ s}^{-1}$ (Ref. [17]) with on-off ratios of 10^3 (Refs. [18,19]). The fundamental optical gap of few-layer phosphorene is also direct and has been measured using photo-

luminescence (PL) [16,20–22] and optical absorption [23]. For monolayer phosphorene, a QP gap of 2.2 eV and an optical gap of 1.3 eV have been found [24]: The difference can be ascribed to the exciton binding energy, which can be as large as 0.9 eV (Ref. [24]).

However, the values of the band gap of both BP and phosphorene must be taken with care as there is a significant temperature dependence in the band gap [22,25,26]: It is increasing with increasing temperature and as such opposite to the behavior typically observed in semiconductors [27]. In addition, it was recently demonstrated that the exciton binding energy depends on the type of substrate due to environmental effects on the dielectric constant [22]. Phosphorene also shows a strong optical anisotropy for light polarization in the two high symmetry directions which is related to the large anisotropy of the electron effective masses [21,23,24,28,29].

From a theoretical point of view, the interest in the physics of phosphorene is enormous and challenging for first-principles theories. Recent *ab initio* calculations, at the DFT-GGA level, predict BP to be metallic [30] while DFT-PBE finds a gap of 0.04 eV (Ref. [31]), in striking disagreement with experiments. Only at the G_0W_0 level the agreement with experiment is obtained and an appreciable band gap opens: The band gap of BP reports values of 0.1 eV (Refs. [30,32]) and 0.3 eV (Ref. [31]) within the G_0W_0 approximation [33,34]. Interestingly, the QP band gap of few-layer phosphorene, calculated by the G_0W_0 approximation, is found to decrease as $\sim 1/N$ (N is the number of layers) from 1.5 eV for monolayer phosphorene to 0.3 eV for bulk BP [30,31]. Extending the calculation to GW with the Bethe Salpeter equation (GW-BSE) [31] and the Kubo formula [35], the optical band gap and optical anisotropy were calculated in agreement with photoluminescence (PL) [16,20–22] and optical absorption [23]. Using a semiempirical interlayer coupling model fitted to first principles calculations, the evolution of the band gap from monolayer to bulk was explained by interlayer coupling [36].

*ehlen@ph2.uni-koeln.de

†gruneis@ph2.uni-koeln.de

However, although the theoretical predictions are in agreement with available experimental results, the application of *GW* approximation to predict the electronic structure of phosphorene, few layer phosphorene, and black phosphorous is highly demanding from a computational point of view and can often hinder the main physical mechanisms in the description of the experimental results. For this reason, the tight-binding approximation, and in particular its semiempirical forms, represents an essential theoretical tool which enables us to interpret the experiments [37], construct a low energy description of the band structure to study the model Hamiltonian [38], and represent a starting point for more advanced calculations [39]. The published tight-binding parameters for black phosphorous and phosphorene usually refer to a four-band model of the system [2,30,40] which, however, may not be suitable to understand many phenomena because it is restricted to a limited energy range. Recently the edge states and Landau levels of phosphorene have been calculated using Wannier functions that define a tight-binding Hamiltonian [41], however an easy parametrization for a full Hamiltonian of the system has not yet been given.

The present paper addresses this issue and is organized as follows: In Sec. II we describe the tight-binding model for the description of the band structure of BP and phosphorene, giving the formulas and meaning of parameters. Then, in Sec. III, we report the results of the experimental measurements of the band structure of BP by ARPES, including both the valence and conduction band (see below). In this section, we also provide the set of TB parameters which describe the measured band structure. Section IV and Sec. V report the analysis of the temperature and doping dependence of the electronic properties. Section VI deals with few-layer phosphorene and its description by zone folding. In particular we unravel the origin of the $1/N$ dependence of the optical band gap of few-layer phosphorene as a function of the number of layers. Then, in Sec. VII we discuss the results and give our conclusions and perspectives.

II. TIGHT-BINDING DESCRIPTION OF BLACK PHOSPHOROUS

A. Crystal structure and Brillouin zones

BP is a layered material dominated by covalent bonds for the intralayer bonding and van der Waals forces for the interlayer bonding, similarly to other layered van-der-Waals materials. At variance with graphene, in BP the sp^3 hybridization of the $3s$, $3p_x$, $3p_y$, and $3p_z$ orbitals leads to the buckled layer structure seen in Fig. 1(a). Under ambient conditions, the stable form of black phosphorous has an orthorhombic crystal structure with lattice and internal parameters reported in Table I.

In this paper we will give a TB description of the electronic properties of BP considering the orthorhombic structure with an AB stacking of the layers which is relevant for almost all of the experiments on exfoliated crystals. We use the irreducible body-centered orthorhombic (*BCO*) cell with four phosphorus atoms for the TB description of BP. For the TB description of N -layer phosphorene through zone folding we will switch to a primitive orthorhombic supercell containing eight phosphorus atoms [see Fig. 1(d)]. The Brillouin zones of the *BCO* and

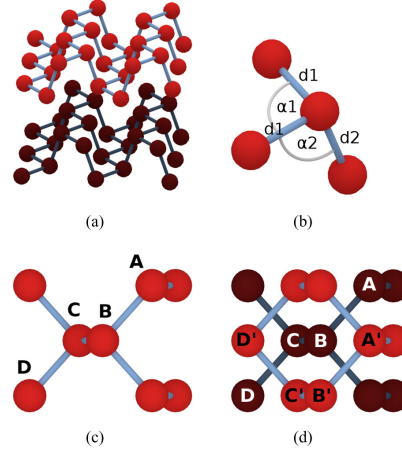


FIG. 1. (a) The layered structure of black phosphorous. The colors denote different layers. (b) Bond angles and bond lengths of black phosphorous (see also Table I for the numerical values). (c) and (d) show the elements in the unit cell of the BCO and the supercell description of BP, respectively.

simple orthorhombic structures as well as their comparison are reported in Figs. 2(a), 2(b), and 2(c).

B. Tight-binding Hamiltonian of black phosphorous

For the TB description we use an orthogonal tight-binding model resulting in the Hamiltonian

$$H_{mn}(\mathbf{k}) = E_m \delta_{mn} + \sum_{\mathbf{R} \neq 0} e^{i\mathbf{k} \cdot \mathbf{R}} \gamma_{mn}(\mathbf{R}). \quad (1)$$

Here E_m are the on-site energies, and the γ_{mn} are hopping parameters with m and n running over the orbitals and lattice sites. The electron wave vector is denoted by \mathbf{k} and the lattice vectors by \mathbf{R} . We employ the Slater Koster scheme for γ_{mn} [43]. This leaves us with four fit parameters $V_{ss\sigma}$, $V_{sps\sigma}$, $V_{pp\sigma}$, and $V_{pp\pi}$ for each order of neighbors that we include in the fit plus the on-site parameters E_s and E_p . We use the $3s$, $3p_x$,

TABLE I. Structural parameters of black phosphorous at room temperature, taken from Ref. [42].

parameter	value	
d_1	2.224 Å	bond length
d_2	2.244 Å	
α_1	96.34°	bond angle
α_2	102.09°	
a	3.3136 Å	lattice parameter
b	10.478 Å	
c	4.3763 Å	

EVOLUTION OF ELECTRONIC STRUCTURE OF FEW- ...

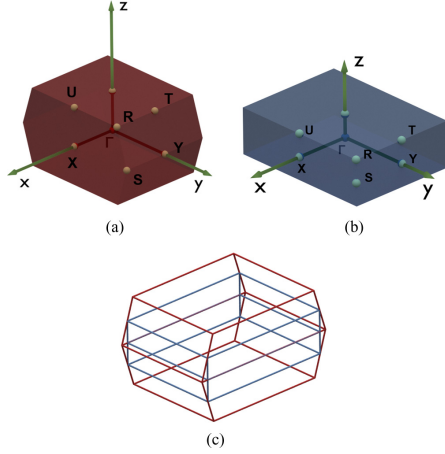
 PHYSICAL REVIEW B **94**, 245410 (2016)


FIG. 2. (a) shows the Brillouin zone for the BCO description of BP; (b) shows the Brillouin zone of the eight-atom supercell with primitive orthorhombic crystal structure. (c) compares both Brillouin zones in terms of size.

$3p_y$, and $3p_z$ orbitals to describe the electron hopping, which results in a 16×16 matrix for the Hamiltonian (four orbitals on four atomic sites in the basis of the BCO description). We end up with a Hamiltonian of the form

$$H = \begin{pmatrix} AA & AB & AC & AD \\ BA & BB & BC & BD \\ CA & CB & CC & CD \\ DA & DB & DC & DD \end{pmatrix}, \quad (2)$$

with each entry $\alpha\beta$, $\alpha, \beta \in \{A, B, C, D\}$ itself being a 4×4 matrix to describe the hopping between the four orbitals centered at sites α and β . Taking the symmetries of the lattice into account, we can simplify Eq. (2) to

$$H = \begin{pmatrix} AA & AB & AC & AD \\ AB^\dagger & AA & BC & AC \\ AC^\dagger & BC^\dagger & AA & AB \\ AD^\dagger & AC^\dagger & AB^\dagger & AA \end{pmatrix}. \quad (3)$$

In general, a 4×4 element $\alpha\beta$ of the Hamiltonian can be expressed as

$$\alpha\beta_{j,o} = \begin{pmatrix} s_\alpha & p_{x,\beta} & p_{y,\beta} & p_{z,\beta} \\ V_{s\sigma\alpha,o} & l_j V_{sp\sigma,o} & m_j V_{sp\sigma,o} & n_j V_{sp\sigma,o} \\ -l_j V_{sp\sigma,o} & a_{j,o} & b_{l_j m_j,o} & b_{l_j n_j,o} \\ -m_j V_{sp\sigma,o} & b_{m_j l_j,o} & a_{m_j,o} & b_{m_j n_j,o} \\ -n_j V_{sp\sigma,o} & b_{n_j l_j,o} & b_{n_j m_j,o} & a_{n_j,o} \end{pmatrix} e^{i\mathbf{k} \cdot \mathbf{d}_{j,o}}$$

with

$$\begin{aligned} a_{u_j,o} &= u_j^2 V_{pp\sigma,o} + (1 - u_j^2) V_{pp\pi,o} \\ b_{s_j t_j,o} &= s_j t_j V_{pp\sigma,o} - s_j t_j V_{pp\pi,o} \end{aligned} \quad (4)$$

$u_j, s_j, t_j \in \{l_j, m_j, n_j\}$,

where o denotes the order of neighbors and j denotes the corresponding sites on said order. The direction cosines of the direction vector pointing from the site on sublattice α to site j on sublattice β with neighbor-order o are l_j , m_j , and n_j . For a given direction vector $\mathbf{d}_j = (d_x, d_y, d_z)^T$ they can be computed by

$$\begin{aligned} l_j &= d_{j,x} / \|\mathbf{d}_j\| \\ m_j &= d_{j,y} / \|\mathbf{d}_j\| \\ n_j &= d_{j,z} / \|\mathbf{d}_j\|. \end{aligned} \quad (5)$$

We can then compute $\alpha\beta$ as

$$\alpha\beta = \sum_\sigma \sum_j \alpha\beta_{j,o}. \quad (6)$$

We fit the TB parameters to describe the experimental (and first-principles) band structure (see below) including any order of neighbors. We find that, in order to describe the

experimental electronic band structure with an accuracy equal to the experimental resolution we need to take into account at least five intralayer and two interlayer matrix elements. Indeed, this is in line with previously published theoretical results [2]. This is, in part, justified noticing that the 6th in-plane and 3rd out-of-plane distances are significantly larger with respect to the previous order (0.5 Å and 1.2 Å, respectively). In this work however, we chose to include the 6th in-plane order in the model, to capture the effects of the higher in-plane orders (see Sec. III). In order to fit this model to our experimental data (see below), we have extracted the ARPES maxima along the energy dispersion curves (EDCs) and employed a steepest-descent algorithm to minimize the residuals between the theoretical bands and the peaks extracted from the ARPES data along the measured path in the reciprocal space.

III. ANGLE-RESOLVED PHOTOEMISSION MEASUREMENTS OF THE THREE-DIMENSIONAL ELECTRONIC STRUCTURE OF BLACK PHOSPHORUS

ARPES was performed at the BaDElPh beamline [44] of the Elettra synchrotron in Trieste (Italy) at temperatures of 20 K. This beamline is dedicated to low photon energies and hence higher bulk sensitivity. We used bulk black-phosphorus

245410-3

N. EHLEN *et al.*

crystals from two providers (one from HQ Graphene and one from smart-elements) which gave identical results. The crystal surfaces were prepared *in situ* in a vacuum better than 10^{-10} mbar by cleaving with a top-post or a scotch tape inside the sample preparation chamber. Immediately after the cleave we determined the high-symmetry directions through low-energy electron diffraction. In order to access both the valence and conduction band of BP, we have performed ARPES on pristine and lithium doped BP. Lithium deposition was carried out in a UHV chamber from SAES getters with the sample at 20 K; the amount of lithium was calibrated by a quartz micro balance.

First, we focus on the measured band dispersion starting by looking to the ΓZ dispersion of pristine BP. Since translational symmetry of the crystal potential is broken at the surface, the component of the electron wave vector \mathbf{k} which is perpendicular to the layers is not *strictly* conserved in ARPES measurements. However, with the assumptions of a free-electron final state, whose energy depends on an inner potential V_0 (Ref. [45]), we can extract the dispersion of k_{\perp} inside the material from the measured kinetic energy and angle of the emitted electrons. Assuming that the emitted electrons are excited into parabolalike bands by the incident photons, we can calculate k_{\perp} inside the material by

$$\hbar k_{\perp} = \sqrt{2m_e(E_{kin}\cos^2\theta + V_0)}. \quad (7)$$

We can thus measure the dispersion k_{\perp} by varying the energy of the incident photon beam. Fig. 3 depicts EDCs for an in-plane $k_{\parallel} = 0$. It can be seen that they consist of a single peak which disperses as a function of photon energy. This peak is assigned to the upper valence band of BP. The inner potential is determined by the fact that the top of the valence band is at the Z point of the BCO Brillouin zone. Fixing the position of the peak to the according position on the Brillouin zone $\mathbf{k} = (0, 0, 2\pi/10.478 \text{ \AA})$ we have thus assigned the spectrum measured with 21 eV photons to the Z point. This yields a value for the inner potential of $V_0 = 19.1 \text{ eV}$ in very good agreement to previous data [6] which yielded $V_0 = 20.0 \pm 0.5 \text{ eV}$. As we will show later, the proper description of the k_{\perp} dispersion is critically important to understand the band-gap evolution as a function of the number of layers. The ARPES geometry employed for these measurements uses a horizontal slit to collect the photoelectrons. This makes it possible for us to measure the ΓX , ΓY , ZT, and ZU high-symmetry directions with high resolution in a single scan.

Notably, BP can also be described by a primitive orthorhombic unit cell, which being larger than the BCO, would produce backfolding of the valence band and thus a second "mirrored" band would be visible in the dispersion. Since this is not the case we confirm that the observed band structure is compatible with the periodicity of the smallest BCO unit cell. We want to underline that we do not observe the additional surface state reported in Refs. [46,47]. Notably, these experiments used photon energies in the range of $\sim 100 \text{ eV}$. The fact that we do not observe a surface state can be probably attributed to the exceptionally low photon energies we used in our spectra, which are much more bulk sensitive with reduced spectral weight on a surface state.

We now turn to the effect of lithium doping on the electronic structure [32]. Figure 4 shows an EDC through the Z point after

PHYSICAL REVIEW B **94**, 245410 (2016)

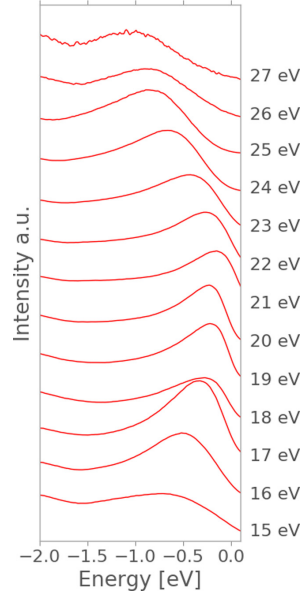


FIG. 3. Plot of the energy dispersion curves measured by ARPES for $k_{\parallel} = 0$ along the ΓZ direction. The EDC at 21 eV corresponds to $k_{\perp} = Z$.

lithium deposition. It can be seen that lithium doping raises the Fermi level by about 0.4 eV making the conduction band accessible by ARPES and turning BP into a metal. This effect is not common to all semiconductors, e.g., lithium doping does not induce the metallization of the wide band gap material hexagonal boron nitride [48]. In the present case, the doping

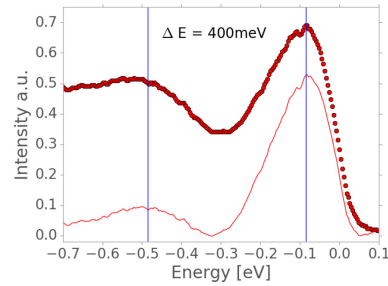


FIG. 4. The EDC corresponding to $k_{\parallel} = 0$ and $k_{\perp} = Z$ of the Li-doped BP sample. The lower curve is the EDC with the Shirley background subtracted. The band gap is indicated as the difference between the valence- and conduction-band maxima.

245410-4

5.1. BAND STRUCTURE ENGINEERING IN BLACK PHOSPHORUS

EVOLUTION OF ELECTRONIC STRUCTURE OF FEW- ...

PHYSICAL REVIEW B **94**, 245410 (2016)

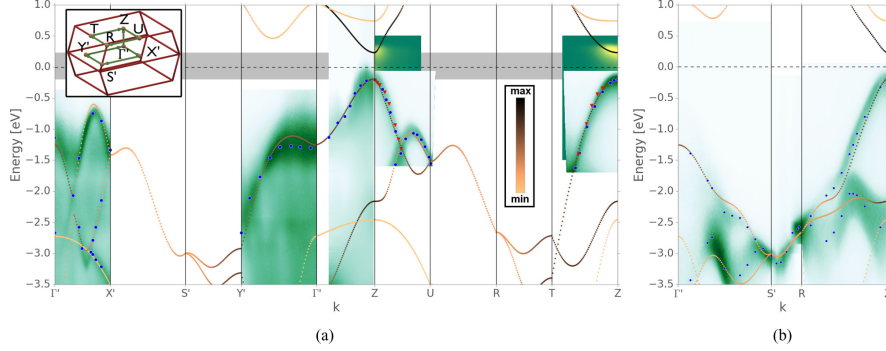


FIG. 5. The ARPES measurements together with the TB fit. \bullet and \blacktriangledown indicate peaks in the ARPES data of undoped and lithium doped BP, respectively. The color code of the TB calculation represents the p_z character of the bands. The inset in (a) depicts a sketch of the BCO BZ with the high symmetry points. The ARPES data of lithium doped BP were up-shifted by a constant energy of 0.32 eV. For this energy shift the valence bands of doped and undoped BP overlap.

induced semiconductor-metal transition is eased by the small band gap of BP.

The doping level we used ensures a rigid shift of the Fermi energy: We verified that the valence band dispersions of pristine and lithium doped BP are identical apart from a constant Fermi level shift (see below). These results are in line with the ARPES spectra obtained with low potassium coverage [49] which also leads to a rigid shift of the band structure [49]. On the contrary, further increasing of potassium doping closes the band gap and can even lead to a band inversion [49].

The shift of the Fermi level across the band gap into the conduction band allows us to extract a value of the “band gap” from the ARPES data of Fig. 4 by taking the difference between valence band maximum and conduction band minimum. We obtain a value of 400 meV which is reasonably close to the transport gap of 330 meV [9]. The remaining differences are ascribed to a combination of several effects such as intrinsic doping by impurities, weak interaction with lithium ions, the total energy resolution of the experiment (20 meV), and the fact that the transport gap was extracted by temperature dependent measurements. However, as was shown recently by Villegas and collaborators [50], the band gap has a strong and anomalous temperature dependence which could affect the transport results.

We now move to the in-plane ARPES data shown in Fig. 5. We have taken ARPES scans of the electronic structure along ZU and ZT directions as well as along $\Gamma'X'$ and $\Gamma'Y'$ (prime in this case denoting the high-symmetry points shifted by a small amount of 0.224 \AA^{-1} along the z axis). In order to directly show that doping causes a rigid band shift, we report both the pristine and doped data relative to the Fermi level of doped BP. Applying a rigid band shift of 320 meV to the ARPES data of pristine BP yields a perfect agreement to the valence bands of doped BP. It can be seen that their dispersion is identical apart from the shift in energy due to doping. This corroborates that the doping is in the rigid band shift regime and that the dispersion of the bands are unaffected by the presence of lithium.

Having the complete measured band dispersion of pristine and doped BP we performed the fit of the TB parameters reported in Sec. II. The ARPES spectrum is a renormalized quasiparticle spectrum including many-body effects that are not captured by a simple tight-binding model. For a Fermi-liquid-like doped black phosphorus, the energy scale of these effects should be small compared to our measured energy scale. We find that the TB model describes both the in-plane and out-of-plane dispersions with excellent accuracy. Moreover, since we included ARPES data of lithium doped BP, we are able to describe also the conduction band close to its minimum. This last result allows us to understand important physical properties of BP and phosphorene which strongly depend on the dispersion of the conduction band: (i) the evolution of the Fermi surface topology of alkali metal doped BP which is predicted to be superconducting [32] and (ii) the dependence of the QP gap of few-layer phosphorene with the number of the layers. The experimental data for the conduction band is limited, not only by the achievable doping levels but

TABLE II. The tight-binding parameters obtained from the fit to the ARPES data. The in-plane and out-of-plane hopping parameters are in units eV.

	order	V_{ssa}	V_{spa}	V_{ppa}	$V_{pp\pi}$
in-plane	1 st	-5.1008	1.0999	4.2100	-0.6709
	2 nd	-4.5895	3.9570	4.8083	-0.9741
	3 rd	-1.6268	0.6693	1.0361	0.2075
	4 th	-1.1674	0.9023	0.76375	-0.1442
	5 th	0.4734	-0.057	0.7221	-0.7869
	6 th	5.0773	1.2546	0.3212	-1.0060
out-of-plane	1 st	0.0848	0.7327	0.6907	0.2313
	2 nd	-0.6868	0.4964	0.0555	-0.2217
on-site	ϵ_s	-14.6830			
	ϵ_p	-1.5992			

245410-5

N. EHLEN *et al.*

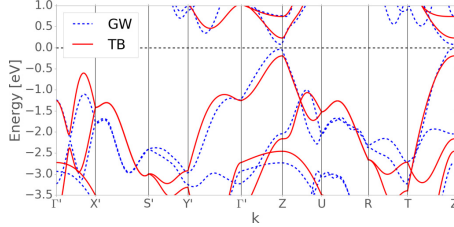
 PHYSICAL REVIEW B **94**, 245410 (2016)


FIG. 6. Theoretical G_0W_0 calculations for the band structure of BP shown in broken blue lines; our TB fit is shown in red. The path through the BZ is the same as for Fig. 5(a).

also because high doping levels cause a nonrigid band shift [49].

The set of TB parameters used in the calculation of the band structure reported in Fig. 5 is summarized in Table II. We find that we need to include at least six nearest in-plane neighbors to get a satisfactory fit result. Using a larger number of parameters leads to a smoother decrease of the absolute number of each hopping parameter but does not improve the fit result. Thus, Table II represents an efficient interpolation scheme with a minimum number of parameters.

We also compared the TB band structure with the state-of-the-art *ab initio* calculations. In Fig. 6 we report the G_0W_0 [51] calculation of the bands for bulk BP. In all the relevant regions of the BZ, the agreement between the two sets of bands is reasonably good. In particular the Γ -Z dispersion of the ARPES fit and in the G_0W_0 calculation has the same features. This indicates that the TB fit of the ARPES data is well suited for the zone-folding approach that we will present in Sec. VI.

IV. TEMPERATURE DEPENDENCE OF THE OPTICAL GAP AND EXCITON BINDING ENERGY

Here we further examine the properties of the band gap of BP by measuring the dependence of the optical band gap as a function of the temperature. Optical absorption measurements were carried out on the same crystal used for ARPES. The measurements were performed using a Bruker 70v spectrometer equipped with a glow-bar source and a DTGS pyroelectric detector. The measured optical density of BP is shown in Fig. 7 and displays a low frequency absorption that increases for lower wave numbers. It can be described with a Drude term due to the presence of free charge carriers in the range of $\sim 10^{17} \text{ cm}^{-3}$. We speculate that these free carriers are induced by oxygen impurities which would be consistent to the P-O vibration observed at $\sim 880 \text{ cm}^{-1}$ [52]. Indeed, DFT calculations have shown that oxygen impurities can donate charge to phosphorene layers [53]. If photons are absorbed across the bandgap of a material, an increase of the optical density is observed at energies which correspond to excitonic and interband transitions [54]. The optical band gap of BP is identified in Fig. 7 by a sharp steplike absorption found at 0.261 eV ($\sim 2100 \text{ cm}^{-1}$) at 40 K, in good agreement with previous optical data [7].

It is important to notice that the steplike gap edge highlights the quasi-2D nature of black phosphorus [55]. The smoothing of the step edge can be explained by temperature broadening roughly on the order of $k_B T$ which gives a broadening of about 200 cm^{-1} at room temperature, in line with the observed effect. With increasing temperature the gap edge feature also shifts to higher energies, reaching a value of 0.285 eV at 300 K (see inset of Fig. 7). This anomalous temperature dependence has been recently explained considering the coupling of the electrons with low-frequency transverse optical modes [50]. We underline that this same temperature dependence of the gap must also be taken into account when performing temperature-dependent transport measurements to extract the

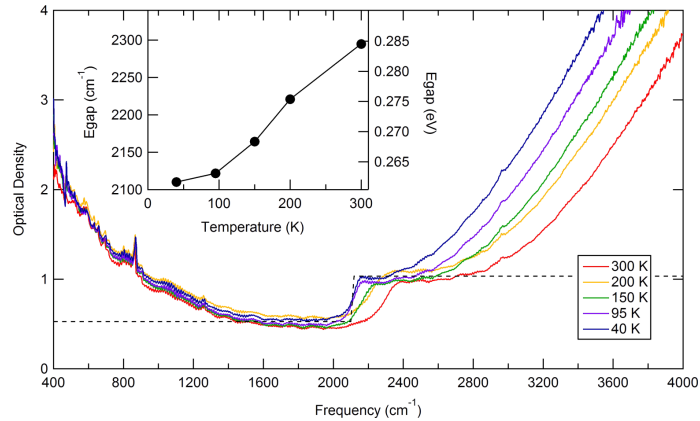


FIG. 7. Infrared optical density of BP at different temperatures. The optical band gap is extracted by fitting the gap edge with a heavy-side function (dashed line). The inset shows the anomalous temperature dependence of the band gap.

245410-6

value of the gap [25]. On top of the temperature dependence, the formation of excitons also affects the optical gap. If the optical gap $E_{\text{gap,optical}}$ is purely excitonic, we can estimate the excitonic binding energy by subtracting the optical band gap at $T = 40$ K from the ARPES band gap:

$$E_{\text{exc}} = E_{\text{gap,ARPES}} - E_{\text{gap,optical}} \approx 140 \text{ meV}. \quad (8)$$

We note, that alternatively to the current approach, there are also purely optical methods for determining the exciton binding energy [54]. These quasiparticle spectroscopy techniques are based on two photon photoabsorption and perform exciton spectroscopy using terahertz light [54].

V. DOPING DEPENDENCE OF THE FERMİ SURFACE

In this section, we examine, using our TB model, the doping dependence of the Fermi surface of BP. The doping dependence of the Fermi surface is relevant for electrostatically gated BP and the description of alkali metal doped BP. The latter has been predicted to become superconducting with experimentally achievable doping levels [32]. The pairing mechanism is thought to be electron-phonon coupling, and the topology of the Fermi surface and the total density of states at the Fermi level have palpable impact on the coupling strength. In particular, the nesting properties of the Fermi surface can lead to instabilities in the electronic system affecting the lattice dynamics and hence T_C . From an experimental point of view, higher doping with respect to the one used in this work may be achieved by liquid ion gating [10] or doping by Ca atoms [56].

Weakly doped BP has only one valley around the Z point. However, a close look to the band structures of Fig. 5 and Fig. 6 shows that with higher doping a second valley of the conduction band becomes occupied. The appearance of multiple Fermi surfaces is positive for superconductivity since it would allow us to obtain coupling from a larger set of phonons not only low \mathbf{q} -vector optical phonons (intra-band scattering) but also high \mathbf{q} -vector optical and acoustic phonons

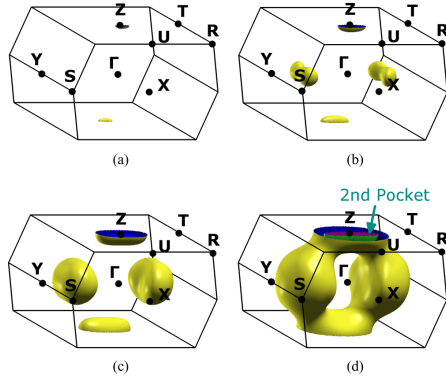


FIG. 8. The Fermi surface of BP in the BCO BZ for doping levels of 50 meV (a), 100 meV (b), 300 meV (c), and 500 meV (d). The appearance of a second pocket is highlighted (see text for discussion).

(mostly via interband scattering). This second valley is located along the $Y\Gamma$ direction in Fig. 5. After further doping, shifting the Fermi level of about 0.8 eV with respect to the pristine case, a second conduction subband in the Z point will be occupied. Notably, these predictions come from the TB fit to doped BP but are in excellent agreement to the *ab initio* G_0W_0 calculations that we showed above in Fig. 6.

Figure 8 depicts the 3D Fermi surface as it evolves as a function of the doping level (indicated in terms of shifts of the Fermi energy 50 meV, 100 meV, 300 meV, and 500 meV) and calculated by the TB approximation. Figure 8(d) shows that at 500 meV electron doping a second electron pocket at the Z point is occupied.

VI. FEW LAYER PHOSPHORENE

A. Zone-folding method

In this section, we apply the zone-folding method to the three-dimensional electronic structure of BP in order to extract the two-dimensional electronic dispersion relations of N -layer phosphorene. This is of high relevance as the synthesis of few-layer phosphorene in large areas that are needed for ARPES is not feasible up to now. Thus for exploration of the electronic structure of few layer phosphorene, a simple theoretical model is needed. Zone folding is performed in the eight-atom cell depicted in Fig. 2(b) with the electron wave vector k_z perpendicular to the phosphorene layers. In this description the periodicity in the k_z direction is halved due to the doubling of the unit cell along the z direction. This folds back the direct band gap from the Z point of the BCO unit cell to the Γ point of the supercell. Modelling the N -layer phosphorene (with the layers located at $z_i = id, i = 1 \dots N$, with d being the interlayer distance) as infinite potential barriers [located at $z = 0$ and $z = (N + 1)d$] we describe the slab as an infinite potential well in the z direction, see Fig. 9. Thus, for N -layer phosphorene the electron wave function at the zeroth and the $(N + 1)$ th layer must be equal to zero which leads to the following quantization condition for its wavelength λ :

$$n\lambda = (N + 1)d, \quad (9)$$

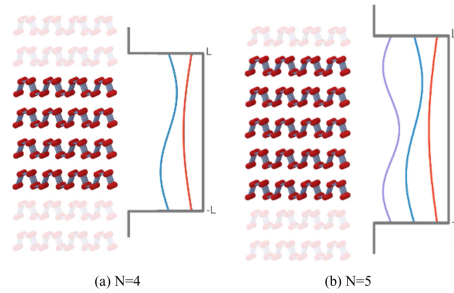


FIG. 9. Schematic representation of the zone-folding method. The orthogonal direction can be thought of as a particle-in-a-box model. This leads to a quantization of the k_z states.

N. EHLEN *et al.*

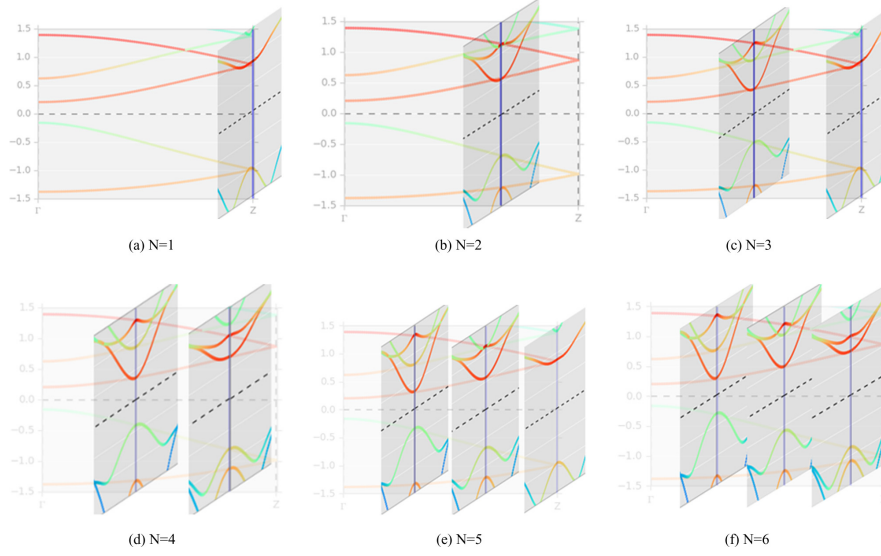
 PHYSICAL REVIEW B **94**, 245410 (2016)


FIG. 10. The application of the zone-folding method to BP. Performing cuts at selected $k_{z,n}$ as given in Eq. (10) yields a set of 2D dispersion relations for N layer phosphorene. Here we show the dispersion along ΓZ of bulk BP. Cuts perpendicular to ΓZ correspond to the dispersion relation of N layer phosphorene in the ΓY direction. Plots for $N = 1 \dots 6$ layered phosphorene are shown. The cuts through the BZ of BP are done increasingly close to the Γ point resulting in the reduction of the band gap for higher N .

with n being an integer. Depending on whether N is even or odd, we obtain quantization conditions for k_z :

$$k_{z,n} = \frac{n\pi}{(N+1)d} \quad (10)$$

$$n = 1, 2, 3, \dots, N/2 \text{ for } N \text{ even}$$

$$n = 1, 2, 3, \dots, (N+1)/2 \text{ for } N \text{ odd.} \quad (11)$$

Thus, knowing the experimental band structure of BP, we can describe the electronic structure of N -layer phosphorene by cuts through the Brillouin zone of bulk BP at the k_z values allowed by the quantization condition. Figure 10 shows a series of plots highlighting the procedure for $N = 1 \dots 6$. For N layer phosphorene we obtain $(N+1)/2$ (for N odd) or $N/2$ (for N even) k_z planes in the 3D band dispersion of BP. The value(s) of k_z determine the dispersion relation of N layer phosphorene in the k_x - k_y plane. It can be seen that for monolayer phosphorene, the cut goes through the Z high-symmetry point of the BZ which has the highest separation between valence and conduction bands (in the presently used eight-atom cell). As a consequence, the gap for monolayer phosphorene will be highest when compared to any other layer number N . For bilayer phosphorene, the k_z is located closer to the Γ point, and as a consequence the gap is reduced. This trend holds as we increase N and the gap is rapidly approaching the bulk value since the k_z move closer towards the Γ point according to Eq. (10).

B. Fermi surfaces of N layer phosphorene

In the remainder of this section we employ the zone-folding method to calculate the electronic properties of few-layer phosphorene. We start with the layer dependence of the Fermi surfaces of doped few-layer phosphorene which can be obtained by zone folding the Fermi surface of BP in the eight-atom supercell. Figure 11(a) shows this Fermi surface at a doping level of 500 meV. It can be seen that, in the plane spanned by ZU and ZT , the Fermi surface does not cover the volume around the ΓZ axis. However, as k_z decreases, the volume around the ΓZ axis becomes occupied. This can be more clearly seen in Fig. 11(b) which displays the contours of the Fermi surface from Fig. 11(a) at $k_z = 0$. This k_z dependence is important for understanding the layer dependent Fermi surface in N layer phosphorene. Figures 11(c)–11(f) depict the Fermi surfaces of $N = 1 \dots 4$ layer phosphorene. A rigid band shift of 500 meV was applied to the zone-folded band structure. It can be seen that the Fermi surface for $N = 1$ consists of pockets in the ΓY direction. For $N \geq 2$, another pocket around the Γ point appears. Such a layer dependence can affect nesting and might lead to layer number dependence in the superconducting properties, similarly to what is expected for few-layer graphene [57].

C. Energy band gaps of N layer phosphorene

We now look in more detail to the valence and conduction band energies of N layer phosphorene and their dependence

245410-8

EVOLUTION OF ELECTRONIC STRUCTURE OF FEW- ...

PHYSICAL REVIEW B 94, 245410 (2016)

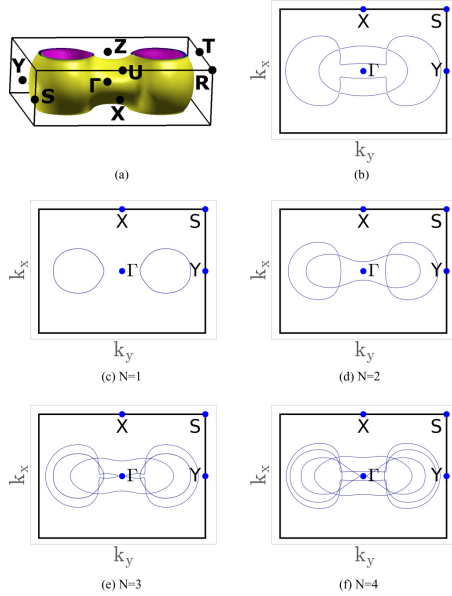


FIG. 11. (a) The Fermi surface of doped BP in the eight-atom supercell for a doping level of 500 meV. (b) Cut through the Γ plane of (a). (c)–(f) The Fermi surfaces for doped 1–4 layer phosphorene. A doping level of 500 meV has been assumed here, too.

on N . To that end we plot the energies obtained from zone folding as a function of layer number N in Fig. 12.

It can be seen that a family pattern emerges which connects the n th valence (conduction) band energies for different N .

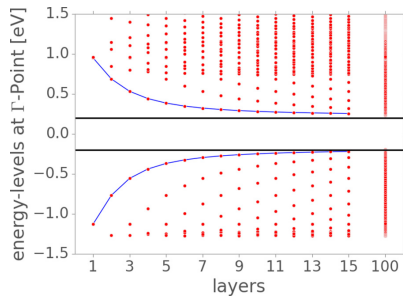


FIG. 12. Energy eigenvalues at the Γ point obtained from zone folding as a function of layer number N . The blue lines connect the energy eigenvalues of the lowest lying conduction band and the uppermost valence band. A $1/N$ law that governs the evolution of eigenvalues and a family pattern can be seen.

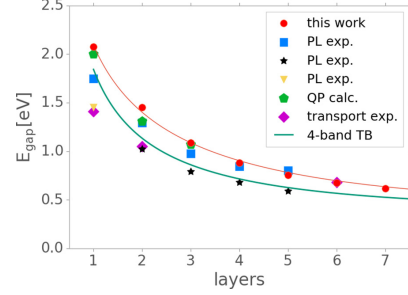


FIG. 13. The QP and optical band gaps of few-layer phosphorene obtained from zone folding the electronic structure of BP are denoted by \bullet . The gap increases when going from bulk BP to monolayer phosphorene. The fit to these data according to Eq. (12) is shown by a solid red line. For comparison we show this work's results along with previously published theoretical and experimental data of N -layer phosphorene: \blacksquare : PL (photoluminescence) data from Ref. [20], \star : PL data from Ref. [21], \blacktriangledown : PL data from Ref. [16], \bullet : QP calculation from Ref. [31], \blacklozenge : transport measurements from Ref. [59]. The turquoise line shows the development for the four-band tight-binding model and parameters given in Ref. [60].

Notably, similar family patterns have also been observed for few-layer graphene [37,58] where the relevant part of the zone-folded band structure is located along the KH line of the hexagonal BZ. The maximum splitting between the two valence (conduction) bands of graphite is at $k_z = 0$ (K point) whereas at the edge of the BZ (H point) the two valence (conduction) bands are degenerate.

Calculating the difference between the lowest conduction band and the highest valence band, which is equal to the QP gap, we compare the QP gap value of N -layer phosphorene (derived from a fit to ARPES data of doped BP) with the experimental optical and transport band gap of N layer phosphorene of previously published works and theoretical calculations. This comparison is shown in Fig. 13. It can be seen that the values of the gap that we obtained from zone folding the band structure of doped BP are in excellent agreement to G_0W_0 calculations of few-layer phosphorene [31]. The optical band gaps of few-layer phosphorene as measured by photoluminescence are smaller when compared to the QP band gaps. Despite some scattering in the experimental data, we can observe an increase of the difference between QP gap and optical band gap with decreasing the number of layers. Again, we infer that this trend can be understood as excitonic effects becoming increasingly important for thinner systems. On the other hand, the large variation among individual experiments could perhaps be explained by (1) different environments which have a large effect on the exciton binding energy and (2) different degrees of oxygen exposure which causes doping and hence a change in the optical response.

The dependence of the gap $E_g(N)$ on the layer number N can be fitted by

$$E_g(N) = 1.99 \frac{e^{-0.18N}}{N^{0.52}} + 0.41. \quad (12)$$

245410-9

N. EHLEN *et al.*

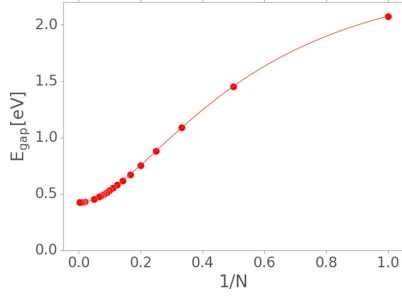
 PHYSICAL REVIEW B **94**, 245410 (2016)


FIG. 14. Evolution of the band gap as a function of layer number N is inversely proportional to the number of layers [see Eq. (12)]. The dots show the actual gaps for given values of $1/N$; the red line shows an interpolated spline between these values.

This mix of shallow exponential decay and N^{-a} dependence is similar to previous results for a four-band tight-binding Hamiltonian that was fit to GW_0 calculations [60]. In order to cover a wider range of N we also show the plot of the band gap as a function of $1/N$ in Fig. 14.

Finally, since zone folding does not capture effects resulting from crystal surfaces, it is interesting to assess the accuracy of zone folding by a comparison of the zone-folded band structure to an explicit TB calculation of N layer phosphorene. The calculation of N layer phosphorene uses an extended Hamiltonian which includes the coupling to adjacent phosphorene layers via the out-of-plane matrix elements. The atoms inside the layers on the two surfaces of the few-layer phosphorene stack will have fewer neighbors to couple to in the extended calculation. This effect is not included in the zone-folding picture which derives the bands of few-layer phosphorene from the BP. The comparison of the zone-folding result and the extended

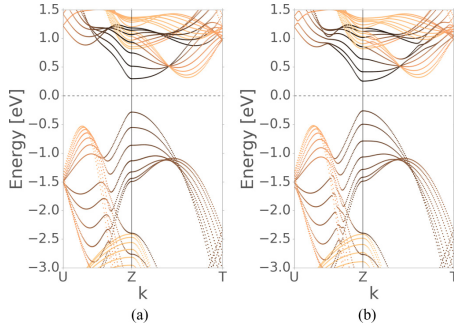


FIG. 15. Comparison of the band structure for $N = 7$ layer phosphorene obtained by (a) zonefolding and (b) an explicit tight-binding calculation using an extended Hamiltonian.

calculation is shown in Fig. 15. Since black phosphorus is a van der Waals material without dangling bonds, the effects of surfaces are believed to be small, and indeed it can be seen that the zone-folding result agrees well with the explicit calculation of N layer phosphorene.

VII. DISCUSSION AND OUTLOOK

ARPES measurements of the three-dimensional electronic structure of BP allowed us to perform a fit of tight-binding parameters of black phosphorus using the Slater-Koster approximation. The experimental data could be described using five in-plane and two out-of-plane neighbor orders. Using this model with our parameters we extract the behavior for the band gap of N -layer phosphorene from the bulk bands using the zone-folding method and find good agreement with calculations and experiments.

Measurements of the optical energy gap indicate that the gap value is close to this separation energy. Moreover the valence band effective mass is not affected by doping in our case, and *ab initio* G_0W_0 calculations are in agreement with the measured conduction band. From these facts we infer that our doping levels by lithium cause little structural and electronic changes apart from the rigid band shift. The ARPES data of pristine and doped BP are therefore used to fit a new set of tight-binding parameters to the experiment. This accurate set of tight-binding parameters is used to predict a transition into a multiple-valley ground state upon alkali metal doping of BP. Already at experimentally accessible doping levels it is possible to obtain a large Fermi surface area and therefore to take advantage of the full phononic coupling, without relevant momentum restrictions. Most importantly, we employ the zone-folding method to predict the electron energy gap of few-layer phosphorene. The predicted values show the same trend as the experimentally observed energy band gaps of few-layer phosphorene. Finally, the experimental band structure data are compared to *ab initio* calculations using the G_0W_0 approximation, and a good agreement is found in most parts of the Brillouin zone. The present work is based on lithium doped BP in the regime of a rigid band shift. It would be interesting to extend it to other alkali or alkaline earth dopants for which effects beyond a rigid band shift could be observed. The proposed tight-binding model can also be useful to describe the electronic structure of gated few-layer phosphorene devices. This would require modifying the on-site tight-binding parameters in a calculation using an extended Hamiltonian of few-layer phosphorene in such a way to model a different charge on each layer.

ACKNOWLEDGMENTS

N.E., B.S., and A.G. acknowledge the ERC Grant No. 648589 ‘SUPER-2D’ and support by DFG through CRC1238 project A1. B.S. and A.G. acknowledge the DFG project GR 3708/2-1. The stay at the Elettra synchrotron for ARPES and optical absorption experiments has been supported by the CERIC-ERIC consortium.

245410-10

- [1] P. W. Bridgman, *J. Am. Chem. Soc.* **36**, 1344 (1914).
- [2] Y. Takao, H. Asahina, and A. Morita, *J. Phys. Soc. Jpn.* **50**, 3362 (1981).
- [3] Y. Maruyama, S. Suzuki, K. Kobayashi, and S. Tanuma, *Physica B+C* **105**, 99 (1981).
- [4] S.-i. Narita, S.-i. Terada, S. Mori, K. Muro, Y. Akahama, and S. Endo, *J. Phys. Soc. Jpn.* **52**, 3544 (1983).
- [5] T. Takahashi, H. Tokailin, S. Suzuki, T. Sagawa, and I. Shirovani, *Phys. Rev. B* **29**, 1105 (1984).
- [6] T. Takahashi, N. Gunasekara, H. Ohsawa, H. Ishii, T. Kinoshita, S. Suzuki, T. Sagawa, H. Kato, T. Miyahara, and I. Shirovani, *Phys. Rev. B* **33**, 4324 (1986).
- [7] A. Morita, *Appl. Phys. A* **39**, 227 (1986).
- [8] S. Endo, Y. Akahama, S.-i. Terada, and S.-i. Narita, *Jpn. J. Appl. Phys.* **21**, L482 (1982).
- [9] R. W. Keyes, *Phys. Rev.* **92**, 580 (1953).
- [10] Y. Saito and Y. Iwasa, *ACS Nano* **9**, 3192 (2015).
- [11] T. Takahashi, H. Tokailin, S. Suzuki, T. Sagawa, and I. Shirovani, *J. Phys. C* **18**, 825 (1985).
- [12] L. Liang, J. Wang, W. Lin, B. G. Sumpter, V. Meunier, and M. Pan, *Nano Lett.* **14**, 6400 (2014).
- [13] X. Ling, H. Wang, S. Huang, F. Xia, and M. S. Dresselhaus, *Proc. Natl. Acad. Sci. USA* **112**, 4523 (2015).
- [14] H. Liu, Y. Du, Y. Deng, and P. D. Ye, *Chem. Soc. Rev.* **44**, 2732 (2015).
- [15] J. Ribeiro-Soares, R. M. Almeida, L. G. Cançado, M. S. Dresselhaus, and A. Jorio, *Phys. Rev. B* **91**, 205421 (2015).
- [16] H. Liu, A. T. Neal, Z. Zhu, Z. Luo, X. Xu, D. Tománek, and P. D. Ye, *ACS Nano* **8**, 4033 (2014).
- [17] L. Li, Y. Yu, G. J. Ye, Q. Ge, X. Ou, H. Wu, D. Feng, X. H. Chen, and Y. Zhang, *Nat. Nanotechnol.* **9**, 372 (2014).
- [18] S. P. Koenig, R. A. Doganov, H. Schmidt, A. H. Castro Neto, and B. Özyilmaz, *Appl. Phys. Lett.* **104**, 103106 (2014).
- [19] V. Tayari, N. Hemswoorth, I. Fakhri, A. Favron, E. Gafures, G. Gervais, R. Martel, and T. Szkopek, *Nat. Commun.* **6**, 7702 (2015).
- [20] J. Yang, R. Xu, J. Pei, Y. W. Myint, F. Wang, Z. Wang, S. Zhang, Z. Yu, and Y. Lu, *Light. Sci. Appl.* **4**, e312 (2015).
- [21] S. Zhang, J. Yang, R. Xu, F. Wang, W. Li, M. Ghufra, Y.-W. Zhang, Z. Yu, G. Zhang, Q. Qin, and Y. Lu, *ACS Nano* **8**, 9590 (2014).
- [22] A. Surrente, A. A. Mitioglu, K. Galkowski, W. Tabis, D. K. Maude, and P. Plochocka, *Phys. Rev. B* **93**, 121405 (2016).
- [23] L. Li, J. Kim, C. Jin, G. Ye, D. Y. Qiu, F. H. da Jornada, Z. Shi, L. Chen, Z. Zhang, F. Yang, K. Watanabe, T. Taniguchi, W. Ren, S. G. Louie, X. Chen, Y. Zhang, and F. Wang, *Nat. Nanotech.* (2016), doi:10.1038/nnano.2016.171.
- [24] X. Wang, A. M. Jones, K. L. Seyler, V. Tran, Y. Jia, H. Zhao, H. Wang, L. Yang, X. Xu, and F. Xia, *Nat. Nano* **10**, 517 (2015).
- [25] D. Warschauer, *J. Appl. Phys.* **34**, 1853 (1963).
- [26] M. Baba, Y. Nakamura, K. Shibata, and A. Morita, *Jpn. J. Appl. Phys.* **30**, L1178 (1991).
- [27] E. Burstein, *Phys. Rev.* **93**, 632 (1954).
- [28] R. Schuster, J. Trinckauf, C. Habenicht, M. Knupfer, and B. Büchner, *Phys. Rev. Lett.* **115**, 026404 (2015).
- [29] X. Ling, S. Huang, E. H. Hasdeo, L. Liang, W. M. Parkin, Y. Tatsumi, A. R. T. Nugraha, A. A. Puzos, P. M. Das, B. G. Sumpter, D. B. Geohegan, J. Kong, R. Saito, M. Drndic, V. Meunier, and M. S. Dresselhaus, *Nano Lett.* **16**, 2260 (2016).
- [30] A. N. Rudenko and M. I. Katsnelson, *Phys. Rev. B* **89**, 201408 (2014).
- [31] V. Tran, R. Soklaski, Y. Liang, and L. Yang, *Phys. Rev. B* **89**, 235319 (2014).
- [32] A. Sanna, A. V. Fedorov, N. I. Verbitskiy, J. Fink, C. Krellner, L. Petaccia, A. Chikina, D. Y. Usachov, A. Grüneis, and G. Profeta, *2D Materials* **3**, 025031 (2016).
- [33] L. Hedin, *Phys. Rev.* **139**, A796 (1965).
- [34] M. S. Hybertsen and S. G. Louie, *Phys. Rev. B* **34**, 5390 (1986).
- [35] T. Low, A. S. Rodin, A. Carvalho, Y. Jiang, H. Wang, F. Xia, and A. H. Castro Neto, *Phys. Rev. B* **90**, 075434 (2014).
- [36] V. Wang, Y. C. Liu, Y. Kawazoe, and W. T. Geng, *J. Phys. Chem. Lett.* **6**, 4876 (2015).
- [37] A. Grüneis, C. Attaccalite, L. Wirtz, H. Shiozawa, R. Saito, T. Pichler, and A. Rubio, *Phys. Rev. B* **78**, 205425 (2008).
- [38] X.-L. Qi and S.-C. Zhang, *Rev. Mod. Phys.* **83**, 1057 (2011).
- [39] E. Cappelluti and G. Profeta, *Phys. Rev. B* **85**, 205436 (2012).
- [40] S. Fukuoka, T. Taen, and T. Osada, *J. Phys. Soc. Jpn.* **84**, 121004 (2015).
- [41] J. L. Lado and J. Fernández-Rossier, *2D Mater.* **3**, 035023 (2016).
- [42] A. Brown and S. Rundqvist, *Acta Crystallogr.* **19**, 684 (1965).
- [43] J. C. Slater and G. F. Koster, *Phys. Rev.* **94**, 1498 (1954).
- [44] L. Petaccia, P. Vilmercati, S. Gorovikov, M. Barnaba, A. Bianco, D. Cocco, C. Masciovecchio, and A. Goldoni, *Nucl. Instrum. Methods Phys. Res., Sect. A: Accelerators, Spectrometers, Detectors and Associated Equipment* **606**, 780 (2009).
- [45] A. Damascelli, *Phys. Scr.* **T109**, 61 (2004).
- [46] C. Q. Han, M. Y. Yao, X. X. Bai, L. Miao, F. Zhu, D. D. Guan, S. Wang, C. L. Gao, C. Liu, D. Qian, and *et al.*, *Phys. Rev. B* **90**, 085101 (2014).
- [47] E. Golias, M. Krivenkov, and J. Sánchez-Barriga, *Phys. Rev. B* **93**, 075207 (2016).
- [48] A. Fedorov, C. S. Praveen, N. I. Verbitskiy, D. Haberer, D. Usachov, D. V. Vyalikh, A. Nefedov, C. Wöll, L. Petaccia, S. Piccinin, H. Sachdev, M. Knupfer, B. Büchner, S. Fabris, and A. Grüneis, *Phys. Rev. B* **92**, 125440 (2015).
- [49] J. Kim, S. S. Baik, S. H. Ryu, Y. Sohn, S. Park, B.-G. Park, J. Denlinger, Y. Yi, H. J. Choi, and K. S. Kim, *Science* **349**, 723 (2015).
- [50] C. E. P. Villegas, A. R. Rocha, and A. Marini, *Nano Lett.* **16**, 5095 (2016).
- [51] All calculations have been performed at the experimental lattice with the Vienna *ab initio* simulation package (VASP) [61,62] and within the generalized gradient approximation [63] (GGA) to density functional theory. We used projected augmented-wave (PAW) [64] pseudopotentials. A cutoff of 300 eV was used for the plane-wave expansion and a 100 eV cutoff for the summation of the response function. BZ sampling has been done with a Γ centered $12 \times 12 \times 8k$ -point grid.
- [52] J. D. Wood, S. A. Wells, D. Jariwala, K.-S. Chen, E. Cho, V. K. Sangwan, X. Liu, L. J. Lauhon, T. J. Marks, and M. C. Hersam, *Nano Lett.* **14**, 6964 (2014).
- [53] A. Ziletti, A. Carvalho, D. K. Campbell, D. F. Coker, and A. H. Castro Neto, *Phys. Rev. Lett.* **114**, 046801 (2015).
- [54] S. W. Koch, M. Kira, G. Khitrova, and H. M. Gibbs, *Nat. Mater.* **5**, 523 (2006).

N. EHLEN *et al.*PHYSICAL REVIEW B **94**, 245410 (2016)

- [55] M. Dressel and G. Grüner, *Electrodynamics of Solids: Optical Properties of Electrons in Matter* (Cambridge University Press, 2002).
- [56] A. V. Fedorov, N. I. Verbitskiy, D. Haberer, C. Struzzi, L. Petaccia, D. Usachov, O. Y. Vilkov, D. V. Vyalikh, J. Fink, M. Knupfer, B. Büchner, and A. Grüneis, *Nat. Commun.* **5**, 4257 (2014).
- [57] E. R. Margine, H. Lambert, and F. Giustino, *Sci. Rep.* **6**, 21414 (2016).
- [58] K. F. Mak, M. Y. Sfeir, J. A. Misewich, and T. F. Heinz, *Proc. Natl. Acad. Sci. USA* **107**, 14999 (2010).
- [59] X. Chen, L. Wang, Y. Wu, H. Gao, Y. Wu, G. Qin, Z. Wu, Y. Han, S. Xu, T. Han, W. Ye, J. Lin, G. Long, Y. He, Y. Cai, W. Ren, and N. Wang, *2D Mater.* **3**, 015012 (2016).
- [60] A. N. Rudenko, S. Yuan, and M. I. Katsnelson, *Phys. Rev. B* **92**, 085419 (2015).
- [61] G. Kresse and J. Furthmüller, *Phys. Rev. B* **54**, 11169 (1996).
- [62] G. Kresse and J. Furthmüller, *Comput. Mater. Sci.* **6**, 15 (1996).
- [63] J. P. Perdew, K. Burke, and M. Ernzerhof, *Phys. Rev. Lett.* **77**, 3865 (1996).
- [64] P. E. Blöchl, *Phys. Rev. B* **50**, 17953 (1994).

5.1.2 Inducing Surface Band Inversion and a Surface Resonance State in Black Phosphorus via Caesium Functionalization

Niels Ehlen, Antonio Sanna, Boris V. Senkovskiy, Luca Petaccia, Alexander V. Fedorov, Gianni Profeta, and Alexander Grüneis.

Direct observation of a surface resonance state and surface band inversion control in black phosphorus.

Physical Review B **97**, 045143 (2018) © [2018] American Physical Society

Doi: <https://doi.org/10.1103/PhysRevB.97.045143>

As mentioned in the introduction to section 5.1, the band gap of black phosphorus can be engineered by doping with potassium [17, 55]. In this publication, Cs doping was used to dope the material past its band gap inversion point. Theoretical tight-binding and density functional theory calculations were used to explain the observed changes in band structure.

Caesium was deposited onto a clean surface of pristine black phosphorus. Angle-dependent x-ray photoemission spectroscopy after doping could be used to confirm the Cs sitting atop the phosphorus layers. Angle-resolved photoemission spectroscopy of the doped surface revealed a band inversion of the conduction (electron-like) and valence (hole-like) bands at the Z -point. A full map of the observed band inversion was recorded. Analysis of the dispersion showed Fermi velocities of $3.68 \times 10^5 \text{ m s}^{-1}$ along Z - T - and $1.02 \times 10^6 \text{ m s}^{-1}$ along Z - U -direction. The anisotropy arises from the peculiar anisotropic crystal structure of BP. The peak widths of the hole-like valence band were very broad. The electron-like conduction band on the other hand was very sharp. Interestingly, even though the conduction band was very sharp, no kink features arising from electron-phonon coupling could be discerned (compare section 3.3).

The difference in broadening of the conduction and valence band hints at the localization of these states, with the sharp electron-like band being located on the surface of the sample and the hole-like band arising from states located in the bulk. The surface-nature of the electron-like conduction band could be verified by energy-dependent ARPES. This technique was used to get information on the out-of-plane dispersion of the bands. The electron-like band showed no out-of-plane k_z dispersion – a signature of two-dimensional electronic states (compare section 2.2). The electron-like band was thus concluded to be localized at the two-dimensional surface of the bulk crystal. Prior theoretical treatment of the band inversion in BP (compare section 2.3) predicted

an anti-crossing forming at the crossing-points of the original electron-like and hole-like bands along Γ - X -direction. On the other hand, the Γ - Y -direction would show a band crossing – topologically protected *via* glide mirror symmetry – leading to the formation of a typical Dirac cone feature in the dispersion [94, 95, 219, 220]. However, in this publication no effects of hybridization and anti-crossing were observed in the ARPES spectra. Using the tight-binding Hamiltonian developed in section 5.1.1, the experimental observations could be reproduced by a two-layer model where individual layers were put on different potentials by modifying the on-site parameters. Putting the top-most layer to a different potential reproduced the observed band inversion. However, using the out-of-plane hopping parameters from the bulk model lead to very strong anti-crossing along Γ - X -direction (corresponding to Z - U in the bulk unit cell) and a Dirac-like state along Γ - Y -direction (corresponding to Z - T in the bulk unit cell), reproducing the previous theoretical predictions. Since the experimental results did not show these effects, the difference needed to be explained. Reducing the out-of-plane hopping parameters by one magnitude reduced the anti-crossing gap to a size where band broadening would make it invisible in experiment. Additionally, artificially breaking glide mirror symmetry *via* modification of hopping parameters showed a small gap opening in the Dirac-like dispersion along Γ - Y -direction. These modifications to the theoretical model reproduced the experimental observations and matched the results of density functional theory calculations.

The DFT models confirmed the localization of the conduction band at the surface of the crystal. They also confirmed the bulk nature of the valence band. The calculations showed best agreement with the experiment, if a stacking fault at the surface was assumed. This stacking fault broke glide mirror symmetry, opening a small gap in the Dirac cone dispersion. It also explained the reduction of the interlayer interaction. The predicted gap in DFT is too small to be observable in ARPES with the experimental broadening of the bulk states.

The DFT calculations predict a hybridization between the conduction band states and the valence band states, establishing the observed conduction band as a surface resonance rather than a “normal” surface state.

Contributions to this publication:

- Main authors of the publication are N. Ehlen and A. Grüneis with smaller contributions from the co-authors
 - Adapt tight-binding Hamiltonian; include staggered electric potential in the model; break glide mirror symmetry by modification of hopping parameters
 - Record and analyze angle-resolved photoemission spectroscopy data
 - Record and analyze x-ray photoemission spectroscopy data
 - Discussion of overlap between ab-initio model and experiment/tight-binding model
 - Produce Figures 1-4, Table 1
-

Publication

PHYSICAL REVIEW B **97**, 045143 (2018)**Direct observation of a surface resonance state and surface band inversion control in black phosphorus**N. Ehlen,^{1,*} A. Sanna,² B. V. Senkovskiy,¹ L. Petaccia,³ A. V. Fedorov,^{1,4} G. Profeta,⁵ and A. Grüneis^{1,†}¹*II. Physikalisches Institut, Universität zu Köln, Zùlpicher Strasse 77, D-50937 Köln, Germany*²*Max-Planck-Institut für Mikrostrukturphysik, Weinberg 2, D-06120 Halle, Germany*³*Eletra Sincrotrone Trieste, Strada Statale 14 km 163.5, I-34149 Trieste, Italy*⁴*IFW Dresden, P.O. Box 270116, Dresden D-01171, Germany*⁵*Department of Physical and Chemical Sciences and SPIN-CNR, University of L'Aquila, Via Vetoio 10, I-67100 Coppito, Italy*

(Received 19 November 2017; published 24 January 2018)

We report a Cs-doping-induced band inversion and the direct observation of a surface resonance state with an elliptical Fermi surface in black phosphorus (BP) using angle-resolved photoemission spectroscopy. By selectively inducing a higher electron concentration ($1.7 \times 10^{14} \text{ cm}^{-2}$) in the topmost layer, the changes in the Coulomb potential are sufficiently large to cause surface band inversion between the parabolic valence band of BP and a parabolic surface state around the Γ point of the BP Brillouin zone. Tight-binding calculations reveal that band gap openings at the crossing points in the two high-symmetry directions of the Brillouin zone require out-of-plane hopping and breaking of the glide mirror symmetry. *Ab initio* calculations are in very good agreement with the experiment if a stacking fault on the BP surface is taken into account. The demonstrated level of control over the band structure suggests the potential application of few-layer phosphorene in topological field-effect transistors.

DOI: [10.1103/PhysRevB.97.045143](https://doi.org/10.1103/PhysRevB.97.045143)**I. INTRODUCTION**

The recent synthesis of metallic black phosphorus (BP) [1,2], the prediction of electron-phonon-mediated superconductivity in lithium-doped BP [2], and its experimental confirmation [3] with $T_C = 3.8$ K have spurred additional interest in alkali-metal-doped BP as it represents an interesting playground to test fundamental physics and technologically relevant effects. In particular, the control of the charge carrier concentration and the electron energy band gap of BP is fundamentally important. The high electron mobility in BP allowed for the fabrication of field-effect transistors (FETs) [4–9] and photodetectors [10] with good characteristics. An insulator-to-metal transition has also been achieved by ionic liquid gating [11]. It has been shown that potassium adsorption onto the BP surface closes the band gap, and an anisotropic Dirac cone was revealed by angle-resolved photoemission spectroscopy (ARPES) [1]. A gate-tunable Stark effect, i.e., the electronic control of the band gap by electric field, has been demonstrated and is directly relevant for optoelectronic applications of BP [12]. An *in situ* electric transport study of the conductivity of the surface of BP showed a huge increase in the conductance and a reduction of the gap upon potassium deposition [13]. This work also hinted at the existence of surface resonant states [13]. The underlying mechanism for understanding these experiments is a charge accumulation on the surface of BP or few-layer phosphorene which can be controlled by an external gate voltage. The physics of surface charge doping in BP must also consider the existence of a surface resonance state. Surface

resonance states have been reported using ARPES [14,15], but a complete ARPES characterization of their dispersion relation is missing. A surface resonance state is localized on the surface of BP, but its energy can lie outside the band gap [16], allowing hybridization with bulk states. Surface states and surface resonance states also play a decisive role for applications of BP beyond standard field-effect control of the carrier concentration. For example, it has been theoretically suggested that an electric field perpendicular to the layers is a means to invert the band gap and to engineer topologically protected edge states in few-layer phosphorene [17,18]. A band inversion of the parabolic valence and conduction bands would result in crossing points that lie along an ellipse in k space. For cuts along the ΓX and ΓY high-symmetry directions of the orthorhombic unit cell [17,18], we would expect two crossing points each. Tight-binding (TB) calculations and a symmetry analysis suggest that the band crossing in the ΓY direction is protected by glide mirror symmetry [19,20]. Experimentally, ARPES measurements of K-doped BP showed a band inversion upon strong K doping [1], and a very recent work [21] analyzed the two high-symmetry crossing points in more detail and found that a gap opens in the ΓX direction, while the size of the gap in ΓY is below the energy resolution. However, a quantitative description of the band inversion observed in ARPES including the effects of interlayer hopping and glide mirror symmetry breaking is still missing. Such realistic models are needed, for example, for the simulation of topological FETs.

This paper addresses these issues and unravels the nature of the surface resonance state and its connection with the increased conductivity and the topology of the band structure. We directly show, using ARPES, that Cs adsorption on the surface of BP induces a massive doping and leads to a surface

*ehlen@ph2.uni-koeln.de

†gruneis@ph2.uni-koeln.de

band inversion between the valence band states of BP and a surface band. The energy of the band inversion observed here for Cs doping is larger than for K doping. We map the full three-dimensional surface-band-inverted Dirac cone and demonstrate that the conduction band is a surface resonance state localized on the topmost phosphorene layer, while the valence band is localized on the subsurface layers below. The region of the inverted bands is accurately mapped and clearly shows the overlapping surface and bulk states. A quantitative TB model developed for pristine BP [22] is adapted for doped BP. It demonstrates the requirements for protecting the band crossings imposed on crystal symmetry. These TB simulations also show that, upon populating the surface resonance state, the interlayer interaction decreases. A microscopic model is obtained from first-principles density functional theory (DFT) calculations. DFT suggests that Cs doping is accompanied by the formation of a stacking fault that decouples surface layers from the substrate. The ARPES spectrum and the occurrence of a band inversion with a negligible gap opening are accurately reproduced by DFT.

II. ANGLE-RESOLVED PHOTOEMISSION SPECTROSCOPY

ARPES was performed at the BaDElPh beamline [23] of the Elettra synchrotron in Trieste, Italy, with linear s and p polarization at temperatures of 20 K. The crystal surfaces were prepared *in situ* in a vacuum better than 5×10^{-11} mbar and at liquid-He temperatures by cleaving with a top post inside the analysis chamber [22]. Immediately after the cleave, we determined the high-symmetry directions through low-energy electron diffraction. Cs deposition was carried out in an ultrahigh-vacuum (UHV) chamber from SAES Getters with the sample at 20 K. We performed stepwise evaporation of Cs, which we monitored by ARPES measurements of the band structure. We found that the changes in the band structure with an increasing amount of Cs deposited are very similar to the ones already reported for K doping [1]. Cs evaporation was stopped after the maximum doping level was reached. Figures 1(a) and 1(b) show sketches of the functionalized BP surface and of the surface Brillouin zone of BP with Γ , X ,

Y , and S high-symmetry points. Prior to Cs deposition we recorded ARPES of the pristine BP crystal to confirm the surface quality and the orientation. We have obtained results in agreement with those published earlier [2,22]. Figures 1(c) and 1(d) show ARPES spectra (taken at $h\nu = 21$ eV with a horizontal entrance slit on the analyzer) after maximum deposition of Cs. These spectra were recorded along the ΓY direction for p -polarized light and s -polarized light, respectively. In Fig. 1(c) we also show a fit of the parabolic band dispersion of the electronlike band which yields an effective electron mass of $m^* = 1.38m_e$ (m_e is the free-electron mass). Figure 1(e) shows the resulting spectrum from adding Figs. 1(c) and 1(d). We find that p -polarized light couples mainly to the electronlike band, while s -polarized light couples to the holelike band. The photoemission intensities for s - and p -polarized light also suggest that the electron- and holelike bands have close to orthogonal symmetries. The ARPES spectra feature a sharp electronlike band and a slightly blurry holelike band. As we will show by DFT, this difference is related to the nature of the wave function of the electronlike band which is localized on the topmost layer and of the holelike band which, on the contrary, is delocalized over several layers underneath the surface. It can be seen that the surface conduction band minimum in Fig. 1(c) is lower in energy than the valence band maximum in Fig. 1(d), indicating a band inversion at the surface.

The dispersion of the surface resonance state and the holelike valence band is studied in more detail by performing an ARPES mapping in the full two-dimensional (2D) Brillouin zone (BZ). Figure 2 displays the full three-dimensional experimental ARPES intensity maxima. Maxima of equienergy contours were obtained from fitting peak ARPES intensities in the radial cuts centered around Γ . The elliptical shape of the equienergy contours can clearly be seen. The ellipses have their short (long) axis in the ΓX (ΓY) directions. The observed anisotropy is consistent with previous optical [24] and scanning tunneling microscopy measurements [25] of pristine BP and supports the band assignment to a phosphorene-derived band. This anisotropy is rooted in the puckered structure of BP and results in a quadratic energy dispersion along ΓY and a linear energy dispersion along ΓX [22]. The ARPES intensity has an inverse angular distribution for energy contours below and

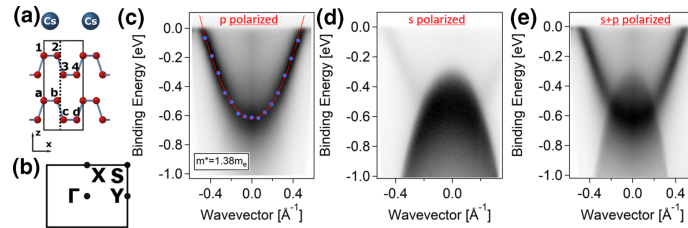


FIG. 1. (a) Sketch of the bilayer phosphorene structure with Cs adsorbed. The dashed line denotes the mirror plane of the glide mirror symmetry. The glide axes are in the x and y directions. The four atoms in the bilayer unit cell are indicated by a - d and 1-4. (b) The surface BZ of BP and the high-symmetry points. Two-dimensional, k -dependent ARPES spectra along the ΓY direction measured with (c) p - and (d) s -polarized light. A fit of the effective electron mass yielding $m^* = 1.38m_e$ is shown (m_e is the free-electron mass). (e) The s - and p -polarized spectra added together.

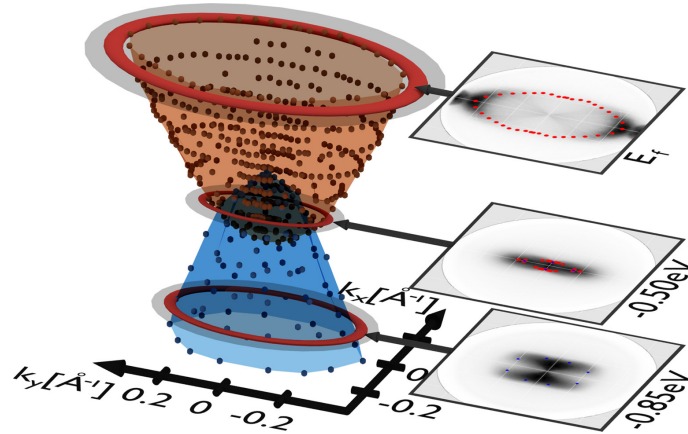


FIG. 2. Three-dimensional energy band dispersion of BP with a monolayer of Cs adsorbed on its surface. The points are the experimental ARPES maxima (measured at $h\nu = 21$ eV with s - and p -polarized light), and the surfaces are an interpolation of the symmetrized data. Red (blue) denotes electronlike (holelike) bands. The right part shows equienergy contours of ARPES data for three binding energies. Additional equienergy contours (see the Appendix) were used to interpolate the three-dimensional dispersion. The left part originates from radial fits to the surfaces of the kind shown on the right.

above the region of band inversion because these states have a different character and hence matrix element. Nevertheless, it is possible to reliably extract ARPES maxima, and more equienergy contours are shown in the Appendix. From ARPES equienergy contours all relevant parameters describing the surface band can be extracted. The region of surface band inversion is clearly seen around the Γ point. Fermi velocities of 3.68×10^5 and 1.02×10^6 m/s are found in the ΓY and ΓX directions, respectively. We find a charge carrier concentration of 1.7×10^{14} cm $^{-2}$. The Fermi velocities are in a range similar to those reported previously for electron-doped BP [1]. The differences are ascribed to the larger doping level we have here.

III. X-RAY PHOTOEMISSION SPECTROSCOPY AND NEAR-EDGE X-RAY ABSORPTION FINE STRUCTURE

The localization on the BP surface is also consistent with the fact that monolayer Cs does not intercalate into the bulk of BP. This is evident from angle-dependent x-ray photoemission spectroscopy (XPS). XPS measurements have been performed at the German-Russian Beamline (RGLB) at the BESSY II synchrotron in Berlin using a photon energy $h\nu = 300$ eV. The results can be seen in Figs. 3(a) and 3(b), which show the XPS spectrum for grazing and normal emission on Cs-doped BP. The spectra are normalized to the P $2p$ core-level intensity. It can be seen that upon doping, the P $2p$ core levels shift

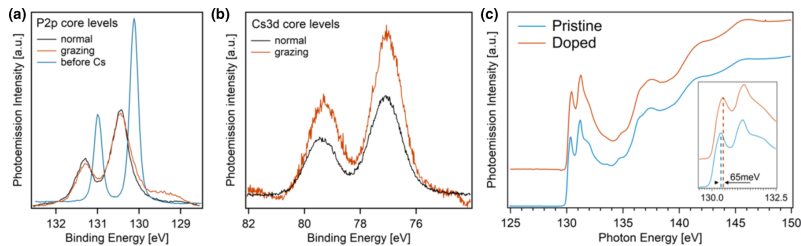


FIG. 3. (a) XPS spectra ($h\nu = 300$ eV) of the P $2p$ core levels before doping (blue) and after Cs doping (black and red). The black spectrum is for normal emission, and the red spectrum is for grazing emission. (b) Cs $3d$ core-level spectrum ($h\nu = 300$ eV) for normal emission (black) and for grazing emission (red). These two spectra are normalized to the corresponding P $2p$ core-level spectra shown in (a). (c) Near-edge x-ray absorption fine-structure spectrum of pristine (blue) and Cs-doped (red) BP measured in the total-electron-yield configuration. The inset shows that the onset of the absorption edge for doped BP is upshifted by ~ 65 meV when compared to pristine BP.

down to higher binding energy, indicating a charge transfer from Cs to P. The Cs $3d$ core levels show an increase in intensity under grazing emission when compared to P $2p$ core levels measured under identical emission angles. This is a clear indicator that Cs lies preferentially on top of the BP surface. Regarding additional evidence of the nature of the surface state, we performed measurements of the near-edge x-ray absorption fine structure (NEXAFS) and observed an upshift of ~ 65 meV in the phosphorene $2p$ absorption edge. Figure 3(c) shows the relevant spectra. The observed shift could be related to the filling of the empty (surface) states upon Cs doping. Due to Pauli blocking, the energetically lowest lying transitions in NEXAFS become forbidden. This in turn shifts the P absorption edge to higher values. This indicates that this band has partial P character.

IV. TIGHT-BINDING DESCRIPTION

A. Interlayer interaction and glide mirror symmetry

For further analysis shown in Fig. 4, we consider the sum of s - and p -polarized ARPES spectra outlined in the previous section. Figure 4(a) shows the sum of the individual spectra together with a TB calculation along the ΓY direction. Figure 4(b) depicts an energy distribution curve from Fig. 4(a) at $k_y = 0$ with two maxima as indicated, corresponding to the intensity maxima of electron- and holelike bands. Figures 4(c) and 4(d) depict the raw ARPES data and their second derivative along the ΓX crystallographic direction (the second derivative is shown to enhance the contrast of the features) together with results of the TB calculation. While the bands are parabolic along ΓY , the situation is quite different along the ΓX

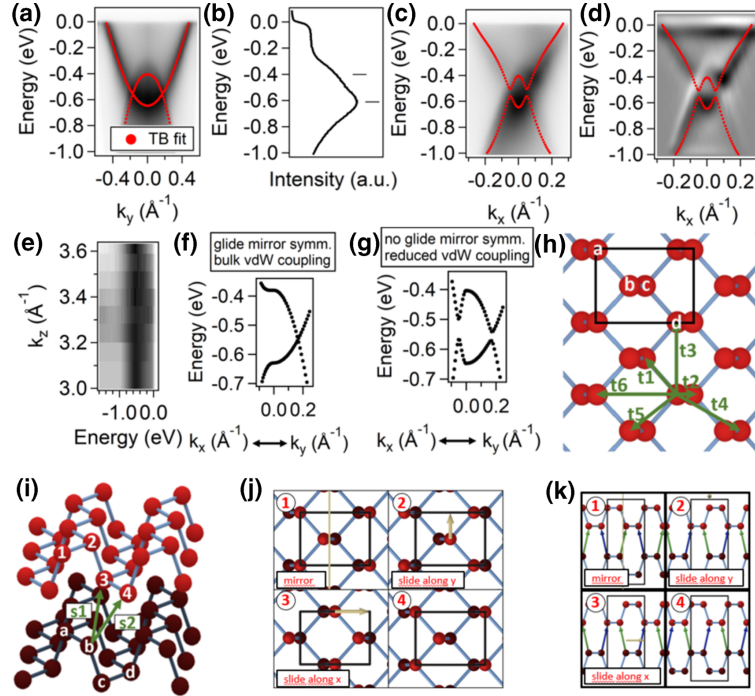


FIG. 4. (a) ARPES scans along the ΓY direction along with a tight-binding (TB) fit. (b) Energy distribution curve at $k = 0$ indicating two peaks at $E = -0.4$ eV and $E = -0.6$ eV. (c) ARPES scan along ΓX with a TB fit. (d) Second derivative of the ΓX scan overlaid on TB results. (e) k_z scan using a photon energy sweep between 15 and 40 eV and the inner potential given in Ref. [22]. (f) and (g) TB calculations assuming an out-of-plane coupling of bulk BP and a TB parametrization that breaks the glide mirror symmetry, respectively. (h) In-plane TB parameters up to the sixth nearest neighbor. (i) Nearest and next-nearest out-of-plane TB parameters. (j) Glide mirror symmetry operations for monolayer phosphorene. (k) Glide mirror symmetry operations for bilayer phosphorene. The arrows denote the nearest-neighbor out-of-plane hopping (parameter $s1$). The Supplemental Material [26] contains a video animation of the glide mirror symmetry operations.

crystallographic direction: here the bands are almost linear. Photon-energy-dependent ARPES allows us to gain information on the spatial localization of the newly found band. The results are shown in Fig. 4(e), indicating a completely flat k_z dispersion as a function of the energy (wave vector perpendicular to the surface) and thus a well-localized surface state. Note that bulk valence bands have been measured under identical conditions and were found to disperse with photon energy [22]. From the TB fit of Fig. 4(a) we directly observe a band inversion of hole- and electronlike bands close to the Γ point along the ΓY crystallographic direction at $k_Y = \pm 0.17 \text{ \AA}^{-1}$. The points where hole- and electronlike bands almost touch each other in the ΓX direction appear at $k_X = \pm 0.06 \text{ \AA}^{-1}$ [see TB fits in Figs. 4(c) and 4(d)]. If we use the out-of-plane TB parameters which accurately describe the bulk [22], the band opening along ΓX is a factor of 5 larger than the experimentally observed overlap between electron- and holelike bands. This is shown in Fig. 4(f), and it is clear that it does not agree with the experimental ARPES results along ΓX . To correctly describe ARPES data along ΓX , we resort to out-of-plane hopping parameters smaller than those for bulk BP. Reducing the parameters by one order of magnitude, we obtain results in excellent agreement with the observed ARPES spectra. The TB calculations along ΓX shown in Fig. 4(c) have been performed with these parameters. The strong decrease in out-of-plane hopping is a hint towards a decrease in the interlayer interaction and will be addressed in more detail by *ab initio* calculations shown later. Finally, let us explore the effects of glide mirror symmetry breaking. This is linked to the band crossing along ΓY , which is stable against any choice of parameters unless glide mirror symmetry is broken. We can address this issue, using TB, purposefully, e.g., by using a different coupling between symmetrically located atoms in the upper and lower layers. We break the glide mirror symmetry of the Hamiltonian by introducing different values for the next-nearest out-of-plane hopping parameters of symmetrically located hopping directions. In the example calculation shown in Fig. 4(g) we assumed a factor of 2 difference in the nearest-neighbor out-of-plane hopping and kept all other parameters equal to the TB parameters used to calculate the bands in Figs. 4(a), 4(c) and 4(d). Our calculations indicate that, indeed, a band gap in the ΓY direction is opened if we break glide mirror symmetry in this way. A video animation in the Supplemental Material illustrates that glide mirror symmetry breaking results in different TB values for the $s1$ parameter connecting atoms $b-3$ and $a-4$ [26]. Experimentally, it is not clear by how much the randomly adsorbed Cs breaks the glide mirror symmetry. Figure 4(g) thus depicts a general case of the band structure of bilayer phosphorene affected by both interlayer coupling and glide mirror symmetry breaking. This is useful not only for describing adsorption but also for describing substrate interaction in future works. The set of TB parameters which was used to calculate Fig. 4(g) is given in the Appendix. The calculations in Figs. 4(a), 4(c) and 4(d) can be reproduced with this set of TB parameters, too. The glide mirror symmetry can be restored by using only a single next-nearest-neighbor hopping as described in the Appendix.

B. Tight-binding Hamiltonian

Let us now discuss the details of the TB calculations. We have used an effective bilayer model with a different on-site potential on each layer. This method has been successfully applied previously and does not require us to account for the puckered nature of the layers (i.e., a different on-site potential *within* one phosphorene layer) [27,28]. The choice of different on-site potentials describes the effects of gating without taking into account the microscopic nature of the Cs adsorption. For a given in-plane Hamiltonian H_0 from Ref. [22] we set up a bilayer Hamiltonian by creating a block-diagonal Hamiltonian matrix with the original H_0 on the block diagonal. The on-site potentials can then be modeled by adding matrices with parameters Δ_1 and Δ_2 along their diagonal (and zero elsewhere) to H_0 . This lifts the degeneracy of the bands. The meaning of such a staggered potential is to account for a higher electron density on the topmost layer as it is in close vicinity to the positively charged Cs ions. Thus the electron energy band mainly located on the topmost layer will be downshifted with respect to the band located on the subsurface layers farther away from Cs. The interlayer interaction is introduced by an out-of-plane hopping Hamiltonian H_{oop} [22] in the off-diagonal blocks. The full Hamiltonian then becomes

$$H = \begin{bmatrix} H_0 + \Delta_1 \cdot \mathbb{1} & H_{oop} \\ H_{oop}^* & H_0 + \Delta_2 \cdot \mathbb{1} \end{bmatrix}. \quad (1)$$

The hopping parameters for the in-plane Hamiltonian H_0 and the out-of-plane Hamiltonian H_{oop} are illustrated in Figs. 1(b) and 1(i). The band inversion is a result of parameters Δ_1 and Δ_2 , which cause the shifts of valence and conduction bands.

C. Graphical representation of glide mirror symmetry

Figure 4(j) illustrates the glide mirror symmetry operations for monolayer phosphorene which involve one mirror operation and two translations by half a lattice vector along x and y , respectively. It can be seen that after application of these three operations, the original configuration is recovered. The same procedure can be applied for bilayer phosphorene, which is the basis for our model. Figure 4(k) depicts how the lattice of bilayer phosphorene changes upon application of each of the three symmetry operations and that it eventually goes back to the original lattice. In Fig. 4(k) we also illustrate that the equality of the nearest out-of-plane hopping [parameter $s1$ in Fig. 4(i)] between atoms $b-3$ and $a-4$ is protected by glide mirror symmetry. It can directly be seen that different hopping parameters between these atoms describe the violation of glide mirror symmetry. The TB calculations of Fig. 4(f) use equal values for the hopping $s1$ between atoms $b-3$ and $a-4$, and no gap opens along ΓY . On the other hand, the TB calculations of Fig. 4(g) use different hopping values of $s1$ between these two pairs of atoms. As a consequence of this symmetry breaking, a gap is opened in the ΓY direction.

V. AB INITIO CALCULATIONS

As the TB includes the effects of the Cs atoms only indirectly (via the electrostatic doping with a staggered

5.1. BAND STRUCTURE ENGINEERING IN BLACK PHOSPHORUS

N. EHLEN *et al.*

PHYSICAL REVIEW B **97**, 045143 (2018)

potential and symmetry breaking as discussed previously), it is interesting to build a microscopic model of Cs adsorbed on the BP surface. Here we perform *ab initio* calculations to calculate the ground-state geometry of Cs on the BP surface and the relative band structure. Since it is impossible to model a random distribution of Cs atoms on the surface, we settled on modeling an ordered structure of Cs atoms at the surface that reproduce the observed doping. The exact location of the Cs atoms is obtained by structural relaxation. The ordered nature of the simulated Cs doping might induce some extra symmetry breaking that may not occur in the real system with a random Cs distribution. We found that the simulations still correctly describe the effect of charge transfer from Cs to P layers and doping, which is the most important effect of the Cs deposition. We have performed an extensive *ab initio* characterization by modeling the system as a two-layer slab of BP with Cs adsorbed on one surface at the lowest-energy position obtained by energy minimization. Before settling on the description via bilayer systems, we checked several slab thicknesses with *ab initio* calculations (one of which is shown in the Appendix). However, for the relevant results (localization of the bands in the presence of stacking faults) the extra layers have negligible effects, while the added bands complicate the band structures. The resulting band structures are reported in Fig. 5 for different

stackings and dopings. In Fig. 5(a) we show the band structure for a two-layer slab with one Cs atom per surface unit cell. Although band inversion at the Γ point is nicely reproduced by our calculation, the experimentally observed band crossing along the ΓX and ΓY directions is not perfectly reproduced at any simulated doping level. In fact, a large anticrossing is always observed in the ΓX direction, and a smaller one is observed in the ΓY direction. This also occurs at any slab thickness (up to six-monolayer slabs considered in our simulations). The character of the two anticrossing bands in Fig. 5(a) is clearly seen by projecting selected (arrows in Fig. 5) Kohn-Sham wave functions $\phi_{nk}(\mathbf{r})$ with band index n at wave vector k on the phosphorus-centered atomic orbitals. The integrated wave function of the electronlike surface state indicates that this state is mostly localized on the topmost P layer with a less than 15% contribution from Cs. We can also gain information on the out-of-plane (z) profile of the projection [see inset in Fig. 5(a)]. The inverted electronlike band [indicated by an orange arrow in Fig. 5(a)] is a surface state, located on the topmost layer, with a small component located on Cs. The holelike band is located on the second layer of the bilayer simulation. However, for real systems with several layers, the holelike state extends into the bulk (see the Appendix). This nicely explains the sharper ARPES features

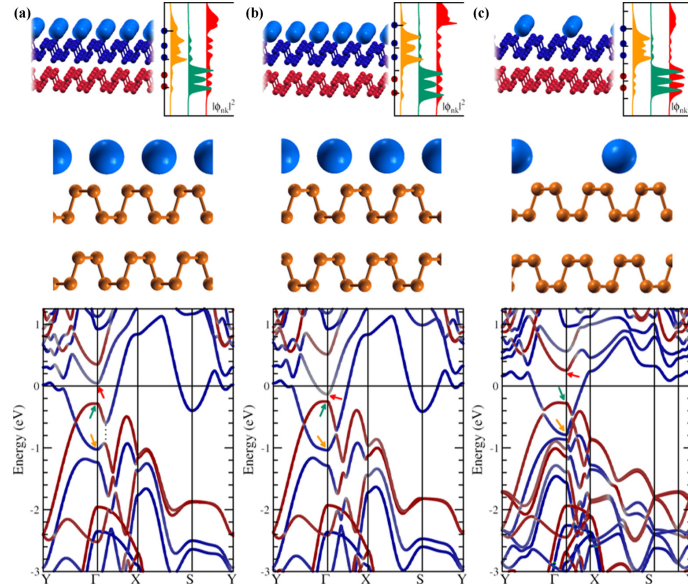


FIG. 5. Structure and electron energy bands of Cs-doped bilayer phosphorene. (a) One Cs atom per unit cell. (b) One Cs atom per unit cell with inverse stacking. (c) One Cs atom per two unit cells with inverse stacking. Colors in the band plots give the projection onto the top layer, Cs (blue), and the bottom layer (dark red). For some selected states at Γ (colored arrows) we show the $|\phi|^2$ integrated in plane and as a function of the out-of-plane coordinate z .

045143-6

for the electronlike band, which is localized only on the top layer, as opposed to the holelike band, which is delocalized over several layers, resulting in broader emission spectra. Since the electronlike band overlaps with the bulklike hole states, it is a surface resonance state. In spite of the overall different orbital character, the tails of these wave functions clearly overlap significantly, allowing a gap opening of ~ 400 meV at the crossing energies, which exceeds the experimental upper bound of 200 meV. It is evident that a refinement of the model is required in order to reproduce the observed experimental band dispersion. We find that this discrepancy can be neatly explained if we consider the possibility of a stacking fault. While the BP stacking is energetically the most favorable (we verified this even in the presence of Cs), the energy differences between different stacking orders of the phosphorene layers are extremely small (of the order of ~ 1.5 meV/atom), and many effects could alter the stacking, including impurities on the BP substrate or adsorbed Cs. Notably, a change in stacking order is a common situation in van der Waals layered materials, for example, in graphite intercalation compounds, where the typical AB (or Bernal) stacking reverts to an AA stacking upon intercalation of alkali atoms [29]. We consider a reverse stacking in which the topmost phosphorene layer is shifted along the armchair direction. The new crystal structure and the calculated band structure are shown in Fig. 5(b). This effect clearly reduces significantly the interaction between hole and electron bands and leads to a band inversion qualitatively identical to the ARPES measurements. This indicates that Cs doping can induce a modification on the BP surface, electronically detaching it from the substrate. For the unit cell shown in Fig. 5(c) the position of the Fermi level is in excellent agreement with the experiment. The band structure is also similar to the experimental one as the extra states around the S point have moved above the Fermi level. Note there is a band folding due to the larger supercell used here, so extra bands appear in the ΓX direction close to the crossing point. The new Cs positions break the glide mirror symmetry that protects the band crossing; this is why the band gap in Fig. 5(c) is opened along the ΓY direction.

VI. CONCLUSIONS AND OUTLOOK

We have shown that the adsorption of a Cs monolayer induces a surface resonance state in BP with an elliptically shaped Fermi surface and an electron density of $1.7 \times 10^{14} \text{ cm}^{-2}$. The energy-level structure is such that holelike and electronlike bands reverse their order around the Γ point of the BZ. TB modeling of the ARPES data indicates a decrease in the interlayer interaction and shows directly that the potential of a random Cs distribution and nonzero interlayer interaction will open band gaps in the ΓX and ΓY crystallographic directions. *Ab initio* calculations are in excellent agreement with the experiment if a stacking fault of the topmost layer by a shift along the armchair direction is taken into account. In this situation, the interlayer interaction decreases. These calculations also indicate that the wave functions of the electronlike and holelike bands are located on the topmost and subsurface phosphorene

layers, respectively. The discovery of a surface resonance state poses the question of whether the observed surface resonance actually hybridizes with the bulk bands or whether the system can simply be thought of as a noninteracting superposition of the surface resonance band with the bulk band. In the latter case none of the suggested topological effects would come into play. Unfortunately, the energy resolution of ARPES is too low to clearly resolve the size of the gap. Thus we have to rely on the calculations discussed above. The theoretical results indicate the hybridization of the surface state with the bulk bands and show the gap formation at the crossing points, suggesting that the physics of bulk band inversion in BP might still be applicable here. Increasing interlayer distance that reduces the out-of-plane coupling might reduce the gap size but would not fundamentally alter the existence of the gap. This poses the question of whether the gap size is sufficiently large to be physically and technologically relevant. On the edge of a phosphorene flake a spin-polarized surface state is predicted to form inside the bulk gap [17]. Thus the operation temperature of a topological FET must be such that temperature cannot excite electrons between the bulk states. The discovery of a surface band inversion that is purely induced by a layer-dependent Coulomb potential [the staggered electric field introduced in Eq. (1)] should stimulate attempts to electronically control the surface band inversion, i.e., to build a switch. For a topological FET device, one wishes to have the crossing points at the Fermi level. This might be achieved in a dual-gate geometry [17] using field-effect or ionic liquid gating. Devices based on field-effect control of the band inversion are limited by the carrier density which can be induced by field-effect gating. The carrier density n is limited by the capacitance ϵ and the dielectric strength of the gate oxide, which limits the gate voltage. We can induce a carrier density $n = \epsilon V/e$ (here e is the elementary charge, and V is the gate voltage). For $\epsilon \sim 20 \text{ nF/cm}^2$ and $V = 80 \text{ V}$ we reach $n = 10^{13} \text{ cm}^{-2}$. These values are indeed possible in experiments of standard FETs [7]. In the present work, we have achieved surface band inversion of about 300 meV separation between valence band maximum and conduction band minimum at about the tenfold carrier density. Thus we expect that surface band inversion can already be achieved at carrier concentrations lower than $n = 10^{14} \text{ cm}^{-2}$. Nevertheless, to fabricate topological FETs high ϵ gate dielectrics might be needed.

Let us now discuss the effects of relative shifts in the energy location of the band gaps along the ΓY and ΓX directions. The existence of a "clean gap" in both directions is necessary for the potential application of phosphorene in a topological FET. It should be noted that in the DFT calculations for Fig. 5(c) the band gaps visible along ΓX and ΓY are located at different energies and do not overlap. In this case it would not be possible to build a topological FET from a slab of multilayer phosphorene. However, while a similar behavior is visible in the TB calculations, the band gap along ΓY is inside the band gap along ΓX in that case. This discrepancy can be explained by the fact that small changes in the band structure can shift these band gaps relative to each other. We thus deem

the theoretical results inconclusive on the nature of the gap. Transport measurements on bulk and few-layer flakes of the material should clarify this question.

Next, it would be interesting to extend the search to other alkali metals or alkali-earth metals [30,31]. In particular, Li doping from ARPES results seems to be much weaker compared to K and Cs doping; no surface state formation or band inversion is observed in Li-doped BP. With the knowledge of the strong size variation of the Fermi surfaces for these dopants, it is interesting to note the intercalant-independent critical temperature found in alkali-metal intercalated BP [3]. The discovery of superconductivity in alkali-metal intercalated BP raises the question of whether the surface resonance state sustains superconductivity. This would call for a combined UHV spectroscopy and transport experiment in which the surface functionalization and electrical conductivity can be determined *in situ* at low temperatures as a function of alkali-metal adsorption. In this context, it is interesting to note that the measured ARPES band structure did not exhibit “kinks” as a result of electron-phonon interaction as theoretically reported [2]. Such “kinks” were measured, e.g., for alkali-metal-doped, superconducting graphene [30]. The Eliashberg function of Li-doped BP suggests a strong coupling to P- and Li-derived phonon modes up to energies of 50 meV [2]. In the present case of Cs-doped BP, we expect a large downshift of the dopant-derived phonons, rendering them unresolvable in ARPES. However, for the P-derived vibrations, no downshift is expected, and hence these vibrations could still be resolvable. Finally, the realization of a tunable 2D electron gas with different carrier densities is of fundamental interest for many applications, such as the direct coupling of surface plasmons to terahertz light, as exploited currently, e.g., in doped graphene

layers [32]; thus the current work suggests the use of BP for terahertz applications.

ACKNOWLEDGMENTS

N.E., B.V.S., A.V.F., and A.G. acknowledge ERC Grant No. 648589 “SUPER-2D” and funding from DFG project CRC 1238 (project A1) and DFG project GR 3708/2-1. The research leading to these results has received funding from the European Community’s Seventh Framework Programme (FP7/2007-2013) under Grant Agreement No. 312284 (CALIPSO). We thank Elettra for the allocation of synchrotron radiation beam time at the BaDEI/Ph beamline. The stay at the Elettra synchrotron was supported by the CERIC-ERIC consortium. The authors thank HZB BESSY II for the beam time allocation.

APPENDIX

1. Equienergy contours of the ARPES intensity

The surface band structure was mapped by ARPES in the full 2D BZ. Here we show the fourfold symmetrized raw ARPES data from which we extracted the maxima to compose the inverted Dirac cone in Fig. 2. The ARPES maxima were evaluated by scanning the ARPES intensity in the radial direction. Figure 6 depicts eight individual equienergy contours in an energy range between the Fermi level and 950 meV binding energy.

2. Tight-binding parameters

Table I shows the TB parameters used for the TB calculations shown in Fig. 4(g) of the main text. The Hamiltonian for these calculations is described in Ref. [22]. The parameters

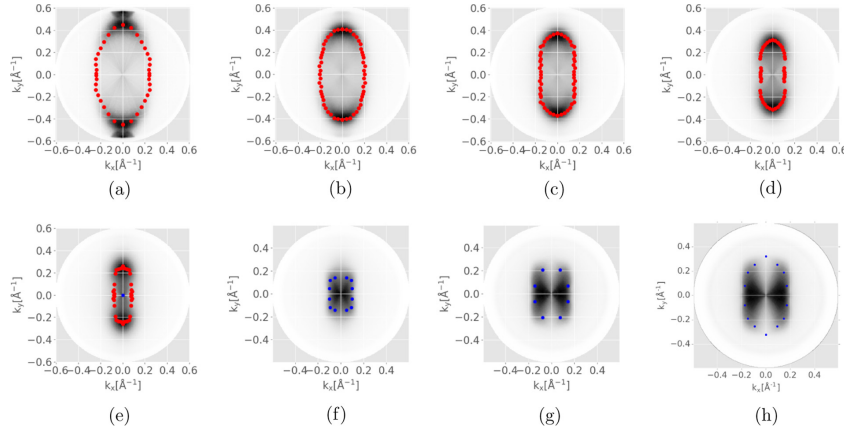


FIG. 6. Equienergy contours for (a) Fermi surface, (b) 100 meV, (c) 200 meV, (d) 300 meV, (e) 400 meV, (f) 700 meV, (g) 850 meV, and (h) 950 meV binding energy. The red and blue dots are the maxima of the electronlike and holelike bands, respectively.

TABLE I. The tight-binding parameters obtained from the fit to the ARPES data of Cs-doped BP. Figures 4(h) and 4(i) depict the hopping of $t1-t6$ and $s1$ and $s2$. By assuming different values for the first out-of-plane hopping parameter ($s1$) depending on the direction we artificially break the glide mirror symmetry that protects the band crossing. This is expressed by different hoppings between atoms $b-3$ and $a-4$. All values are in eV.

	Order	V_{ssa}	V_{spa}	V_{ppa}	$V_{pp\pi}$
In plane ($t1-t6$)	$t1$	-4.4642	0.9836	4.1682	-1.8475
	$t2$	-5.0011	3.9096	5.3775	-0.7643
	$t3$	-1.1726	1.2455	1.6278	0.1603
	$t4$	-0.4074	-0.0972	1.1678	-0.3980
	$t5$	1.0374	0.0672	0.8531	-0.5446
	$t6$	4.3436	1.6451	1.3796	-0.4215
Out of plane ($s1-s2$)	$s1$ ($b-3$)	0.0170	0.1466	0.1382	0.0462
	$s1$ ($a-4$)	0.0085	0.0733	0.0691	0.0231
	$s2$	-0.0687	0.0496	0.0056	-0.0222
On site	ϵ_s	-14.9881			
	ϵ_p	-1.2376			
Potential	Δ_1	-1.0867			
	Δ_2	-0.4199			

in Table I purposefully break the mirror glide symmetry. This is achieved by assuming a factor of 2 higher values for the nearest-neighbor out-of-plane hopping between atoms $b-3$ than for atoms $a-4$. The TB calculations shown in Figs. 4(a), 4(c) and 4(d) can be obtained by setting the out-of-plane hopping for atoms $b-3$ equal to that for atoms $a-4$.

3. Wave function localization for four-layer phosphorene

In order to investigate the localization of the wave function for the electronlike and holelike bands, we performed

ab initio calculations of the band structure for Cs monolayer adsorbed onto a four-layer phosphorene. The resulting band structure is reported in Fig. 7. The main point is that in this conventional geometry the only surface states are those of the electronlike bands with important contributions from the Cs atoms (green and blue lines in Fig. 7), while all the hole states are delocalized in the slab. This is clearly seen by observing the plots of the in-plane integrals of the Kohn-Sham orbitals $|\phi_{n\mathbf{k}}|^2$.

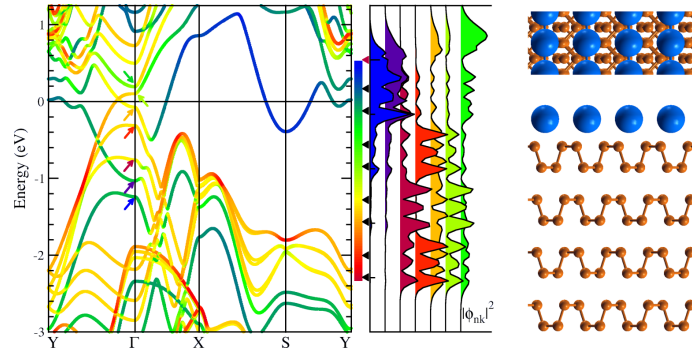


FIG. 7. Left: Band structure of a Cs-doped four-layer phosphorene in the original BP-like geometry. Colors indicate the center of mass of the states according to the color scale in the middle (where black triangles give the position of P atoms and a red triangle gives that of Cs). Middle: The xy integral of $|\phi_{n\mathbf{k}}|^2$ for selected states (shown by arrows in the band plot). Right: The crystal structure of this system.

- [1] J. Kim, S. S. Baik, S. H. Ryu, Y. Sohn, S. Park, B.-G. Park, J. Denlinger, Y. Yi, H. J. Choi, and K. S. Kim, Observation of tunable band gap and anisotropic Dirac semimetal state in black phosphorus, *Science* **349**, 723 (2015).
- [2] A. Sanna *et al.*, First-principles and angle-resolved photoemission study of lithium doped metallic black phosphorus, *2D Mater.* **3**, 025031 (2016).
- [3] R. Zhang, J. Waters, A. K. Geim, and I. V. Grigorieva, Intercalant-independent transition temperature in superconducting black phosphorus, *Nat. Commun.* **8**, 15036 (2017).
- [4] H. Liu *et al.*, Phosphorene: An unexplored 2D semiconductor with a high hole mobility, *ACS Nano* **8**, 4033 (2014).
- [5] S. P. Koenig, R. A. Doganov, H. Schmidt, A. H. Castro Neto, and B. Özyilmaz, Electric field effect in ultrathin black phosphorus, *Appl. Phys. Lett.* **104**, 103106 (2014).
- [6] L. Li *et al.*, Black phosphorus field-effect transistors, *Nat. Nanotechnol.* **9**, 372 (2014).
- [7] V. Tayari *et al.*, Two-dimensional magnetotransport in a black phosphorus naked quantum well, *Nat. Commun.* **6**, 7702 (2015).
- [8] X. Chen *et al.*, High-quality sandwiched black phosphorus heterostructure and its quantum oscillations, *Nat. Commun.* **6**, 7315 (2015).
- [9] V. Tayari, N. Hemsworth, O. Cyr-Choinière, W. Dickerson, G. Gervais, and T. Szkopek, Dual-Gate Velocity-Modulated Transistor Based on Black Phosphorus, *Phys. Rev. Appl.* **5**, 064004 (2016).
- [10] Q. Guo *et al.*, Black phosphorus mid-infrared photodetectors with high gain, *Nano Lett.* **16**, 4648 (2016).
- [11] Y. Saito and Y. Iwasa, Ambipolar insulator-to-metal transition in black phosphorus by ionic-liquid gating, *ACS Nano* **9**, 3192 (2015).
- [12] Y. Liu *et al.*, Gate-tunable giant Stark effect in few-layer black phosphorus, *Nano Lett.* **17**, 1970 (2017).
- [13] C. Han *et al.*, Surface functionalization of black phosphorus via potassium toward high-performance complementary devices, *Nano Lett.* **17**, 4122 (2017).
- [14] C. Q. Han *et al.*, Electronic structure of black phosphorus studied by angle-resolved photoemission spectroscopy, *Phys. Rev. B* **90**, 085101 (2014).
- [15] E. Golias, M. Krivenkov, and J. Sánchez-Barriga, Disentangling bulk from surface contributions in the electronic structure of black phosphorus, *Phys. Rev. B* **93**, 075207 (2016).
- [16] E. Kneeder, D. Skelton, K. E. Smith, and S. D. Kevan, Surface-State–Surface-Resonance Transition on Ta(011), *Phys. Rev. Lett.* **64**, 3151 (1990).
- [17] Q. Liu, X. Zhang, L. B. Abdalla, A. Fazzio, and A. Zunger, Switching a normal insulator into a topological insulator via electric field with application to phosphorene, *Nano Lett.* **15**, 1222 (2015).
- [18] S. Yuan, E. van Veen, M. I. Katsnelson, and R. Roldán, Quantum Hall effect and semiconductor-to-semimetal transition in biased black phosphorus, *Phys. Rev. B* **93**, 245433 (2016).
- [19] S. S. Baik, K. S. Kim, Y. Yi, and H. J. Choi, Emergence of two-dimensional massless Dirac fermions, chiral pseudospins, and Berry's phase in potassium doped few-layer black phosphorus, *Nano Lett.* **15**, 7788 (2015).
- [20] B. Ghosh, B. Singh, R. Prasad, and A. Agarwal, Electric-field tunable Dirac semimetal state in phosphorene thin films, *Phys. Rev. B* **94**, 205426 (2016).
- [21] J. Kim, S. S. Baik, S. W. Jung, Y. Sohn, S. H. Ryu, H. J. Choi, B.-J. Yang, and K. S. Kim, Two-Dimensional Dirac Fermions Protected by Space-Time Inversion Symmetry in Black Phosphorus, *Phys. Rev. Lett.* **119**, 226801 (2017).
- [22] N. Ehlen, B. V. Senkovskiy, A. V. Fedorov, A. Perucchi, P. Di Pietro, A. Sanna, G. Profeta, L. Petaccia, and A. Grüneis, Evolution of electronic structure of few-layer phosphorene from angle-resolved photoemission spectroscopy of black phosphorus, *Phys. Rev. B* **94**, 245410 (2016).
- [23] L. Petaccia *et al.*, BaDElPh: A 4 m normal-incidence monochromator beamline at Elettra, *Nucl. Instrum. Methods Phys. Res., Sect. A* **606**, 780 (2009).
- [24] X. Ling *et al.*, Anisotropic electron-photon and electron-phonon interactions in black phosphorus, *Nano Lett.* **16**, 2260 (2016).
- [25] B. Kiraly, N. Hauptmann, A. N. Rudenko, M. I. Katsnelson, and A. A. Khajetoorians, Probing single vacancies in black phosphorus at the atomic level, *Nano Lett.* **17**, 3607 (2017).
- [26] See Supplemental Material at <http://link.aps.org/supplemental/10.1103/PhysRevB.97.045143> for animations of the glide mirror symmetry operations for monolayer and bilayer phosphorene. The animation for the bilayer case contains arrows indicating the out-of-plane hopping matrix element s_1 .
- [27] K. Dolui and S. Y. Quek, Quantum-confinement and structural anisotropy result in electrically-tunable Dirac cone in few-layer black phosphorus, *Sci. Rep.* **5**, 11699 (2015).
- [28] A. N. Rudenko, S. Yuan, and M. I. Katsnelson, Toward a realistic description of multilayer black phosphorus: From *GW* approximation to large-scale tight-binding simulations, *Phys. Rev. B* **92**, 085419 (2015).
- [29] M. S. Dresselhaus and G. Dresselhaus, Intercalation compounds of graphite, *Adv. Phys.* **51**, 1 (2002).
- [30] A. V. Fedorov *et al.*, Observation of a universal donor-dependent vibrational mode in graphene, *Nat. Commun.* **5**, 4257 (2014).
- [31] N. I. Verbitskiy *et al.*, Environmental control of electron-phonon coupling in barium doped graphene, *2D Mater.* **3**, 045003 (2016).
- [32] Y. Harada *et al.*, Giant terahertz-wave absorption by monolayer graphene in a total internal reflection geometry, *ACS Photonics* **4**, 121 (2017).

5.2 Optical Properties in Heterostructures of Epitaxial Monolayer MoS₂ on Graphene/Ir(111) Substrates.

Niels Ehlen, Joshua Hall, Boris V Senkovskiy, Martin Hell, Jun Li, Alexander Herman, Dmitry Smirnov, Alexander Fedorov, Vladimir Yu Voroshnin, Giovanni Di Santo, Luca Petaccia, Thomas Michely, and Alexander Grüneis.

Narrow photoluminescence and Raman peaks of epitaxial MoS₂ on graphene/Ir(111) 2D Materials **6** 011006 (2019)

Doi: <https://doi.org/10.1088/2053-1583/aaebd3>

This publication is a result of the work leading to the author's MSc thesis [114].

As a direct band gap semiconductor, monolayer 2H-MoS₂ is a candidate for use in optical devices. However, most research in this direction for a long time was conducted on exfoliated samples. The exfoliation method is inherently limited to small sample sizes and cannot be scaled up. This is a problem for applications outside of the laboratory but also in fundamental research. Many powerful experimental methods require larger sample sizes than those produced by exfoliation. Research into bottom up large area growth of TMDs and the properties of these epitaxially grown layers is thus important. In this publication, the optical properties of epitaxially grown MoS₂-graphene heterostructures were reported.

Usually, photoluminescence in adlayers is quenched by metallic substrates, as they provide non-radiative recombination channels. Nevertheless, in this paper a PL-signal of monolayer MoS₂ on a metallic graphene/iridium(111) substrate was detected. The observation could be explained by a small interaction between adlayer and substrate. The graphene layer decoupled the epitaxially grown MoS₂ from the iridium surface. Combining experiment and theory, the exciton binding energy in the MoS₂/graphene heterostructure was extracted.

MoS₂ was grown on a metallic graphene/Ir(111) substrate using molecular beam epitaxy [4]. Investigation with scanning tunneling microscopy showed growth of mostly monolayer islands of MoS₂ with some small bilayer islands. Macroscopic alignment of the islands was confirmed using low-energy electron diffraction. XPS measurements confirmed the quality of the samples and showed a shift of the Mo3d core levels by about 0.95 eV compared to elemental molybdenum on a Gr/Ir(111) substrate. In comparison with similar measurements of MoS₂ islands on an Au(111) substrate [221], this

measurement lacked secondary components in its peak structure. The secondary peaks were attributed to metallic molybdenum clusters and contributions from the edges of the flakes in the other publications. As STM measurements revealed no molybdenum clusters on the islands, the missing of satellite peaks was attributed to the fact that no excess molybdenum was left over in the samples after formation of the MoS₂ layer. The missing edge contributions were explained by the large island size confirmed by STM. Large MoS₂ islands implied a small edge contribution compared to the contribution from the two-dimensional “bulk”. In other publications, XPS measurements of MoS₂ on a gold substrates showed an asymmetry of the sulfur 2*p* peak due to satellite peaks arising from an interaction with the gold substrate. Such an asymmetry was not visible in the present publication.

After the structural investigation, ARPES was performed on the samples. The MoS₂ bands were clearly visible, analysis of the bands at the *K*-point of MoS₂ revealed a band splitting of 144 meV. No hybridization between the MoS₂ bands and the Dirac cone of graphene could be discerned in the dispersion. Focussing on the graphene Dirac cone, a small p-type doping of graphene was found. From the Fermi surface, the hole density was determined as $p = 1.484 \times 10^{13} \text{ cm}^{-2}$. After the measurements of the pristine MoS₂ layer, the sample was doped using lithium evaporation. The doping shifted the conduction band below the Fermi level and enabled the experimental determination of the electronic band gap of Li-doped MoS₂. The size of the band gap was found to be 1.975 eV.

With the electronic structure determined, the focus was shifted to the photoluminescent properties of the structure. Temperature-dependent photoluminescence measurements revealed the appearance of a PL-peak below 170 K. Analysis of the peak showed a strongly reducing peak width with decreasing temperature. The total peak area on the other hand stayed constant throughout the cooling procedure. At 8 K, a full-width at half-maximum of 18 meV was determined, the peak was centered around 1.945 eV. Combining the experimentally determined electronic band gap of Li-doped MoS₂ with theoretical calculations on its doping dependence [39] and subtracting the energy of the photoluminescence peak, the exciton binding energy could be estimated at about 480 meV.

The appearance of a PL signal on the metallic substrate was surprising. Metallic substrates provide non-radiative recombination channels and are known for quenching the optical response of two-dimensional materials deposited atop of them. In particular, graphene is known as a good energy sink [8, 65–67]. The observation of a photoluminescence signal hence implied a low interaction between graphene and epitaxial MoS₂.

The missing satellite peaks in the XPS measurements of the sulfur $2p$ states and the missing hybridization of MoS_2 and graphene bands in ARPES supported the hypothesis of small interaction between graphene and MoS_2 . To further corroborate the hypothesis, temperature-dependent Raman spectroscopy was performed on the sample. The temperature dependence of the Raman peaks showed a different thermal expansion coefficient for the MoS_2 -islands and the Gr/Ir(111) substrate. The thermal expansion of MoS_2 was found to be close to the value for freestanding MoS_2 . In contrast, the interstitial graphene layer was confirmed to be pinned to the iridium substrate, following the thermal expansion of bulk iridium. The difference in thermal expansion between the epitaxial MoS_2 layer and graphene was used as another confirmation of low interaction between MoS_2 and graphene. The MoS_2 /graphene heterostructure can hence be thought of as a good approximation for freestanding MoS_2 . The graphene layer effectively decoupled the MoS_2 from the underlying substrate.

Contributions to this publication:

- Main authors of the publication are N. Ehlen and A. Grüneis with smaller contributions from the co-authors
 - Optimize growth of MoS_2 in our MBE-chamber
 - Record and analyze x-ray photoemission spectroscopy data
 - Record and analyze angle-resolved photoemission spectroscopy data
 - Record and analyze photoluminescence spectra
 - Record and analyze Raman spectra
 - Produce Figures 1-5, Table 1
-

5.2. OPTICAL PROPERTIES IN HETEROSTRUCTURES OF EPITAXIAL MONOLAYER MOS₂ ON GRAPHENE/IR(111) SUBSTRATES.

Publication

2D Materials

LETTER

Narrow photoluminescence and Raman peaks of epitaxial MoS₂ on graphene/Ir(1 1 1)

To cite this article: Niels Ehlen *et al*/2019 *2D Mater.* **6** 011006

View the [article online](#) for updates and enhancements.



IOP | ebooks™

Bringing you innovative digital publishing with leading voices to create your essential collection of books in STEM research.

Start exploring the collection - download the first chapter of every title for free.

This content was downloaded from IP address 134.95.7.248 on 03/05/2019 at 13:37

2D Materials



LETTER

Narrow photoluminescence and Raman peaks of epitaxial MoS₂ on graphene/Ir(1 1 1)RECEIVED
20 August 2018REVISED
18 October 2018ACCEPTED FOR PUBLICATION
26 October 2018PUBLISHED
12 November 2018Niels Ehlen^{1,6}, Joshua Hall¹, Boris V Senkovskiy¹, Martin Hell¹, Jun Li¹, Alexander Herman¹, Dmitry Smirnov², Alexander Fedorov^{1,3}, Vladimir Yu Voroshnin⁴, Giovanni Di Santo⁵, Luca Petaccia⁵, Thomas Michely¹ and Alexander Grüneis^{1,6}¹ II. Physikalisches Institut, Universität zu Köln, Zùlpicher StraÙe 77, 50937 Köln, Germany² Institute of Solid State and Materials Physics, Technische Universität Dresden, 01062 Dresden, Germany³ IFW Dresden, Helmholtzstraße 20, 01069 Dresden, Germany⁴ Helmholtz-Zentrum Berlin für Materialien und Energie, Elektronenspeicherring BESSY II, Albert-Einstein-StraÙe 15, 12489 Berlin, Germany⁵ Elettra Sincrotrone Trieste, Strada Statale 14 km 163.5, 34149 Trieste, Italy⁶ Authors to whom any correspondence should be addressed.E-mail: ehlen@ph2.uni-koeln.de (Niels Ehlen) and gruneis@ph2.uni-koeln.de (Alexander Grüneis)**Keywords:** molecular beam epitaxy, MoS₂, graphene, ARPES, photoluminescence**Abstract**

We report on the observation of photoluminescence (PL) with a narrow 18 meV peak width from molecular beam epitaxy grown MoS₂ on graphene/Ir(1 1 1). This observation is explained in terms of a weak graphene-MoS₂ interaction that prevents PL quenching expected for a metallic substrate. The weak interaction of MoS₂ with the graphene is highlighted by angle-resolved photoemission spectroscopy and temperature dependent Raman spectroscopy. These methods reveal that there is no hybridization between electronic states of graphene and MoS₂ as well as a different thermal expansion of both materials. Molecular beam epitaxy grown MoS₂ on graphene is therefore an important platform for optoelectronics which allows for large area growth with controlled properties.

1. Introduction

Following in the wake of graphene research, the optical properties of monolayer MoS₂ and related materials have stimulated intense research efforts over the last years [1–3]. The MoS₂ monolayer can take the form of 2H or 1T (1T') crystal structures [4], with the 2H phase being a two-dimensional semiconductor with a direct band gap that exhibits photoluminescence [1]. Research has shown promise for applications of MoS₂ as field effect transistors, electroluminescent devices [5, 6] and in the area of spintronics [7]. However, most progress in our understanding of this material is still based on exfoliated layers, e.g. the recently observed record narrow luminescence of 5 meV [8]. Small flake size and the inherent inability of exfoliation for scale up impedes not only scientific research using methods where a large area film with a single orientation is needed. It also precludes the development of MoS₂ based electronics.

Thus, considerable efforts have been devoted to the synthesis of large area transition metal dichalcogenides (TMDCs) on metals and insulators [9–12].

The main difficulties which are common for TMDCs grown on a substrate are island growth and the nucleation of bilayer before saturation of a complete monolayer, the existence of mirror domains and the fact that some growth approaches rely on a metallic substrate. The latter not only quenches the luminescence but also demands transferring the TMDC layer for electrical applications. For MoSe₂ grown on bilayer graphene, photoluminescence was observed [13]. However, for MoS₂, the prototypical TMDC, no such observation has been shown. A clean and scalable approach to MoS₂ and other TMDC synthesis is very low pressure chemical vapour deposition (CVD) using a catalytically active metallic substrate to support the decomposition of a sulphur containing precursor molecule. For example, simultaneous supply of Mo and H₂S molecules yields large islands and even single domain monolayer coverage of MoS₂ on Au(1 1 1) [14, 15]. However, the substantial interaction and hybridization with the metallic substrate modifies the properties of the layer substantially. This is a drawback specifically when considering potential applications in optics. Due to the low reactivity of van der Waals substrates like graphene or

5.2. OPTICAL PROPERTIES IN HETEROSTRUCTURES OF EPITAXIAL MONOLAYER MoS₂ ON GRAPHENE/IR(111) SUBSTRATES.

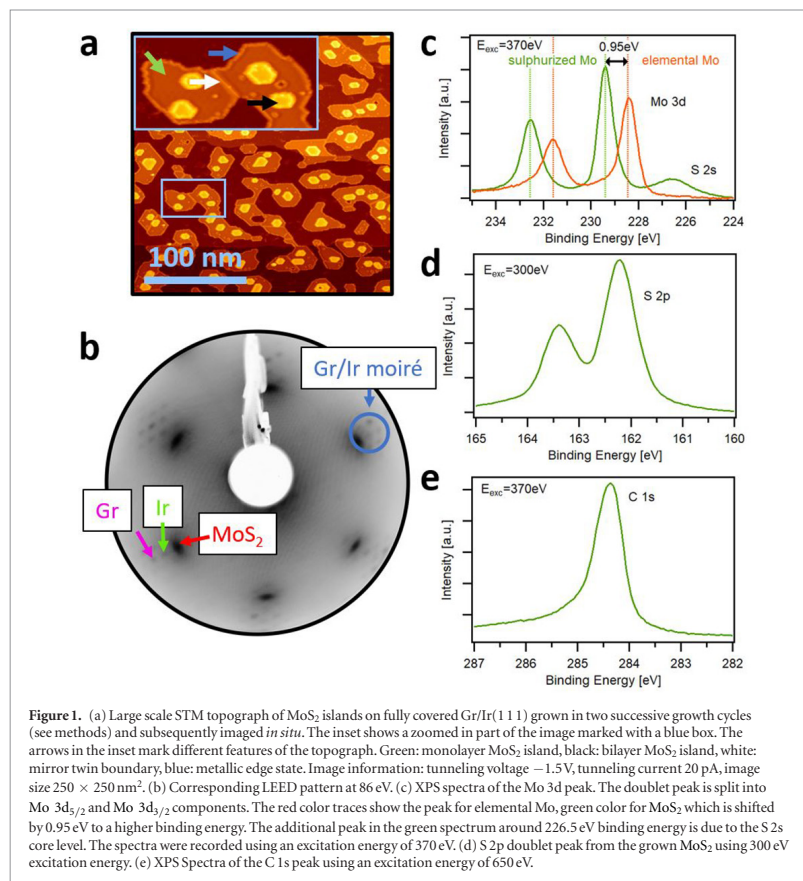


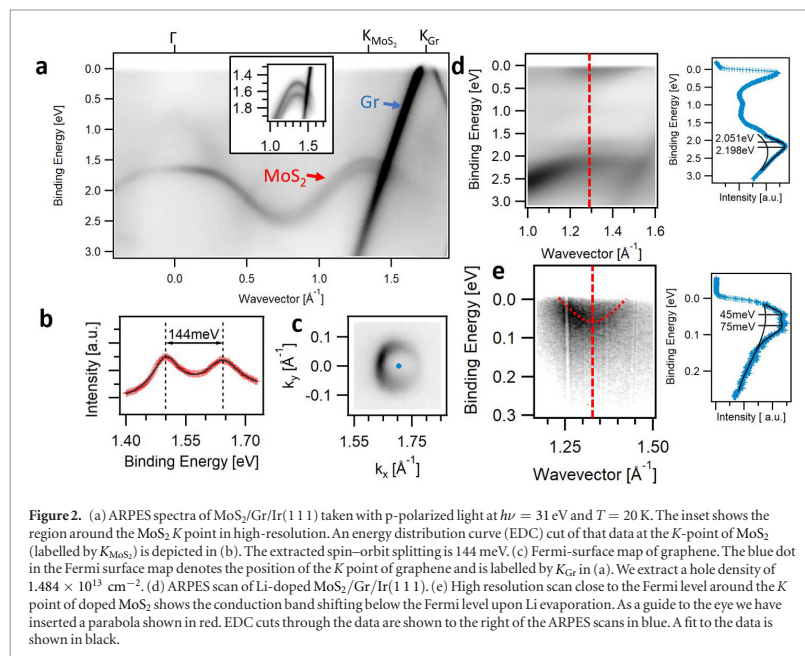
Figure 1. (a) Large scale STM topograph of MoS₂ islands on fully covered Gr/Ir(111) grown in two successive growth cycles (see methods) and subsequently imaged *in situ*. The inset shows a zoomed in part of the image marked with a blue box. The arrows in the inset mark different features of the topograph. Green: monolayer MoS₂ island, black: bilayer MoS₂ island, white: mirror twin boundary, blue: metallic edge state. Image information: tunneling voltage -1.5 V, tunneling current 20 pA, image size 250×250 nm². (b) Corresponding LEED pattern at 86 eV. (c) XPS spectra of the Mo 3d peak. The doublet peak is split into Mo 3d_{5/2} and Mo 3d_{3/2} components. The red color traces show the peak for elemental Mo, green color for MoS₂ which is shifted by 0.95 eV to a higher binding energy. The additional peak in the green spectrum around 226.5 eV binding energy is due to the S 2s core level. The spectra were recorded using an excitation energy of 370 eV. (d) S 2p doublet peak from the grown MoS₂ using 300 eV excitation energy. (e) XPS Spectra of the C 1s peak using an excitation energy of 650 eV.

hexagonal boron nitride, neither phase pure layers nor a well defined epitaxial relation could be realized up to now with such sulphur containing precursor molecules [16]. Through molecular beam epitaxy (MBE) using elemental sulphur—supplied e.g. from a valved sulphur cracker cell or from a Knudsen cell releasing elemental sulphur out of a compound like FeS₂—phase pure and epitaxial transition metal disulphide layers could be grown even on van der Waals substrates to which they are only weakly bonded [17, 18].

However, a complete spectroscopic characterization of such heterostructures is missing so far despite the fundamental interest in MoS₂ on graphene (MoS₂/Gr) e.g. as a photodetector [19]. Moreover, none of the above mentioned works on MBE grown MoS₂ reported optical (photoluminescence or Raman) characterization of the material. This is surprising because optical methods are a main tool for the investigation of exfoliated MoS₂ [3]. The lack of optical spectroscopy characterization for MBE grown

MoS₂ might be explained by the fact that these methods are less prevalent in the MBE community.

The present manuscript addresses these points and, besides structural investigation, investigates MBE-grown MoS₂ spectroscopically using x-ray photoemission spectroscopy (XPS), angle-resolved photoemission spectroscopy (ARPES) and optical (Raman and luminescence) methods. For the monolayer islands of MoS₂ epitaxially grown on a closed layer of graphene on Ir(111), as seen by scanning tunneling microscopy (STM) and low energy electron diffraction (LEED), the band structure measured by ARPES highlights the absence of any hybridization between MoS₂ and graphene. Our results reveal that the photoluminescence (PL) of MoS₂/Gr/Ir(111) is present despite the metallic substrate. We compare the optical bandgap obtained from PL measurements of the pristine MoS₂/Gr/Ir(111) system to the energy separation between valence and conduction bands of the lithium (Li) doped system that we measured using ARPES. By



careful analysis of this data and taking into account the doping induced bandgap renormalization, we estimate an exciton binding energy of 480 meV. The temperature dependence of the bond lengths in graphene and MoS₂ is probed using Raman spectroscopy. We find that the lattice expansion of graphene and MoS₂ behave completely different. Graphene's lattice expansion is dictated by the underlying Ir. The layer of MoS₂, which is not in direct contact with the Ir(111), roughly follows the lattice expansion expected for freestanding MoS₂. Our findings introduce MBE grown MoS₂/Gr as a highly ordered, epitaxial heterostructure with a sharp optical emission that can be grown in large scale.

2. Experimental results

2.1. Structure and electronic properties

Prior to the analysis of the electronic and optical properties of the MoS₂ layer, we present in figure 1 its microscopic, structural and chemical characterization. In (a), a large scale STM topograph of the MoS₂ island layer is shown. The islands rest on the Gr/Ir(111) substrate, which has two monatomic step edges crossing the topograph horizontally. A large fraction of the substrate is covered by monolayer islands (green arrow in the inset), decorated with small bilayer islands (black arrow). On both, the monolayer and the bilayer, the metallic edge state [20] surrounding the islands can be observed (blue arrow), since the bias voltage lies in the band gap of the semiconductor

MoS₂. Bright lines, running across the MoS₂ islands can be identified as (mirror) twin boundaries (white arrow) [21]. The MoS₂ islands are extremely clean with a negligible density of defects. Subfigure (b) displays a LEED pattern of the sample, indicating the epitaxial relation between the substrate and the adlayer. Going from outside to inside, the first order Gr and Ir(111) spots and their associated moiré can be seen. Farthest inside, slightly rotationally broadened first order MoS₂ diffraction spots indicate a lattice constant of $(3.13 \pm 0.03) \text{ \AA}$, in line with the literature [22]. To probe the chemical properties, XPS was performed. Figure 1(c) compares the Mo 3d core level of elemental molybdenum in red (produced by evaporating molybdenum onto the Gr/Ir(111) surface without any source for sulphur) to the grown MoS₂/Gr/Ir(111) structure in green. It can be seen that the Mo 3d core level is shifted to higher binding energy by 0.95 eV. This shift is in line with earlier observations of MoS₂ grown on a gold substrate [10]. In these previous results, a splitting of the Mo 3d core level was observed into three components (low binding-energy, mid binding-energy and high binding-energy component) [10]. In comparison, our Mo 3d peak lacks the reported low binding-energy and mid binding-energy components which are attributed to metallic Mo and Mo on the edge of a flake. For the low binding-energy peak, we attribute this to the fact that all available Mo was used up in the reaction to form MoS₂ and no elemental Mo is left over. The absence of the mid binding-energy component

can be explained by the large island size achieved in this work. This increases the ‘bulk’ versus the edge contribution to a point where the edge contribution is negligible. The sulphur 2p peak is shown in figure 1(d). Our analysis confirms the growth of crystalline MoS₂ and the absence of amorphous MoS₃ [23]. Results of MoS₂ grown on gold show an asymmetry in the S 2p peak [15] compared to the present work. This can be explained by the influence of the gold substrate on the lower sulphur layer. This asymmetry is not visible for MoS₂/Gr/Ir(111), suggesting a negligible influence of the Gr/Ir(111) substrate on the lower sulphide layer and thus a weak interaction of the substrate with the grown MoS₂ islands. As we will discuss later, this weak interaction is key to observing PL. The C 1s peak of the graphene layer is shown in figure 1(e).

Figure 2 shows angle-resolved photoemission spectroscopy (ARPES) results of the same system. An overview scan depicting the bands of graphene, MoS₂ and the Ir substrate is shown in figure 2(a). The *K* point of graphene is at $\sim 1.7 \text{ \AA}^{-1}$ and the *K* point of MoS₂ at $\sim 1.3 \text{ \AA}^{-1}$, both are indicated at the top *x*-axis. The valence band (VB) maximum of MoS₂ appears at the *K*-point consistent with monolayer MoS₂. For comparison, bilayer MoS₂ (shown in the supporting information) has the VB maximum at the Γ point. By taking the distance between the VB maximum of MoS₂ at the *K*-point to the Fermi level (approximately 1.5 eV), it suggests that the Fermi level is closer to the conduction band (CB) than to the valence band of MoS₂ as the measured electronic bandgap is typically below 2.6 eV [3]. The splitting of the VB at the MoS₂ *K*-point due to spin-orbit interaction is clearly seen in the high resolution scan shown in the inset to figure 2(a). The fit to the energy distribution curve from a cut through the MoS₂ *K*-point is shown in figure 2(b) and reveals a band splitting due to spin-orbit coupling of 144 meV. Interestingly, graphene is more hole doped than it was before MoS₂ growth, the Dirac-point binding energy is evaluated to be $E_{\text{Dirac}} = -0.25 \text{ eV}$ compared to $E_{\text{Dirac}} = -0.1 \text{ eV}$ in the pristine case [24]. The hole doping can be seen from the ARPES scans and the map shown in figures 2(a) and (c). The fact that hole doping increases after performing the MoS₂ growth on Gr/Ir(111) is also evident from a comparison to other works on Gr/Ir(111) [25, 26]. Analysis of the Fermi surface yields a hole concentration of $1.48 \times 10^{13} \text{ cm}^{-2}$. As we will see later, this hole doping is also responsible for the shift of the Raman active *G* band of Gr. Regarding the origin of the hole doping, we believe that sulphur intercalation under graphene can be excluded because we performed a test experiment where we exposed Gr/Ir to an equal amount of sulphur vapor and did not observe an increase in the hole concentration in graphene. Notably, ARPES does not show any hybridization between MoS₂ and graphene bands which supports the idea that MoS₂ is weakly interacting with Gr.

In order to measure the CB edge using ARPES, we have performed Li doping which induces an electron transfer from Li to the MoS₂ layer thereby populating its CB. Figures 2(d) and (e) show ARPES spectra of Li doped MoS₂/Gr heterostructures. The doping turns MoS₂ into a metal which is corroborated from the ARPES observation of a CB at the *K* point of MoS₂ (the CB is visible as a parabola crossing the Fermi level in figure 2(e)). Assuming a circular Fermi surface of Li-doped MoS₂, we estimate an electron concentration on the MoS₂ layer of 3.2×10^{13} electrons per cm².

The VB shifts down in energy and broadens but is otherwise unchanged. A Li induced phase transition in MoS₂ has been predicted theoretically [27, 28] and experimentally reported in Li intercalated quantum dots [29]. Interestingly, in the present system we do not observe a structural phase transition of MoS₂ to a 1T (or 1T') phase which would be visible as a different band structure in the ARPES measurements [28, 30].

An energy distribution curve (EDC) through the *K* point yields peaks for the VBs and the CBs. In order to fit these EDCs, we have constrained the VB spin-orbit coupling (SOC) to vary only within a $\pm 10 \text{ meV}$ window around 144 meV as observed for the pristine system. The resulting fits for the spin-orbit split VB maxima are shown in figure 2(d). Regarding the CB, we are unable to perform a fit with only one component. Using two components, we can obtain a good fit as shown in figure 2(d). However, the obtained splitting of 30 meV is probably not due to SOC but due to other effects such as the appearance of an extra band or linewidth broadening induced by the disorder in the Li layer. Nevertheless, since the splitting is comparably small, we can use estimate the separation between VB and CB. Taking the peak at 75 meV (CB minimum) and 2.05 eV (upper VB maximum) we find a difference that is equal to 1.975 eV. This value is similar to what has been measured in potassium intercalated monolayer MoS₂ on bulk MoS₂ where 1.86 eV was found [31]. In the next section we compare the obtained VB-CB separation to the energy of the PL to estimate a lower bound of the exciton binding energy.

The EDC curve also depicts small peaks at about 1.0 eV and 1.7 eV that appear only after Li deposition. We speculate that these could be related to either mid-gap states, Li induced defect states or polaronic bands, similar to what has been shown already [32].

2.2. Luminescent properties

Samples prepared and characterized in this way have then been transferred without exposure to air to an ultra-high-vacuum (UHV) PL/Raman system [33]. Despite the MoS₂ islands are grown on a metallic substrate we were able to detect PL at low temperatures. Figure 3(a) shows the PL spectra as the sample temperature is lowered. Besides the peak that originates from the PL a second order 2D Raman peak from graphene is seen

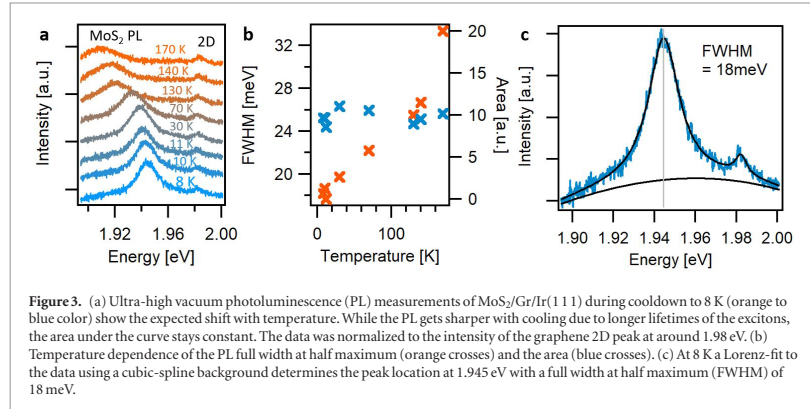


Figure 3. (a) Ultra-high vacuum photoluminescence (PL) measurements of MoS₂/Gr/Ir(111) during cooldown to 8 K (orange to blue color) show the expected shift with temperature. While the PL gets sharper with cooling due to longer lifetimes of the excitons, the area under the curve stays constant. The data was normalized to the intensity of the graphene 2D peak at around 1.98 eV. (b) Temperature dependence of the PL full width at half maximum (orange crosses) and the area (blue crosses). (c) At 8 K a Lorentz-fit to the data using a cubic-spline background determines the peak location at 1.945 eV with a full width at half maximum (FWHM) of 18 meV.

slightly above 1.98 eV. A shift towards higher energy and a narrowing of the linewidth can be observed with decreasing temperature for the PL related peak while the Raman peak of graphene is not shifting. Figure 3(b) shows the dependence of the area and FWHM of the PL peaks. The area under the PL is temperature independent suggesting that the peak becoming more prominent is due to the reduced FWHM at low temperatures. Figure 3(c) shows the PL spectrum recorded at 8 K with a maximum at $E = 1.945$ eV together with a lineshape analysis. The narrow width of 18 meV of the PL points towards a long excitonic lifetime at low temperatures. This value is smaller than the observed PL linewidth of 120 meV of CVD grown MoS₂ on graphene [9] but it is still above the record measured excitonic linewidth of 4.5 meV in hBN/MoS₂/hBN van der Waals heterostructures [8]. Despite ARPES was carried out at 20 K and PL at 8 K we believe that the spectra are comparable as the PL of MoS₂ for 10 K, 20 K and 40 K has been observed to be not discernible [34].

Next, we consider the relation between the CB-VB separation from ARPES of doped MoS₂ (1.976 eV) and the PL peak (1.945 eV). Naively (assuming that the Li doping does not affect the band gap value) one might expect that the difference between these two values (30 meV) is equal to the exciton binding energy. However, considering that the bandgap is related to the dielectric function and that doping leads to better screening, we expect a decrease of the bandgap. This has been observed for carbon nanotubes [35, 36] and graphene nanoribbons [37] and theoretically calculated for TMDCs [38, 39]. According to quasiparticle calculations, the band gap renormalization due to doping is expected to be the dominant factor that needs to be considered for the determination of exciton binding energies out of such an experiment. For example, for the present carrier concentration of $3.2 \times 10^{13} \text{ cm}^{-2}$ (as estimated by ARPES) a band gap reduction by 450 meV is predicted [39]. Ignoring this effect would therefore only yield a lower bound of the exciton binding energy. However, if we include the cal-

culated reduction of the ARPES band gap by doping (450 meV), we can estimate an exciton binding energy of about 480 meV. Indeed, this value is very similar to related experiments. Ugeda *et al* found an exciton binding energy of 550 meV for MoSe₂ on bilayer graphene on 6H-SiC(0001) by comparing PL and STS data [13]. A recent study combining ARPES and inverse photoemission of the MoS₂/Au system by Park *et al* found an exciton binding energy of 90 meV [40]. This value is considerably lower because of better screening on Au and highlights the important role of the dielectric environment. Furthermore, a decrease in the band gap upon photodoping has also been observed [41].

The appearance of PL is surprising because one would expect exciton quenching by the graphene or the metallic substrate by either Förster or Dexter transfer processes [19]. Electroluminescence of monolayer MoS₂ on a gold surface has been observed previously [42] by tunneling electrons directly into the MoS₂ via an STM tip. Experimentally it is known that the interaction between graphene and MoS₂ or semiconducting quantum dots results in luminescence quenching [19, 43, 44]. To the best of our knowledge there is no theoretical study of the mechanism of exciton quenching in the present system. However, a theoretical study of exciton quenching of luminescent molecules on graphene [45] suggests that both Förster and Dexter processes are relevant and graphene is an efficient energy sink. We speculate that the same is true for the present system.

The efficiency of luminescence quenching in exfoliated MoS₂/Gr heterostructures is reduced by the intercalation of adsorbates into the interface [19]. In the present case however, we can rule out such effects because we keep the sample always in either N₂ or high vacuum (samples were carried from the growth chamber to the UHV PL/Raman system in a vacuum suitcase or a vacuum tight N₂ container). The transferred samples still show a LEED pattern and the apparent height of the MoS₂ islands in STM is unchanged. Therefore, we believe that intercalation of adsorbates into the MoS₂/

5.2. OPTICAL PROPERTIES IN HETEROSTRUCTURES OF EPITAXIAL MONOLAYER MOS₂ ON GRAPHENE/IR(111) SUBSTRATES.

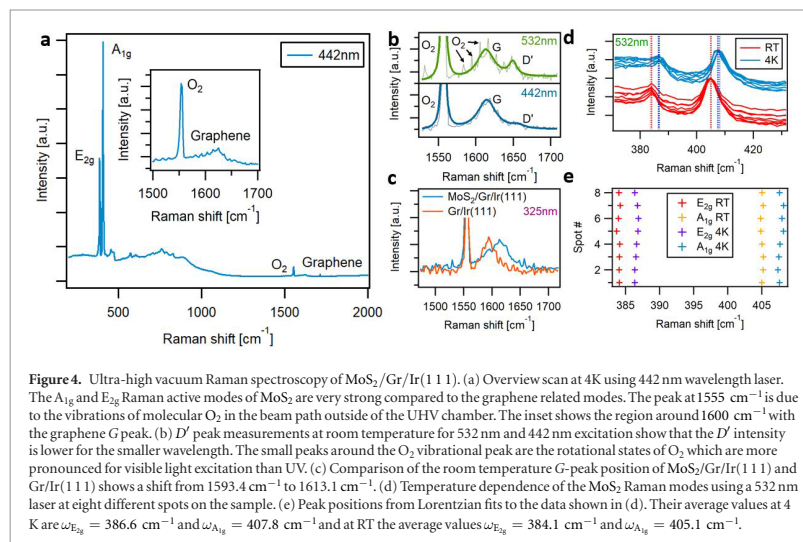


Figure 4. Ultra-high vacuum Raman spectroscopy of MoS₂/Gr/Ir(111). (a) Overview scan at 4K using 442 nm wavelength laser. The A_{1g} and E_{2g} Raman active modes of MoS₂ are very strong compared to the graphene related modes. The peak at 1555 cm⁻¹ is due to the vibrations of molecular O₂ in the beam path outside of the UHV chamber. The inset shows the region around 1600 cm⁻¹ with the graphene G peak. (b) D' peak measurements at room temperature for 532 nm and 442 nm excitation show that the D' intensity is lower for the smaller wavelength. The small peaks around the O₂ vibrational peak are the rotational states of O₂ which are more pronounced for visible light excitation than UV. (c) Comparison of the room temperature G-peak position of MoS₂/Gr/Ir(111) and Gr/Ir(111) shows a shift from 1593.4 cm⁻¹ to 1613.1 cm⁻¹. (d) Temperature dependence of the MoS₂ Raman modes using a 532 nm laser at eight different spots on the sample. (e) Peak positions from Lorentzian fits to the data shown in (d). Their average values at 4 K are $\omega_{E_{2g}} = 386.6$ cm⁻¹ and $\omega_{A_{1g}} = 407.8$ cm⁻¹ and at RT the average values $\omega_{E_{2g}} = 384.1$ cm⁻¹ and $\omega_{A_{1g}} = 405.1$ cm⁻¹.

Gr interface is not responsible for the appearance of PL. Instead, we suspect that the key for PL observation is the relatively weak graphene-MoS₂ interaction as already discussed in the context of XPS and ARPES data analysis. To learn more about this interaction, we show temperature dependent Raman spectroscopy data taken inside UHV in the next section.

2.3. Vibrational properties and strain

Raman spectra have been taken in the same experimental setup as the PL measurements inside a vacuum better than 2×10^{-10} mbar (see methods). Figure 4(a) shows an overview Raman spectrum taken at 4 K using a 442 nm excitation. The MoS₂ related phonons with A_{1g} and E_{2g} symmetry are strong in intensity compared to graphene (see inset of figure 4(a)) and have a splitting of 21 cm⁻¹. A comparison of G band Raman spectra for 442 nm and 532 nm excitation is shown in figure 4(b). A shoulder at ~ 1650 cm⁻¹ can be identified which is attributed to the D' band because its intensity is changing with laser energy [52, 53], as one can see from figure 4(b). The appearance of the D' Raman band is ascribed to translational symmetry breaking by the MoS₂ islands (see the STM image in figure 1(a)) which act as scattering centers for graphene electrons. Importantly, the graphene G band prior to MoS₂ synthesis is not visible by 442 nm and 532 nm excitation [54]. However, it can be detected using UV excitation [54]. The comparison of UV Raman spectra for Gr/Ir(111) and the MoS₂/Gr/Ir(111) heterostructure are shown in figure 4(c). A shift of G band position from 1593 cm⁻¹ (Gr/Ir) to 1613 cm⁻¹ (MoS₂/Gr/Ir) is observed. The frequency upshift by 20 cm⁻¹ can be explained by two effects that take place after growth of MoS₂. First, graphene becomes p-doped (that we have

analyzed by ARPES). The G band frequency upshift upon p-doping has been reported in the literature [54–57]. For the observed hole concentration of 1.48×10^{13} cm⁻² an upshift from the position of charge neutral graphene by ~ 18 cm⁻¹ is predicted [56]. Neglecting the small initial p-doping of Gr/Ir(111), this is in very good agreement to the observed 20 cm⁻¹ upshift. Notably, the precise value of the upshift depends also on the substrate and other works report values in the range of ~ 5 –10 cm⁻¹ [54, 55, 57]. Second, we believe that after MoS₂ growth, Gr on Ir(111) becomes flatter which leads to compressive strain in Gr. This is corroborated by the fact that the Gr/Ir(111) moiré spots in the LEED pattern become weaker after MoS₂ growth. The wavyness of the moiré can help to relax some of the strain in the Gr/Ir(111) system. However, after MoS₂ growth, as Gr becomes flatter, it also acquires compressive strain which is known to cause an upshift in the G band frequency [55, 58].

Let us now move to the investigation of temperature induced strain in the heterostructure. Raman spectroscopy is a well suited tool to investigate the change of bond length due to strain via the frequency change of Raman active vibrations. The behavior of the frequency change versus temperature yields information on how strongly bonded graphene and MoS₂ are to each other and to the substrate. For example, if both layers would follow the thermal expansion of the Ir substrate, we can assume that they are strongly bonded to each other. For graphene which is in direct contact to the Ir surface and fully covering it, one might expect that the C–C bond length follows the thermal expansion of the bulk Ir. However, the situation of MoS₂ is less obvious because it is not in direct contact to the Ir and not a complete monolayer which can make it

Table 1. The frequency of the E_{2g} and A_{1g} is denoted by ω , χ denotes the change of phonon frequency with temperature and γ the Grüneisen parameter.

Mode	ω (cm^{-1})	χ ($\text{cm}^{-1} \text{K}^{-1}$)	γ (ML)	γ (bulk)
A_{1g}	405.1 ^a , 403.0 ^b , 402.4 ^c , 408.4 ^d , 405.0 ^e	-0.013 ^f , -0.0123 ^d , -0.0143 ^e	0.21 ^e	0.21 ^g
E_{2g}	384.1 ^a , 384.5 ^b , 385.3 ^c , 382.6 ^d , 385.0 ^e	-0.011 ^f , -0.0132 ^d , -0.0179 ^e	0.65 ^e	0.42 ^g

^a This work MoS₂/Gr/Ir(111) measured at RT.

^b Lee *et al* exfoliated MoS₂ on SiO₂ [46].

^c Rice *et al* [47] have determined ω on a polymer and γ from four point bending.

^d Sahoo *et al* [48] have determined ω on SiO₂ and χ between 80 K – 473 K.

^e Najmaei *et al* [49] have determined χ in the range 300 K – 500 K.

^f Yan *et al* [50] have performed measurements of χ for suspended monolayers and found that χ for sapphire supported monolayer is similar.

^g Sugai *et al* [51].

easier to maintain a thermal expansion coefficient of its own. Figure 4(d) depicts scans at several spots on the sample performed at RT and at 4 K. It can be seen that, upon cooling the phonons harden by 2.7 cm^{-1} (the A_{1g} mode) and by 2.6 cm^{-1} (the E_{2g} mode). The temperature dependent phonon frequency is phenomenologically described as $\Delta\omega = \chi\Delta T$ where $\Delta\omega$ is the frequency shift and χ is a phonon shift per Kelvin. For MoS₂ there is a consensus in the literature that $\chi \sim -0.01 \text{ cm}^{-1} \text{K}^{-1}$ [48, 59, 60] (see table 1). Interestingly, this number is largely independent of the substrate and holds also for freestanding layers [50]. It is approximately the same for both A_{1g} and E_{2g} phonon modes. Plugging in $\Delta T \sim 290 \text{ K}$, we would expect a shift by $\Delta\omega = 3.5 \text{ cm}^{-1}$ for freestanding MoS₂ which is close to explaining the experimental value, but not in perfect agreement with the measured 2.6 cm^{-1} . Considering alternative scenarios, the other extremum is strongly substrate bound MoS₂. In this case, the phonon shift is dictated by the temperature induced substrate strain ϵ caused by the change of the substrate lattice parameter, to which MoS₂ would be pinned. This strain can be derived from the linear thermal expansion coefficient of iridium [61, 62]. We proceed by first applying this analysis to the graphene G band and then to MoS₂. The strain ϵ and the phonon shift $\Delta\omega$ are linked to each other via the Grüneisen parameter γ and the phonon mode degeneracy n as $\Delta\omega = \epsilon n \gamma \omega_0$. Here ω_0 is the phonon frequency of the unstrained system. The temperature induced strain ϵ for the Ir substrate yields $\epsilon = 0.134\%$. Plugging this into the above equation for the graphene G mode with E_{2g} symmetry and using $\omega_0 = 1593.2 \text{ cm}^{-1}$, $n = 2$, $\gamma = 2$, we obtain $\omega = 1604.1 \text{ cm}^{-1}$ (in [54] this analysis has been performed for the first time for Gr/Ir(111) and more details can be found there). Importantly, the temperature dependent upshift in ω upon cooling for the G band is in good agreement to the experiment. This implies that graphene is pinned to the Ir substrate [54].

Performing the same estimation for MoS₂ we try to obtain a value for the temperature dependent phonon energy shift. The Grüneisen parameters of monolayer MoS₂ are reported in the literature as $\gamma_{A_{1g}} = 0.21$ and $\gamma_{E_{2g}} = 0.65$ ([47]). If we now apply

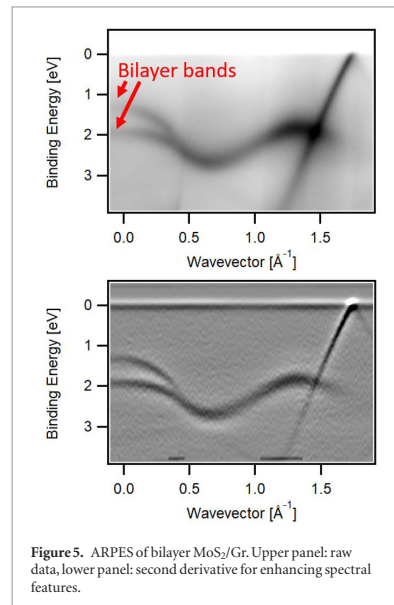


Figure 5. ARPES of bilayer MoS₂/Gr. Upper panel: raw data, lower panel: second derivative for enhancing spectral features.

the above formula, assuming that ϵ is that of the strained Ir substrate, we find $\Delta\omega_{A_{1g}} = 0.11 \text{ cm}^{-1}$ and $\Delta\omega_{E_{2g}} = 0.67 \text{ cm}^{-1}$. This does not agree with experiment at all. Notably, also using the Grüneisen parameter of bulk MoS₂ ($\gamma_{A_{1g}} = 0.21$ and $\gamma_{E_{2g}} = 0.42$ from [51]) would not improve agreement. We thus conclude that MoS₂ does not follow the thermal expansion of Ir and its behaviour is better described by the expansion expected for a freestanding monolayer. Graphene, however, is stronger interacting with the Ir substrate and its Raman shift as a function of temperature can be fully understood by the thermal expansion of the substrate. The absence of strain in MoS₂ is also consistent with our previous STM and LEED investigations [18] that display an extremely weak interaction of the MoS₂ with the substrate: entire islands can be moved by the STM tip and depending on the growth conditions, MoS₂ islands can also be grown with a broad angular

distribution on $\text{Gr}/\text{Ir}(111)$ without any measurable change of lattice parameter. Therefore strain and stress in MoS_2 can be ruled out to very good approximation.

3. Conclusion and outlook

We have characterized the epitaxially grown $\text{MoS}_2/\text{Gr}/\text{Ir}(111)$ system combining XPS, ARPES, Raman and PL measurements. STM, LEED and XPS confirm the good quality of our grown samples. We have observed a PL-signal with small FWHM suggesting a long excitonic lifetime. This surprising result is the first clear observation of photoluminescence of epitaxially grown MoS_2 on a metallic substrate. The absence of the expected quenching of the PL intensity on a metallic surface can potentially be explained by a weak interaction between the epitaxial MoS_2 and the substrate as is suggested by our XPS, ARPES and temperature dependent Raman measurements. Using Li deposition, we induced doping of MoS_2 into a degenerate semiconductor. From the analysis of ARPES data of Li doped MoS_2 we obtained the band gap. Using theoretical calculations on the band gap renormalization due to doping, we estimate an exciton binding energy of 480 meV. Our results suggest that the MoS_2 -islands are only weakly interacting with the Gr/Ir surface which could explain the absence of quenching, but the microscopic mechanisms are still unclear. Theoretical calculations for the Dexter- and Förster-type energy transfer from the islands into the graphene substrate are thus needed to quantitatively explain the observed PL. With this background it would be interesting to grow MoS_2 on hexagonal boron nitride (h-BN) using the same method as used for this work and compare FWHM and intensity of the PL. Indeed, previous experiments on h-BN capped MoS_2 [8] have shown an increase in the PL intensity upon h-BN encapsulation. Similarly, it was shown that chemical treatment of MoS_2 flakes via an organic superacid increased PL quantum yield to near unity [63], similar treatment of epitaxially grown MoS_2 monolayers might increase PL intensity even more. Regarding applications in valleytronics, it should be taken into account that the selection rules for optical absorption of circularly polarized light depend on the MoS_2 domain type regarding the inversion symmetry. Based on the MoS_2 unit cell there are two possible domain structures which are related to each other by 180° rotation. It has been shown previously that samples grown by a similar process than ours on Au exhibit preferentially one domain [15]. In our STM figure, we observe domain boundaries corroborating the existence of both domains. A detail analysis of the ratio of the two domains by circular polarized PL or x-ray photoelectron diffraction is an interesting future work. The proposed growth method might also be useful for the fabrication of photodetectors based on MoS_2/Gr heterostructure. To that end, we suggest the synthesis

of monolayer graphene which is then transferred to Si oxide. Such a sample can be used as a substrate for the growth of monolayer MoS_2 islands. After having electrically contacted graphene, light illumination with a photon energy, could efficiently excite electron-hole pairs in MoS_2 . It has been shown [19] that the proximity to graphene can lead to an efficient carrier transfer from MoS_2 to graphene. If a voltage is applied to graphene, the current measured depends on the illumination.

4. Appendix/supporting information

4.1. ARPES of bilayer MoS_2

Figure 5 depicts ARPES spectra of bilayer MoS_2 that has been grown by doubling the deposited amount of Mo. This resulted in 1.4 monolayers (ML) of MoS_2 but growth conditions were specifically tuned to induce bilayer growth via sulphur pressure in the chamber and cycled growth (see methods section). It is clear from ARPES that the VB maximum is not at the K point but at the Γ point (note the splitting of the band at Γ into two subbands, one with a higher binding energy of approximately 1.9 eV and one with a lower binding energy of approximately 1.3 eV).

5. Methods

5.1. X-ray photoemission spectroscopy

XPS was performed at the German–Russian beamline (RGLBL) of the HZB BESSY II synchrotron in Berlin (Germany) with a beam energy of 650 eV and pass energy of 20 eV in a normal emission geometry. The $\text{MoS}_2/\text{Gr}/\text{Ir}(111)$ samples were prepared *in situ* and measured in a vacuum better than 5×10^{-10} mbar.

5.2. Angle-resolved photoemission spectroscopy

ARPES was performed at the BaDElPh beamline [64] of the Elettra synchrotron in Trieste (Italy) with linear s- and p-polarisation at $h\nu = 31$ eV at temperatures of 20 K. The $\text{MoS}_2/\text{Gr}/\text{Ir}(111)$ samples were prepared *in situ* and measured in a vacuum better than 5×10^{-11} mbar. Li deposition was carried out in an ultra-high vacuum (UHV) chamber from SAES getters with the sample at 20 K. We performed stepwise evaporation of Li which we monitored by ARPES measurements of the band structure. Li evaporation was stopped after the desired doping level was reached.

5.3. Scanning tunneling spectroscopy and microscopy

Scanning tunneling microscopy was conducted in a home built variable temperature STM apparatus in Cologne at a base pressure below 8×10^{-11} mbar. For image processing the software WSxM was used [65].

5.4. Growth

We employ molecular beam epitaxy via a two-step process [18]: In the first step, with the sample held

at room temperature, Mo is evaporated at a rate of $\approx 1.4 \times 10^{16}$ atoms $\text{m}^{-2} \text{s}^{-1}$ into a S background pressure of $p \approx 5 \times 10^{-9}$ mbar onto Gr/Ir(111). The elemental S background atmosphere is achieved by heating a pyrite (FeS_2) filled crucible to ≈ 500 K. During the second step, the sample is annealed for 300 s at $T = 1050$ K in a S pressure of $p \approx 2 \times 10^{-9}$ mbar. These two steps constitute one growth cycle.

To obtain a MoS_2 layer with good orientation by epitaxy also for coverages beyond 0.4 ML the total coverage was deposited in subsequent growth cycles each yielding a coverage of ≈ 0.35 ML MoS_2 . Using this technique we realized two cycle MoS_2 samples (nominal coverage 0.7 ML) and four cycle MoS_2 samples (nominal coverage 1.4 ML).

5.5. Ultra-high vacuum Raman and photoluminescence spectroscopy

UHV Raman measurements were performed in the back-scattering geometry using commercial Raman systems (Renishaw) integrated in a homebuilt optical chamber [33], where the exciting and Raman scattered light were coupled into the vacuum using a $50\times$ long-working distance microscope objective with an NA of ~ 0.4 and a focal distance of 20.5 mm for lasers with wavelength 442 nm and 532 nm. For the UV laser, a UV compatible microscope objective has been used. The $20\times$ UV objective has a focal distance equal to 13 mm and an NA = 0.32. A sketch of our experimental setup is shown in a previous work [33]. Power densities in the range of 100 kW cm^{-2} have been employed for all laser energies. The position of the laser on the sample could be checked by a camera in the laser path. All spectra have been calibrated in position and intensity to the O_2 vibration at 1555 cm^{-1} [66].

Acknowledgments

NE, JH, AH, TM and AG acknowledge support through the CRC 1238 within project A01. NE, BVS, MH, AF and AG acknowledge the ERC grant no. 648589 ‘SUPER-2D’ and funding from DFG project GR 3708/2-1. AG acknowledges INST 216/808-1 FUGG and support from the ‘Quantum Matter and Materials’ (QM2) initiative. We thank HZB for the allocation of synchrotron radiation beamtime. NE, MH, JL and AG acknowledge support from the Horizon 2020 EC programme under Grant Agreement No. 730872 (CALIPSOplus) and from the CERIC-ERIC consortium for their stay at the Elettra synchrotron.

ORCID iDs

Joshua Hall  <https://orcid.org/0000-0002-7009-5602>
 Boris V Senkovskiy  <https://orcid.org/0000-0003-1443-6780>
 Giovanni Di Santo  <https://orcid.org/0000-0001-9394-2563>

Luca Petaccia  <https://orcid.org/0000-0001-8698-1468>

Alexander Grüneis  <https://orcid.org/0000-0003-2448-6060>

References

- [1] Mak K F, Lee C, Hone J, Shan J and Heinz T F 2010 Atomically thin MoS_2 : a new direct-gap semiconductor *Phys. Rev. Lett.* **105** 136805
- [2] Manzeli S, Ovchinnikov D, Pasquier D, Yazyev O V and Kis A 2017 2D transition metal dichalcogenides *Nat. Rev. Mater.* **2** 17033
- [3] Wang G, Chernikov A, Glazov M M, Heinz T F, Marie X, Amand T and Urbaszk B 2017 Excitons in atomically thin transition metal dichalcogenides *Rev. Mod. Phys.* **90** 21001
- [4] Chhowalla M, Shin H S, Eda G, Li L-J, Loh K P and Zhang H 2013 The chemistry of two-dimensional layered transition metal dichalcogenide nanosheets *Nat. Chem.* **5** 263
- [5] Radisavljevic B, Radenovic A, Brivio J, Giacometti V and Kis A 2011 Single-layer MoS_2 transistors *Nat. Nanotechnol.* **6** 147
- [6] Lien D-H, Amani M, Desai S B, Ahn G H, Han K, He J-H, Ager J W, Wu M C and Javey A 2018 Large-area and bright pulsed electroluminescence in monolayer semiconductors *Nat. Commun.* **9** 1229
- [7] Kim J *et al* 2017 Observation of ultralong valley lifetime in $\text{WSe}_2/\text{MoS}_2$ heterostructures *Sci. Adv.* **3** e1700518
- [8] Cadiz F *et al* 2017 Excitonic linewidth approaching the homogeneous limit in MoS_2 -based van der Waals heterostructures *Phys. Rev. X* **7** 021026
- [9] McCreary K M, Hanbicki A T, Robinson J T, Cobas E, Culbertson J C, Friedman A L, Jernigan G G and Jonker B T 2014 Large-area synthesis of continuous and uniform MoS_2 monolayer films on graphene *Adv. Funct. Mater.* **24** 6449–54
- [10] Bruix A, Führtbauer H G, Tuxen A K, Walton A S, Andersen M, Porsgaard S, Besenbacher F, Hammer B and Lauritsen J V 2015 *In situ* detection of active edge sites in single-layer MoS_2 catalysts *ACS Nano* **9** 9322–30
- [11] Kastl C *et al* 2018 Multimodal spectromicroscopy of monolayer WS_2 enabled by ultra-clean van der Waals epitaxy *2D Mater.* **5** 045010
- [12] Zhang Y *et al* 2016 Electronic structure, surface doping, and optical response in epitaxial WSe_2 thin films *Nano Lett.* **16** 2485–91
- [13] Ugeda M M *et al* 2014 Giant bandgap renormalization and excitonic effects in a monolayer transition metal dichalcogenide semiconductor *Nat. Mater.* **13** 1091
- [14] Grønberg S S, Ulstrup S, Bianchi M, Dendzik M, Sanders C E, Lauritsen J V, Hofmann P and Miwa J A 2015 Synthesis of epitaxial single-layer MoS_2 on Au(111) *Langmuir* **31** 9700
- [15] Bana H *et al* 2018 Epitaxial growth of single-orientation high-quality MoS_2 monolayers *2D Mater.* **5** 035012
- [16] Miwa J A, Ulstrup S, Sørensen S G, Dendzik M, Čabo A G, Bianchi M, Lauritsen J V and Hofmann P 2015 Electronic structure of epitaxial single-layer MoS_2 *Phys. Rev. Lett.* **114** 1–5
- [17] Fu D *et al* 2017 Molecular beam epitaxy of highly crystalline monolayer molybdenum disulfide on hexagonal boron nitride *J. Am. Chem. Soc.* **139** 9392–400
- [18] Hall J, Pielic B, Murray C, Jolie W, Wekking T, Busse C, Kralj M and Michely T 2018 Molecular beam epitaxy of quasi-freestanding transition metal disulfide monolayers on van der Waals substrates: a growth study *2D Mater.* **5** 025005
- [19] Froehlicher G, Lorchat E and Berciaud S 2018 Charge versus energy transfer in atomically thin graphene-transition metal dichalcogenide van der Waals heterostructures *Phys. Rev. X* **8** 1–15
- [20] Bollinger M V, Lauritsen J V, Jacobsen K W, Nørskov J K, Helveg S and Besenbacher F 2001 One-dimensional metallic edge states in moS_2 *Phys. Rev. Lett.* **87** 196803
- [21] Jolie W *et al* 2018 Luttinger liquid in a box: electrons confined within MoS_2 mirror twin boundaries not yet published

5.2. OPTICAL PROPERTIES IN HETEROSTRUCTURES OF EPITAXIAL MONOLAYER MoS₂ ON GRAPHENE/IR(111) SUBSTRATES.

- [22] Young P A 1968 Lattice parameter measurements on molybdenum disulfide *J. Phys. D: Appl. Phys.* **1** 936–8
- [23] Casalongue H G S *et al* 2014 Operando characterization of an amorphous molybdenum sulfide nanoparticle catalyst during the hydrogen evolution reaction *J. Phys. Chem. C* **118** 29252–9
- [24] Kralj M, Pletikosić I, Petrović M, Pervan P, Milun M, N' Diaye A T, Busse C, Michely T, Fujii J and Vobornik I 2011 Graphene on Ir(111) characterized by angle-resolved photoemission *Phys. Rev. B* **84** 075427
- [25] Pletikosić I, Kralj M, Pervan P, Brako R, Coraux J, N' Diaye A T, Busse C and Michely T 2009 Dirac cones and minigaps for graphene on Ir(111) *Phys. Rev. Lett.* **102** 056808
- [26] Starodub E, Bostwick A, Moreschini L, Nie S, Gabaly F E, McCarty K F and Rotenberg E 2011 In-plane orientation effects on the electronic structure, stability, and Raman scattering of monolayer graphene on Ir(111) *Phys. Rev. B* **83** 125428
- [27] Nasr Esfahani D, Leenaerts O, Sahin H, Partoens B and Peeters F M 2015 Structural transitions in monolayer MoS₂ by lithium adsorption *J. Phys. Chem. C* **119** 10602–9
- [28] Zheng Y, Huang Y, Shu H, Zhou X, Ding J, Chen X and Lu W 2016 The effect of lithium adsorption on the formation of 1T-MoS₂ phase based on first-principles calculation *Phys. Lett. A* **380** 1767–71
- [29] Chen W *et al* 2018 Quantum dots of 1T phase transitional metal dichalcogenides generated via electrochemical lithium intercalation *ACS Nano* **12** 308–16
- [30] He H, Lu P, Wu L, Zhang C, Song Y, Guan P and Wang S 2016 Structural properties and phase transition of Na adsorption on monolayer MoS₂ *Nanoscale Res. Lett.* **11** 330
- [31] Eknapakul T *et al* 2014 Electronic structure of a quasi-freestanding MoS₂ monolayer *Nano Lett.* **14** 1312–6
- [32] Kang M, Jung S W, Shin W J, Sohn Y, Ryu S H, Kim T K, Hoesch M and Kim K S 2018 Holstein polaron in a valley-degenerate two-dimensional semiconductor *Nat. Mater.* **17** 676–80
- [33] Grüneis A, Senkovskiy B, Fedorov A, Hell M and Michel S 2017 Ultrahigh vacuum optical spectroscopy of chemically functionalized graphene nanoribbons *Reference Module in Chemistry, Molecular Sciences and Chemical Engineering* (Amsterdam: Elsevier)
- [34] Hu Y, Zhang F, Titze M, Deng B, Li H and Cheng G J 2018 Straining effects in MoS₂ monolayer on nanostructured substrates: temperature-dependent photoluminescence and exciton dynamics *Nanoscale* **10** 5717–24
- [35] Spataru C D and Léonard F 2010 Tunable band gaps and excitons in doped semiconducting carbon nanotubes made possible by acoustic plasmons *Phys. Rev. Lett.* **104** 177402
- [36] Hartleb H, Späth F and Hertel T 2015 Evidence for strong electronic correlations in the spectra of gate-doped single-wall carbon nanotubes *ACS Nano* **9** 10461–70
- [37] Senkovskiy B V *et al* 2017 Semiconductor-to-metal transition and quasiparticle renormalization in doped graphene nanoribbons *Adv. Electron. Mater.* **3** 1600490
- [38] Gao S, Liang Y, Spataru C D and Yang L 2016 Dynamical excitonic effects in doped two-dimensional semiconductors *Nano Lett.* **16** 5568–73
- [39] Liang Y and Yang L 2015 Carrier plasmon induced nonlinear band gap renormalization in two-dimensional semiconductors *Phys. Rev. Lett.* **114** 063001
- [40] Park S, Mutz N, Schultz T, Blumstengel S, Han A, Aljarb A, Li L, List-Kratochvil E J W, Amsalem P and Koch N 2018 Direct determination of monolayer MoS₂ and WSe₂ exciton binding energies on insulating and metallic substrates *2D Mater.* **5** 025003
- [41] Pogna E A A *et al* 2016 Photo-induced bandgap renormalization governs the ultrafast response of single-layer MoS₂ *ACS Nano* **10** 1182–8
- [42] Krane N, Lotze C, Läger J M, Reecht G and Franke K J 2016 Electronic structure and luminescence of quasi-freestanding MoS₂ nanopatches on Au(111) *Nano Lett.* **16** 5163–8
- [43] Gaudreau L, Tielrooij K J, Prawiroatmodjo G E, Osmond J, De Abajo F J and Koppens F H 2013 Universal distance-scaling of nonradiative energy transfer to graphene *Nano Lett.* **13** 2030–5
- [44] Federspiel F *et al* 2015 Distance dependence of the energy transfer rate from a single semiconductor nanostructure to graphene *Nano Lett.* **15** 1252–8
- [45] Malic E, Appel H, Hofmann O T and Rubio A 2014 Förster-induced energy transfer in functionalized graphene *J. Phys. Chem. C* **118** 9283–9
- [46] Lee C, Yan H, Brus L E, Heinz T F, Hone J and Ryu S 2010 Anomalous lattice vibrations of single- and few-layer MoS₂ *ACS Nano* **4** 2695–700
- [47] Rice C, Young R J, Zan R, Bangert U, Wolverson D, Georgiou T, Jalil R and Novoselov K S 2013 Raman-scattering measurements and first-principles calculations of strain-induced phonon shifts in monolayer MoS₂ *Phys. Rev. B* **87** 1–5
- [48] Sahoo S, Gaur A P S, Ahmadi M, Guinel M J-F and Katiyar R S 2013 Temperature-dependent Raman studies and thermal conductivity of few-layer MoS₂ *J. Phys. Chem. C* **117** 9042–7
- [49] Najmaei S, Ajayan P M and Lou J 2013 Quantitative analysis of the temperature dependency in Raman active vibrational modes of molybdenum disulfide atomic layers *Nanoscale* **5** 9758–63
- [50] Yan R, Simpson J R, Bertolazzi S, Brivio J, Watson M, Wu X, Kis A, Luo T, Hight Walker A R and Xing H G 2014 Thermal conductivity of monolayer molybdenum disulfide obtained from temperature-dependent Raman spectroscopy *ACS Nano* **8** 986–93
- [51] Sugai S and Ueda T 1982 High-pressure Raman spectroscopy in the layered materials 2H-MoS₂, 2H-MoSe₂, and 2H-MoTe₂ *Phys. Rev. B* **26** 6554–8
- [52] Canado L G *et al* 2006 General equation for the determination of the crystallite size L_a of nanographite by Raman spectroscopy *Appl. Phys. Lett.* **88** 163106
- [53] Pimenta M A, Dresselhaus G, Dresselhaus M S, Canado L G, Jorio A and Saito R 2007 Studying disorder in graphite-based systems by Raman spectroscopy *Phys. Chem. Chem. Phys.* **9** 1276–90
- [54] Hell M *et al* 2018 Resonance Raman spectrum of doped epitaxial graphene at the Lifshitz transition *Nano Lett.* **18** 6045–56
- [55] Lazzeri M and Mauri F 2006 Nonadiabatic Kohn anomaly in a doped graphene monolayer *Phys. Rev. Lett.* **97** 266407
- [56] Das A *et al* 2008 Monitoring dopants by Raman scattering in an electrochemically top-gated graphene transistor *Nat. Nanotechnol.* **3** 210
- [57] Chen C-F *et al* 2011 Controlling inelastic light scattering quantum pathways in graphene *Nature* **471** 617
- [58] Mohiuddin T M G *et al* 2009 Uniaxial strain in graphene by Raman spectroscopy: g peak splitting, Grüneisen parameters, and sample orientation *Phys. Rev. B* **79** 205433
- [59] Su L, Zhang Y, Yu Y and Cao L 2014 Dependence of coupling of quasi 2-D MoS₂ with substrates on substrate types, probed by temperature dependent Raman scattering *Nanoscale* **6** 4920–7
- [60] Yang T, Huang X, Zhou H, Wu G and Lai T 2016 Excitation mechanism of A_{1g} mode and origin of nonlinear temperature dependence of Raman shift of CVD-grown mono- and few-layer MoS₂ films *Opt. Express* **24** 12281
- [61] White G K and Pawlowicz A T 1970 Thermal expansion of rhodium, iridium, and palladium at low temperatures *J. Low Temp. Phys.* **2** 631–9
- [62] Halvorson J J and Wimber R T 1972 Thermal expansion of iridium at high temperatures *J. Appl. Phys.* **43** 2519–22
- [63] Amani M *et al* 2015 Near-unity photoluminescence quantum yield in MoS₂ *Science* **350** 1065–8
- [64] Petaccia L, Vilmercati P, Gorovikov S, Barnaba M, Bianco A, Cocco D, Masciovecchio C and Goldoni A 2009 BaD EIPh: A normal-incidence monochromator beamline at Elettra *Nucl. Instrum. Methods Phys. Res. A* **606** 780–4
- [65] Horcas I, Fernandez R, Gomez-Rodriguez J, Colchero J, Gomez-Herrero J and Baro A 2007 Wsxn: a software for scanning probe microscopy and a tool for nanotechnology *Rev. Sci. Instrum.* **78** 013705
- [66] Faris G W and Copeland R A 1997 Ratio of oxygen and nitrogen Raman cross sections in the ultraviolet *Appl. Opt.* **36** 2684–5

5.3 Strained Alkali Metal Quantum Wells Synthesized on Bilayer Graphene

Niels Ehlen, Martin Hell, Giovanni Marini, Yannic Falke, Boris V. Senkovskiy, Charlotte Herbig, Christian Teichert, Wouter Jolie, Thomas Michely, Jose Avila, Giovanni Di Santo, Diego M. de la Torre, Luca Petaccia, Gianni Profeta, and Alexander Grüneis *Massive and massless charge carriers in an epitaxially strained alkali metal quantum well on graphene.*

Nature Communications **11**, 1340 (2020)

Doi: <https://doi.org/10.1038/s41467-020-15130-1>

Graphene was the first two-dimensional material produced. As such, it is the most researched 2D material in both theory and experiment. Years of optimization have lead to well established growth techniques allowing for high-quality, large-area samples. Graphene is thus an ideal platform for general investigations in Van der Waals single- and multi-layer crystals.

For monolayer graphene on iridium(111), strong Cs doping was shown to dope the crystal past the Lifshitz transition. Additionally, the Cs layers lead to a large modification of the band structure of monolayer graphene (compare appendix A.2.1.4). Similarly, the high-doping regime of bilayer graphene is interesting and not well researched. The additional carbon layer potentially changes the interaction with the adatoms significantly compared to the observed behaviour in monolayer graphene.

In the present publication, bilayer graphene was synthesized by first growing a graphene monolayer on Ir(111) using chemical vapor deposition and then evaporating carbon atoms from a carbon source using electron beam heating. The growth was monitored *in-situ* using Raman spectroscopy. The bilayer nature of the sample was confirmed afterwards using angle-resolved photoemission spectroscopy and low energy electron diffraction. The observed band structure was in line with the Bernal (AB) stacked graphene bilayer structure, showing two π -bands separated by about 320 meV in energy (compare section 2.5.2).

The bilayer structure was exposed to large amounts of caesium by evaporation from a getter (also compare appendix A.2.1.4). The amount of deposited caesium was monitored using a quartz micro balance. The Cs adlayers grew in a 2×2 superstructure and imposed a crystal potential strong enough to induce zone-folding on the electronic bands of bilayer graphene as evidenced by ARPES (compare again appendix A.2.1.4).

After doping, the bands of graphene showed a large downshift in energy. However, unlike the monolayer case, it was not possible to dope the bilayer graphene sample past the Lifshitz transition. Only one π -band was visible in ARPES scans after doping, hinting at a weakening of the interlayer interaction between the two graphene layers. Additionally, four parabolic Cs bands occurred around the Γ -point. Their dispersion was confirmed to be approximately isotropic *via* ARPES maps of the Fermi surface. A fit of the parabolic bands in order from higher to lower binding energy of the band minimum found effective masses of $m_1 = 1.0$, $m_2 = 1.0$, $m_3 = 0.8$, $m_4 = 0.6$ in units of the free electron mass. The emergence of the four parabolic Cs bands in ARPES in conjunction with the 2×2 superstructure formation were clear indications of growth of an ordered quantum well structure. As there is a correspondence between the number of bands and the number of orbitals in a unit cell, it was clear that at least four Cs atoms had to be part of the basis of the 2×2 superstructure cell. Comparing lattice parameters of the observed superstructure and bulk caesium crystals implied the formation of one individual caesium layer per Cs atom in the supercell. Consequently, at least four layers of Cs presumably were grown with the Cs evaporation procedure.

To further elucidate the grown structure, *ab-initio* density functional theory calculations were performed. From a combination of total energy considerations and a comparison of the theoretical band structures with the experimental electronic dispersion, the most likely growth structures were determined. In the determined structures, one layer of Cs intercalated between the bilayer graphene and the Ir(111) substrate, one layer of Cs intercalated between the two graphene layers and either three or four layers of Cs grew on top of the topmost graphene layer. From these results, it was clear why the interlayer interaction between both graphene layers was reduced so strongly after doping as implicated by the ARPES results. Intercalation of Cs significantly increased the interlayer distance of the two graphene layers, reducing the interlayer interaction accordingly. Comparing the lattice constant of bulk Cs with the lattice constant of the Cs layers grown atop the bilayer graphene structure in a 2×2 superstructure, the strain in the grown structure was determined to be approximately 11%.

Finally, an energy-dependent analysis of the k -space broadening of the lowest Cs quantum well band revealed a constant full width at half maximum very close to the instrument resolution for binding energies between zero and approximately 130 meV. The small FWHM confirmed the quality of the grown Cs film with low defect density. On the other hand, the missing quadratic background implied small electron-electron interactions and hence small Fermi liquid corrections (compare section 3.3). The grown structure was thus determined as a good candidate for research in two-dimensional

Fermi gases. The energy-dependent broadening additionally revealed a step-like structure around 150 meV. This behaviour is often a sign of many-body effects due to electron-phonon coupling. However, in this case it could be shown that the behaviour arose due to hybridization between the graphene and Cs bands.

The observed growth of several ordered Cs layers atop a Van der Waals material like graphene opens up new possible endeavors for producing heterostructures made up of Van der Waals materials, conventional metals, and semiconductors. Usually, metals energetically favour the formation of clusters when evaporated onto a graphene substrate. With the observation of ordered growth of Cs layers, the Cs layers could in principle be used as buffer layers to grow other metallic or semiconducting films atop graphene.

Contributions to this publication:

- Main authors of the publication are N. Ehlen, M. Hell and A. Grüneis with smaller contributions from the co-authors
 - Record and analyze angle-resolved photoemission spectroscopy data
 - Analyze band masses of Cs quantum well structure
 - Analyze zone-folding band structure
 - Record Low energy electron diffraction images
 - Analyze kink in the dispersion and interaction between Cs and C bands
 - Analyze broadening of ARPES data
 - Produce Figures 1g, 2, 4 as well as the background in Figure 3c,d,g,h
-

Publication











ARTICLE



<https://doi.org/10.1038/s41467-020-15130-1>

OPEN

Massive and massless charge carriers in an epitaxially strained alkali metal quantum well on graphene

Martin Hell^{1,7}, Niels Ehlen^{1,7}, Giovanni Marini², Yannic Falke¹, Boris V. Senkovskiy¹, Charlotte Herbig¹, Christian Teichert^{1,3}, Wouter Jolie^{1,4}, Thomas Michely¹, Jose Avila⁵, Giovanni Di Santo⁶, Diego M. de la Torre¹, Luca Petaccia⁶, Gianni Profeta² & Alexander Grüneis¹

We show that Cs intercalated bilayer graphene acts as a substrate for the growth of a strained Cs film hosting quantum well states with high electronic quality. The Cs film grows in an fcc phase with a substantially reduced lattice constant of 4.9 Å corresponding to a compressive strain of 11% compared to bulk Cs. We investigate its electronic structure using angle-resolved photoemission spectroscopy and show the coexistence of massless Dirac and massive Schrödinger charge carriers in two dimensions. Analysis of the electronic self-energy of the massive charge carriers reveals the crystallographic direction in which a two-dimensional Fermi gas is realized. Our work introduces the growth of strained metal quantum wells on intercalated Dirac matter.

¹IL Physikalisches Institut, Universität zu Köln, Zùlpicher Strasse 77, 50937 Köln, Germany. ²Department of Physical and Chemical Sciences and SPIN-CNR, University of L'Aquila, Via Vetoio 10, I-67100 Coppito, Italy. ³Institute of Physics, Montanuniversität Leoben, Franz Josef Str. 18, 8700 Leoben, Austria. ⁴Institute for Molecules and Materials, Radboud University, AJ Nijmegen, Netherlands. ⁵ANTARES Beamline, Synchrotron SOLEIL & Université Paris-Saclay, L'Orme des Merisiers, Saint Aubin-BP 48, 91192 Gif sur Yvette Cedex, France. ⁶Elettra Sincrotrone Trieste, Strada Statale 14 km 163.5, 34149 Trieste, Italy. ⁷These authors contributed equally: Martin Hell, Niels Ehlen. ✉email: hell@ph2.uni-koeln.de; ehlen@ph2.uni-koeln.de; gruneis@ph2.uni-koeln.de

Van-der-Waals heteroepitaxy¹, that is the growth of dissimilar two-dimensional (2D) materials on top of each other is a major working horse for current 2D materials science. Graphene has turned out to be an excellent substrate for van-der-Waals heteroepitaxy and the growth of transition metal dichalcogenides such as MoS₂, MoSe₂, or TaS₂ has been achieved on epitaxial monolayer graphene^{2–6}. Epitaxial growth of thin films of conventional materials such as simple metals on van-der-Waals substrates is complicated by the notoriously low wettability of van-der-Waals materials^{7–9}. Improving the wettability of graphene for adsorbed water has been achieved by doping graphene¹⁰ and changing the layer under graphene⁷. Yet, the growth techniques and the characterization of hybrid structures consisting of van-der-Waals materials and metals are unexplored. Its development can have a large impact on electronic structure engineering of 2D matter and extend growth techniques that use van-der-Waals materials as substrates. Here we introduce an epitaxial growth method for the synthesis of crystalline and strained alkali-metal films on top of bilayer graphene. Electronic structure characterization of the bilayer graphene/alkali-metal film heterostructure highlights the joint occurrence of graphene-derived Dirac Fermions and alkali metal-derived Schrödinger Fermions. The strain in the alkali-metal layer is a consequence of the lattice mismatch to graphene and the relatively high ductility of alkali metals. Graphene hosts ordered layers of alkali metals either adsorbed onto¹¹ or intercalated in between individual graphene sheets¹² or between the substrate and graphene¹³. The mechanism which dictates the alkali-metal order is the Coulomb repulsion between ionized alkali atoms. For cesium (Cs) adsorbed on or intercalated underneath monolayer graphene, a perfect order in a (2 × 2) or a ($\sqrt{3} \times \sqrt{3}$)R30° superlattice has been observed^{11,14–16}. The interaction of epitaxial bilayer graphene with Cs has revealed that, at low Cs coverages, the energetically favorable position of Cs is below the bilayer¹⁴. However, the structure and the electronic properties of the large Cs coverages on bilayer graphene are completely unexplored. The growth of a 2D alkali-metal film is interesting because it is one of the best realizations of a non-interacting 2D Fermi liquid which is termed 2D Fermi gas. A Fermi gas consists of noninteracting electrons, and therefore it is an important starting point for the study of Fermion systems upon switching on interactions. Other metals than the alkali metals do not realize a Fermi gas because of interactions, e.g., hybridization, electron–electron, and electron–phonon coupling, as evidenced by deviations from the parabolic free electron like band structure^{17,18}. A 2D alkali-metal film has a much lower electron density than other 2D metal films and hence is expected to have less deviations from the free electron like behavior. Experimentally, the degree of electron interaction can be probed by measurement of Σ , the complex-valued self-energy function, via angle-resolved photoemission spectroscopy (ARPES). In particular, $\Im\Sigma$, the imaginary part of Σ , is proportional to the photohole scattering rate. Thus, ARPES can be used to identify a realization of a Fermi gas in a 2D alkali-metal film.

In the present work we study the interaction of epitaxial bilayer graphene with high Cs coverages by performing longer Cs evaporation onto the graphene bilayer than the previous reports^{11,14,15}. In these conditions, Cs intercalates under and in between the graphene bilayer and even grows on top of bilayer as a crystalline, thin Cs film. Intercalation between the graphene layers has been reported in the literature^{12,19–21}. The Cs film that grows on top adopts a highly compressed (~11%) fcc structure which is different from the Cs bcc bulk structure. This observation is reminiscent of the phase transition of many alkali metals to an fcc structure under pressure^{22–26} which has been observed for lithium²⁷, potassium²⁸, and rubidium²⁹. Bulk Cs has been

reported to maintain the bcc structure (this phase is termed Cs-I) down to 4 K^{30,31}, and a bcc to fcc (Cs-II) structural transition has been observed at a pressure of 23.7 kbar²⁵. The additional Cs phases termed Cs-III, Cs-IV, and Cs-V appear upon further compression^{32–34}. Theoretically, *ab initio* methods predict that the Cs-I and Cs-II structures are degenerate to within several meV of energy and there is no consensus which is the structure of the ground state^{35–37}. It has been pointed out that electronic and dynamical effects are also important for the bcc to fcc structural transition^{37,38}. Moreover, the ground state structure of a thin Cs film can also be different from the bulk Cs structure. Electronic and dimensional effects on the structure highlight the usefulness of applying ARPES and *ab initio* calculations in tandem since the structure of a material is also encoded in its band structure. The ARPES investigation shows the coexistence of a series of parabolic Cs 6s derived quantum well states and a linear graphene-derived dispersion relation. The quantum well states have a very narrow energy broadening and analysis of the self-energy indicates that there are certain crystallographic directions in which the observed broadening is dominated by instrument resolution rather than quasiparticle lifetime. The vibrational structure of pristine and Cs-intercalated bilayer graphene/Ir(111) is characterized. We show how Raman spectroscopy can be used to identify epitaxial pristine and doped bilayer graphene from the position and Fano asymmetry of the Raman *G* mode of bilayer graphene.

Results and discussion

Characterization of epitaxial bilayer graphene. The low energy electron diffraction (LEED) pattern of epitaxial bilayer graphene on Ir(111) is shown in Fig. 1a and shows six diffraction spots with a very weak moiré pattern (see “Methods” section for synthesis). The six diffraction spots that correspond to bilayer graphene are sharp and hence indicate negligible azimuthal disorder. The weak moiré pattern in LEED is an interesting feature that is not observed in monolayer graphene/Ir(111) which has a pronounced moiré pattern in LEED³⁹. In the upper panel of Fig. 1b, we show a scanning tunneling microscopy (STM) topograph of a region with monolayer and bilayer domains visible. The lower panel of Fig. 1b, depicts a line profile of the height (*z*) variation of a scan across the domain boundary. The scan of the *z* profile in the bilayer domain reveals that the corrugation in the bilayer domain is at least a factor 3 larger compared with the monolayer domain which is the reason for the weak moiré pattern observed in LEED. We note that for ARPES and Raman, the synthesized sample had a complete bilayer coverage while for the STM measurements shown in Fig. 1b, the bilayer coverage was chosen about 50% (also see Supplementary Fig. 1). Figure 1c depicts an ARPES scan of bilayer graphene/Ir(111) which shows two π bands (labels π_1 and π_2) instead of one π band which is observed for monolayer graphene/Ir(111). The two observed parabolic π valence bands are consistent with Bernal (or AB) stacking⁴⁰ and in agreement with earlier reports on bilayer graphene on Ir(111)¹⁴. An equi-energy cut around the *K* point at a binding energy $E_B = 0.7$ eV is shown in Fig. 1d. For clarity, we display the second derivative of the raw ARPES data. It can be seen that the equi-energy surface consists of two concentric triangularly warped contours that are centered around the *K* point corresponding to the two π bands of bilayer graphene. In Fig. 1e, we investigate the photon energy dependence of the ARPES spectra around the *K* point of bilayer graphene for photon energies $h\nu = 30$ eV, $h\nu = 40$ eV, and $h\nu = 50$ eV using circular polarized light. Both π bands are observed for $h\nu = 40$ eV whereas for $h\nu = 30$ eV and $h\nu = 50$ eV only one π band can be observed clearly. We attribute this variation in ARPES intensity to a matrix element effect⁴¹. In Fig. 1f, we show

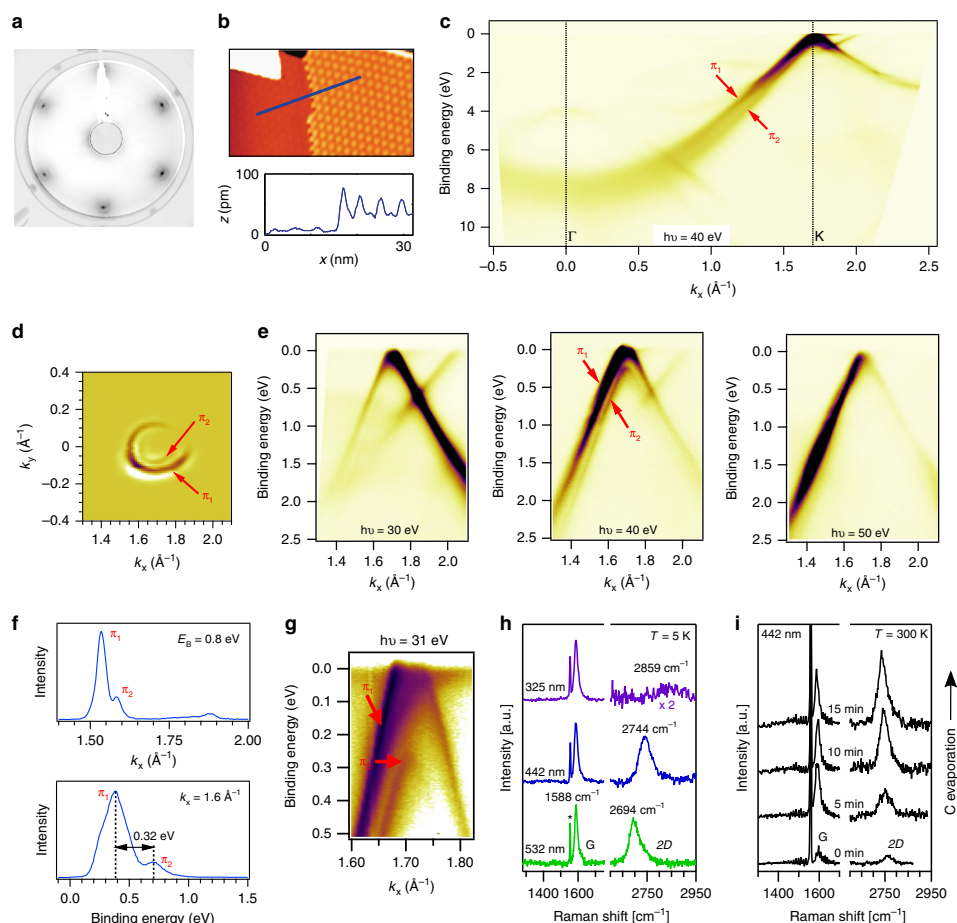


Fig. 1 Characterization of bilayer graphene/Ir(111). **a** LEED pattern ($E = 98$ eV and $T = 20$ K) and **b** upper panel: STM topograph taken at 300 K over monolayer (left) and bilayer (right) graphene on Ir(111). Lower panel: height profile along blue line in STM topograph. **c** ARPES scan along the Γ KM direction of the first Brillouin zone (BZ). Labels π_1 and π_2 indicate the two π valence bands. **d** ARPES map composed of second derivative images at a constant binding energy $E_b = 0.7$ eV as a function of 2D wavevector. **e** ARPES scans along the Γ K direction for three different values of $h\nu$ as indicated. **f** Momentum distribution curve (top) and energy distribution curve (bottom) for the $h\nu = 40$ eV ARPES scan of **e**. **c–f** are measured with circularly polarized light at $T = 70$ K. **g** ARPES scan taken with linearly p polarized light at $h\nu = 31$ eV and $T = 15$ K measured along the Γ K direction. **h** Ultra-high vacuum (UHV) Raman spectra of bilayer graphene grown in one step for three laser excitations as indicated. The G and 2D modes are indicated and the feature at 1550 cm^{-1} denoted by *** is due to O_2 in the laser path outside the UHV chamber. **i** UHV Raman spectra of initial stages of bilayer growth during step-by-step carbon deposition onto monolayer graphene, i.e., the sample was cooled to room temperature after each C evaporation cycle.

an analysis of the two π bands from the ARPES spectrum of bilayer graphene measured at $h\nu = 40$ eV. In the upper panel of Fig. 1f, a momentum dispersion curve is shown. The two indicated peaks correspond to the π bands. In the lower panel an energy distribution curve close to the K point is shown. Two peaks that are split by $\Delta E = 0.32$ eV can be observed. The splitting is in reasonable agreement to tight-binding calculations with parameters fit to graphite⁴² and to ARPES experiments with bilayer graphene on SiC⁴³ which yield a splitting of ~ 0.4 eV. In Fig. 1g, we show an observation of the π band structure using $h\nu = 31$ eV and linearly p polarized light. In these conditions, both π

bands are visible. The visibility of the second band in these conditions can be explained by the different photon energy and polarization used, as well as by the better resolution set for these measurements⁴⁴.

The Raman spectra of the bilayer graphene sample are displayed in Fig. 1h for three laser excitation wavelengths (532, 442, and 325 nm). Raman spectroscopy has been performed after growth without exposure to ambient conditions in a home-built ultra-high vacuum (UHV) Raman system^{15,45}. The observed Raman spectra of bilayer graphene in the region of the G and 2D bands show strong differences from the monolayer case

performed in identical conditions¹⁵. These differences can be used for easy identification of epitaxial bilayer graphene similar to what is routinely performed on exfoliated graphene samples. For bilayer graphene, the overall Raman intensity is increased dramatically compared with monolayer and, at particular laser energies, a strong 2D mode appears only for bilayer graphene/Ir(111)⁴⁵. We attribute the presence of a Raman signal for bilayer graphene to the larger corrugation of bilayer as discussed above. The corrugation increases the distance to the metal which implies a weaker screening of the electric field of the incident light. The Raman G band spectrum of epitaxial bilayer graphene is peaked at 1588 cm^{-1} (for $T = 5\text{ K}$). Comparing the bilayer G band peak maximum to the one of monolayer graphene/Ir(111) which is located at 1604 cm^{-1} (also for $T = 5\text{ K}$), we see that the G band of epitaxially grown bilayer graphene is downshifted by 16 cm^{-1} . The downshift of the C-C vibrational frequency in bilayer graphene points to an increase in the C-C bond length and is also consistent with the larger corrugation as observed by STM. Finally we note also that there is a small shoulder around 1630 cm^{-1} which we observe only after C evaporation onto the sample and thus we relate it to the presence of bilayer graphene.

The second-order Raman mode of epitaxial bilayer graphene appears in the region of $2500\text{--}2800\text{ cm}^{-1}$ in Fig. 1h. Unlike for epitaxial monolayer graphene on Co⁴⁶ and on Ir¹⁵ with no or very weak 2D signal, the present epitaxial bilayer graphene

sample shows a strong 2D signal when measured with blue or green light excitation (442 and 532 nm). The intensity of the 2D mode for ultraviolet (UV) excitation (325 nm) is much weaker in agreement with previous works⁴⁷.

Figure 1i shows a series of UHV Raman measurements upon the growth of bilayer graphene with stepwise C evaporation onto a monolayer graphene sample. In this experiment we have deposited C onto a heated monolayer graphene sample for a time as indicated in Fig. 1i. After each C deposition, the sample was cooled to room temperature and a Raman spectrum was taken followed by the next C deposition. The difference of this method to the method used in Fig. 1h is that the samples shown in Fig. 1h are made by one step C deposition. This series highlights that the G band and 2D band intensities and lineshapes are a highly nonlinear function of the bilayer coverage: already at low bilayer coverages we start to observe the G and 2D Raman modes. Thus, UHV Raman spectroscopy is useful to characterize the growth of epitaxial bilayer graphene on Ir(111) in situ as a quick alternative to more demanding methods such as ARPES or STM.

Cesium-derived quantum well states. Figure 2a depicts the LEED pattern of bilayer graphene/Ir(111) after evaporation of Cs. It can be seen that, in addition to the diffraction spots of bilayer graphene (cf. Fig. 1a) new spots due to the Cs lattice appear.

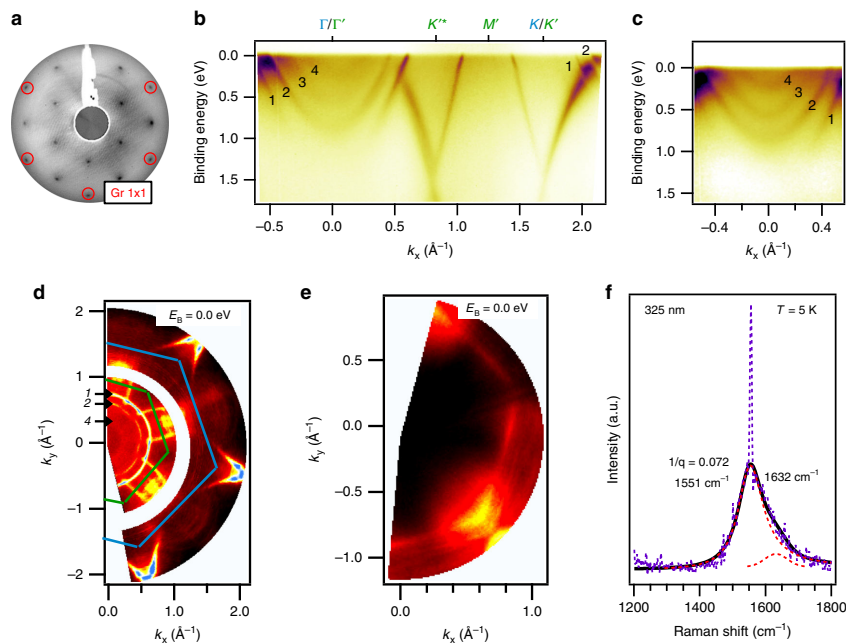


Fig. 2 Characterization of bilayer graphene/Ir(111) after evaporation of Cs. **a** LEED pattern ($E = 98\text{ eV}$ and $T = 20\text{ K}$) and **b** ARPES scan ($h\nu = 31\text{ eV}$ and $T = 17\text{ K}$) of bilayer graphene/Ir(111) with Cs evaporated onto it. The quantum well states are labeled by 1-4. **c** Zoom-in into the region around Γ that shows four parabolic Cs quantum well states (1-4). **d** ARPES map at the Fermi energy ($E_F = 0.0\text{ eV}$) of Cs-functionalized bilayer graphene. The quantum well states 1, 2, and 4 are indicated. The blue and the green partial hexagons denote the original and the zone-folded BZ, respectively. **e** Map as in **d** but before Cs deposition. **f** UHV Raman spectrum in the region of the G peak with a fit of the lineshape and the Fano parameter $1/q$. The black line is the fit to the experimental data which are in violet color and dashed. The two red dashed line profiles centered at 1551 cm^{-1} and 1632 cm^{-1} are used for the fitting. These two peaks are assigned to the graphene peak and to the feature that we observed before bilayer growth (cf. Fig. 1i and the discussion in the text), respectively.

Cs grows in a 2×2 superstructure with respect to the graphene lattice. The corrugation of bilayer graphene that we have discussed in Fig. 1a, b is significantly reduced by Cs intercalation. This is evident from previous works which measured Fourier transform scanning tunneling spectroscopy on Cs-intercalated bilayer graphene¹⁴. We believe that the flat substrate obtained by Cs intercalation is also important for the subsequent growth of Cs films. Figure 2b depicts an ARPES scan along the $\Gamma K M$ direction of the original Brillouin zone (BZ). The interesting features that can be observed from the ARPES scan are (1) a large downshift of the Dirac points corresponding to an electron doping, (2) a single π band at the K point which is broadened in the $\Gamma'K'^*$ (KM) direction, (3) a 2×2 zone folding of the band structure yielding a new Dirac cone at the K'^* point, and (4) a series of Cs-derived quantum well states located at the BZ center that cross the Fermi level (E_F). Let us now discuss observations (1)–(4) in more detail. First, the Cs doping causes a partial charge transfer of the 6s electron to graphene and thus a downshift in energy of the full band structure. Second, an important difference to the ARPES spectrum before Cs doping is that in the present case we have a single π band while before doping we have two π bands (see Fig. 1b). The disappearance of one π band means that the out-of-plane coupling between the two graphene layers ceases. We explain this by Cs intercalation in between the bilayer which is consistent with the observed Cs 2×2 order which is also observed in graphite intercalation compounds¹⁹. Third, the zone folding of the band structure is caused by the Coulomb potential of the Cs 2×2 superstructure. The zone folding of the electronic structure of graphene is similar to what we have observed recently for Cs-functionalized monolayer graphene/Ir(111)¹⁶ and what has been reported for oxygen intercalated graphene⁴⁸. Zone folding causes the appearance of a new BZ with new high-symmetry points that are labeled by Γ' , K' , K'^* , and M' that are indicated in Fig. 2b (see Fig. 1e of ref. 16 for a sketch of the zone-folded BZ). The broadening of the π conduction band of graphene along the $\Gamma'K'^*$ (KM) direction is a result of covalent bonding of C to Cs and also present in the calculations that we will show later. Fourth, a series of four quantum well states with parabolic dispersion can be observed around the Γ point. Considering the linearity of graphene related bands in Fig. 2b, we observe that the dispersion of one π branch is nonlinear in the regions of $k = 1.7 - 2.0 \text{ \AA}^{-1}$ and $k = 0.5 - 0.86 \text{ \AA}^{-1}$. However, a linear dispersion is observed in the other branch, that is for the regions of $k = 1.5 - 1.7 \text{ \AA}^{-1}$ and $k = 0.86 - 1.0 \text{ \AA}^{-1}$. Irrespective of the existence of one nonlinear branch, Dirac Fermion behavior is retained for important physical properties such as the optical properties. These are determined by the electronic states far away from the K point, i.e., by states from the nonlinear bands. In the visible spectral range, graphene absorbs about 2.3% of light, independent of the photon energy up to $\sim 3 \text{ eV}$ ⁴⁹. From Fig. 2b, it is clear that the Dirac crossing point appears at roughly 1.5 eV binding energy. This means that an optical transition induced by light of 3 eV energy involves states in the nonlinear segment of the band structure and yet results in an optical absorption governed by Dirac Fermions.

Figure 2c shows the cut through Γ at improved contrast and with the quantum well states labeled by 1–4. We performed a parabolic fit of the quantum well state dispersion measured by ARPES to extract the electron effective mass. From the fits we found that, starting from high binding energy, the masses of the sub bands 1–4 are equal to $m_1 = 1.0m_0$, $m_2 = 1.0m_0$, $m_3 = 0.8m_0$, and $m_4 = 0.6m_0$. Here m_0 is the free electron mass. Since the bottom of the parabolic band of the quantum well state 1 has a very low ARPES intensity, a parabolic fit of this band is too unreliable to draw conclusions regarding Fermi gas behavior from it. Instead, we will evaluate the self-energy of this band later in the

paper to confirm a Fermi gas behavior. The origin of the deviations from the free electron mass of quantum well states 3 and 4 could be related to zone folding of the bulk Cs band structure or the fact the Cs orbitals that make up quantum well states 3 and 4 are adjacent to graphene. Quantum well state 3 comes from Cs orbitals that belong to the first layer of Cs atoms grown on top of the bilayer and quantum well state 4 is from Cs orbitals of intercalated Cs atoms. The proximity of C and Cs orbitals can cause hybridization between them¹⁶ which is clearly visible from Fig. 2b. The hybridization of the C-derived π bands and the Cs quantum wells is clearly visible along the $\Gamma'K'^*$ direction of the π band. Importantly, we have not been able to synthesize structures with more Cs bands than observed in Fig. 2c. Figure 2d shows a 2D ARPES intensity map at constant energy $E = E_F$. In the ARPES map we observe three circular equi-energy contours around the Γ point that correspond to quantum well states 1, 2, and 4. The quantum well state 3 is not observable at E_F due to its weak intensity relative to the other features. The isotropic shape of the quantum well states in wavevector space highlights that these are free electron like states. For comparison, we show in Fig. 2e the map of pristine bilayer graphene taken in an identical configuration before Cs deposition. This reveals that the round features close to Γ are indeed Cs induced quantum well states and do not stem e.g., from Ir. Figure 2f depicts a UHV Raman spectrum of Cs-doped complete bilayer graphene (Cs doping was carried out after the Raman spectra shown in Fig. 1h were taken). The Raman G band of Cs-doped bilayer graphene has a large downshift and a Fano asymmetric shape which arises from electron doping and is in agreement to previous works on monolayer graphene^{15,16}. Performing a fit with one Fano line and one line for the feature at 1632 cm^{-1} that we identified already in the pristine bilayer samples (see Fig. 1i), we find a G band position at 1551 cm^{-1} which can be explained by the previously established relation between doping and G band frequency¹⁵.

Density functional theory (DFT). We employ DFT in order to identify the structure of the Cs/bilayer graphene system. The correct structure should fulfill two criteria. First, its energy must be within $k_B T$ to the calculated global energy minimum (k_B is the Boltzmann constant and $T = 300 \text{ K}$). Second, its band structure must be in agreement with the experimental ARPES spectra. We apply constraints regarding the possible structures that we derive from the Cs amount deposited and the Cs structure observed. We have deposited about five atomic layers of Cs onto bilayer graphene but will consider also structures with four and six Cs layers to take into account Cs loss during the intercalation and inaccuracies of the quartz microbalance. We observed a 2×2 Cs order with respect to graphene which enforces an in-plane Cs–Cs distance of 4.94 \AA . Since we observed four Cs-derived bands, it is clear that we have at least four Cs layers. More layers are possible if their Cs atoms are fully ionized and hence their bands are above E_F . Indeed, a Cs layer intercalated in between graphene and the Ir (111) substrate is fully ionized¹⁶ and the electronic band formed by these Cs orbitals is located above E_F and hence cannot be measured using ARPES. However, intercalation of a second Cs layer under graphene has not been reported and for Cs-intercalated monolayer graphene, excess Cs forms a layer on top of graphene rather than a second intercalant layer¹⁶. For the discussion of possible structures, it is convenient to adopt the following notation for the structure that consists of bilayer graphene and Cs layers which can be intercalated or adsorbed. In our notation, an $\ell m n$ system represents ℓ Cs layers intercalated in between Ir(111) and the bottom graphene layer, m Cs layers intercalated in between the two graphene layers, and n Cs layers grown on top of bilayer graphene. All Cs layers have a 2×2 Cs

order with respect to graphene. We have analyzed, using DFT, all possible ℓmn structures that fulfill the above mentioned constraints. In particular, we cast the above mentioned constraints as $\ell + m + n = 4, \dots, 6$, $\ell = 0, 1$, $m = 0, \dots, 3$, and $n = 0, \dots, 6$. Applying these constraints results in the following 24 possible ℓmn structures: $\ell mn = 004, 005, 006, 013, 014, 015, 022, 023, 024, 031, 032, 033, 103, 104, 105, 112, 113, 114, 121, 122, 123, 130, 131, \text{ and } 132$. We have systematically investigated the stability, the total energy and the electronic energy band structure of these ℓmn structures and find that the 113 phase has lowest total energy. We find that most of these structures can be excluded from being candidates that can describe the experimental results on the basis of having a too high total energy or a misfit of the electronic structure with the experiment.

The formation energy difference between any given ℓmn phase and the reference 113 configuration is defined as $E_X(\mu_{\text{Cs}}) = E_X - E_{113} - (N_X^{\text{Cs}} - N_{113}^{\text{Cs}})\mu_{\text{Cs}}$, where μ_{Cs} is the chemical potential of the Cs atom. The number of Cs atoms in the X-phase is given by N_X^{Cs} and in the ground state by N_{113}^{Cs} . In Table 1 we report ΔE_X for the six structures having lowest energy, assuming Cs-rich experimental conditions ($\mu_{\text{Cs}} = E_{\text{Cs-Bulk}}$), where $E_{\text{Cs-Bulk}}$ is the energy per atom in the stable Cs bulk phase. Varying μ_{Cs} between $E_{\text{Cs-Bulk}}$ and $E_{\text{Cs-atom}}$ (energy of an isolated Cs atom) in order to mimic Cs-rich and Cs-poor experimental conditions, we find that the 114 phase is favored for $\mu_{\text{Cs}} - E_{\text{Cs-Bulk}} > 6$ meV. Figure 3a, b depicts sketches of the 113 structure. In Fig. 3c, d, we show a comparison of the experimental ARPES spectra to calculations of the 113 electronic structure which reveals reasonable agreement to the ARPES measurements. Interestingly, the 114 band structure is in better agreement with the ARPES experiment (Fig. 3e–h depict the structure and electronic structure of the 114 phase, respectively). The Supplementary Fig. 2 contains comparisons between the DFT calculations and ARPES of several ℓmn structures.

The improved agreement to the experiment is particularly true for the Cs-derived quantum well states. Since the 114 phase has five incompletely ionized Cs layers, we obtain five calculated Cs bands. This seems to be inconsistent to the experiment at first sight since the ARPES band structure shows only four Cs quantum well states. Nevertheless, a close look to the comparison of ARPES with the calculated band structures in Fig. 3g, h reveals that only four Cs bands cross E_F and that two Cs band merge with each other below E_F . Since the photoemission intensity of the lowest energy Cs state is practically equal to zero around the Γ point, we cannot exclude the presence of a fifth Cs band in its proximity. Given the better agreement of the 114 band structure with the ARPES and the unknown experimental μ_{Cs} value, we conclude that the experimental structure is likely the 114 phase.

Thus, let us summarize our findings on the layer-by-layer intercalation of bilayer graphene with Cs. With increasing Cs

amount, the Cs will first intercalate between the bilayer graphene and the metal followed by intercalation in between the bilayer. Finally, adsorption on top of bilayer graphene will occur. From an energetic perspective, such a hierarchy of intercalation events is reasonable because intercalated Cs has a higher binding energy than adsorbed Cs. Energetically preferred intercalation of Cs was reported also for graphene monolayer/Ir¹¹ and the long-standing literature of intercalated few-layer graphene^{12,20} and graphite intercalation compounds¹⁹ have made a case that the intercalation of Cs in between the bilayer is not surprising. What is rather surprising in the present work is the fact that high-quality Cs quantum wells can be grown on top of such intercalated samples.

Wetting of bilayer graphene by Cs. Let us now discuss the reason why Cs metal grows in 2D films on bilayer graphene and does not form clusters like most other metals do. Because of their low cohesive energy, alkali metals generally possess a relatively high ratio between adhesive energy on graphene and cohesive energy (E_a/E_c)^{50,51}. This ratio is generally very low for nonalkali metals (the only notable exceptions are Nd and Sm). The low value of E_a/E_c is ultimately the reason why most of the transition metals, noble metals, and rare earth metals favor a 3D growth mode when deposited on graphene as highlighted in refs. ^{50,51}. For Cs however, this ratio is relatively higher than for other metals and also higher than for other alkali metals. In particular, the E_a of Cs on graphene is comparably high with respect to other alkali metals⁵² and its surface energy is among the lowest in the periodic table⁵³ (nonalkali metals can have up to 10–50 times higher surface energy). In fact, the bcc (110) Cs surface energy has been experimentally measured⁵⁴ to be $\approx 0.095 \text{ Jm}^{-2}$. Following the technique illustrated in ref. ⁵⁵, we calculated the surface energy of the (111) surface of fcc Cs $\gamma_{111}^{\text{fcc}} = 0.06 \text{ Jm}^{-2}$. This is the same value reported for the hexagonal (0001) surface in ref. ⁵⁵, which is not surprising given the similarity between the two stackings.

Realization of a 2D Fermi gas. The energy and wavevector dependence of $\Im\Sigma$, the imaginary part of the self-energy, of the Cs 6s derived quantum well states is analyzed in order to unravel the scattering mechanism. Figure 4a depicts a high-resolution ARPES scans of the quantum well state 1. Figure 4b depicts a scan through the ARPES intensity at a constant binding energy, i.e., a momentum distribution curve and reveals a full width at half maximum (FWHM) of $\Delta k = 0.009 \text{ \AA}^{-1}$ (or a FWHM of 0.16° in angular scale). Comparing this angular FWHM to the instrument resolution of 0.1° we see that the measured FWHM is strongly affected by the broadening induced by the instrument resolution. We now proceed to the analysis of the energy dependence of the imaginary part of the self-energy. This quantity is related to the FWHM Δk and the Fermi velocity v_F via $\Im\Sigma = v_F \Delta k$. By investigation of the energy dependence $\Im\Sigma(E)$ the various origins (e.g., impurity scattering, electron–phonon scattering, electron–electron scattering) of the lifetime broadening can be extracted. For example, impurity scattering gives a constant contribution to $\Im\Sigma(E)$, electron–phonon scattering a step-like contribution⁵⁶ and electron–electron scattering in a 2D Fermi gas has a quadratic energy dependence $\propto E^2 |\ln(E)|$ ^{56–58}. Matthiessen’s rule states that these contributions to $\Im\Sigma(E)$ are additive, and because of their distinct functional form, individual contributions can generally be extracted. For example, a detailed analysis of the strength of each of these contributions was performed, using ARPES, for the Sr₂RuO₄ compound⁵⁸. The $\Im\Sigma(E)$ for the Cs-derived quantum well state 1 (cf. Figs. 2b, c, 4a) is plotted in Fig. 4c. It can be seen that, moving away from the Fermi level, the $\Im\Sigma(E)$ is constant up to an energy of 150 meV where it suddenly increases. The constant value of $\Im\Sigma(E)$ for E

Table 1 Energy differences $\Delta E^X(\mathbf{0})$ of the six lowest energy ℓmn structures with respect to the ground state phase 113 ($\Delta E^X(\mathbf{0})$ is explained in the main text).

Structure ℓmn	$\Delta E^X(\mathbf{0})$ (eV/unit cell)
122	0.100
121	0.100
131	0.050
112	0.035
114	0.030
113	0.000

Here ℓmn denotes ℓ Cs layers intercalated in between the graphene bilayer and the substrate, m Cs layers intercalated in between the bilayer, n Cs layers adsorbed to the graphene bilayer.

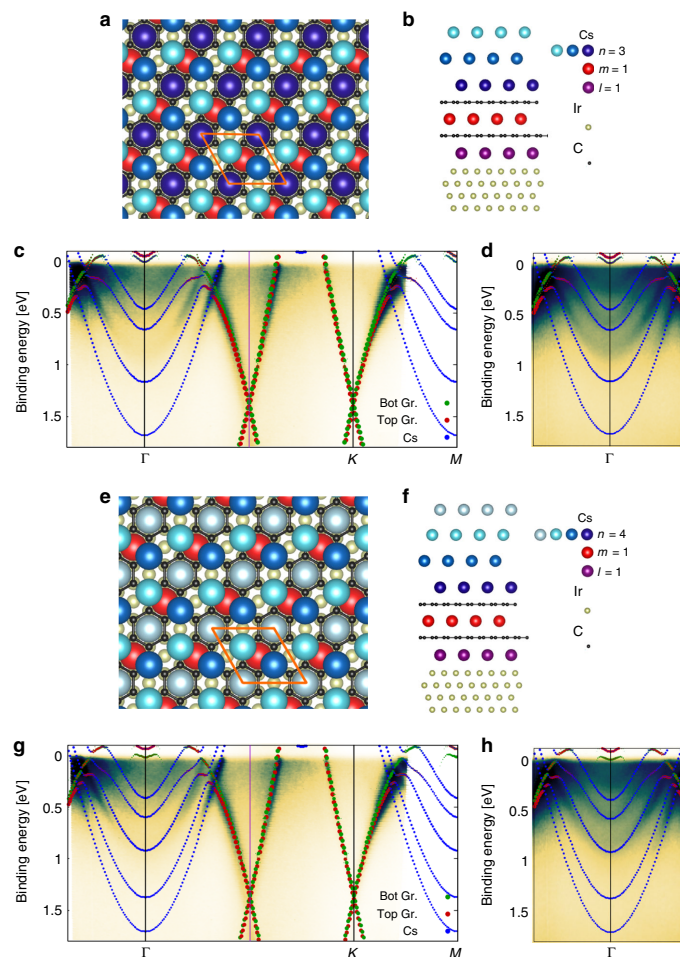


Fig. 3 Comparison of band structure calculations to ARPES experiment. **a, b** $\ell mn = 113$ structural model viewed from top and from the side. The unit cell is indicated by an orange rhombus in **a**. **c** ARPES data overlaid by the DFT calculations of the 113 structure shown in **a, b**. **d** Region of the quantum well states overlaid with the calculation with a modified color scale to **c**. **e, f** $\ell mn = 114$ structural model viewed from top and from the side. **g, h** like in **c, d** but for $\ell mn = 114$.

between the Fermi level and binding energy of 150 meV can be taken as an indication for a very weak or absent electron–electron scattering. The large energy range where $\Im\Sigma(E)$ is equal to a constant value does not exclude the inclusion of a component due to electron–electron scattering. Nevertheless, it puts an upper limit to the contribution of electron–electron scattering which we extract from the fit shown in Fig. 4c. Note, that $\Im\Sigma(E)$ of conventional metals and their surface states (e.g., Cu, Mo, and Ag⁵⁹) in a similar energy range as plotted in Fig. 4c display the typical quadratic behavior in E and a “kink” due to electron–phonon coupling. Qualitative comparison of the contribution of the electron–electron scattering term for the Sr₂RuO₄ compound⁵⁸, the surface states of conventional metals⁵⁹ and the present Cs metal quantum well state 1 suggests that the present system has

the lowest contribution of electron–electron scattering to $\Im\Sigma(E)$. The step-like behavior of $\Im\Sigma$ around 150 meV of the Cs quantum well states can in principle have two possible origins. One is that this feature looks similar to a “kink” feature that is induced by electron–phonon coupling and the other possibility is the opening of a scattering channel for photoholes to the graphene band. The graphene π band and the Cs-derived quantum well state band number 1 (see Fig. 2b) cross each other in this region of the BZ and at this energy. We hence carried out a careful ARPES investigation of this feature as a function of the electron wavevector along the α , β , γ , and δ directions in the BZ (Fig. 4e). These directions correspond to angles of 0°, 3°, 6°, and 9° with respect to the ΓK direction, respectively. Figure 4d reveals that the described “kink” feature appears at different energies for each slice α - δ .

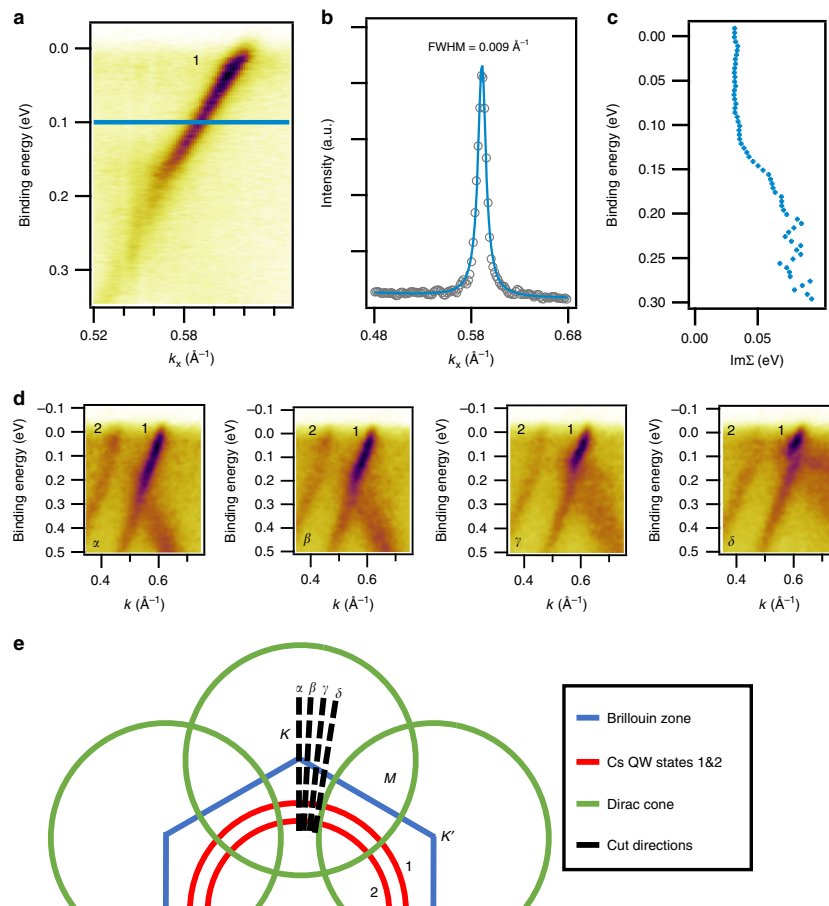


Fig. 4 Self-energy analysis of the quantum well state. **a** High-resolution ARPES scan ($h\nu = 31$ eV, $T = 20$ K) of the deepest Cs quantum well state. **b** Momentum distribution curve of the cut at $E = E_F - 0.1$ eV. **c** Imaginary part of the self-energy $\Im\Sigma(E)$ as a function of binding energy E . **d** Region where quantum well state bands 1 and 2 cross with the graphene band. Scans $\alpha - \delta$ shown are radial cuts for different angles around the Γ points in steps of 3 degrees. **e** Sketch of the Fermi surface and the cuts $\alpha - \delta$ of **d**.

Inspecting its energy location, it can be seen that it appears at the crossing point between the graphene band and the band of the quantum well state 1. We hence attribute this feature to the interaction of the Cs quantum well state with the graphene band rather than to electron-phonon coupling. The sketch in Fig. 4e depicts the Fermi surface with the Cs-derived quantum well states and the graphene-derived Dirac cones. It can be seen that along TK (cut α) the quantum well states and the Dirac cones do not cross at E_F . Therefore, the carriers along the TK direction have a weak scattering rate and this direction corresponds to the realization of a Fermi gas. For the other cuts β - δ , the crossing point between the quantum well states and the Dirac cone moves up towards the Fermi energy and scattering of quantum well states at E_F increases which can be seen from the width of the quantum well states in the ARPES experiment shown in Fig. 4d. We have also performed an analysis of the self-energy of quantum well

state 2 which is shown in the Supplementary Fig. 3. We find that $\Im\Sigma(E)$ of quantum well state 2 is significantly higher at all investigated energies E . In particular, for binding energies $E < 100$ meV, the $\Im\Sigma(E)$ of quantum well state 2 is equal to 150 meV. This value has to be compared with an $\Im\Sigma(E) \sim 30$ meV for quantum well state 1 in the same energy range. The larger $\Im\Sigma(E)$ of quantum well state 2 can be attributed to the larger scattering rate in this band due to hybridization with C states (cf. Fig. 3).

Conclusions and outlook. In conclusion, we have prepared Cs-intercalated epitaxial bilayer graphene and used it as a substrate for the growth of epitaxially strained Cs quantum wells. This material system is a realization of a vertical heterostructure between a layered material and a metal quantum well. The well-ordered growth of Cs is understood from the improved flatness of

bilayer graphene after Cs intercalation and the energy balance of the Cs surface free energy and the adhesion energy to intercalated bilayer graphene. A Cs layer forms on the intercalated bilayer graphene if the surface free energy of Cs metal is smaller than the adhesion energy to the intercalated bilayer substrate. In this case, the Cs metal can wet the intercalated bilayer graphene and an ordered thin film can grow. We have also computed the surface energy of the fcc Cs(111) surface and found that it has a very low value compared with other metals. Furthermore, alkali metals are very soft materials, and in particular Cs has a very low bulk modulus^{35,37,60} ($B_0 \approx 2$ GPa). This allows Cs to match the graphene lattice parameter with an 11% in-plane compressive strain. While we can understand from these arguments why alkali metals can wet the substrate, one would expect that a Cs layer forms equally well on monolayer graphene. Nevertheless, we have not been able to grow an ordered Cs thin film on monolayer graphene under the same conditions. We thus speculate this could be related to the adhesion energy which might be lower for the monolayer. This could be due to the fact that Cs intercalates in a $\sqrt{3} \times \sqrt{3}$ pattern under graphene which does not form a commensurate superstructure with the observed Cs 2×2 film that grows on top of graphene.

Performing ARPES, we investigated the electronic structure and found quantum well states with a parabolic electron energy dispersion coming from the Cs 6s electrons as well as a Dirac like dispersion of the π electrons of graphene. The electronic structure of this heterostructure thus hosts both, Schrödinger and Dirac like charge carriers. By analyzing the ARPES data we have found that the linewidth of the Cs bands is extremely narrow and $\Im\Sigma(E)$ is constant as a function of binding energy E until the value of E which corresponds to the crossing point of the quantum well state and the Dirac cone. At the crossing point, the lifetime of the carriers decreases (revealed by an increase of $\Im\Sigma$) because of hybridization between the Cs and C bands. The sharpness of the quantum well state bands is a result of the low electron density and the constant value of $\Im\Sigma(E)$ points towards a small contribution of the electron–electron scattering suggesting that this system is a realization of a 2D Fermi gas. Regarding further photoemission experiments, we expect that this system is suitable for laser ARPES measurements employing the commonly used $h\nu = 6.05$ eV. The Cs quantum well state 4 (see Fig. 2c) has a Fermi wavevector $\sim 0.2 \text{ \AA}^{-1}$, similarly to the Cu(111) surface state that was probed using this laser source. Thus, part of the observed ARPES spectra could also be measured by laser ARPES. Such a laser ARPES experiment would benefit from better spatial, energy and momentum resolution as compared with the synchrotron light source used here. This experiment could therefore be useful for the investigation of fine details in the quantum well states such as electron–phonon coupling and spin–orbit interactions.

We believe that the Cs/bilayer graphene heterostructure which we have synthesized can serve as a substrate to grow quantum wells made of conventional metals and semiconductors on top. The role of Cs would be crucial in such an experiment since it could provide the large adhesion energy needed so that the conventional metal or semiconductor wets the surface. The large adhesion energy could come from deposited metals that form alloys with Cs. For example, Cs forms a well-studied alloy with Au⁶¹ and an interesting future experiment could therefore be to grow Au on top of the Cs/bilayer graphene heterostructure. Another interesting future experiment is the study of the plasmon dispersion relation of the thin Cs film/bilayer graphene heterostructure. The plasmon dispersion can be studied using high-resolution electron energy loss spectroscopy and could reveal the presence of two distinct plasmon dispersion relations that correspond to 2D massive and massless particles. A knowledge

of the plasmon dispersion relations would also allow to assess the usefulness of this material for nanoplasmonics. Finally, it would be interesting to vary the alkali-metal type and hence the electron density in the hybrid structure.

Methods

Growth. Bilayer graphene was synthesized on Ir(111) by a two-step procedure which involves growth of monolayer graphene by chemical vapor deposition³⁹ followed by C deposition via electron beam evaporation onto the monolayer graphene with the sample at a temperature of 1000 °C^{14,62}. The amount of carbon deposited for the growth of the second layer, i.e., the bilayer coverage, was controlled by the evaporation time. We have investigated samples between monolayer and full bilayer coverage. The optimum growth time was determined by the appearance of two sharp π valence bands in the band structure that we observed using ARPES. The quality of bilayer graphene was investigated using LEED, STM, ARPES, and UHV Raman spectroscopy. The combined application of these methods corroborates the formation of AB (or Bernal) stacked bilayer graphene which is discussed in the following. Additional C 1s core level measurements by X-ray photoelectron spectroscopy are shown in the Supplementary Fig. 4. In the next step of the sample preparation, we evaporate Cs to a thickness of about two unit cells (corresponding to the bulk bcc structure) onto bilayer graphene at room temperature. The evaporation is calibrated by a quartz microbalance.

Angle-resolved photoemission spectroscopy. ARPES measurements were carried out at the ANTARES beamline⁶³ of the SOLEIL synchrotron in St. Aubin (France) and at the BaDElPh beamline⁶⁴ of the Elettra synchrotron in Trieste (Italy). The pristine bilayers (Fig. 1c–f) have been measured at the ANTARES using a hemispherical MBS A1 analyzer with circularly polarized light at $T = 70$ K. One pristine scan (Fig. 1g) and all Cs-doped bilayer graphene (Figs. 2b–e, 3c, d) have been measured at BaDElPh using a Specs Phoibos 150 analyzer and linearly polarized light at temperatures between $T = 15$ K and $T = 20$ K. LEED was measured at $T = 20$ K. The Cs deposition was carried out in one step from SAES getters with the sample at room temperature. The Fermi surface maps from Fig. 2d, e have been generated from a symmetrized azimuthal sweep of the first BZ.

UHV Raman spectroscopy. UHV Raman measurements were performed with the sample at $T = 5$ K and at $T = 300$ K in the back-scattering geometry using a commercial Raman system (Renishaw) integrated in a homebuilt optical chamber⁴⁵. The exciting and Raman scattered light were coupled into the vacuum using a $\times 50$ long-working distance microscope objective with an NA of ~ 0.4 and a focal distance of 20.5 mm for lasers with wavelength 442 and 532 nm. For the UV laser, UV compatible optical elements have been used. The $\times 20$ UV objective has a focal distance equal to 13 mm and an NA = 0.32. The position of the laser on the sample was checked by a camera in the laser path. All spectra have been calibrated in position to the O_2 vibration at 1555 cm^{-1} (see ref. ⁶⁵). The O_2 vibration is visible in the spectra due to the laser path outside the UHV. In Fig. 1h, we have guided the laser through an Ar gas filled acrylic tube in order to minimize O_2 Raman intensity while in Fig. 1i, the laser beam went through air explaining the larger O_2 Raman mode intensity in Fig. 1i. Sample preparation and measurement were done in situ and the sample was never exposed to air. In particular, the deposition of Cs in UHV Raman experiments has been performed in the same manner as in the ARPES studies.

Scanning tunneling microscopy. For STM, a sample with an only partial bilayer coverage was grown, enabling imaging of bilayer and monolayer graphene areas in a single topograph. Sample preparation and imaging was conducted in the UHV system ATHENE with a base pressure below 1×10^{-10} mbar. Image processing was conducted with the WSxM software⁶⁶.

Computational details and Cs layer stability. We perform DFT calculations with the projector augmented-wave pseudopotential method⁶⁷, adopting PBE (GGA) exchange and correlation functional⁶⁸. An energy cutoff of 400 eV for the plane wave basis and $14 \times 14 \times 1$ Monkhorst-Pack grid⁶⁹ for BZ sampling were used in order to ensure a total energy convergence of 1 meV. In our calculations of the Cs layer, we obtain a bulk bcc equilibrium lattice constant of 6.16 Å, $\sim 2\%$ larger than the experimental one³⁰. Our results are in line with those in ref. ³⁷, predicting that Cs-II (fcc) is the ground state (only 1 meV difference with respect to Cs-I). As pointed out in ref. ³⁸, also the hexagonal close packed (hcp) structure, which is very similar to the fcc structure, should emerge as a competing phase at low temperature. Indeed, we find that hcp and fcc phases are energetically degenerate up to less than 1 meV. We found that the lowest energy phase contains only one Cs atom intercalated inside the graphene bilayer, while the other three stay on top of the bilayer. Other configurations, with two, three, or four Cs in between the two carbon layers are higher in energy by 0.054 eV, 0.135 eV, and 0.316 eV per unit cell, respectively. The intercalation process of one layer of Cs atoms inside the graphene bilayer lowers the energy of the system by 0.615 eV per unit cell. In our simulations, we have varied the stacking of the three Cs layers atop of bilayer graphene to find the minimum energy

configuration. The three Cs layers on top can be arranged either according to the fcc(111) stacking (ABC) or alternatively according to the hcp stacking (ABA). These two configurations are similar and the energy difference between them is below 1 meV, so it is difficult to establish which one is observed experimentally. Nevertheless, the corresponding band structures are almost identical. Importantly, the in-plane lattice parameter of the Cs fcc trilayer is compressed by 11% with respect to the fcc (hcp) ground state; this, in turn, corresponds to an effective in-plane stress of 11 kbar, while the Cs–Cs out-of-plane distance is compatible with the equilibrium bulk fcc phase in the out-of-plane direction. Regarding the structure of bilayer graphene, we observe, that after the intercalation, graphene changes from AB (Bernal) to AA stacking for all investigated structures. This is consistent with previous findings on Li-intercalated graphene⁷⁰.

The thickness-dependent stability of the Cs film grown on intercalated bilayer graphene is investigated using DFT. There are two energies that contribute to the total energy of the Cs film. One is the adsorption energy which is negative and the other one is the compression energy which is positive. We show that the adsorption of strained Cs layers on the intercalated graphene bilayer is energetically favored. Let us first consider the binding energy for one Cs atom on the Cs-intercalated graphene in the 2×2 unit cell, defined as $\Delta E_1 = E_{\text{Cs-adsorbed}} - E_{\text{Cs-bulk}}$. Here, $E_{\text{Cs-adsorbed}}$ is the total energy of the Cs atom on the graphene and $E_{\text{Cs-bulk}}$ is the total energy per atom of Cs in its equilibrium bulk form. The result $\Delta E_1 = -0.092$ eV means that the adsorption of Cs onto the bilayer is energetically favored. The same quantity can also be calculated increasing the number of adsorbed Cs layers. In particular, for the trilayer, the formation energy is equal to $\Delta E_3 = (E_{\text{trilayer}} - 3E_{\text{Cs-bulk}})/3 = -0.04$ eV. This demonstrates that the trilayer is still favored with respect to the formation of the unstrained bulk Cs. The same calculation for the case of four Cs layers (following the same fcc stacking) on top of the intercalated graphene bilayer results in a small positive value of $\Delta E_4 = 0.005$ eV. This would suggest that $n = 3$ is the limit for the Cs film thickness. Nevertheless, the analysis from the DFT section suggests that the 114 phase with $n = 4$ is a possibility. The value of ΔE_4 is small compared with the energy corresponding to room temperature and the experimental μ_{Cs} value may be higher than $E_{\text{Cs-bulk}}$. Moreover, the calculation does not include external effects such as the film morphology which might alter the value of the computed energies. It is therefore likely that systems up to $n = 4$ Cs layers can be stabilized.

Data availability

The datasets generated during and/or analyzed during the current study are available from the corresponding author on reasonable request.

Received: 2 August 2019; Accepted: 21 February 2020;

Published online: 12 March 2020

References

- Koma, A. Van der waals epitaxy-a new epitaxial growth method for a highly lattice-mismatched system. *Thin Solid Films* **216**, 72–76 (1992).
- Zhang, Y. et al. Direct observation of the transition from indirect to direct bandgap in atomically thin epitaxial MoSe₂. *Nat. Nanotechnol.* **9**, 111–115 (2013).
- Ugeda, M. M. et al. Giant bandgap renormalization and excitonic effects in a monolayer transition metal dichalcogenide semiconductor. *Nat. Mater.* **13**, 1091–1095 (2014).
- Miwa, J. A. et al. Van der Waals epitaxy of two-dimensional MoS₂-graphene heterostructures in ultrahigh vacuum. *ACS Nano* **9**, 6502–6510 (2015).
- Hall, J. et al. Molecular beam epitaxy of quasi-freestanding transition metal disulfide monolayers on van der Waals substrates: a growth study. *2D Mater.* **5**, 025005 (2018).
- Ehlen, N. et al. Narrow photoluminescence and Raman peaks of epitaxial MoS₂ on graphene/Ir(111). *2D Mater.* **6**, 011006 (2018).
- Annamalai, M. et al. Surface energy and wettability of van der Waals structures. *Nanoscale* **8**, 5764–5770 (2016).
- Shin, Y. J. et al. Surface-energy engineering of graphene. *Langmuir* **26**, 3798–3802 (2010).
- Raj, R., Maroo, S. C. & Wang, E. N. Wettability of graphene. *Nano Lett.* **13**, 1509–1515 (2013).
- Hong, G. et al. On the mechanism of hydrophilicity of graphene. *Nano Lett.* **16**, 4447–4453 (2016).
- Petrovic, M. et al. The mechanism of caesium intercalation of graphene. *Nat. Commun.* **4**, 2772 (2013).
- Kanetani, K. et al. Ca intercalated bilayer graphene as a thinnest limit of superconducting CaCa. *Proc. Natl Acad. Sci. USA* **109**, 19610–19613 (2012).
- Schumacher, S. et al. The backside of graphene: manipulating adsorption by intercalation. *Nano Lett.* **13**, 5013–5019 (2013).
- Jolie, W. et al. Suppression of quasiparticle scattering signals in bilayer graphene due to layer polarization and destructive interference. *Phys. Rev. Lett.* **120**, 106801 (2018).
- Hell, M. et al. Resonance Raman spectrum of doped epitaxial graphene at the Lifshitz transition. *Nano Lett.* **18**, 6045–6056 (2018).
- Ehlen, N. et al. Origin of the flat band in heavily Cs-doped graphene. *ACS Nano* **14**, 1055–1069 (2020).
- Jaklevic, R. C. & Lambe, J. Experimental study of quantum size effects in thin metal films by electron tunneling. *Phys. Rev. B* **12**, 4146–4160 (1975).
- Vyalikh, D. V. et al. Quantum-well states in bilayers of Ag and Au on W(110). *Surf. Sci.* **540**, L638–L642 (2003).
- Dresselhaus, M. S. & Dresselhaus, G. Intercalation compounds of graphite. *Adv. Phys.* **51**, 1–186 (2002).
- Zhao, W., Tan, P. H., Liu, J. & Ferrari, A. C. Intercalation of few-layer graphite flakes with FeCl₃: Raman determination of Fermi level, layer by layer decoupling, and stability. *J. Am. Chem. Soc.* **133**, 5941–5946 (2011).
- Sugawara, K., Kanetani, K., Sato, T. & Takahashi, T. Fabrication of Li-intercalated bilayer graphene. *AIP Adv.* **1**, 022103 (2011).
- Olinger, B. & Shaner, J. W. Lithium, compression and high-pressure structure. *Science* **219**, 1071–1072 (1983).
- Hanfland, M., Loa, I. & Syassen, K. Sodium under pressure: bcc to fcc structural transition and pressure-volume relation to 100 GPa. *Phys. Rev. B* **65**, 184109 (2002).
- Takemura, K. & Syassen, K. High-pressure phase transitions in potassium and phase relations among heavy alkali metals. *Phys. Rev. B* **28**, 1193–1196 (1983).
- Hall, H. T., Merrill, L. & Barnett, J. D. High pressure polymorphism in cesium. *Science* **146**, 1297–1299 (1964).
- Takemura, K. & Syassen, K. High pressure equation of state of rubidium. *Solid State Commun.* **44**, 1161–1164 (1982).
- Smith, H., Berliner, R. & Jorgensen, J. Martensitic transformation from BCC to 9R and FCC in metallic lithium. *Phys. B* **156-157**, 53–55 (1989).
- Gieblowitz, T. M., Overhauser, A. W. & Werner, S. A. Direct observation of the charge-density wave in potassium by neutron diffraction. *Phys. Rev. Lett.* **56**, 1485–1488 (1986).
- Templeton, I. M. Observation of a martensitic transformation in rubidium? *J. Phys. F Met. Phys.* **12**, L121 (1982).
- Anderson, M. S. & Swenson, C. A. Experimental equations of state for cesium and lithium metals to 20 kbar and the high-pressure behavior of the alkali metals. *Phys. Rev. B* **31**, 668–680 (1985).
- Swenson, C. A. Compression of the alkali metals to 10000 atmospheres at low temperature. *Phys. Rev.* **99**, 423–430 (1955).
- McMahon, M. I., Nelmis, R. J. & Rekihi, S. Complex crystal structure of cesium-III. *Phys. Rev. Lett.* **87**, 25502 (2001).
- Delattre, J. & Badding, J. Rietveld refinement of the crystal structure of Cs(IV), ad-electron metal. *J. Solid State Chem.* **144**, 16–19 (1999).
- Schwarz, U., Takemura, K., Hanfland, M. & Syassen, K. Crystal structure of cesium-V. *Phys. Rev. Lett.* **81**, 2711–2714 (1998).
- Xie, J. et al. Phonon instabilities in high-pressure bcc-fcc and the isostructural fcc-fcc phase transitions of Cs. *Phys. Rev. B* **62**, 3624–3629 (2000).
- Sigalas, M., Bacalis, N. C., Papaconstantopoulos, D. A., Mehl, M. J. & Switendick, A. C. Total-energy calculations of solid H, Li, Na, K, Rb, and Cs. *Phys. Rev. B* **42**, 11637–11643 (1990).
- Xie, Y. et al. Origin of bcc to fcc phase transition under pressure in alkali metals. *N. J. Phys.* **10**, 063022 (2008).
- Skriver, H. L. Crystal structure from one-electron theory. *Phys. Rev. B* **31**, 1909–1923 (1985).
- Coraux, J., NDiaye, A. T., Busse, C. & Michely, T. Structural coherency of graphene on Ir(111). *Nano Lett.* **8**, 565–570 (2008).
- Trickey, S. B., Müller-Plathe, F., Diercksen, G. H. F. & Boettger, J. C. Interplanar binding and lattice relaxation in a graphite dilayer. *Phys. Rev. B* **45**, 4460–4468 (1992).
- Ohta, T. et al. Interlayer interaction and electronic screening in multilayer graphene investigated with angle-resolved photoemission spectroscopy. *Phys. Rev. Lett.* **98**, 206802 (2007).
- Grüneis, A. et al. Tight-binding description of the quasiparticle dispersion of graphite and few-layer graphene. *Phys. Rev. B* **78**, 205425 (2008).
- Ohta, T., Bostwick, A., Seyller, T., Horn, K. & Rotenberg, E. Controlling the electronic structure of bilayer graphene. *Science* **313**, 951–954 (2006).
- Hwang, C. et al. Direct measurement of quantum phases in graphene via photoemission spectroscopy. *Phys. Rev. B* **84**, 125422 (2011).
- Hell, M. G. et al. Combined ultra high vacuum Raman and electronic transport characterization of large-area graphene on SiO₂. *Phys. Status Solidi B* **255**, 1800456 (2018).
- Usachov, D. Y. et al. Raman spectroscopy of lattice-matched graphene on strongly interacting metal surfaces. *ACS Nano* **11**, 6336–6345 (2017).
- Calizo, I., Bejenari, I., Rahman, M., Liu, G. & Balandin, A. A. Ultraviolet Raman microscopy of single and multilayer graphene. *J. Appl. Phys.* **106**, 043509 (2009).

48. Lin, Y. et al. Observation of intercalation-driven zone folding in quasi-free-standing graphene energy bands. *Phys. Rev. B* **99**, 035428 (2019).
49. Nair, R. R. et al. Fine structure constant defines visual transparency of graphene. *Science* **320**, 1308 (2008).
50. Chan, K. T., Neaton, J. B. & Cohen, M. L. First-principles study of metal adatom adsorption on graphene. *Phys. Rev. B* **77**, 235430 (2008).
51. Liu, J. et al. The dependence of graphene Raman D-band on carrier density. *Nano Lett.* **13**, 6170–6175 (2013).
52. Jin, K.-H., Choi, S.-M. & Jhi, S.-H. Crossover in the adsorption properties of alkali metals on graphene. *Phys. Rev. B* **82**, 033414 (2010).
53. Vitos, L., Ruban, A., Skriver, H. & Kollár, J. *Surf. Energy Met. Surf. Sci.* **411**, 186–202 (1998).
54. Tyson, W. & Miller, W. Surface free energies of solid metals: estimation from liquid surface tension measurements. *Surf. Sci.* **62**, 267–276 (1977).
55. Tran, R. et al. Surface energies of elemental crystals. *Sci. Data* **3**, 160080 (2016).
56. Fink, J. et al. Dressing of the charge carriers in high-Tc superconductors. In *Very High Resolution Photoelectron Spectroscopy*, 295–325 (Springer Berlin Heidelberg, Berlin, Heidelberg, 2007). <https://doi.org/10.1007/3-540-68133-7>.
57. Hodges, C., Smith, H. & Wilkins, J. W. Effect of Fermi surface geometry on electron–electron scattering. *Phys. Rev. B* **4**, 302–311 (1971).
58. Ingle, N. J. C. et al. Quantitative analysis of Sr₂RuO₄ angle-resolved photoemission spectra: many-body interactions in a model Fermi liquid. *Phys. Rev. B* **72**, 205114 (2005).
59. Hofmann, P., Sklyadnaya, I. Y., Rienks, E. D. L. & Chulkov, E. V. Electron-phonon coupling at surfaces and interfaces. *N. J. Phys.* **11**, 125005 (2009).
60. Carlesi, S., Franchini, A., Bortolani, V. & Martinelli, S. Cesium under pressure: first-principles calculation of the bcc-to-fcc phase transition. *Phys. Rev. B* **59**, 11716–11719 (1999).
61. Martin, W., Freyland, W., Lamparter, P. & Steeb, S. Structure and density of gold-cesium-melts. II. Neutron diffraction with molten gold-cesium-alloys. *Phys. Chem. Liq.* **10**, 61–76 (1980).
62. Herbig, C. et al. From permeation to cluster arrays: graphene on Ir(111) exposed to carbon vapor. *Nano Lett.* **17**, 3105–3112 (2017).
63. Avila, J. & Asensio, M. C. First nanoARPES user facility available at SOLEIL: an innovative and powerful tool for studying advanced materials. *Synchrotron Radiat. N.* **27**, 24–30 (2014).
64. Petaccia, L. et al. BaD ElPh: a 4 m normal-incidence monochromator beamline at Elettra. *Nucl. Instrum. Methods Phys. Res. Sect. A* **606**, 780–784 (2009).
65. Faris, G. W. & Copeland, R. A. Ratio of oxygen and nitrogen Raman cross sections in the ultraviolet. *Appl. Opt.* **36**, 2684–2685 (1997).
66. Horcas, I. et al. WSXM: a software for scanning probe microscopy and a tool for nanotechnology. *Rev. Sci. Instrum.* **78**, 013705 (2007).
67. Blöchl, P. E. Projector augmented-wave method. *Phys. Rev. B* **50**, 17953–17979 (1994).
68. Perdew, J. P., Burke, K. & Ernzerhof, M. Generalized gradient approximation made simple. *Phys. Rev. Lett.* **77**, 3865–3868 (1996).
69. Monkhorst, H. J. & Pack, J. D. Special points for Brillouin-zone integrations. *Phys. Rev. B* **13**, 5188–5192 (1976).
70. Caffrey, N. M. et al. Structural and electronic properties of Li-intercalated graphene on SiC(0001). *Phys. Rev. B* **93**, 195421 (2016).

Acknowledgements

M.H., N.E., Y.F., B.S., D.T., and A.G. acknowledge the ERC-grant no. 648589 “SUPER-2D”, funding from Quantum Matter and Materials and the Deutsche Forschungsgemeinschaft under Germany’s Excellence Strategy—Cluster of Excellence Matter and Light for Quantum Computing (ML4Q) EXC 2004/1 390534769. M.H., N.E., A.G., W.J. and T.M. acknowledge funding from CRC1238 (project number

277146847, subproject A01). We acknowledge Elettra Sincrotrone Trieste for providing access to its synchrotron radiation facilities. The research leading to this result has been also supported by the project CALIPSOplus under Grant Agreement 730872 from the EU Framework Programme for Research and Innovation HORIZON 2020. We acknowledge SOLEIL for provision of synchrotron radiation facilities (Proposal No. 20180831). The Synchrotron SOLEIL is supported by the Centre National de la Recherche Scientifique (CNRS) and the Commissariat à l’Energie Atomique et aux Energies Alternatives (CEA), France. This work was also supported by a public grant by the French National Research Agency (ANR) as part of the “Investissements d’Avenir” (reference: ANR-17-CE09-0016-05). CT acknowledges support by the Alexander von Humboldt Stiftung. WJ acknowledges support from the Alexander von Humboldt Foundation via the Feodor Lynen Research Fellowship.

Author contributions

M.H. prepared bilayer graphene samples and carried out UHV Raman experiments with help from D.T. and B.S., M.H., N.E., Y.F., B.S., and A.G. prepared and carried out the ARPES experiments and Elettra and SOLEIL. N.E. and B.S. performed the ARPES data analysis and N.E. performed the self-energy analysis. G.D.S., J.A. and L.P. were responsible for the synchrotron beamlines. C.H., C.T., and W.J. prepared bilayer graphene samples and carried out the STM investigations. The STM investigations and research into bilayer growth were directed by T.M., G.M. and G.P. performed the DFT calculations. A.G. planned the research and directed the experimental work. All authors contributed to the discussions and the writing of the paper.

Competing interests

The authors declare no competing interests.

Additional information

Supplementary information is available for this paper at <https://doi.org/10.1038/s41467-020-15130-1>.

Correspondence and requests for materials should be addressed to M.H., N.E. or A.Gün.

Peer review information *Nature Communications* thanks Jacek Majewski, Sekhar C. Ray and the other, anonymous, reviewer(s) for their contribution to the peer review of this work.

Reprints and permission information is available at <http://www.nature.com/reprints>

Publisher’s note Springer Nature remains neutral with regard to jurisdictional claims in published maps and institutional affiliations.



Open Access This article is licensed under a Creative Commons Attribution 4.0 International License, which permits use, sharing, adaptation, distribution and reproduction in any medium or format, as long as you give appropriate credit to the original author(s) and the source, provide a link to the Creative Commons license, and indicate if changes were made. The images or other third party material in this article are included in the article’s Creative Commons license, unless indicated otherwise in a credit line to the material. If material is not included in the article’s Creative Commons license and your intended use is not permitted by statutory regulation or exceeds the permitted use, you will need to obtain permission directly from the copyright holder. To view a copy of this license, visit <http://creativecommons.org/licenses/by/4.0/>.

© The Author(s) 2020

Chapter 6

Conclusions

In this thesis, several ways of modifying the electronic band structure of (quasi-)two-dimensional crystals and the resulting effects were explored in graphene, black phosphorus and MoS₂. Modifications included adsorption and intercalation of several different alkali metals as well as formation of heterostructures. To enable the investigation of these effects, all growths and experiments were performed in ultra-high vacuum conditions, guaranteeing high-quality samples. The ultra-high vacuum helped with avoiding sample contamination and oxidation. The latter was particularly important for the cleaved black phosphorus bulk crystals. The main experimental method used to characterize the materials before and after modification was angle-resolved photoemission spectroscopy. The experiments were performed at several different beamline endstations in synchrotron radiation facilities. Additional photoluminescence spectroscopy and Raman spectroscopy measurements were performed at home in a lab based ultra-high vacuum laboratory setup. The ARPES measurements enabled a direct observation of the effects on the electronic band structure. How those changes in band structure affected the optical properties could then be investigated using photoluminescence spectroscopy. Additionally, Raman spectroscopy could be used to learn about effects on the phonons in the samples.

The experimental results were combined with theoretical tight-binding calculations. Fitting the tight-binding parameters to the experimental band structure allowed for insights into the influence of individual parameters on the electronic structure. This enabled a direct interpretation of the effects of functionalization. The combination of experiment and theory allowed for a good understanding of the observed changes. They complemented each other to give a more complete picture on the modifications of the electronic structure. An overview over the main findings of this thesis is given in the following.

As few-layer phosphorene was only obtainable *via* exfoliation, powerful measurement techniques requiring large area samples could not be used on the available samples. As an alternative, the electronic properties of bulk black phosphorus were investigated using a combination of angle-resolved photoemission experiments and tight-binding theory in section 5.1.1. The results from the observation of bulk BP were then used to gain insights into the behaviour of few-layer phosphorene. The experimental band structure of pristine BP along several high-symmetry directions was obtained with ARPES. Doping the crystal with lithium allowed for a downshift of the bands and the appearance of the bottom of the conduction band at the Z -point in the ARPES spectra. Comparison of the valence band dispersion before and after Li doping showed a perfect match after accounting for an energy offset from the donated electrons. The matching band masses hence indicated a rigid band shift upon lithium doping. The spectra of Li-doped samples were consequently used to extract a value of approximately 400 meV for the experimental electronic band gap of bulk black phosphorus. Comparison with optical measurements netted an exciton binding energy of ≈ 140 meV. Theoretical G_0W_0 calculations of the band structure showed good agreement to the experimental dispersion, though the theoretical calculation underestimated the experimental band gap. To obtain a good theoretical model of the electronic bands of BP, a tight-binding model with a full set of valence orbitals was developed and fitted to the experimental values. Keeping the lithium doping in the region of rigid band shift allowed for the inclusion of the experimental bulk band gap and the effective masses of the conduction band in the fit. The resulting model could be used to monitor the doping dependence of the bulk Fermi surface. To gain insight into the features of few-layer phosphorene, a zone-folding method was applied to the tight-binding Hamiltonian. The outcome for the layer-dependent band gap reproduced theoretical predictions and experimental results of other publications. The good agreement implies that the properties of few-layer phosphorene can mostly be understood *via* this zone-folding mechanism without taking into account surface effects or hybridization between bands on different layers. This result could be further verified by comparing the zone-folded band structure with the band structure of few-layer phosphorene explicitly calculated using the hopping parameters obtained for the bulk model. The resulting band structures were very similar, hybridization or surface effects gave only very small corrections to the zone-folded band model. The zone-folded Hamiltonian was then used to predict doping dependent Fermi surfaces in the case of rigid band shifts. The knowledge of the Fermi surfaces is important to determine nesting conditions and predict possible strong coupling directions for ground states such as charge density waves or superconductivity.

In section 5.1.2, a surface band inversion was induced in bulk black phosphorus using caesium doping. Evaporation of Cs onto the surface of bulk BP lead to a shift of the conduction band past the bulk valence band at the Z-point of the bulk Brillouin zone. Energy dependent ARPES confirmed the surface nature of the conduction band. The k_x - k_y -dependence of the resulting dispersion was mapped out. The charge carrier concentration was determined as $1.7 \times 10^{14} \text{ cm}^{-2}$ from the Fermi surface area, the Fermi velocities for Z - T and Z - U directions (Γ - Y and Γ - X directions in the surface Brillouin zone) were found to be $3.68 \times 10^5 \text{ m s}^{-1}$ and $1.02 \times 10^6 \text{ m s}^{-1}$ respectively. A two-dimensional tight-binding model was developed from the bulk tight-binding model produced in section 5.1.1 and used to explain the observed band structure. Importantly, to explain the experimental band structure, a reduction of the interlayer interaction and a breaking of glide mirror symmetry had to be artificially inserted in the TB model. Intercalation of Cs below the first layer of BP could be ruled out as a reason for the reduced interlayer interaction by angle dependent XPS measurements. The artificial modifications to the TB model could be understood from DFT. The experimental dispersion was well reproduced with the density functional theory approach when assuming a stacking fault of the topmost layer of black phosphorus. This stacking fault decreases the interlayer interaction and explains the glide mirror symmetry breaking. Moreover, calculations of thicker slabs confirmed a localization of the conduction band at the surface layer in agreement with the ARPES experiments. The valence band was confirmed to arise from bulk states. The interaction and hybridization of the surface-like conduction band with the bulk-like valence band established the observed band as a surface resonance state. The high Fermi velocities and charge carrier concentration in Cs doped black phosphorus introduce the material as a potential candidate for applications in field effect transistors with large on-off ratios and good switching characteristics [88, 222]. The achieved large band inversion *via* doping is promising for applications in room temperature devices. As calculations suggest the hybridization between surface state and bulk bands, the interlayer interaction should lead to much bigger band gap reopening if the emergence of a stacking fault of the topmost layer can be avoided. The strong dependence of the band inversion on the doping level suggests a large tuneability of induced charge carrier concentration, band gap and potentially interlayer interaction. Applying alkali metal doping to a black phosphorus field effect transistor geometry is thus a promising future experiment in the search for new FETs with good switching characteristics. The dopants could induce the band gap inversion and localization of the conduction band at the surface. The field-effect gate voltage could then be used to shift the Fermi level within the band inverted band structure

topology.

Another promising two-dimensional semiconductor is Molybdenum Disulfide. In section 5.2, epitaxially grown MoS₂ on a graphene/iridium(111) substrate has been examined. The fundamental properties of the sample were characterized with scanning tunneling microscopy, low-energy electron diffraction, x-ray photoemission spectroscopy and ARPES. To determine the band gap of the epitaxial MoS₂ layer, the sample was doped using lithium until the conduction band appeared in ARPES spectra. The experimental band gap was found to be 1.975 eV. From the Fermi surface, an electron doping of $3.2 \times 10^{13} \text{ cm}^{-2}$ was determined. Combining the knowledge of band gap and electron doping density with theoretical calculations on the band gap renormalization [39] a pristine gap of approximately 2.425 eV was estimated. Investigating the photoluminescent properties of pristine MoS₂/Gr/Ir(111), a sharp photoluminescent peak with a full width at half maximum of 18 meV at $T = 8 \text{ K}$ was observed centered at an energy of 1.945 eV. Comparison of the estimated pristine band gap with the position of the photoluminescence peak – and thus the excitonic band gap – gave an exciton binding energy of approximately 480 meV. The observation of a photoluminescent peak in this material was surprising as graphene is usually a good energy sink which leads to quenching of optical excitations in adsorbed molecules and layers atop graphene [8, 65–67]. The appearance of the peak thus suggests a low interaction between MoS₂ and graphene. This assumption was corroborated by missing hybridization effects between MoS₂ and graphene bands in ARPES and missing satellite peaks in XPS. Temperature dependent measurements of the Raman maxima of MoS₂ and graphene gave further credence to the assumption of low substrate adlayer interaction. From the shift in peak position with temperature, it was concluded that the thermal expansion of the graphene layer is locked to the iridium(111) substrate. On the other hand, the thermal expansion of the MoS₂ adlayer was closer to that expected of a freestanding layer – again confirming a low interaction with the graphene layer. The low interaction between graphene and MoS₂ enables the use of the material in opto-electrical applications. While the low interaction with graphene plausibly explained the experimental observations, a true microscopic understanding of the coupling mechanisms of graphene and MoS₂ is still missing and could be an interesting future subject of investigation. Better understanding of the coupling could enable explicit modification of the MoS₂/Gr/Ir(111) properties. For now, the results suggest the MoS₂/graphene heterostructure as a good approximation of freestanding MoS₂. An interstitial graphene layer hence seems an effective way of decoupling epitaxial MoS₂ from any substrate interaction. As graphene is stable at the growth temperatures re-

quired for the epitaxial MoS₂ growth and mostly decouples the properties of the MoS₂ adlayer from the iridium(111) bulk substrate, sample growth and conclusions on the properties should in general be applicable to MoS₂ samples grown on graphene with a non-metallic bulk substrates – a requirement for applications using the semiconducting properties of MoS₂.

In section 5.3, the properties under high Cs doping levels of bilayer graphene grown epitaxially on the (111) surface of a bulk iridium crystal were investigated. The growth was monitored using the G to 2D peak ratio in Raman spectroscopy. The characterization of the pristine sample with ARPES showed purely Bernal stacked bilayer graphene with a small inherent hole doping. Heavy Cs doping lead to the formation of a 2×2 superstructure visible in low-energy electron diffraction experiments. The superperiodic potential formed by the Cs atoms was strong enough to shift the spectral weight of the graphene bands from the base Brillouin zone to the zone-folded 2×2 superstructure Brillouin zone. Charge transfer from the adsorbed Cs atoms to the bilayer graphene structure lead to a shift of the Dirac point to approximately 1.5 eV binding energy. The energy-splitting between the bands located on the upper and lower graphene layer disappeared after caesium evaporation. Around the Γ -point, four parabolic bands arising from the deposited caesium appeared. From this result it was clear that the evaporated caesium grew in crystalline layers with at least four atoms in the 2×2 -superstructure unit cell. Combining theoretical calculations for the total energy of potential bilayer graphene caesium hybrid structures with a comparison of predicted band structures *versus* the experimental results gave the most probable crystals structures as one caesium layer intercalated between the bulk iridium substrate and the lower graphene layer, one caesium layer intercalated between the two graphene layers, and three or four caesium layers grown epitaxially on top of the topmost graphene layer. The perfect 2×2 superstructure allowed the comparison of the lattice parameter of the grown Cs layers with the lattice parameter of bulk Cs and netted a compressive in-plane strain of 11%. Analysis of the imaginary self-energy of the caesium derived band with the highest binding energy showed a band broadening at the edge of instrument resolution suggesting the material as a candidate for research into two dimensional Fermi gases. Observation of the structure in laser based ARPES systems with better energy and momentum resolution would be interesting as future experiments in this regard. The growth of well-defined Cs layers on a Van der Waals material establishes the possibility of producing new interfaces between Van der Waals layers and conventional metals or semiconductors. Normally, these materials favour formation of clusters on graphene due to a low ratio of adhesive and cohesive energy on the surface. The Cs layers could

function as buffer layers for the growth of other quantum well structures and could ultimately allow for the introduction of conventional bulk thin film structures in Van der Waals heteroepitaxy.

Bibliography

- [1] K. S. Novoselov, A. K. Geim, S. V. Morozov, D. Jiang, Y. Zhang, S. V. Dubonos, I. V. Grigorieva, and A. A. Firsov, “Electric field in atomically thin carbon films,” *Science*, vol. 306, no. 5696, pp. 666–669, 2004.
- [2] N. D. Mermin, “Crystalline order in two dimensions,” *Physical Review*, vol. 176, no. 1, pp. 250–254, 1968.
- [3] E. Gerstner, “Nobel Prize 2010: Andre Geim & Konstantin Novoselov,” *Nature Physics*, vol. 6, p. 836, 2010.
- [4] J. Hall, B. Pielic, C. Murray, W. Jolie, T. Wekking, C. Busse, M. Kralj, and T. Michely, “Molecular beam epitaxy of quasi-freestanding transition metal disulphide monolayers on van der Waals substrates: a growth study,” *2D Materials*, vol. 5, no. 2, p. 025005, 2018.
- [5] S. S. Grønberg, S. Ulstrup, M. Bianchi, M. Dendzik, C. E. Sanders, J. V. Lauritsen, P. Hofmann, and J. A. Miwa, “Synthesis of Epitaxial Single-Layer MoS₂ on Au(111),” *Langmuir*, vol. 31, no. 35, pp. 9700–9706, 2015.
- [6] D. Marchenko, A. Varykhalov, M. R. Scholz, G. Bihlmayer, E. I. Rashba, A. Rybkin, A. M. Shikin, and O. Rader, “Giant Rashba splitting in graphene due to hybridization with gold,” *Nature Communications*, vol. 3, no. 1, pp. 1–6, 2012.
- [7] E. Courtade, B. Han, S. Nakhaie, C. Robert, X. Marie, P. Renucci, T. Taniguchi, K. Watanabe, L. Geelhaar, J. M. Lopes, and B. Urbaszek, “Spectrally narrow exciton luminescence from monolayer MoS₂ and MoSe₂ exfoliated onto epitaxially grown hexagonal BN,” *Applied Physics Letters*, vol. 113, no. 3, p. 032106, 2018.
- [8] G. Froehlicher, E. Lorchat, and S. Berciaud, “Charge Versus Energy Transfer in Atomically Thin Graphene-Transition Metal Dichalcogenide van der Waals Heterostructures,” *Physical Review X*, vol. 8, no. 1, pp. 1–15, 2018.

- [9] J. Avila and M. C. Asensio, “First NanoARPES User Facility Available at SOLEIL: An Innovative and Powerful Tool for Studying Advanced Materials,” *Synchrotron Radiation News*, vol. 27, no. 2, pp. 24–30, 2014.
- [10] W. Chen, Z. Sun, Z. Wang, L. Gu, X. Xu, S. Wu, and C. Gao, “Direct observation of van der Waals stacking–dependent interlayer magnetism,” *Science*, vol. 366, no. 6468, pp. 983–987, 2019.
- [11] M. Onodera, S. Masubuchi, R. Moriya, and T. Machida, “Assembly of van der Waals heterostructures: Exfoliation, searching, and stacking of 2D materials,” *Japanese Journal of Applied Physics*, vol. 59, no. 1, p. 010101, 2020.
- [12] R. Nandkishore, L. S. Levitov, and A. V. Chubukov, “Chiral superconductivity from repulsive interactions in doped graphene,” *Nature Physics*, vol. 8, pp. 158–163, 2012.
- [13] M. G. Hell, N. Ehlen, B. V. Senkovskiy, E. H. Hasdeo, A. Fedorov, D. Dombrowski, C. Busse, T. Michely, G. di Santo, L. Petaccia, R. Saito, and A. Grüneis, “Resonance Raman Spectrum of Doped Epitaxial Graphene at the Lifshitz Transition,” *Nano Letters*, vol. 18, no. 9, pp. 6045–6056, 2018.
- [14] A. V. Fedorov, N. I. Verbitskiy, D. Haberer, C. Struzzi, L. Petaccia, D. Usachov, O. Y. Vilkov, D. V. Vyalikh, J. Fink, M. Knupfer, B. Büchner, and A. Grüneis, “Observation of a universal donor-dependent vibrational mode in graphene,” *Nature Communications*, vol. 5, p. 3257, 2014.
- [15] B. M. Ludbrook, G. Levy, P. Nigge, M. Zonno, M. Schneider, D. J. Dvorak, C. N. Veenstra, S. Zhdanovich, D. Wong, P. Dosanjh, C. Straßer, A. Stöhr, S. Forti, C. R. Ast, U. Starke, A. Damascelli, and J. C. Séamus Davis, “Evidence for superconductivity in Li-decorated monolayer graphene,” *Proceedings of the National Academy of Sciences of the United States of America*, vol. 112, no. 38, pp. 11795–11799, 2015.
- [16] N. Ehlen, A. Sanna, B. Senkovskiy, L. Petaccia, A. Fedorov, G. Profeta, and A. Grüneis, “Direct observation of a surface resonance state and surface band inversion control in black phosphorus,” *Physical Review B*, vol. 97, no. 4, p. 045143, 2018.
- [17] J. Kim, S. S. Baik, S. W. Jung, Y. Sohn, S. H. Ryu, H. J. Choi, B. J. Yang, and K. S. Kim, “Two-Dimensional Dirac Fermions Protected by Space-Time

- Inversion Symmetry in Black Phosphorus,” *Physical Review Letters*, vol. 119, no. 22, p. 226801, 2017.
- [18] Y. Liu, N. O. Weiss, X. Duan, H. C. Cheng, Y. Huang, and X. Duan, “Van der Waals heterostructures and devices,” *Nature Reviews Materials*, vol. 1, p. 16042, 2016.
- [19] L. A. Walsh and C. L. Hinkle, “van der Waals epitaxy: 2D materials and topological insulators,” *Applied Materials Today*, vol. 9, pp. 504–515, 2017.
- [20] K. S. Novoselov, A. Mishchenko, A. Carvalho, and A. H. Castro Neto, “2D materials and van der Waals heterostructures,” *Science*, vol. 353, no. 6298, p. aac9439, 2016.
- [21] A. K. Geim and I. V. Grigorieva, “Van der Waals heterostructures,” *Nature*, vol. 499, no. 7459, pp. 419–425, 2013.
- [22] H. Fang, C. Battaglia, C. Carraro, S. Nemsak, B. Ozdol, J. S. Kang, H. A. Bechtel, S. B. Desai, F. Kronast, A. A. Unal, G. Conti, C. Conlon, G. K. Palsson, M. C. Martin, A. M. Minor, C. S. Fadley, E. Yablonovitch, R. Maboudian, and A. Javey, “Strong interlayer coupling in van der Waals heterostructures built from single-layer chalcogenides,” *Proceedings of the National Academy of Sciences of the United States of America*, vol. 111, no. 17, pp. 6198–6202, 2014.
- [23] F. Ceballos, M. Z. Bellus, H. Y. Chiu, and H. Zhao, “Probing charge transfer excitons in a MoSe₂-WS₂ van der Waals heterostructure,” *Nanoscale*, vol. 7, pp. 17523–17528, 2015.
- [24] S. Nigar, Z. Zhou, H. Wang, and M. Imtiaz, “Modulating the electronic and magnetic properties of graphene,” *RSC Advances*, vol. 7, pp. 51546–51580, 2017.
- [25] C. N. Rao and R. Voggu, “Charge-transfer with graphene and nanotubes,” *Materials Today*, vol. 13, no. 9, pp. 34–40, 2010.
- [26] D. Choudhury, B. Das, D. D. Sarma, and C. N. Rao, “XPS evidence for molecular charge-transfer doping of graphene,” *Chemical Physics Letters*, vol. 497, no. 1-3, pp. 66–69, 2010.
- [27] I. Gierz, C. Riedl, U. Starke, C. R. Ast, and K. Kern, “Atomic hole doping of graphene,” *Nano Letters*, vol. 8, no. 12, pp. 4603–4607, 2008.

- [28] H. Liu, Y. Liu, and D. Zhu, “Chemical doping of graphene,” *Journal of Materials Chemistry*, vol. 21, no. 10, pp. 3335–3345, 2011.
- [29] S. Schumacher, F. Huttmann, M. Petrović, C. Witt, D. F. Förster, C. Vo-Van, J. Coraux, A. J. Martínez-Galera, V. Sessi, I. Vergara, R. Rückamp, M. Grüninger, N. Schleheck, F. Meyer Zu Heringdorf, P. Ohresser, M. Kralj, T. O. Wehling, and T. Michely, “Europium underneath graphene on Ir(111): Intercalation mechanism, magnetism, and band structure,” *Physical Review B*, vol. 90, no. 23, p. 235437, 2014.
- [30] A. Grüneis, C. Attaccalite, A. Rubio, S. L. Molodtsov, D. V. Vyalikh, J. Fink, R. Follath, and T. Pichler, “Preparation and electronic properties of potassium doped graphite single crystals,” *Physica Status Solidi (B) Basic Research*, vol. 245, no. 10, pp. 7072–7076, 2008.
- [31] D. Nevola, B. C. Hoffman, A. Bataller, H. Ade, K. Gundogdu, and D. B. Dougherty, “Rigid valence band shift due to molecular surface counter-doping of MoS₂,” *Surface Science*, vol. 679, pp. 254–258, 2019.
- [32] N. Ehlen, B. Senkovskiy, A. Fedorov, A. Perucchi, P. Di Pietro, A. Sanna, G. Profeta, L. Petaccia, and A. Grüneis, “Evolution of electronic structure of few-layer phosphorene from angle-resolved photoemission spectroscopy of black phosphorous,” *Physical Review B*, vol. 94, no. 24, p. 245410, 2016.
- [33] L. Waldecker, A. Raja, M. Rösner, C. Steinke, A. Bostwick, R. J. Koch, C. Jozwiak, T. Taniguchi, K. Watanabe, E. Rotenberg, T. O. Wehling, and T. F. Heinz, “Rigid Band Shifts in Two-Dimensional Semiconductors through External Dielectric Screening,” *Physical Review Letters*, vol. 123, no. 20, p. 26403, 2019.
- [34] P. Wang, R. Khan, Z. Liu, B. Zhang, Y. Li, S. Wang, Y. Wu, H. Zhu, Y. Liu, G. Zhang, D. Liu, S. Chen, L. Song, and Z. Sun, “A non-rigid shift of band dispersions induced by Cu intercalation in 2H-TaSe₂,” *Nano Research*, vol. 13, pp. 353–357, 2020.
- [35] T. Fujiwara, S. Nishino, S. Yamamoto, T. Suzuki, M. Ikeda, and Y. Ohtani, “Total-energy assisted tight-binding method based on local density approximation of density functional theory,” *Journal of the Physical Society of Japan*, vol. 87, no. 6, p. 064802, 2018.

- [36] P. Turchi, A. Gonis, and L. Colombo, “Tight-binding approach to computational materials science.,” in *Materials Research Society symposium proceedings Volume 491*, 1998.
- [37] R. Hoffmann, *Solids and Surfaces: A Chemist’s View of Bonding in Extended Structures*. Wiley, 1989.
- [38] N. W. Ashcroft and N. D. Mermin, *Solid State Physics*. Saunders College Publishing, 1978.
- [39] Y. Liang and L. Yang, “Carrier Plasmon Induced Nonlinear Band Gap Renormalization in Two-Dimensional Semiconductors,” *Physical Review Letters*, vol. 114, no. 6, p. 063001, 2015.
- [40] S. Gao, Y. Liang, C. D. Spataru, and L. Yang, “Dynamical Excitonic Effects in Doped Two-Dimensional Semiconductors,” *Nano Letters*, vol. 16, no. 9, pp. 5568–5573, 2016.
- [41] B. V. Senkovskiy, A. V. Fedorov, D. Haberer, M. Farjam, K. A. Simonov, A. B. Preobrajenski, N. Mårtensson, N. Atodiresei, V. Caciuc, S. Blügel, A. Rosch, N. I. Verbitskiy, M. Hell, D. V. Evtushinsky, R. German, T. Marangoni, P. H. van Loosdrecht, F. R. Fischer, and A. Grüneis, “Semiconductor-to-Metal Transition and Quasiparticle Renormalization in Doped Graphene Nanoribbons,” *Advanced Electronic Materials*, vol. 3, no. 4, p. 1600490, 2017.
- [42] H. Hartleb, F. Späth, and T. Hertel, “Evidence for Strong Electronic Correlations in the Spectra of Gate-Doped Single-Wall Carbon Nanotubes,” *ACS Nano*, vol. 9, no. 10, pp. 10461–10470, 2015.
- [43] C. D. Spataru and F. Léonard, “Tunable band gaps and excitons in doped semiconducting carbon nanotubes made possible by acoustic plasmons,” *Physical Review Letters*, vol. 104, no. 17, p. 177402, 2010.
- [44] R. C. Dynes and C. M. Varma, “Superconductivity and electronic density of states,” *Journal of Physics F: Metal Physics*, vol. 6, no. 7, p. L215, 1976.
- [45] S. Blundell, *Magnetism in Condensed Matter*. Oxford University Press, 2003.
- [46] C. M. Teodorescu and G. A. Lungu, “Band ferromagnetism in systems of variable dimensionality,” *Journal of Optoelectronics and Advanced Materials*, vol. 10, no. 11, pp. 3058–3068, 2008.

- [47] G. Long, S. Xu, T. Zhang, Z. Wu, W. K. Wong, T. Han, J. Lin, Y. Cai, and N. Wang, “Charge density wave phase transition on the surface of electrostatically doped multilayer graphene,” *Applied Physics Letters*, vol. 109, no. 18, p. 183107, 2016.
- [48] R. Langer, P. Błoński, C. Hofer, P. Lazar, K. Mustonen, J. C. Meyer, T. Susi, and M. Otyepka, “Tailoring Electronic and Magnetic Properties of Graphene by Phosphorus Doping,” *ACS Applied Materials and Interfaces*, vol. 12, no. 30, pp. 34074–34085, 2020.
- [49] F. Joucken, J. Avila, Z. Ge, E. A. Quezada-Lopez, H. Yi, R. Le Goff, E. Baudin, J. L. Davenport, K. Watanabe, T. Taniguchi, M. C. Asensio, and J. Velasco, “Visualizing the Effect of an Electrostatic Gate with Angle-Resolved Photoemission Spectroscopy,” *Nano Letters*, vol. 19, no. 4, pp. 2682–2687, 2019.
- [50] A. J. Jones, R. Muzzio, P. Majchrzak, S. Pakdel, D. Curcio, K. Volckaert, D. Biswas, J. Gobbo, S. Singh, J. T. Robinson, K. Watanabe, T. Taniguchi, T. K. Kim, C. Cacho, N. Lanata, J. A. Miwa, P. Hofmann, J. Katoch, and S. Ulstrup, “Observation of Electrically Tunable van Hove Singularities in Twisted Bilayer Graphene from NanoARPES,” *Advanced Materials*, vol. 32, no. 31, p. 2001656, 2020.
- [51] P. V. Nguyen, N. C. Teutsch, N. P. Wilson, J. Kahn, X. Xia, A. J. Graham, V. Kandyba, A. Giampietri, A. Barinov, G. C. Constantinescu, N. Yeung, N. D. Hine, X. Xu, D. H. Cobden, and N. R. Wilson, “Visualizing electrostatic gating effects in two-dimensional heterostructures,” *Nature*, vol. 572, no. 7768, pp. 220–223, 2019.
- [52] J. Li, L. Lin, D. Rui, Q. Li, J. Zhang, N. Kang, Y. Zhang, H. Peng, Z. Liu, and H. Q. Xu, “Electron-Hole Symmetry Breaking in Charge Transport in Nitrogen-Doped Graphene,” *ACS Nano*, vol. 11, no. 5, pp. 4641–4650, 2017.
- [53] I. Pletikosić, M. Kralj, P. Pervan, R. Brako, J. Coraux, A. T. N’Diaye, C. Busse, and T. Michely, “Dirac cones and minigaps for graphene on Ir(111),” *Physical Review Letters*, vol. 102, no. 5, p. 056808, 2009.
- [54] Y. Liu, Z. Qiu, A. Carvalho, Y. Bao, H. Xu, S. J. Tan, W. Liu, A. H. Castro Neto, K. P. Loh, and J. Lu, “Gate-Tunable Giant Stark Effect in Few-Layer Black Phosphorus,” *Nano Letters*, vol. 17, no. 3, pp. 1970–1977, 2017.

-
- [55] J. Kim, S. S. Baik, S. H. Ryu, Y. Sohn, S. Park, B. G. Park, J. Denlinger, Y. Yi, H. J. Choi, and K. S. Kim, “Observation of tunable band gap and anisotropic Dirac semimetal state in black phosphorus,” *Science*, vol. 349, no. 6249, pp. 723–726, 2015.
- [56] M. Javaid, S. P. Russo, K. Kalantar-Zadeh, A. D. Greentree, and D. W. Drumm, “Band structure and giant Stark effect in two-dimensional transition-metal dichalcogenides,” *Electronic Structure*, vol. 1, no. 1, p. 015005, 2018.
- [57] A. Grüneis, C. Attaccalite, A. Rubio, D. V. Vyalikh, S. L. Molodtsov, J. Fink, R. Follath, W. Eberhardt, B. Büchner, and T. Pichler, “Angle-resolved photoemission study of the graphite intercalation compound KC8: A key to graphene,” *Physical Review B*, vol. 80, no. 7, p. 075431, 2009.
- [58] M. Petrović, I. Šrut Rakić, S. Runte, C. Busse, J. T. Sadowski, P. Lazić, I. Pletikosić, Z. H. Pan, M. Milun, P. Pervan, N. Atodiresei, R. Brako, D. Šokčević, T. Valla, T. Michely, and M. Kralj, “The mechanism of caesium intercalation of graphene,” *Nature Communications*, vol. 4, no. 1, p. 2772, 2013.
- [59] K. Koāmider and J. Fernández-Rossier, “Electronic properties of the MoS₂-WS₂ heterojunction,” *Physical Review B*, vol. 87, no. 7, p. 075451, 2013.
- [60] E. V. Calman, M. M. Fogler, L. V. Butov, S. Hu, A. Mishchenko, and A. K. Geim, “Indirect excitons in van der Waals heterostructures at room temperature,” *Nature Communications*, vol. 9, no. 1, p. 1895, 2018.
- [61] Y. Cao, V. Fatemi, S. Fang, K. Watanabe, T. Taniguchi, E. Kaxiras, and P. Jarillo-Herrero, “Unconventional superconductivity in magic-angle graphene superlattices,” *Nature*, vol. 556, no. 7699, pp. 43–50, 2018.
- [62] E. Suárez Morell, J. D. Correa, P. Vargas, M. Pacheco, and Z. Barticevic, “Flat bands in slightly twisted bilayer graphene: Tight-binding calculations,” *Physical Review B*, vol. 82, no. 12, p. 121407, 2010.
- [63] S. Carr, D. Massatt, S. Fang, P. Cazeaux, M. Luskin, and E. Kaxiras, “Twistronics: Manipulating the electronic properties of two-dimensional layered structures through their twist angle,” *Physical Review B*, vol. 95, no. 7, p. 075420, 2017.
- [64] J. Coraux, A. T. N’Diaye, M. Engler, C. Busse, D. Wall, N. Buckanie, F.-J. Meyer zu Heringdorf, R. van Gastel, B. Poelsema, and T. Michely, “Growth of graphene on Ir(111),” *New Journal of Physics*, vol. 11, no. 2, p. 023006, 2009.

- [65] L. Gaudreau, K. J. Tielrooij, G. E. Prawiroatmodjo, J. Osmond, F. J. De Abajo, and F. H. Koppens, “Universal distance-scaling of nonradiative energy transfer to graphene,” *Nano Letters*, vol. 13, no. 5, pp. 2030–2035, 2013.
- [66] F. Federspiel, G. Froehlicher, M. Nasilowski, S. Pedetti, A. Mahmood, B. Doudin, S. Park, J.-O. Lee, D. Halley, B. Dubertret, P. Gilliot, and S. Berciaud, “Distance Dependence of the Energy Transfer Rate from a Single Semiconductor Nanostructure to Graphene,” *Nano Letters*, vol. 15, no. 2, pp. 1252–1258, 2015.
- [67] E. Malic, H. Appel, O. T. Hofmann, and A. Rubio, “Förster-induced energy transfer in functionalized graphene,” *Journal of Physical Chemistry C*, vol. 118, no. 17, pp. 9283–9289, 2014.
- [68] P. Matyba, A. Carr, C. Chen, D. L. Miller, G. Peng, S. Mathias, M. Mavrikakis, D. S. Dessau, M. W. Keller, H. C. Kapteyn, and M. Murnane, “Controlling the electronic structure of graphene using surface-adsorbate interactions,” *Physical Review B*, vol. 92, no. 4, p. 041407, 2015.
- [69] T. Ohta, A. Bostwick, J. L. McChesney, T. Seyller, K. Horn, and E. Rotenberg, “Interlayer interaction and electronic screening in multilayer graphene investigated with angle-resolved photoemission spectroscopy,” *Physical Review Letters*, vol. 98, p. 206802, 2007.
- [70] R. Gross and A. Marx, *Festkörperphysik*. de Gruyter, 2018.
- [71] R. Eisberg and R. Resnick, *Quantum Physics of Atoms, Molecules, Solids, Nuclei, and Particles, 2nd Edition*. Wiley, 1985.
- [72] T. Nilges, P. Schmidt, and R. Wehrich, “Phosphorus: The Allotropes, Stability, Synthesis, and Selected Applications,” in *Encyclopedia of Inorganic and Bioinorganic Chemistry* (R. A. Scott, ed.), Wiley, 2018.
- [73] F. Xia, H. Wang, and Y. Jia, “Rediscovering black phosphorus as an anisotropic layered material for optoelectronics and electronics,” *Nature Communications*, vol. 5, no. 1, p. 4458, 2014.
- [74] Y. Yi, X. F. Yu, W. Zhou, J. Wang, and P. K. Chu, “Two-dimensional black phosphorus: Synthesis, modification, properties, and applications,” *Materials Science and Engineering R: Reports*, vol. 120, no. 1, pp. 1–33, 2017.

- [75] P. W. Bridgman, "Two new modifications of phosphorus," *Journal of the American Chemical Society*, vol. 36, no. 7, pp. 1344–1363, 1914.
- [76] S. Fukuoka, T. Taen, and T. Osada, "Electronic structure and the properties of phosphorene and few-layer black phosphorus," *Journal of the Physical Society of Japan*, vol. 84, p. 121004, 2015.
- [77] A. Brown and S. Rundqvist, "Refinement of the crystal structure of black phosphorus," *Acta Crystallographica*, vol. 19, pp. 684–685, 1965.
- [78] D. W. Boukhvalov, A. N. Rudenko, D. A. Prishchenko, V. G. Mazurenko, and M. I. Katsnelson, "Chemical modifications and stability of phosphorene with impurities: A first principles study," *Physical Chemistry Chemical Physics*, vol. 17, no. 23, pp. 15209–15217, 2015.
- [79] T. H. Lee, S. Y. Kim, and H. W. Jang, "Black phosphorus: Critical review and potential for water splitting photocatalyst," *Nanomaterials*, vol. 6, no. 11, p. 194, 2016.
- [80] R. Gusmão, Z. Sofer, and M. Pumera, "Black Phosphorus Rediscovered: From Bulk Material to Monolayers," *Angewandte Chemie - International Edition*, vol. 56, no. 28, pp. 8052–8072, 2017.
- [81] J. Qiao, X. Kong, Z. X. Hu, F. Yang, and W. Ji, "High-mobility transport anisotropy and linear dichroism in few-layer black phosphorus," *Nature Communications*, vol. 5, no. 1, pp. 1–7, 2014.
- [82] J. O. Island and A. Castellanos-Gomez, "Black Phosphorus-Based Nanodevices," in *Semiconductors and Semimetals* (F. Iacopi, J. J. Boeckl, and J. Chennupati, eds.), pp. 279–303, Elsevier, 2016.
- [83] B. Radisavljevic, A. Radenovic, J. Brivio, V. Giacometti, and A. Kis, "Single-layer MoS₂ transistors," *Nature Nanotechnology*, vol. 6, no. 3, pp. 147–150, 2011.
- [84] R. Fivaz and E. Mooser, "Mobility of charge carriers in semiconducting layer structures," *Physical Review*, vol. 163, no. 3, p. 743, 1967.
- [85] J. Miao, L. Zhang, and C. Wang, "Black phosphorus electronic and optoelectronic devices," *2D Materials*, vol. 6, no. 3, p. 032003, 2019.

- [86] M. B. Tahir, N. Fatima, U. Fatima, and M. Sagir, "A review on the 2D black phosphorus materials for energy applications," *Inorganic Chemistry Communications*, vol. 124, p. 108242, 2021.
- [87] F. Xia, H. Wang, J. C. Hwang, A. H. Neto, and L. Yang, "Black phosphorus and its isoelectronic materials," *Nature Reviews Physics*, vol. 1, no. 4, pp. 306–317, 2019.
- [88] L. Li, Y. Yu, G. J. Ye, Q. Ge, X. Ou, H. Wu, D. Feng, X. H. Chen, and Y. Zhang, "Black phosphorus field-effect transistors," *Nature Nanotechnology*, vol. 9, no. 5, pp. 372–377, 2014.
- [89] H. Li, L. Ye, and J. Xu, "High-Performance Broadband Floating-Base Bipolar Phototransistor Based on WSe₂/BP/MoS₂ Heterostructure," *ACS Photonics*, vol. 4, no. 4, pp. 823–829, 2017.
- [90] G. Hu, T. Albrow-Owen, X. Jin, A. Ali, Y. Hu, R. C. Howe, K. Shehzad, Z. Yang, X. Zhu, R. I. Woodward, T. C. Wu, H. Jussila, J. B. Wu, P. Peng, P. H. Tan, Z. Sun, E. J. Kelleher, M. Zhang, Y. Xu, and T. Hasan, "Black phosphorus ink formulation for inkjet printing of optoelectronics and photonics," *Nature Communications*, vol. 8, no. 1, p. 278, 2017.
- [91] S. Y. Cho, Y. Lee, H. J. Koh, H. Jung, J. S. Kim, H. W. Yoo, J. Kim, and H. T. Jung, "Superior Chemical Sensing Performance of Black Phosphorus: Comparison with MoS₂ and Graphene," *Advanced Materials*, vol. 28, no. 32, pp. 7020–7028, 2016.
- [92] X. Y. Zhou, R. Zhang, J. P. Sun, Y. L. Zou, D. Zhang, W. K. Lou, F. Cheng, G. H. Zhou, F. Zhai, and K. Chang, "Landau levels and magneto-transport property of monolayer phosphorene," *Scientific Reports*, vol. 5, no. 1, p. 12295, 2015.
- [93] R. Fei, V. Tran, and L. Yang, "Topologically protected Dirac cones in compressed bulk black phosphorus," *Physical Review B*, vol. 91, no. 19, p. 195319, 2015.
- [94] S. S. Baik, K. S. Kim, Y. Yi, and H. J. Choi, "Emergence of Two-Dimensional Massless Dirac Fermions, Chiral Pseudospins, and Berrys Phase in Potassium Doped Few-Layer Black Phosphorus," *Nano Letters*, vol. 15, no. 12, pp. 7788–7793, 2015.

- [95] B. Ghosh, B. Singh, R. Prasad, and A. Agarwal, “Electric-field tunable Dirac semimetal state in phosphorene thin films,” *Physical Review B*, vol. 94, no. 20, p. 205426, 2016.
- [96] H. Hedayat, A. Ceraso, G. Soavi, S. Akhavan, A. Cadore, C. Dallera, G. Cerullo, A. C. Ferrari, and E. Carpene, “Non-equilibrium band broadening, gap renormalization and band inversion in black phosphorus,” *2D Materials*, vol. 8, no. 2, p. 025020, 2021.
- [97] R. Zhang, J. Waters, A. K. Geim, and I. V. Grigorieva, “Intercalant-independent transition temperature in superconducting black phosphorus,” *Nature Communications*, vol. 8, p. 15036, 2017.
- [98] Y. Feng, H. Sun, J. Sun, Z. Lu, and Y. You, “Prediction of phonon-mediated superconductivity in hole-doped black phosphorus,” *Journal of Physics Condensed Matter*, vol. 30, p. 015601, 2018.
- [99] X. Li, J. Sun, P. Shahi, M. Gao, A. H. MacDonald, Y. Uwatoko, T. Xiang, J. B. Goodenough, J. Cheng, and J. Zhou, “Pressure-induced phase transitions and superconductivity in a black phosphorus single crystal,” *Proceedings of the National Academy of Sciences of the United States of America*, vol. 115, no. 40, pp. 9935–9940, 2018.
- [100] M. Alidoust, M. Willatzen, and A. P. Jauho, “Control of superconducting pairing symmetries in monolayer black phosphorus,” *Physical Review B*, vol. 99, no. 12, p. 125417, 2019.
- [101] T. H. Choudhury, X. Zhang, Z. Y. Al Balushi, M. Chubarov, and J. M. Redwing, “Epitaxial Growth of Two-Dimensional Layered Transition Metal Dichalcogenides,” *Annual Review of Materials Research*, vol. 50, no. 1, pp. 155–177, 2020.
- [102] A. Y. Liu, “Electron-phonon coupling in compressed 1 T -TaS₂: Stability and superconductivity from first principles,” *Physical Review B*, vol. 79, no. 22, p. 220515, 2009.
- [103] M. Calandra, I. I. Mazin, and F. Mauri, “Effect of dimensionality on the charge-density wave in few-layer 2 H -NbSe₂,” *Physical Review B*, vol. 80, no. 24, p. 241108, 2009.

- [104] M. Johannes, I. Mazin, and C. Howells, “Fermi-surface nesting and the origin of the charge-density wave in NbSe₂,” *Physical Review B*, vol. 73, no. 20, p. 205102, 2006.
- [105] Y. Ge and A. Y. Liu, “First-principles investigation of the charge-density-wave instability in 1T-TaSe₂,” *Physical Review B*, vol. 82, no. 15, p. 155133, 2010.
- [106] J. Kačmarčík, Z. Pribulová, C. Marcenat, T. Klein, P. Rodière, L. Cario, and P. Samuely, “Specific heat measurements of a superconducting NbS₂ single crystal in an external magnetic field: Energy gap structure,” *Physical Review B*, vol. 82, no. 1, p. 014518, 2010.
- [107] C. Heil, S. Poncé, H. Lambert, M. Schlipf, E. R. Margine, and F. Giustino, “Origin of Superconductivity and Latent Charge Density Wave in NbS₂,” *Physical Review Letters*, vol. 119, no. 8, p. 087003, 2017.
- [108] Y. Kim, S. Lee, J. G. Song, K. Y. Ko, W. J. Woo, S. W. Lee, M. Park, H. Lee, Z. Lee, H. Choi, W. H. Kim, J. Park, and H. Kim, “2D Transition Metal Dichalcogenide Heterostructures for p- and n-Type Photovoltaic Self-Powered Gas Sensor,” *Advanced Functional Materials*, vol. 30, no. 43, p. 2003360, 2020.
- [109] H. Wang, F. Liu, W. Fu, Z. Fang, W. Zhou, and Z. Liu, “Two-dimensional heterostructures: Fabrication, characterization, and application,” *Nanoscale*, vol. 6, no. 21, pp. 12250–12272, 2014.
- [110] T. Niu and A. Li, “From two-dimensional materials to heterostructures,” *Progress in Surface Science*, vol. 90, no. 1, pp. 21–45, 2015.
- [111] S. Manzeli, D. Ovchinnikov, D. Pasquier, O. V. Yazyev, and A. Kis, “2D transition metal dichalcogenides,” *Nature Reviews Materials*, vol. 2, no. 6, p. 17033, 2017.
- [112] E. Cappelluti, R. Roldán, J. A. Silva-Guillén, P. Ordejón, and F. Guinea, “Tight-binding model and direct-gap/indirect-gap transition in single-layer and multi-layer MoS₂,” *Physical Review B*, vol. 88, no. 7, p. 075409, 2013.
- [113] E. Ridolfi, D. Le, T. S. Rahman, E. R. Mucciolo, and C. H. Lewenkopf, “A tight-binding model for MoS₂ monolayers,” *Journal of Physics: Condensed Matter*, vol. 27, no. 36, p. 365501, 2015.

- [114] N. Ehlen, *Spectroscopic characterization of 1H-MoS2 and 1H-TaS2*. Msc thesis, University of Cologne, 2019.
- [115] D. Gupta, V. Chauhan, and R. Kumar, “A comprehensive review on synthesis and applications of molybdenum disulfide (MoS₂) material: Past and recent developments,” *Inorganic Chemistry Communications*, vol. 121, p. 108200, 2020.
- [116] M. M. Ugeda, A. J. Bradley, S.-F. Shi, F. H. da Jornada, Y. Zhang, D. Y. Qiu, W. Ruan, S.-K. Mo, Z. Hussain, Z.-X. Shen, F. Wang, S. G. Louie, and M. F. Crommie, “Giant bandgap renormalization and excitonic effects in a monolayer transition metal dichalcogenide semiconductor,” *Nature Materials*, vol. 13, no. 12, pp. 1091–1095, 2014.
- [117] X. Fan, D. J. Singh, and W. Zheng, “Valence Band Splitting on Multilayer MoS₂: Mixing of Spin-Orbit Coupling and Interlayer Coupling,” *Journal of Physical Chemistry Letters*, vol. 7, no. 12, pp. 2175–2181, 2016.
- [118] G. Wang, A. Chernikov, M. M. Glazov, T. F. Heinz, X. Marie, T. Amand, and B. Urbaszek, “Excitons in atomically thin transition metal dichalcogenides,” *Reviews of Modern Physics*, vol. 90, no. 2, p. 21001, 2017.
- [119] S. Oh and H. J. Choi, “Orbital angular momentum analysis for giant spin splitting in solids and nanostructures,” *Scientific Reports*, vol. 7, no. 1, p. 2024, 2017.
- [120] D. Shin, H. Hübener, U. De Giovannini, H. Jin, A. Rubio, and N. Park, “Phonon-driven spin-Floquet magneto-valleytronics in MoS₂,” *Nature Communications*, vol. 9, no. 1, p. 638, 2018.
- [121] J. Henk, A. Ernst, and P. Bruno, “Spin polarization of the L-gap surface states on Au(111),” *Physical Review B*, vol. 68, no. 16, p. 165419, 2003.
- [122] Z. Y. Zhu, Y. C. Cheng, and U. Schwingenschlögl, “Giant spin-orbit-induced spin splitting in two-dimensional transition-metal dichalcogenide semiconductors,” *Physical Review B*, vol. 84, no. 15, p. 153402, 2011.
- [123] D. Xiao, G. B. Liu, W. Feng, X. Xu, and W. Yao, “Coupled spin and valley physics in monolayers of MoS₂ and other group-VI dichalcogenides,” *Physical Review Letters*, vol. 108, no. 19, p. 196802, 2012.

- [124] Z. Gong, G. B. Liu, H. Yu, D. Xiao, X. Cui, X. Xu, and W. Yao, “Magnetoelectric effects and valley-controlled spin quantum gates in transition metal dichalcogenide bilayers,” *Nature Communications*, vol. 4, no. 1, p. 2053, 2013.
- [125] G. B. Liu, W. Y. Shan, Y. Yao, W. Yao, and D. Xiao, “Three-band tight-binding model for monolayers of group-VIB transition metal dichalcogenides,” *Physical Review B*, vol. 88, no. 8, p. 085433, 2013.
- [126] J. G. Roch, G. Froehlicher, N. Leisgang, P. Makk, K. Watanabe, T. Taniguchi, and R. J. Warburton, “Spin-polarized electrons in monolayer MoS₂,” 2019.
- [127] F. Zahid, L. Liu, Y. Zhu, J. Wang, and H. Guo, “A generic tight-binding model for monolayer, bilayer and bulk MoS₂,” *AIP Advances*, vol. 3, no. 5, p. 05211, 2013.
- [128] H. Zeng, J. Dai, W. Yao, D. Xiao, and X. Cui, “Valley polarization in MoS₂ monolayers by optical pumping,” *Nature Nanotechnology*, vol. 7, no. 8, pp. 490–493, 2012.
- [129] Y. T. Wang, C. W. Luo, A. Yabushita, K. H. Wu, T. Kobayashi, C. H. Chen, and L. J. Li, “Ultrafast Multi-Level Logic Gates with Spin-Valley Coupled Polarization Anisotropy in Monolayer MoS₂,” *Scientific Reports*, vol. 5, p. 8289, 2015.
- [130] R. Pisoni, A. Kormányos, M. Brooks, Z. Lei, P. Back, M. Eich, H. Overweg, Y. Lee, P. Rickhaus, K. Watanabe, T. Taniguchi, A. Imamoglu, G. Burkard, T. Ihn, and K. Ensslin, “Interactions and Magnetotransport through Spin-Valley Coupled Landau Levels in Monolayer MoS₂,” *Physical Review Letters*, vol. 121, no. 24, p. 247701, 2018.
- [131] J. R. Schaibley, H. Yu, G. Clark, P. Rivera, J. S. Ross, K. L. Seyler, W. Yao, and X. Xu, “Valleytronics in 2D materials,” *Nature Reviews Materials*, vol. 1, p. 16055, 2016.
- [132] E. C. Ahn, “2D materials for spintronic devices,” *npj 2D Materials and Applications*, vol. 4, p. 17, 2020.
- [133] W. Han, “Perspectives for spintronics in 2D materials,” *APL Materials*, vol. 4, p. 032401, 2016.

- [134] K. F. Mak, K. L. McGill, J. Park, and P. L. McEuen, “The valley hall effect in MoS₂ transistors,” *Science*, vol. 344, no. 6191, pp. 1489–1492, 2014.
- [135] Y. Liu, Y. Gao, S. Zhang, J. He, J. Yu, and Z. Liu, “Valleytronics in transition metal dichalcogenides materials,” *Nano Research*, vol. 12, pp. 2695–2711, 2019.
- [136] Y. K. Luo, J. Xu, T. Zhu, G. Wu, E. J. McCormick, W. Zhan, M. R. Neupane, and R. K. Kawakami, “Opto-valleytronic spin injection in monolayer MoS₂/few-layer graphene hybrid spin valves,” *Nano Letters*, vol. 17, no. 6, pp. 3877–3883, 2017.
- [137] A. H. Castro Neto, F. Guinea, N. M. Peres, K. S. Novoselov, and A. K. Geim, “The electronic properties of graphene,” *Reviews of Modern Physics*, vol. 81, p. 109, 2009.
- [138] E. McCann and M. Koshino, “The electronic properties of bilayer graphene,” *Reports on Progress in Physics*, vol. 76, no. 5, p. 056503, 2013.
- [139] A. V. Rozhkov, A. O. Sboychakov, A. L. Rakhmanov, and F. Nori, “Electronic properties of graphene-based bilayer systems,” *Physics Reports*, vol. 64, pp. 1–104, 2016.
- [140] P. R. Wallace, “The band theory of graphite,” *Physical Review*, vol. 71, no. 9, p. 622, 1947.
- [141] R. Saito, G. Dresselhaus, and M. S. Dresselhaus, *Physical Properties of Carbon Nanotubes*. Imperial College Press, 1998.
- [142] R. Skomski, P. A. Dowben, M. Sky Driver, and J. A. Kelber, “Sublattice-induced symmetry breaking and band-gap formation in graphene,” *Materials Horizons*, vol. 1, no. 6, pp. 563–571, 2014.
- [143] A. Bostwick, T. Ohta, J. L. McChesney, K. V. Emtsev, T. Seyller, K. Horn, and E. Rotenberg, “Symmetry breaking in few layer graphene films,” *New Journal of Physics*, vol. 9, p. 385, 2007.
- [144] J. Sławińska, I. Zasada, and Z. Klusek, “Energy gap tuning in graphene on hexagonal boron nitride bilayer system,” *Physical Review B*, vol. 81, no. 15, p. 155433, 2010.

- [145] E. Doni and G. P. Parravicini, “Energy bands and optical properties of hexagonal boron nitride and graphite,” *Il Nuovo Cimento B Series 10*, vol. 64, pp. 117–144, 1969.
- [146] U. R. Singh, M. Prada, V. Strenzke, B. Bosnjak, T. Schmirander, L. Tiemann, and R. H. Blick, “Sublattice symmetry breaking and ultralow energy excitations in graphene-on- hBN heterostructures,” *Physical Review B*, vol. 102, no. 24, p. 245134, 2020.
- [147] L. Yan, M. Hua, Q. Zhang, T. U. Ngai, Z. Guo, T. C. Wu, T. Wang, and N. Lin, “Symmetry breaking in molecular artificial graphene,” *New Journal of Physics*, vol. 21, p. 083005, 2019.
- [148] S. Berciaud, M. Potemski, and C. Faugeras, “Probing electronic excitations in mono- to pentalayer graphene by micro magneto-raman spectroscopy,” *Nano Letters*, vol. 14, no. 8, pp. 4548–4553, 2014.
- [149] P. Goswami, “Theoretical elucidation of possibility of Majorana modes in a two dimensional Dirac system,” *arXiv*, 2014.
- [150] M. I. Katsnelson, K. S. Novoselov, and A. K. Geim, “Chiral tunnelling and the Klein paradox in graphene,” *Nature Physics*, vol. 2, p. 620625, 2006.
- [151] Y. Liu, G. Bian, T. Miller, and T. C. Chiang, “Visualizing electronic chirality and Berry phases in graphene systems using photoemission with circularly polarized light,” *Physical Review Letters*, vol. 107, p. 166803, 2011.
- [152] M. L. Sadowski, G. Martinez, M. Potemski, C. Berger, and W. A. De Heer, “Landau level spectroscopy of ultrathin graphite layers,” *Physical Review Letters*, vol. 97, p. 266405, 2006.
- [153] D. Haberer, L. Petaccia, A. V. Fedorov, C. S. Praveen, S. Fabris, S. Piccinin, O. Vilkov, D. V. Vyalikh, A. Preobrajenski, N. I. Verbitskiy, H. Shiozawa, J. Fink, M. Knupfer, B. Büchner, and A. Grüneis, “Anisotropic Eliashberg function and electron-phonon coupling in doped graphene,” *Physical Review B*, vol. 88, no. 8, p. 081401, 2013.
- [154] J. Chapman, Y. Su, C. A. Howard, D. Kundys, A. N. Grigorenko, F. Guinea, A. K. Geim, I. V. Grigorieva, and R. R. Nair, “Superconductivity in Ca-doped graphene laminates,” *Scientific Reports*, vol. 6, p. 23254, 2016.

- [155] A. M. Black-Schaffer and C. Honerkamp, “Chiral d-wave superconductivity in doped graphene,” *Journal of Physics Condensed Matter*, vol. 26, p. 423201, 2014.
- [156] D. Makogon, R. Van Gelderen, R. Roldán, and C. M. Smith, “Spin-density-wave instability in graphene doped near the van Hove singularity,” *Physical Review B*, vol. 84, no. 12, p. 125404, 2011.
- [157] C. Honerkamp, “Density waves and cooper pairing on the honeycomb lattice,” *Physical Review Letters*, vol. 100, p. 146404, 2008.
- [158] I. F. Herbut, “Interactions and phase transitions on Graphene’s honeycomb lattice,” *Physical Review Letters*, vol. 97, p. 146401, 2006.
- [159] M. L. Kiesel, C. Platt, W. Hanke, D. A. Abanin, and R. Thomale, “Competing many-body instabilities and unconventional superconductivity in graphene,” *Physical Review B*, vol. 86, no. 2, p. 020507, 2012.
- [160] P. Rosenzweig, H. Karakachian, D. Marchenko, K. Küster, and U. Starke, “Overdoping Graphene beyond the van Hove Singularity,” *Physical Review Letters*, vol. 125, p. 176403, 2020.
- [161] C. Struzzi, C. S. Praveen, M. Scardamaglia, N. I. Verbitskiy, A. V. Fedorov, M. Weinl, M. Schreck, A. Grüneis, S. Piccinin, S. Fabris, and L. Petaccia, “Controlled thermodynamics for tunable electron doping of graphene on Ir(111),” *Physical Review B*, vol. 94, no. 8, p. 085427, 2016.
- [162] D. Szczśniak, “Superconducting properties of lithium-decorated bilayer graphene,” *Europhysics Letters*, vol. 111, no. 1, p. 18003, 2015.
- [163] E. R. Margine, H. Lambert, and F. Giustino, “Electron-phonon interaction and pairing mechanism in superconducting Ca-intercalated bilayer graphene,” *Scientific Reports*, vol. 6, p. 21414, 2016.
- [164] A. P. Durajski, K. M. Skoczylas, and R. Szcześniak, “Superconductivity in bilayer graphene intercalated with alkali and alkaline earth metals,” *Physical Chemistry Chemical Physics*, vol. 21, pp. 5925–5931, 2019.
- [165] K. Kanetani, K. Sugawara, T. Sato, R. Shimizu, K. Iwaya, T. Hitosugi, and T. Takahashi, “Ca intercalated bilayer graphene as a thinnest limit of superconducting C₆Ca,” *Proceedings of the National Academy of Sciences of the United States of America*, vol. 109, no. 48, pp. 19610–19613, 2012.

- [166] S. C. Fang, X. J. Zheng, H. Q. Lin, and Z. B. Huang, “Electric field-induced chiral $d + id$ superconductivity in AA-stacked bilayer graphene: A quantum Monte Carlo study,” *Journal of Physics Condensed Matter*, vol. 33, p. 025601, 2021.
- [167] Z. Qiao, X. Li, W. K. Tse, H. Jiang, Y. Yao, and Q. Niu, “Topological phases in gated bilayer graphene: Effects of Rashba spin-orbit coupling and exchange field,” *Physical Review B*, vol. 87, no. 12, p. 125405, 2013.
- [168] Z. Qiao, W. K. Tse, H. Jiang, Y. Yao, and Q. Niu, “Two-dimensional topological insulator state and topological phase transition in bilayer graphene,” *Physical Review Letters*, vol. 107, p. 256801, 2011.
- [169] H. Yoo, R. Engelke, S. Carr, S. Fang, K. Zhang, P. Cazeaux, S. H. Sung, R. Hovden, A. W. Tsen, T. Taniguchi, K. Watanabe, G. C. Yi, M. Kim, M. Luskin, E. B. Tadmor, E. Kaxiras, and P. Kim, “Atomic and electronic reconstruction at the van der Waals interface in twisted bilayer graphene,” *Nature Materials*, vol. 18, pp. 448–453, 2019.
- [170] H. Hertz, “Ueber einen Einfluss des ultravioletten Lichtes auf die elektrische Entladung,” *Annalen der Physik und Chemie*, vol. 267, no. 8, pp. 983–1000, 1887.
- [171] A. Einstein, “Über einen die Erzeugung und Verwandlung des Lichtes betreffenden heuristischen Gesichtspunkt,” *Annalen der Physik*, vol. 322, no. 6, pp. 132–148, 1905.
- [172] A. Damascelli, Z. Hussain, and Z.-X. Shen, “Angle-resolved photoemission studies of the cuprate superconductors,” *Reviews of Modern Physics*, vol. 75, no. 2, pp. 473–541, 2003.
- [173] A. Damascelli, “Probing the Electronic Structure of Complex Systems by ARPES,” *Physica Scripta*, vol. T109, no. T109, p. 61, 2004.
- [174] A. T. Paxton, “An Introduction to the Tight Binding Approximation – Implementation by Diagonalisation,” in *NIC Series Volume 42 : Multiscale Simulation Methods in Molecular Sciences*, ch. 5, pp. 145–176, John von Neumann Institute for Computing Jülich, 2009.
- [175] K. F. Henrik Bruus, *Many-Body Quantum Theory in Condensed Matter Physics—An Introduction*. Oxford University Press, 2004.

- [176] A. Altland and B. Simons, *Condensed Matter Field Theory*. Cambridge University Press, 2006.
- [177] L. D. Landau, “ON THE THEORY OF THE FERMI LIQUID,” in *Collected Papers of L.D. Landau*, pp. 752–760, Pergamon Press, 1965.
- [178] L. D. Landau, “The Theory of a Fermi Liquid,” *Zh. Eksp. Teor. Fiz.*, vol. 30, no. 6, p. 1058, 1956.
- [179] G. Baym and C. Pethick, *Landau Fermi-Liquid Theory: Concepts and Applications*. Wiley, 2007.
- [180] J. Fink, S. Borisenko, A. Kordyuk, A. Koitzsch, J. Geck, V. Zabolotnyy, M. Knupfer, B. Büchner, and H. Berger, “Dressing of the charge carriers in high-Tc superconductors,” in *Very High Resolution Photoelectron Spectroscopy*, pp. 295–325, Springer, 2007.
- [181] N. J. Ingle, K. M. Shen, F. Baumberger, W. Meevasana, D. H. Lu, Z. X. Shen, A. Damascelli, S. Nakatsuji, Z. Q. Mao, Y. Maeno, T. Kimura, and Y. Tokura, “Quantitative analysis of Sr₂RuO₄ angle-resolved photoemission spectra: Many-body interactions in a model Fermi liquid,” *Physical Review B*, vol. 72, no. 20, p. 205114, 2005.
- [182] M. r. n. D. Inosov, *Angle-Resolved Photoelectron Spectroscopy Studies of the Many-Body Effects in the Electronic Structure of High-Tc Cuprates*. PhD thesis, TU Dresden, 2008.
- [183] J. J. Quinn and R. A. Ferrell, “Electron self-energy approach to correlation in a degenerate electron gas,” *Physical Review*, vol. 112, no. 3, p. 812, 1958.
- [184] D. Coffey and K. S. Bedell, “Nonanalytic contributions to the self-energy and the thermodynamics of two-dimensional fermi liquids,” *Physical Review Letters*, vol. 71, p. 1043, 1993.
- [185] A. V. Chubukov, D. L. Maslov, S. Gangadharaiah, and L. I. Glazman, “Singular perturbation theory for interacting fermions in two dimensions,” *Physical Review B*, vol. 71, no. 20, p. 205112, 2005.
- [186] S. Gangadharaiah, D. L. Maslov, A. V. Chubukov, and L. I. Glazman, “Interacting fermions in two dimensions: Beyond the perturbation theory,” *Physical Review Letters*, vol. 94, p. 156407, 2005.

- [187] P. Hofmann, I. Y. Sklyadneva, E. D. Rienks, and E. V. Chulkov, “Electron-phonon coupling at surfaces and interfaces,” *New Journal of Physics*, vol. 11, p. 125005, 2009.
- [188] C. Kirkegaard, T. K. Kim, and P. Hofmann, “Self-energy determination and electron-phonon coupling on Bi(110),” *New Journal of Physics*, vol. 7, p. 99, 2005.
- [189] M. R. Norman, H. Ding, H. Fretwell, M. Randeria, and J. C. Campuzano, “Extraction of the electron self-energy from angle-resolved photoemission data: Application to $\text{Bi}_2\text{Sr}_2\text{CaCu}_2\text{O}_{8+x}$,” *Physical Review B*, vol. 60, no. 10, p. 7585, 1999.
- [190] A. Sanna, J. A. Flores-Livas, A. Davydov, G. Profeta, K. Dewhurst, S. Sharma, and E. K. Gross, “Ab initio eliashberg theory: Making genuine predictions of superconducting features,” *Journal of the Physical Society of Japan*, vol. 87, p. 041012, 2018.
- [191] J. Shi, S. J. Tang, B. Wu, P. T. Sprunger, W. L. Yang, V. Brouet, X. J. Zhou, Z. Hussain, Z. X. Shen, Z. Zhang, and E. W. Plummer, “Direct extraction of the eliashberg function for electron-phonon coupling: A case study of $\text{Be}(10\bar{1}0)$,” *Physical Review Letters*, vol. 92, p. 186401, 2004.
- [192] D. J. Griffiths, *Introduction to Electrodynamics*. Cambridge University Press, 2005.
- [193] M. Fox, *A Student’s Guide to Atomic Physics*. Cambridge University Press, 2018.
- [194] H. A. Kramers, “Théorie générale de la rotation paramagnétique dans les cristaux,” *Proceedings of the Royal Netherlands Academy of Arts and Sciences*, vol. 33, no. 6-10, pp. 959–972, 1930.
- [195] X. Mao, Z. Liu, J. Li, C. Li, S. Teng, Y. Liu, and X. Xu, “Induced valley and spin splitting in monolayer MoS_2 by interfacial magnetic proximity of half-Heusler LiBeN substrate,” *Journal of Magnetism and Magnetic Materials*, vol. 512, p. 167061, 2020.
- [196] P. Pfeffer and W. Zawadzki, “Spin splitting of conduction subbands in III-V heterostructures due to inversion asymmetry,” *Physical Review B*, vol. 59, no. 8, p. R5312, 1999.

- [197] C. R. Ast and I. Gierz, “Sp-band tight-binding model for the Bychkov-Rashba effect in a two-dimensional electron system including nearest-neighbor contributions from an electric field,” *Physical Review B*, vol. 86, no. 8, p. 085105, 2012.
- [198] L. Petersen and P. Hedegård, “Simple tight-binding model of spin-orbit splitting of sp-derived surface states,” *Surface Science*, vol. 459, no. 1-2, pp. 49–56, 2000.
- [199] S. Konschuh, M. Gmitra, and J. Fabian, “Tight-binding theory of the spin-orbit coupling in graphene,” *Physical Review B*, vol. 82, no. 24, p. 245412, 2010.
- [200] E. I. Rashba, “Properties of semiconductors with an extremum loop. I. Cyclotron and combinational resonance in a magnetic field perpendicular to the plane of the loop,” *Soviet Physics, Solid State*, vol. 2, pp. 1109–1122, 1960.
- [201] G. Dresselhaus, “Spin-Orbit Coupling Effects in Zinc Blende Structures,” *Physical Review*, vol. 100, no. 2, pp. 580–586, 1955.
- [202] A. N. Rudenko, S. Yuan, and M. I. Katsnelson, “Toward a realistic description of multilayer black phosphorus: From GW approximation to large-scale tight-binding simulations,” *Physical Review B*, vol. 92, no. 8, p. 085419, 2015.
- [203] A. P. Horsfield and A. M. Bratkovsky, “Ab initio tight binding,” *Journal of Physics Condensed Matter*, vol. 12, no. 2, p. R1, 2000.
- [204] D. Y. Usachov, “Angular Mapping Modes for ARPES,” tech. rep., St Petersburg State University.
- [205] M. Fox, *Optical properties of solids*. Oxford University Press, 2 ed., 2013.
- [206] C. Herbig, T. Knispel, S. Simon, U. A. Schröder, A. J. Martínez-Galera, M. A. Arman, C. Teichert, J. Knudsen, A. V. Krasheninnikov, and T. Michely, “From Permeation to Cluster Arrays: Graphene on Ir(111) Exposed to Carbon Vapor,” *Nano Letters*, vol. 17, no. 5, pp. 3105–3112, 2017.
- [207] W. Jolie, J. Lux, M. Pörtner, D. Dombrowski, C. Herbig, T. Knispel, S. Simon, T. Michely, A. Rosch, and C. Busse, “Suppression of Quasiparticle Scattering Signals in Bilayer Graphene Due to Layer Polarization and Destructive Interference,” *Physical Review Letters*, vol. 120, p. 106801, 2018.
- [208] H. Jiang, H. Shi, X. Sun, and B. Gao, “Optical Anisotropy of Few-Layer Black Phosphorus Visualized by Scanning Polarization Modulation Microscopy,” *ACS Photonics*, vol. 5, no. 6, pp. 2509–2515, 2018.

- [209] Q. Zeng, B. Sun, K. Du, W. Zhao, P. Yu, C. Zhu, J. Xia, Y. Chen, X. Cao, Q. Yan, Z. Shen, T. Yu, Y. Long, Y. K. Koh, and Z. Liu, “Highly anisotropic thermoelectric properties of black phosphorus crystals,” *2D Materials*, vol. 6, no. 4, p. 045009, 2019.
- [210] H. Liu, A. T. Neal, Z. Zhu, Z. Luo, X. Xu, D. Tománek, and P. D. Ye, “Phosphorene: An unexplored 2D semiconductor with a high hole mobility,” *ACS Nano*, vol. 8, no. 4, pp. 4033–4041, 2014.
- [211] X. Chen, L. Wang, Y. Wu, H. Gao, Y. Wu, G. Qin, Z. Wu, Y. Han, S. Xu, T. Han, W. Ye, J. Lin, G. Long, Y. He, Y. Cai, W. Ren, and N. Wang, “Probing the electronic states and impurity effects in black phosphorus vertical heterostructures,” *2D Materials*, vol. 3, no. 1, p. 015012, 2016.
- [212] S. Zhang, J. Yang, R. Xu, F. Wang, W. Li, M. Ghufran, Y. W. Zhang, Z. Yu, G. Zhang, Q. Qin, and Y. Lu, “Extraordinary photoluminescence and strong temperature/angle-dependent raman responses in few-layer phosphorene,” *ACS Nano*, vol. 8, no. 9, pp. 9590–9596, 2014.
- [213] J. Yang, R. Xu, J. Pei, Y. W. Myint, F. Wang, Z. Wang, S. Zhang, Z. Yu, and Y. Lu, “Optical tuning of exciton and trion emissions in monolayer phosphorene,” *Light: Science and Applications*, vol. 4, no. 7, p. 312, 2015.
- [214] V. Tran, R. Soklaski, Y. Liang, and L. Yang, “Layer-controlled band gap and anisotropic excitons in few-layer black phosphorus,” *Physical Review B*, vol. 89, no. 23, p. 235319, 2014.
- [215] A. Sanna, A. V. Fedorov, N. I. Verbitskiy, J. Fink, C. Krellner, L. Petaccia, A. Chikina, D. Y. Usachov, A. Grüneis, and G. Profeta, “First-principles and angle-resolved photoemission study of lithium doped metallic black phosphorous,” *2D Materials*, vol. 3, p. 025031, 2016.
- [216] M. Yi and Z. Shen, “A review on mechanical exfoliation for the scalable production of graphene,” *Journal of Materials Chemistry A*, vol. 3, pp. 11700–11715, 2015.
- [217] N. Ehlen, *Tight Binding Description of Alkali Metal Doped Phosphorene*. Bsc thesis, University of Cologne, 2015.
- [218] J. C. Slater and G. F. Koster, “Simplified LCAO Method for the Periodic Potential Problem,” *Physical Review*, vol. 94, no. 6, pp. 1498–1524, 1954.

- [219] Q. Liu, X. Zhang, L. B. Abdalla, A. Fazio, and A. Zunger, “Switching a normal insulator into a topological insulator via electric field with application to phosphorene,” *Nano Letters*, vol. 15, no. 2, pp. 1222–1228, 2015.
- [220] S. Yuan, E. Van Veen, M. I. Katsnelson, and R. Roldán, “Quantum Hall effect and semiconductor-to-semimetal transition in biased black phosphorus,” *Physical Review B*, vol. 93, no. 24, p. 245433, 2016.
- [221] A. Bruix, H. G. Füchtbauer, A. K. Tuxen, A. S. Walton, M. Andersen, S. Porsgaard, F. Besenbacher, B. Hammer, and J. V. Lauritsen, “In Situ Detection of Active Edge Sites in Single-Layer MoS₂ Catalysts,” *ACS Nano*, vol. 9, no. 9, pp. 9322–9330, 2015.
- [222] X. Li, Z. Yu, X. Xiong, T. Li, T. Gao, R. Wang, R. Huang, and Y. Wu, “High-speed black phosphorus field-effect transistors approaching ballistic limit,” *Science Advances*, vol. 5, no. 6, p. eaau3194, 2019.
- [223] C. E. Sanders, M. Dendzik, A. S. Ngankeu, A. Eich, A. Bruix, M. Bianchi, J. A. Miwa, B. Hammer, A. A. Khajetoorians, and P. Hofmann, “Crystalline and electronic structure of single-layer TaS₂,” *Physical Review B*, vol. 94, no. 8, p. 081404, 2016.
- [224] T. O. Wehling, E. Şaşlıoğlu, C. Friedrich, A. I. Lichtenstein, M. I. Katsnelson, and S. Blügel, “Strength of effective coulomb interactions in graphene and graphite,” *Physical Review Letters*, vol. 106, no. 23, p. 236805, 2011.
- [225] WaveMetrics, “IGOR Pro,” 2016.
- [226] G. Van Rossum and F. L. Drake, “Python 3 Tutorial,” *Python Software Foundation (docs@python.org)*, 2012.
- [227] J. D. Hunter, “Matplotlib: A 2D graphics environment,” *Computing in Science and Engineering*, vol. 9, no. 3, pp. 90—95, 2007.
- [228] P. Ramachandran and G. Varoquaux, “Mayavi: 3D visualization of scientific data,” *Computing in Science and Engineering*, 2011.
- [229] Blender-Online-Community, “Blender - a 3D modelling and rendering package,” tech. rep., Blender Foundation, Stichting Blender Foundation, Amsterdam, 2020.

- [230] C. R. Harris, K. J. Millman, S. J. van der Walt, R. Gommers, P. Virtanen, D. Cournapeau, E. Wieser, J. Taylor, S. Berg, N. J. Smith, R. Kern, M. Picus, S. Hoyer, M. H. van Kerkwijk, M. Brett, A. Haldane, J. F. del Río, M. Wiebe, P. Peterson, P. Gérard-Marchant, K. Sheppard, T. Reddy, W. Weckesser, H. Abbasi, C. Gohlke, and T. E. Oliphant, “Array programming with NumPy,” *Nature*, vol. 585, no. 7825, pp. 357—362, 2020.
- [231] P. Virtanen, R. Gommers, T. E. Oliphant, M. Haberland, T. Reddy, D. Cournapeau, E. Burovski, P. Peterson, W. Weckesser, J. Bright, S. J. van der Walt, M. Brett, J. Wilson, K. J. Millman, N. Mayorov, A. R. Nelson, E. Jones, R. Kern, E. Larson, C. J. Carey, I. Polat, Y. Feng, E. W. Moore, J. VanderPlas, D. Laxalde, J. Perktold, R. Cimrman, I. Henriksen, E. A. Quintero, C. R. Harris, A. M. Archibald, A. H. Ribeiro, F. Pedregosa, P. van Mulbregt, A. Vijaykumar, A. P. Bardelli, A. Rothberg, A. Hilboll, A. Kloeckner, A. Scopatz, A. Lee, A. Rokem, C. N. Woods, C. Fulton, C. Masson, C. Häggström, C. Fitzgerald, D. A. Nicholson, D. R. Hagen, D. V. Pasechnik, E. Olivetti, E. Martin, E. Wieser, F. Silva, F. Lenders, F. Wilhelm, G. Young, G. A. Price, G. L. Ingold, G. E. Allen, G. R. Lee, H. Audren, I. Probst, J. P. Dietrich, J. Silterra, J. T. Webber, J. Slavič, J. Nothman, J. Buchner, J. Kulick, J. L. Schönberger, J. V. de Miranda Cardoso, J. Reimer, J. Harrington, J. L. C. Rodríguez, J. Nunez-Iglesias, J. Kuczynski, K. Tritz, M. Thoma, M. Newville, M. Kümmerer, M. Bolingbroke, M. Tartre, M. Pak, N. J. Smith, N. Nowaczyk, N. Shebanov, O. Pavlyk, P. A. Brodtkorb, P. Lee, R. T. McGibbon, R. Feldbauer, S. Lewis, S. Tygier, S. Sievert, S. Vigna, S. Peterson, S. More, T. Pudlik, T. Oshima, T. J. Pingel, T. P. Robitaille, T. Spura, T. R. Jones, T. Cera, T. Leslie, T. Zito, T. Krauss, U. Upadhyay, Y. O. Halchenko, and Y. Vázquez-Baeza, “SciPy 1.0: fundamental algorithms for scientific computing in Python,” *Nature Methods*, vol. 17, pp. 261–272, 2020.

Appendix A

Appendix

A.1 Momentum Space Wave Function of the Infinite Quantum Well

The momentum space wavefunctions of the infinite quantum well can be determined by a Fourier transform of the position space wave functions. The position space wave functions of the centered infinite square well with width L are given by [71]

$$\psi_n(x) = \begin{cases} \sqrt{\frac{2}{L}} \sin(k_n x), & \text{for } n \text{ even} \\ \sqrt{\frac{2}{L}} \cos(k_n x), & \text{for } n \text{ odd} \end{cases} \quad (\text{A.1})$$

$$k_n = \frac{n\pi}{L}. \quad (\text{A.2})$$

The Fourier transform for even n is given by

$$\Phi_{n \text{ even}}(p) = \frac{1}{\sqrt{2\pi\hbar}} \int_{-L/2}^{L/2} \psi_n(x) \exp(-ikx) dx \quad (\text{A.3})$$

$$\begin{aligned} &= \frac{-i}{\sqrt{4\pi\hbar L}} \int_{-L/2}^{L/2} (e^{i(k_n-k)x} - e^{-i(k_n+k)x}) dx \\ &= \frac{-i}{\sqrt{4\pi\hbar L}} \left\{ \frac{-i}{k_n - k} [e^{i(k_n-k)x}]_{-L/2}^{L/2} - \frac{i}{k_n + k} [e^{-i(k_n+k)x}]_{-L/2}^{L/2} \right\} \\ &= -\frac{iL}{\sqrt{4\pi\hbar L}} \left\{ \frac{1}{\frac{1}{2}(n\pi - kL)} \sin\left(\frac{1}{2}(n\pi - kL)\right) \right. \\ &\quad \left. - \frac{1}{\frac{1}{2}(n\pi + kL)} \sin\left(\frac{1}{2}(n\pi + kL)\right) \right\}. \quad (\text{A.4}) \end{aligned}$$

The last line can be further simplified by considering that for even n it is

$$\sin\left(n\frac{\pi}{2} + k\frac{L}{2}\right) = -\sin\left(n\frac{\pi}{2} - k\frac{L}{2}\right) \quad (\text{A.5})$$

and thus

$$\frac{1}{\frac{1}{2}(n\pi + kL)} \sin\left(\frac{1}{2}(n\pi + kL)\right) = -\frac{\frac{1}{2}(n\pi - kL) \sin\left(\frac{1}{2}(n\pi - kL)\right)}{\frac{1}{2}(n\pi + kL) \frac{1}{2}(n\pi - kL)}. \quad (\text{A.6})$$

Using the sinc-function $\text{sinc}(x) = \frac{\sin(x)}{x}$ equation (A.4) can then be reformulated

$$\Phi_{n \text{ even}}(p) = -i\sqrt{\frac{L}{4\pi\hbar}} \left\{ 1 + \frac{\frac{1}{2}(n\pi - kL)}{\frac{1}{2}(n\pi + kL)} \right\} \text{sinc}\left(\frac{1}{2}(n\pi - kL)\right) \quad (\text{A.7})$$

$$= -i\sqrt{\frac{L}{\pi\hbar}} \frac{n\pi}{n\pi + kL} \text{sinc}\left(\frac{1}{2}(n\pi - kL)\right). \quad (\text{A.8})$$

Equivalently, the solution for odd n is given by

$$\Phi_{n \text{ odd}}(p) = \sqrt{\frac{L}{\pi\hbar}} \frac{n\pi}{n\pi + kL} \text{sinc}\left(\frac{1}{2}(n\pi - kL)\right). \quad (\text{A.9})$$

A.2 Works by the Author

A.2.1 Summaries of other works related to the topic of this thesis

A.2.1.1 Study of Charge Density Waves in VSe_2

Wouter Jolie, Timo Knispel, **Niels Ehlen**, Konstantin Nikonov, Carsten Busse, Alexander Grüneis, and Thomas Michely

Charge density wave phase of VSe_2 revisited.

Physical Review B **99** 115417 (2019)

Doi: <https://doi.org/10.1103/PhysRevB.99.115417>

1T-vanadium diselenide in its bulk form undergoes a quantum phase transition into a charge density wave ground state below critical temperatures around 100 K. Investigating this CDW ground-state with scanning tunneling microscopy revealed a 4×4 charge density modulation on the surface in line with earlier investigations. Performing scanning-tunneling spectroscopy (STS) in this ground state to determine the density of states revealed a strong reduction of the spectral weight at the Fermi level. This dip hinted at a (partial) gap opening as expected from a charge density wave transition. To rule out more simple explanations of this strong reduction, independent experimental methods were used to determine the density of states without the effects of the charge density wave. Angle-resolved photoemission spectroscopy images were taken along high-symmetry directions to determine the experimental band dispersion of the valence bands. A nearest neighbour tight-binding description of VSe_2 was developed and the parameters were fitted to the experimental dispersion relation. From this tight-binding fit, the electronic density of states without the charge density wave transition was calculated. Comparison with the STS data showed good agreement around the Fermi energy with the exception of the dip in spectral weight in the STS data right at the Fermi level. This confirmed the reduction of the density of states to be a feature of the partial gap opening in the charge density wave state. With this confirmation, the charge density wave gap was determined to be $2\Delta = (24 \pm 6)\text{meV}$.

A.2.1.2 Study of Charge Density Waves in TaS₂

Joshua Hall, **Niels Ehlen**, Jan Berges, Erik van Loon, Camiel van Efferen, Clifford Murray, Malte Rösner, Jun Li, Boris V. Senkovskiy, Martin Hell, Matthias Rolf, Tristan Heider, Maria C. Asensio, Lukasz Plucinski, Tim Wehling, Alexander Grüneis, and Thomas Michely

Environmental Control of Charge Density Wave Order in Monolayer 2H-TaS₂

ACS Nano **13**,9 10210-10220 (2019)

Doi: <https://doi.org/10.1021/acsnano.9b03419>

In monolayer 2H-tantalum disulfide grown on graphene/Ir(111) a 3×3 charge density wave was found *via* scanning tunneling microscopy. Scanning tunneling spectroscopy revealed a partial gap opening with a gap size of $2\Delta = (32 \pm 9)\text{meV}$.

In TaS₂ on Au(111) no charge density wave had been found experimentally, it was thus important to determine the differences between both systems to establish important aspects of charge density wave formation in TaS₂. In particular, the TaS₂ monolayer had been highly doped on the Au(111) substrate with an excess of 0.3 electrons per unit cell [223]. To get a good estimate of the doping level of the sample on Gr/Ir(111), a tight-binding model of 2H-TaS₂ was fitted to the experimental dispersion relation extracted from angle-resolved photoemission spectroscopy data and standing-wave patterns in STM/STS. From the tight-binding fit, the doping level was determined as an excess of 0.1 electrons per unit cell *versus* half-filling. Additional measurements of bilayer TaS₂ on graphene/Ir(111) revealed a 2×2 CDW structure. Similarly, lithium doping of monolayer TaS₂ islands showed hints of a 2×2 modulation of the charge density. These results hinted at doping levels being crucial in determining the appearance of a charge density wave ground state.

In order to bring together all these results, theoretical density functional theory calculations were used to determine critical points and lattice instabilities in the phonon dispersion for different doping levels and hybridizations between substrate and TaS₂. These calculations reproduced the 3×3 and 2×2 CDW phases and confirmed a change from the 3×3 phase to the 2×2 phase with Li doping. Crucially, no charge density wave phase was found for doping levels exceeding 0.27 electrons per unit cell, thus explaining the missing CDW phase in TaS₂ on Au(111).

A.2.1.3 Investigation of Graphene at High Doping Levels Towards the Lifshitz Transition

Martin G. Hell, **Niels Ehlen**, Boris V. Senkovskiy, Eddwi H. Hasdeo, Alexander Fedorov, Daniela Dombrowski, Casten Busse, Thomas Michely, Giovanni di Santo, Luca Petaccia, Riichiro Saito, and Alexander Grüneis

Resonance Raman Spectrum of Doped Epitaxial Graphene at the Lifshitz Transition.
ACS Nano Letters **18**, 9, 6045-6056 (2018)

Doi: <https://doi.org/10.1021/acs.nanolett.8b02979>

The doping dependence of the Raman G-peak phonon of graphene was studied. The peak showed a doping dependent broadening and a shift in energy. To assign the correct doping levels to a given Raman spectrum, the Fermi surface was examined using angle-resolved photoemission spectroscopy. From the ratio of the areas of the Fermi surface and the Brillouin zone, it was possible to experimentally determine the carrier concentration for a given amount of doping. Additionally, analyzing kink features in the dispersion allowed for the extraction of self-energies. This way, the electron-phonon coupling constant for individual doping levels could be determined. These doping dependent electron-phonon coupling constants could be used to determine the deformation potential D^2 . With these results as a basis, the observed experimental shift of the Raman G-mode could be fitted using a model that combined static and dynamic effects on the up- and downshift of the Raman modes with doping.

A.2.1.4 Exploration of the Electronic Properties of Graphene at the Lifshitz Transition

Niels Ehlen, Martin Hell, Giovanni Marini, Eddwi Hesky Hasdeo, Riichiro Saito, Yannic Falke, Mark Oliver Goerbig, Giovanni Di Santo, Luca Petaccia, Gianni Profeta, and Alexander Grüneis

Origin of the Flat Band in Heavily Cs-Doped Graphene.
ACS Nano **14**, 1, 1055-1069 (2020)

Doi: <https://doi.org/10.1021/acsnano.9b08622>

Increasing the Cs doping further compared to section A.2.1.3 allowed reaching the doping levels required for the Lifshitz transition. The deposited Cs grew in an ordered fashion as revealed by low-energy electron diffraction. A 2×2 and a $\sqrt{3} \times \sqrt{3}$

superstructure were visible in LEED images. Interestingly, the 2×2 superstructure produced a modulation of the crystal potential strong enough to induce zone-folding in angle-resolved photoemission spectroscopy. These zone-folding effects turned out to be crucial for the observation of a flat band around the Γ -point of the dispersion relation. The effects could be reproduced and disentangled by a simple tight-binding model. The zone-folding from the superstructure folded the three inequivalent M-points of the original Brillouin zone onto the Γ -point. In combination with the doping effect of the Cs layers, the saddle point of the original dispersion ended up at the Fermi level around Γ . There, it hybridized with the partially ionized Cs-band and caused an anti-crossing at the touching points. The anti-crossing flattened out the top part of the band and changed the topology of the dispersion from saddle to extremal point. The peculiar shape of the dispersion was crucial when investigating possible quantum phase transitions. The conversion of the saddle point to an extremum with mexican-hat like shape changed the energy-dependence of the density of states to $1/\sqrt{E}$. The density of states at the Fermi level was evaluated to be $N(0) = 2.56 \text{ eV}^{-1}$. With the help of the Stoner criterion, a critical on-site Coulomb potential of $U_{\text{crit}} = 0.4 \text{ eV}$ could be determined. This critical U_{crit} was much smaller than typical values of U in graphene [224]. Thus, a ferromagnetic instability for low temperatures was predicted, though other competing ground states could not be ruled out.

Density functional theory calculations found excellent agreement of theory and experiment and confirmed the high-density of states at the Fermi level. It could be shown that the hybridization with Cs and the resulting anti-crossing was crucial for the flatness of the band at the Fermi level.

A.2.2 List of Publications

Evolution of electronic structure of few-layer phosphorene from angle-resolved photoemission spectroscopy of black phosphorous

N. Ehlen *et al.*, *Phys. Rev. B*, **94**, 245410 (2016)

Doi: <https://doi.org/10.1103/PhysRevB.94.245410>

Spectroscopic characterization of $N = 9$ armchair graphene nanoribbons

B.V. Senkovskiy *et al.*, *Phys. Status Solidi RRL*, **11**:1700157 (2017)

Doi: <https://doi.org/10.1002/pssr.201700157>

Synthesis and spectroscopic characterization of alkali-metal intercalated ZrSe_2

K. Nikonov *et al.*, *Dalton Trans.*, **47**, 2986-2991 (2018)

Doi: <https://doi.org/10.1039/C7DT03756B>

Quasi-two-dimensional thermoelectricity in SnSe

V. Tayari *et al.*, *Phys. Rev. B*, **97**, 045424 (2018)

Doi: <https://doi.org/10.1103/PhysRevB.97.045424>

Direct observation of a surface resonance state and surface band inversion control in black phosphorus

N. Ehlen *et al.*, *Phys. Rev. B*, **97**, 045143 (2018)

Doi: <https://doi.org/10.1103/PhysRevB.97.045143>

Finding the hidden valence band of $N = 7$ armchair graphene nanoribbons with angle-resolved photoemission spectroscopy

B.V. Senkovskiy *et al.*, *2D Mater.*, **5**, 035007 (2018)

Doi: <https://doi.org/10.1088/2053-1583/aabb70>

Boron-Doped Graphene Nanoribbons: Electronic Structure and Raman Fingerprint

B.V. Senkovskiy *et al.*, *ACS Nano*, **12**, 8, 7571–7582 (2018)

Doi: <https://doi.org/10.1021/acsnano.8b04125>

Resonance Raman Spectrum of Doped Epitaxial Graphene at the Lifshitz Transition

M.G. Hell *et al.*, *Nano Lett.*, **18**, 9, 6045–6056 (2018)

Doi: <https://doi.org/10.1021/acs.nanolett.8b02979>

Emergent Dirac carriers across a pressure-induced Lifshitz transition in black phosphorus

P. Di Pietro *et al.*, *Phys. Rev. B*, **98**, 165111 (2018)

Doi: <https://doi.org/10.1103/PhysRevB.98.165111>

Narrow photoluminescence and Raman peaks of epitaxial MoS₂ on graphene/Ir(111)

N. Ehlen *et al.*, *2D Mater.*, **6**, 011006 (2018)

Doi: <https://doi.org/10.1088/2053-1583/aaebd3>

Combined Ultra High Vacuum Raman and Electronic Transport Characterization of Large-Area Graphene on SiO₂

M.G. Hell *et al.*, *Phys. Status Solidi B*, **255**:1800456 (2018)

Doi: <https://doi.org/10.1002/pssb.201800456>

Charge density wave phase of VSe₂ revisited

W. Jolie *et al.*, *Phys. Rev. B*, **99**, 115417 (2019)

Doi: <https://doi.org/10.1103/PhysRevB.99.115417>

Comprehensive tunneling spectroscopy of quasifreestanding MoS₂ on graphene on Ir(111)

C. Murray *et al.*, *Phys. Rev. B*, **99**, 115434

Doi: <https://doi.org/10.1103/PhysRevB.99.115434>

Environmental Control of Charge Density Wave Order in Monolayer 2H – TaS₂

J. Hall *et al.*, *ACS Nano*, **13**, 9, 10210–10220 (2019)

Doi: <https://doi.org/10.1021/acsnano.9b03419>

Origin of the Flat Band in Heavily Cs-Doped Graphene

N. Ehlen *et al.*, *ACS Nano*, **14**, 1, 1055–1069 (2020)

Doi: <https://doi.org/10.1021/acsnano.9b08622>

Reversible crystalline-to-amorphous phase transformation in monolayer MoS₂ under grazing ion irradiation

P. Valerius *et al.*, *2D Mater.*, **7**, 025005 (2020)

Doi: <https://doi.org/10.1088/2053-1583/ab5df4>

Massive and massless charge carriers in an epitaxially strained alkali metal quantum well on grapheneN. Ehlen *et al.*, *Nat. Commun.*, **11**, 1340 (2020)Doi: <https://doi.org/10.1038/s41467-020-15130-1>**Photothermal bottom-up graphene nanoribbon growth kinetics**Y. Falke *et al.*, *Nano Letters*, **20**, 7, 4761–4767 (2020)Doi: <https://doi.org/10.1021/acs.nanolett.0c00317>**A.2.3 List of Major Presentations****Narrow photoluminescence and Raman peaks of epitaxial MoS₂ on graphene/Ir(111)***EMRS Spring Meeting 2019*, Nizza, France, May 2019

Contributed Talk

Narrow photoluminescence and Raman peaks of epitaxial MoS₂ on graphene/Ir(111)*ELETTRA Synchrotron Scientific Seminar*, Trieste, Italy, January 2019

Invited Talk

Evolution of electronic structure of few-layer phosphorene from angle-resolved photoemission spectroscopy of black phosphorous*DPG Spring Meeting 2017*, Dresden, Germany, March 2017

Contributed Talk

Electron energy dispersion of pristine and alkali-metal doped black phosphorous: a combined ARPES and tight-binding study*European Conference on Nanofilms 2016*, Bilbao, Spain, October 2016

Contributed Talk

Electronic Properties of Black Phosphorus and Few-Layer Phosphorene: a combined ARPES and tight-binding study*ewe/G2D*, Bensberg, Germany, May 2016

Poster

A.3 Dedication and Thanks

I want to thank Professor Alexander Grüneis for the support and help throughout my work. I owe a lot to him for what I have learned during my time at his research group. His guidance was invaluable for my work. I also want to thank Professor Markus Grüninger, Professor Andrea Damascelli, Professor Achim Rosch, and Dr. Wouter Jolie for their roles for this thesis as second examiner, third examiner, chair of the committee, and notes taker respectively.

My wife Alexandra Ehlen provided emotional support throughout the years and was very accepting of all the travels I did for work. For that, I thank her deeply.

Others I want to thank include:

My parents and my brother who were important support especially - but not only - during the Corona pandemic.

My dear colleagues and collaborators I worked and published with. In particular Martin Hell, Boris Senkovskiy, and Yannic Falke with whom I worked many years on several topics and published many papers. Our scientific and non-scientific discussions were invaluable. All other members of our work group contributed to the stimulating and exciting environment that made the research in this thesis possible. The list includes, but is not limited to, Alexander Fedorov, Konstantin Nikonov, Alexander Chernov, Nihit Saigal, Jun Li, Hesky Hasdeo, and Alessandro D'Elia.

I also thank Professor Thomas Michely and his work group for many successful collaborations between our work groups. In particular, I thank Wouter Jolie not only for his role as a note taker during the defence of my thesis but also for the fruitful conversations resulting in several collaborations. I also want to name among others Joshua Hall, Timo Knispel, Clifford Murray, and Phillip Valerius for our cooperations on transition-metal dichalcogenides.

I want to thank Professors Mark O. Goerbig and Dmitry Usachov for hosting me at their research groups in Paris and Saint Petersburg respectively.

The beamline scientists and technicians at Diamond Synchrotron in Oxford, BESSY II in Berlin, Soleil Synchrotron in Paris and Elettra Sincrotrone in Trieste. Their excellent work at their respective endstations enabled many of the experiments discussed in this thesis. These people include José Avila, María C. Asensio, Timur Kim, Alexei Nefedov, and Anna Makarova. Special thanks to Luca Petaccia and Giovanni Di Santo from BaDElPh beamline at Elettra for hosting us many times throughout my work. They always ensured perfect measurement conditions and were involved with many of the publications mentioned in this thesis.

Another thanks to Giovanni Marini and Professor Gianni Profeta from the university of L'Aquila for their support on the theory side. Their calculations and our discussions were a large help in understanding many of the reported results in this thesis. I also thank Antonio Sanna from the Max Plank Institute of microstructure physics for his density function calculations and theoretical support of our publications on black phosphorus.

All other co-authors of the publications mentioned in this thesis also deserve many thanks, their contributions and knowledge were invaluable.

All the dear friends and colleagues throughout Europe and beyond who I got to know during my work on this thesis. Among the ones not yet mentioned in this section yet I especially want to name Andrea Bliesener and Robin Bernhardt.

All the people working in the physics department of the University of Cologne, who provide the academic, technical and administrative framework without which this thesis would not have been possible. You made coming to work a pleasure.

And finally anyone who supported me throughout the years and whom I unfairly forgot to mention in this dedication.

A.4 Data Availability

The samples measured in the publications were destroyed in the measurement process, recipes for reproducing the samples are given in their corresponding publications. The data collected is backed-up on our work-group internal PCs and available upon request. The data is additionally backed up on the back-up TSM service of the University of Cologne under the node “nehlen2”.

A.5 Used Tools

The data reported in this thesis was collected at many different experimental setups. The details on the data collection are given within the individual publications. The data analysis was performed with a combination of Igor Pro 6.0 [225] and python [226]. The python scripts produced during the work on this thesis are backed up on the TSM service of the University of Cologne (see appendix A.4). Figures were produced using Igor Pro [225], python's matplotlib library [227], the mayavi python api [228], and Blender 3D 2.8 [229]. In some cases, InkScape was used to combine the individual outputs into one whole figure.

The tight-binding codes were written using python, relying on the numpy [230] and scipy [231] libraries for the linear algebra and minimization procedures. The code is included on the TSM backup.

L^AT_EX was used for the production of this thesis.

A.6 Declaration of Authorship

(Gemäß der Promotionsordnung vom 12. März 2020)

Hiermit versichere ich an Eides statt, dass ich die vorliegende Dissertation selbstständig und ohne die Benutzung anderer als der angegebenen Hilfsmittel und Literatur angefertigt habe. Alle Stellen, die wörtlich oder sinngemäß aus veröffentlichten und nicht veröffentlichten Werken dem Wortlaut oder dem Sinn nach entnommen wurden, sind als solche kenntlich gemacht. Ich versichere an Eides statt, dass diese Dissertation noch keiner anderen Fakultät oder Universität zur Prüfung vorgelegen hat; dass sie - abgesehen von unten angegebenen Teilpublikationen und eingebundenen Artikeln und Manuskripten - noch nicht veröffentlicht worden ist sowie, dass ich eine Veröffentlichung der Dissertation vor Abschluss der Promotion nicht ohne Genehmigung des Promotionsausschusses vornehmen werde. Die Bestimmungen dieser Ordnung sind mir bekannt. Darüber hinaus erkläre ich hiermit, dass ich die Ordnung zur Sicherung guter wissenschaftlicher Praxis und zum Umgang mit wissenschaftlichem Fehlverhalten der Universität zu Köln gelesen und sie bei der Durchführung der Dissertation zugrundeliegenden Arbeiten und der schriftlich verfassten Dissertation beachtet habe und verpflichte mich hiermit, die dort genannten Vorgaben bei allen wissenschaftlichen Tätigkeiten zu beachten und umzusetzen. Ich versichere, dass die eingereichte elektronische Fassung der eingereichten Druckfassung vollständig entspricht.

Teilpublikationen

Evolution of electronic structure of few-layer phosphorene from angle-resolved photoemission spectroscopy of black phosphorous

N. Ehlen *et al.*, *Phys. Rev. B*, **94**, 245410 (2016)

Doi: <https://doi.org/10.1103/PhysRevB.94.245410>

Direct observation of a surface resonance state and surface band inversion control in black phosphorus

N. Ehlen *et al.*, *Phys. Rev. B*, **97**, 045143 (2018)

Doi: <https://doi.org/10.1103/PhysRevB.97.045143>

Narrow photoluminescence and Raman peaks of epitaxial MoS₂ on graphene/Ir(111)

N. Ehlen *et al.*, *2D Mater.*, **6**, 011006 (2018)

Doi: <https://doi.org/10.1088/2053-1583/aebd3>

Massive and massless charge carriers in an epitaxially strained alkali metal quantum well on graphene

N. Ehlen *et al.*, *Nat. Commun.*, **11**, 1340 (2020)

Doi: <https://doi.org/10.1038/s41467-020-15130-1>



Autor

17.06.2021, Köln

Datum